# Numerical Simulation of the Ore Forming Fluid Migration in the Sediment-hosted Stratiform Copper Deposit, Zambian Copperbelt.

**Lyudmyla Koziy**

M. Sc. (National Taras Shevchenko University of Kyiv, Ukraine)

UNIVERSITY OF TASMANIA

Submitted in fulfillment of the requirements for the Degree of Doctor of Philosophy

Hobart, Australia
January, 2007

# Declaration

This thesis contains no material which has been accepted for the award of any other degree or diploma in any tertiary institution and, to the best of my knowledge and belief, contains no copy or paraphrase of material previously published or written by another person, except where due reference is made in the text of the thesis.

This thesis may be available for loan and limited copying in accordance with the Copyright Act 1968.

Lyudmyla Koziy

January, 2007

# Abstract

A finite element numerical model was developed and applied to study density-driven convective flow as a potential ore-forming mechanism for sediment-hosted stratiform copper deposits in the Zambian Copperbelt (ZCB).

The numerical model simulates free thermohaline convection in an inhomogeneous, anisotropic, compressible porous medium completely saturated by a compressible fluid bearing dissolved sodium chloride. The model also takes into account possible inner salt and heat sources to simulate rock salt dissolution and heat emission by a magmatic intrusion.

The model employs the finite element Petrov-Galerkin method with non-symmetrical 'upwinding' weighting functions. An implicit time-stepping scheme with 'weightings' involves an iterative procedure within each time step to handle the nonlinearity of the problem.

The model validation was carried out by 1) comparison of the numerical results with analytical solutions for simplified problems; 2) application of the model to three problems of free thermal convection (anisotropy effect, convective cell aspect ratio as a function of the Rayleigh number, and free discharge) and comparison with published results of numerical and experimental studies; 3) simulation of the ground-water flow in a complex faulted sedimentary section of the McArthur Basin (Northern Territory, Australia) to compare the model output with the results of an independent study (Garven et al., 2001).

The model was applied to a 43.5km x 17km numerical domain, representing a theoretical geological section of the ZCB. The section incorporates elements of basement, footwall succession (Mindola Clastic Formation), Ore Shale, hanging wall Upper Roan dolomites, salt layer, Mwashia dolomitic and siliciclastic members and overlying Kundelungu shales. As a layer-cake structure of the section shows no significant topography, density variations due to geothermal gradient and Roan Salt dissolution are considered the main mechanism driving pore fluid circulation.

Sixteen potential paleo-hydrologic scenarios were tested to study factors controlling ore-forming fluid flow: fault network configuration, salt layer geometry, rock salt physical characteristics, and piercement structures.

The simulations showed notable convective flow through the basement; the result corroborates the hypothesis of a basement source for the metals contained in the Copperbelt orebodies (Sweeney et al., 1991). Supporting the study of fluid inclusion data (Annels, 1989), the modeling confirms ore body formation under low-temerature and high salinity conditions. It also showed significant lateral flow of the rising basement fluid through the Mindola Clastic Formation beneath the Ore Shale seal; as a consequence, notable amounts of Cu can be precipitated in the footwall clastics even assuming its low depositional efficiency, as supported by geochemical and petrographic data. Low permeability shales and the salt layer form barriers to cross-stratal fluid flow; nevertheless, horizontal flow rates in the Ore Shale are sufficient for formation of ore bodies assuming this unit was an effective chemical trap. Tested scenarios revealed the essential influence of Upper Roan Salt dissolution on fluid flow and, therefore, amount of metal precipitated.

In summary, the study suggests that free convection driven by geothermal gradient and dissolution of the massive Roan Salt sheet can be an effective ore-forming mechanism in the stratiform ZCB system. The rising basement fluid is redirected laterally beneath the Copperbelt Orebody Member – Mindola Clastic Formation interface. The flow rates of the metal-transporting fluid are shown to be capable of forming ore bodies within the Ore Body Member and underlying footwall. The modeled amount of potentially precipitated Cu agrees with the available geochemical and petrographic data.

# Acknowledgements

I would like to express my sincere gratitude to my principal supervisor Ross Large for his support, considerable input, encouragement, and patience throughout my thesis. I am also very grateful for him allowing me to follow my own approach to fulfillment of this project.

I would also like to thank my second supervisor Stuart Bull for sharing his knowledge and experience that very much facilitated my work on the 'geologic' part of the thesis and greatly contributed to my understanding of the basin geology.

I am grateful to David Selley for his help in development of the strategy of the simulation scenarios and guidance in the vast amount of publications on the ZCB.

I appreciate beneficial discussions, at different stages of the project, with David Cooke, Ron Berry, Peter McGoldrick and Michael Solomon. I also acknowledge the help of Jianwen Yang and Christian Schardt in my first steps in groundwater modeling.

A special thank goes to Janet Counsell for her help in improvement of my writing skills.

Finally, I am grateful to my family and friends for their unfailing support and encouragement.

# Content

# List of Figures

# List of Tables

# List of Appendices

# Appendix 4    Middle primary fault extension. Supplementary figures.

# 1 Introduction

## 1.1 Background, significance and aims of the study

Sediment-hosted stratiform copper deposits represent one of the major sources of copper. Their contribution into the world copper production constitutes about 20-25% (Kirkham, 1989). Some of the deposits also produce significant amounts of cobalt, silver, uranium, and other metals. The Zambian Copperblelt (ZCB) is a world-class sediment-hosted copper and cobalt district and forms a significant part of the world dominating sediment-hosted stratiform copper province, the Central African Copperbelt.

Though the problem of the origin of sediment-hosted stratiform copper deposits has been studied for more than a century (Boyle, 1989), the aspects of ore formation are still debated including: source of metals and other constituents (sulphur and reductants); origin of transporting fluids; manner of transport of the constituents to the deposition sites; mechanism driving metal-bearing fluid migration; timing of mineralization; mechanism of sulfide precipitation (Boyle, 1989; Selley et al, 2005).

Some geologists recognized the deposits to be syngenetic in origin, acknowledging the link between stratigraphy and ore location (Mendelsohn, 1961; Fleischer et al., 1976). Other, taking into account the evidence of postdepositional metasomatism, replacive texture, and time constrains for metal accumulation, considered them epigenetic hydrothermal (Bateman, 1930; Jackson, 1932; Unrug, 1988; Hoeve and Quirt, 1989). At present, a diagenetic origin for the stratiform copper-cobalt deposits is generally accepted (Annels, 1989). However, the question of metal provenance still remains.

In many studies (Jowett, 1989; Walker, 1989; Sverjensky, 1989) red-beds, incorporating, as detritus, copper-rich mafic rocks (basalt) or felsic rocks which contain copper-rich mafic minerals (horn blende, pyroxene, biotite, magnetite) are viewed as a source of metals. However, unlike other well-known districts such as the Kupferschiefer (Central Europe) and White Pine (USA), in the ZCB, the amount of metal in the deposits is large relative the volume of red-beds. This gave rise to other hypotheses, for example, Hitzman's (2000) suggestion about a large-scale tectonic displacement of the Zambian deposits from their source rocks. Another possible

source of the copper has been considered – intrusive granites or the rocks of the Basement Complex. However, it was demonstrated, (Garlick and Brummer, 1951) that the granites were part of the basement. Considering the basement as a potential source rock, natural questions arise concerning the possibility of significant fluid flow through this low-permebility unit, the causes of the fluid migration, and the mechanism that delivers the brine to the depositional sites.

The finite-element numerical model, developed as a part of this project, has been applied to a two-dimensional section which incorporates the main features of the ZCB (rift basin structure of the Lower Roan Group, layer-cake configuration of the overlying marine strata). The aim of this modeling is to provide answers to the following questions:

- plausibility of the basement as a source of metals;
- possibility of significant fluid flow through this low-permeability section;
- effectiveness of free thermohaline convection (induced by the geothermal gradient coupled with dissolution of the Upper Roan Salt) as a mechanism driving paleoflow;
- influence of various factors (thickness of the section, configuration of the fault network, geometry and physical properties of the salt layer, piercement structure cutting through the low-permeability Upper Roan and Lower Mwashia strata) on the structure and intensity of the pore fluid flow;
- possibility of the formation of high-grade ore bodies within the time constraints of the basin evolution;
- availability of thermal and chemical (chloride concentration) conditions necessary for the mineralization;
- potential of the saline brine, formed as a result of the Upper Roan Salt dissolution, to be the ZCB ore fluid.

In previous studies, various mechanisms driving fluid flow have been considered. Thus, Kirkham (1989) outlines the following: (1) evaporitic pumping in sabkhas (Renfro, 1974; Smith, 1976); (2) formation dewatering during compaction (White, 1971; Ruelle, 1982; Lustwerk and Wasserman, 1989); (3) the paleotopographic gravity hydraulic head in underlying fluvial aquifers that persist after a major marine transgression (von Hoyningen-Huene, 1963; White, 1971; Lur'ye and Gablina, 1972); (4) the release of pressurized formational fluids during

tectonic activity (Breit et al., 1987); (5) topographic inversion (Garven and Freeze, 1984; Bethke, 1986; Oliver, 1986; Appold and Garven, 2000); (6) the decrease in buoyancy and rise of fluids caused by thermal activity (Jowett, 1986; Garven et al., 2001; Yang et al., 2004a); (7) the diapiric rise of salt structures causing and permitting fluid migration (Light et al., 1987). Additional to this list, free thermohaline convection should be mentioned as a mechanism driving groundwater flow near salt formations, e.g. domes (Herbert et al., 1988; Evans et al., 1991; Oldenburg and Pruess, 1995) and sheets (Sarkar et al., 1995; Simmons et al., 2001).

Significant volumes of polilithic breccia within the Upper Roan Group (Binda and Porada, 1995; Porada and Berhorst, 2000) have been ascribed a sedimentary interpretation related to salt dissolution-mobilization processes (Wendorff, 2000a; 2000b; 2003). The widespread presence of stratabound breccias in the ZCB suggests the existence, at some stage, of substantial halite bodies. A novel aspect of the present study is that the model takes into account a constant NaCl influx into the system due to the Upper Roan Salt layer dissolution, incorporating inner sources of salt.

Numerical models have been previously used for the simulation of ore forming fluid flow for several types of deposits: fault-controlled tin deposit (Jiang et al., 1997), basin bound MVT deposits (Garven and Freeze, 1984; Appold and Garven, 2000), SEDEX deposits (Garven et al., 2001; Yang, 2004b), VHMS deposit (Schardt et al., 2005). The present study is among a few (Jowett, 1986: one-dimensional finite-difference model of conductive heat flow; Swenson et al., 2004: a two-dimensional model of topography- and thermally-driven flow) applications of a numerical model to the study of a sediment-hosted stratiform copper deposit, and it is a first attempt to use a numerical model of this complexity for the ZCB.

The two-dimensional model simulates free thermohaline convection in an inhomogeneous, anisotropic, compressible porous medium saturated by a compressible fluid bearing dissolved NaCl. The model also allows inner salt and heat sources to simulate rock salt dissolution and heat emission by a magmatic intrusion. The model employs the finite element Petrov-Galerkin method with non-symmetrical 'upwinding' weighting functions. An implicit time-stepping scheme with 'weightings' involves an iterative procedure within each time step to handle the nonlinearity of the problem.

## 1.2 Organization of the thesis

A mathematical model generally includes the following components:

- physical model of the object;
- mathematical description (set of governing equations, boundary and initial condition);
- numerical solution;
- model validation;
- model application and interpretation of the results;

The organization of the thesis is consistent with this structure. The physical model, the concept of porous media, continuum approach to its description on the macroscopic level etc., is not addressed here, as it has been elaborated for years and is covered in a number of theoretical works, for example, (Bear, 1972; Bear and Corapcioglu, 1982).

Chapter 2 presents the mathematical description of the model, a set of governing equations, boundary and initial conditions, and also gives a justification for the choice of equations of state.

Chapter 3 contains the description of the numerical procedure used to solve approximately the set of governing equations. The chapter covers the procedure of obtaining the weak (integral) form of each governing equation, the explanation of the choice of shape and weight functions, the way of handling the mesh of non-rectangular finite elements, the time-stepping scheme, and the method used for the solution of the final matrix equation.

Since there is no way to check the correctness of the results of the simulation for the ZCB section, significant consideration was given to validation of the model. Chapter 4 contains step-by-step comparison of the simulation results with the analytic solutions obtained for the simplified one-dimensional problem and testing of the time-stepping procedure. Then the model is applied to several problems of free convection in porous media (anisotropy effect, convective cell aspect ratio as a function of the Rayleigh number, and free discharge). The results are compared with a number of published works. After that, an attempt is made to reproduce results of the simulation by Garven et al. (2001) on the McArthur basin. In this case, the model is applied to a faulted sedimentary structure, considering free thermal convection a driving mechanism for the ground-water flow. The last step is free thermohaline convection simulation for three sets of boundary and initial conditions, which shows

a good correspondence with published data. The fulfilled tests provide evidence to conclude that the built numerical model produces credible results.

Chapter 5 gives a general description of the ZCB geology, explains chosen values of physical properties of the rock units comprising the model section and parametrization of rock salt dissolution.

Chapter 6 incorporates simulation results on fourteen scenarios which investigate the effect of the section thickness (which grows as younger strata are deposited), geometry and physical properties of the salt layer (degree of anisotropy, permeability value), faulting structures piercing Upper Roan, Lower Mwashia and Kundelungu strata, salt sheet dissolution and the salt transport involvement into the simulation. In the last section of the chapter, the plausibility of formation of high-grade ore bodies within the Copperbelt Orebody Member and the footwall is assessed.

Chapter 7 contains summarizing conclusions on the results of the study.

The Appendix includes supplementary figures which are thought to be illustrative for some details of the numerical study. It also contains results of the simulation for two additional scenarios which helped to develop the strategy of the last set of case studies.

# 2  Mathematical Model

A mathematical model consists of a set of differential equations that are known to govern the flow of groundwater. The governing equations presented below originate from basic physical principles and are based on the continuum approach to the representation of a porous medium (Bear, 1972). Euler's method for describing motion in a fluid system is adopted (Loytsyanski, 1970).

The porous medium is assumed to be

- inhomogeneous,
- anisotropic,
- compressible,
- completely saturated by a compressible fluid bearing dissolved sodium chloride.

## 2.1 Governing equations

A set of governing equations describing a continuum must reflect the following physical laws: the principle of conservation of matter, the first law of thermodynamics, and Newton's second law. These principles result in the continuity equation, mass transport equation, heat transport equation and momentum transport equation.

### 2.1.1 Continuity equation

For a porous medium continuum, the fluid mass conservation equation may be presented in the general form as (Bear, 1972):

$$\frac{\partial(\rho_f n)}{\partial t} + div(\rho_f \vec{q}) = 0, \qquad\qquad \textbf{Equation 2.1}$$

where

| | | |
|---|---|---|
| $n$ | = | porosity |
| $\rho_f$ | = | pore fluid density |
| $\vec{q} = (q_1, q_2, q_3)$ | = | the specific discharge vector |
| $t$ | = | time |

It is assumed that the porous matrix may undergo deformation, but only vertical consolidation of the medium is considered. In this case, using equivalent fresh-water head formulation, (2.1) may be rewritten in the form:

$$\underbrace{\rho_f[n\beta_c + (1-n)\alpha_c]\rho_0 g}_{S_{0\varphi}}\frac{\partial \varphi_0}{\partial t} + \frac{\partial}{\partial x_i}(\rho_f q_i) = 0,$$                        **Equation 2.2**

where the summation convention is applicable and the following notation is used:

| | | |
|---|---|---|
| $\rho_0$ | = | reference value of fluid density |
| $\varphi_0 = \dfrac{p}{\rho_0 g} + z$ | = | equivalent freshwater head |
| $p$ | = | pressure |
| $z$ | = | elevation |
| $g$ | = | gravitational acceleration |
| $S_{0\varphi} = \rho_f \rho_0 g[n\beta_c + (1-n)\alpha_c]$ | = | specific mass storativity related to potential changes |
| $\alpha_c$ | = | coefficient of bulk compressibility of the porous matrix |
| $\beta_c$ | = | coefficient of compressibility of the fluid |
| $\vec{x} = (x_1, x_2, x_3)$ | = | Cartezian coordinates |

Accepting the Boussinesq approximation, under which density variations are considered as influential only in buoyancy terms, (2.2) becomes:

$$S_0 \frac{\partial \varphi_0}{\partial t} + \frac{\partial}{\partial x_i}(q_i) = 0,$$                        **Equation 2.3**

where

$$S_0 = \rho_0 g[n\beta_c + (1-n)\alpha_c] \qquad = \text{ specific volumetric storativity}$$

## 2.1.2 Equation of motion

In a porous medium, the momentum transport equation is expressed in the form of Darcy's law (Bear, 1972):

$$q_i = nV_i = -\frac{k_{ij}}{\mu}\left[\frac{\partial p}{\partial x_j} + \rho_f g \frac{\partial z}{\partial x_j}\right],$$                        **Equation 2.4**

where

| | | |
|---|---|---|
| $V_i$ | = | pore velocity components |
| $k_{ij}$ | = | components of the permeability tensor |
| $\mu$ | = | dynamic viscosity of the fluid |

or, in the head-based formulation:

$$q_i = -\frac{k_{ij}\rho_0 g}{\mu}\left[\frac{\partial \varphi_0}{\partial x_j} + \frac{\rho_f - \rho_0}{\rho_0}\frac{\partial z}{\partial x_j}\right] = -K_{ij}\left[\frac{\partial \varphi_0}{\partial x_j} + \rho_r \frac{\partial z}{\partial x_j}\right],$$

**Equation 2.5**

where

$$K_{ij} = \frac{k_{ij}\rho_0 g}{\mu}$$     =  components of the hydraulic conductivity tensor

$$\rho_r = \frac{\rho_f - \rho_0}{\rho_0}$$     =  relative fluid density,

Sedimentary rocks show appreciable anisotropy. In stratified sediments, permeability has been found to be greater parallel to the bedding than perpendicular to it (Pettijohn, 1975). So we define components of the permeability tensor, taking into account the anisotropy of the porous matrix and also the effect of the inclination of the sediment bedding plane relative to the global coordinate system (Fig. 2.1).
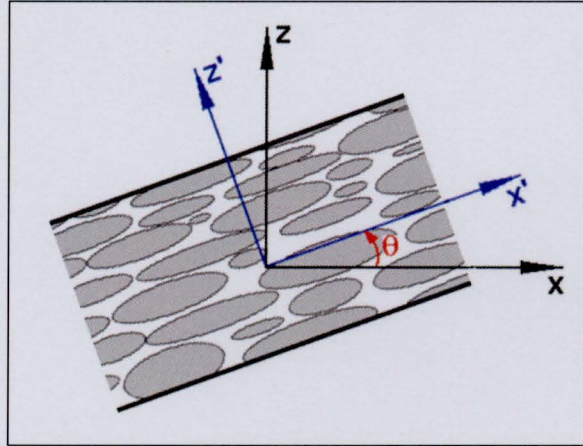


**Figure 2.1 Local coordinate system aligned with bedding.**

Let $k_{lw}$ and $k_{cw}$ be coefficients of permeability in the direction parallel and perpendicular to bedding relatively and $\theta$ is the counterclockwise rotation angle of the local coordinate system, aligned with bedding, relative to the global coordinate system. Components of the permeability tensor in the global coordinate system are expressed (Bear, 1972):

$$k_{11} = \frac{k_{lw} + k_{cw}}{2} + \frac{k_{lw} - k_{cw}}{2}\cos 2\theta\,;$$

$$k_{12} = k_{21} = -\frac{k_{lw} - k_{cw}}{2}\sin 2\theta\,;$$

**Equation 2.6**

$$k_{22} = \frac{k_{lw} + k_{cw}}{2} - \frac{k_{lw} - k_{cw}}{2}\cos 2\theta\,;$$

where

$k_{lw}$               =   permeability lengthwise the sediment layer

$k_{cw}$              =   permeability crosswise the sediment layer

$\theta$                  =   angle between x-axis and bedding plane of the sediment layer

## 2.1.3 Heat balance equation

In a porous medium heat is transported in the following ways (Bear, 1972):

1)      through the fluid phase by conduction;

2)      through the fluid phase by advection;

3)      through the fluid phase by heat dispersion due to the presence of grains and interconnected pore system;

4)      through the solid phase by conduction;

5)      from the solid phase to the fluid one.

These mechanisms are reflected in the equation of conservation of fluid energy:

$$c_f \rho_f \left( \frac{\partial T_f}{\partial t} + V_i \frac{\partial T_f}{\partial x_i} \right) = -\frac{\partial J_{hi}}{\partial x_i} + h_f (T_s - T_f) + \varepsilon + \rho_f Q_T^f \qquad \textbf{Equation 2.7}$$

and the equation of conservation of energy of the solid matrix:

$$c_s \rho_s \frac{\partial T_s}{\partial t} = -\frac{\partial J_{hsi}}{\partial x_i} + h_s (T_f - T_s) + \rho_s Q_T^s , \qquad \textbf{Equation 2.8}$$

where

$c_f$              =   heat capacity of the fluid (specific heat)

$T_f$              =   temperature of the fluid phase

$T_s$              =   temperature of the solid phase

$h_f$              =   heat transfer coefficient for fluid phase

$J_{hi}$            =   components of the heat flux due to conduction, dispersion and presence of concentration gradient

$\varepsilon$                 =   the rate of energy dissipation by viscous stresses

$Q_T^f$            =   specific rate of heat emission from heat sources in the fluid phase

$\rho_s$               =   density of the solid phase

$c_s$               =   heat capacity of the solid matrix

$J_{hsi} = -(\lambda_s)_{ij} \dfrac{\partial T_s}{dx_j}$     =   conductive heat flux in the solid

$(\lambda_s)_{ij}$          =   thermal conductivity of the solid matrix (second –rank symmetrical tensor)

$h_s$              =   heat transfer coefficient for solid phase

$Q_T^s$            =   specific rate of heat emission from heat sources in the solid phase

The term $c_f \rho_f V_i \dfrac{\partial T_f}{\partial x_i}$ in the left side of the equation (2.7) accounts for the

changes in thermal energy due to advection, the actual movement of fluid mass from one location to another. Terms in the right side represent heat flux due to conduction, dispersion and presence of concentration gradient (first term), heat transfer from the solid matrix to the fluid phase (second term), dissipation of thermal energy by viscous stresses (third term), and heat emission from inner sources (fourth term).

Here $J_{hi}$ can be expressed as:

$$J_{hi} = -\lambda_f \delta_{ij} \frac{\partial T_f}{\partial x_j} - (\lambda_{disp})_{ij} \frac{\partial T_f}{\partial x_j} - (L_D)_{ij} \frac{\partial S}{\partial x_j},$$   **Equation 2.9**

where

| | | |
|---|---|---|
| $\lambda_f$ | = | coefficient of thermal conductivity of the fluid saturating the void space of the porous medium domain |
| $\delta_{ij}$ | = | Kronecker symbol |
| $(\lambda_{disp})_{ij}$ | = | components of the tensor of thermal dispersion |
| $(L_D)_{ij}$ | = | Duffour coefficients |
| $S$ | = | mass fraction, defined as mass of the dissolved substunce per unit mass of solution |

Accordingly to (Bear, 1972),

$$(\lambda_{disp})_{ij} = \rho_f c_f \left[ \alpha_T V_q \delta_{ij} + (\alpha_L - \alpha_T) \frac{q_i q_j}{V_q} \right],$$   **Equation 2.10**

where

| | | |
|---|---|---|
| $\alpha_L$ | = | longitudinal thermodispersivity of the fluid |
| $\alpha_T$ | = | transversal thermodispersivity of the fluid |
| $V_q = \sqrt{q_i q_i}$ | = | absolute Darcy fluid flux |

Equation (2.8) represents the balance of the heat flux through the **solid phase** by conduction and heat transfer from the fluid phase to the solid matrix.

In many cases, the difference in temperature between the fluid and the solid is considered as negligible (Bear, 1972), i.e. $T_f = T_s \equiv T$. Based on this assumption, by adding (2.7) multiplied by porosity, $n$, to (2.8) multiplied by *(1-n)*, these two equations reduce to the single **equation of conservation of energy of the saturated porous medium**:

$$c_e \frac{\partial T}{\partial t} + \rho_f c_f q_i \frac{\partial T}{\partial x_i} = \frac{\partial}{\partial x_i} \left( \{(\lambda_e)_{ij} + n(\lambda_{disp})_{ij}\} \frac{\partial T}{\partial x_j} \right) + n \frac{\partial}{\partial x_i} \left( (L_D)_{ij} \frac{\partial S}{\partial x_j} \right) + n\varepsilon + Q_T$$

**Equation 2.11**

Here

$$c_e = n\rho_f c_f + (1-n)\rho_s c_s$$

is the effective heat capacity of the saturated porous medium,

$$(\lambda_e)_{ij} = \left[ n\lambda_f \delta_{ij} + (1-n)(\lambda_s)_{ij} \right]$$

is the effective thermal conductivity of the saturated porous medium;

where

$$Q_T = n\rho_f Q_T^f + (1-n)\rho_s Q_T^s$$

is the rate of heat emission from inner sources. $Q_T$ may describe, for example, heat production as a consequence of radioactive decay or, as in this study, heat emitted by the magmatic intrusion into the sedimentary structure.

In the model being described, we do not take into account the Dufour effect and the effect of heat dissipation due to viscous stress, hence the final form of the heat balance equation becomes:

$$c_e \frac{\partial T}{\partial t} + \rho_f c_f \underbrace{nV_i}_{q_i} \frac{\partial T}{\partial x_i} = \frac{\partial}{\partial x_i}\left( \{(\lambda_e)_{ij} + n(\lambda_{disp})_{ij}\}\frac{\partial T}{\partial x_j} \right) + Q_T. \qquad \textbf{Equation 2.12}$$

## 2.1.4 Dissolved substance balance equation

If we define a mass density $\rho_\alpha$ of a dissolved substance $\alpha$ as the mass of $\alpha$ per unit volume of solution, then the equation of mass conservation of $\alpha$ species is (Bear, 1972):

$$\frac{\partial \rho_\alpha}{\partial t} + \vec{V} grad\rho_\alpha - div\left[(\underline{K_S} + \underline{D_S})grad\rho_\alpha\right] = I_\alpha, \qquad \textbf{Equation 2.13}$$

where $\underline{D_S}$ is a second-rank tensor relating the dispersive flux to $grad\rho_\alpha$, the tensor $\underline{K_S}$ describes the effect of molecular diffusion in a porous medium.

Here $\underline{K_S} = K_S E$, $K_S$ is the coefficient of molecular diffusion in a porous medium and $E$ is the identity matrix. The term in the right side of (2.13), $I_\alpha$, describes the rate of inner sources of the substance $\alpha$.

Introducing a dimensionless salinity of the interstitial fluid, S, as the total dissolved mass per unit mass of solution (Phillips, 1991), which, in the case of the only dissolved admixture component present, is identical with the mass fraction of species $\alpha$ (Bear, 1972), $S = \dfrac{\rho_\alpha}{\rho_f}$, a conservation equation for $S$ directly follows from (2.13) (Phillips, 1991):

11

$$\frac{\partial S}{\partial t} + V_i \frac{\partial S}{\partial x_i} = \frac{\partial}{\partial x_i}\left(\{k_S \delta_{ij} + D_{ij}\}\frac{\partial S}{\partial x_j}\right) + Q_S,$$

**Equation 2.14**

where

$k_S$            = coefficient of molecular diffusivity in pore water

$D_{ij}$           = components of the tensor of mechanical dispersion

$Q_S = \dfrac{I_\alpha}{\rho_f}$    = specific rate of inner sources of the dissolved substance

A standard model for dispersion (Oldenburg and Pruess, 1995) is implemented here:

$$D_{ij} = \left[\alpha_T^S \delta_{ij} V_q + (\alpha_L^S - \alpha_T^S)\frac{q_i q_j}{V_q}\right]/n$$

**Equation 2.15**

Here

$\alpha_L^S$       = longitudinal dispersivity

$\alpha_T^S$       = transverse dispersivity

## 2.1.5 Equations of state

In the present study, buoyancy forces are considered as a primary driving mechanism activating groundwater flow. Density differences, as the factor initiating the migration of water, and viscosity, influencing ability of the strata to transmit fluid, may effect flow significantly, enhancing or retarding various basin processes. Hence proper estimation of these properties of the fluid is very important. In Chapter 4, the effect of the fluid density and viscosity parametrization on the simulation results is shown (Section 4.3).

Equations of state describe dependence of physical properties of the fluid, such as density, viscosity, heat capacity, thermal conductivity, from thermodynamic characteristics of the system. Physical properties of pore water in sedimentary basins can vary by more than 25% for density and by one order of magnitude for viscosity due to significant temperature and pressure variations (Adams and Bachu, 2002). Hydrothermal fluid in rocks near bedded-salt formations may contain high concentrations of dissolved salt. Properties of the brines are different from ones of fresh or less-saline groundwater. So salinity should to be considered as an additional factor, which, along with pressure and temperature, affects the transport properties of the fluid.

Various algorithms to calculate water density and viscosity as a function of temperature, pressure and salinity have been published over the years. Their comprehensive review is given in (Adams and Bachu, 2002).

### *Fluid density*

Based on the comparison of the algorithms presented in (Adams and Bachu, 2002), in our model we adopt the formulation by (Batzle andWang, 1992). This algorithm is shown to be versatile for studies within sedimentary basins because:

1) its applicability range is sufficiently wide for the purposes of the study (see Table 2.1);

2) over a wide range of salinity, it predicts density values similar to other algorithms (Rowe and Chou, 1970), (McCain, 1991), (Kemp et al., 1989);

3) this algorithm does not have the shortcomings peculiar to some algorithms comparable by applicability range like, for example, (Phillips et al., 1981) or (Palliser and McKibbin, 1998 a,b,c) (Table 2.1). Thus former algorithm produces markedly lower density at high salinity values and it also lacks fit with freshwater density, while the latter greatly overestimates the density up to the saturation point (approximately 26 wt% NaCl), after which it underestimates it.

unlike

| Study | Pressure (MPa) | Temperature (C) | Salinity (NaCl mass fraction) |
|---|---|---|---|
| Batzle and Wang (1992) | 5-100 | 20-350 | $\leq 0.32$ |
| Phillips et al. (1981) | 0-50 | 10-350 | $\leq 0.26$ |
| Palliser and McKibbin (1998b) | 0.1-300 | 0-374.15 | $\leq 1.0$ |

**Table 2.1 Applicability range of various algorithms for calculating brine density.**

Accordingly to (Batzle andWang, 1992), the density of fresh water, $\rho_W$, and the brine density, $\rho_B$, are expressed as polynomials:

$$\rho_W = \rho_W(T,P) = 10^3[1+10^{-6}(-80T-3.3T^2+0.00175T^3+$$
$$+489P-2TP++0.016T^2P- \qquad \text{Equation 2.16}$$
$$-1.3\times10^{-5}T^3P-0.333P^2-0.002TP^2)]$$

and

$$\rho_B = \rho_B(T, P, S) =$$

$$= \rho_W + 10^3 S\{0.668 + 0.44S + 10^{-6}[300P - 2400PS + \qquad\qquad \text{Equation 2.17}$$
$$+ T(80 + 3T - 3300S - 13P + 47PS)]\}$$

In the above relations, $\rho_W$ and $\rho_B$ are in $kg/m^3$, NaCl mass fraction, $S$, is dimensionless (or in other words, $kg$ of the dissolved salt per $kg$ of solution), pressure, $P$, is in MPa, temperature, $T$, is in $^oC$. In Figure 2.2 we show density dependence on temperature at various conditions.
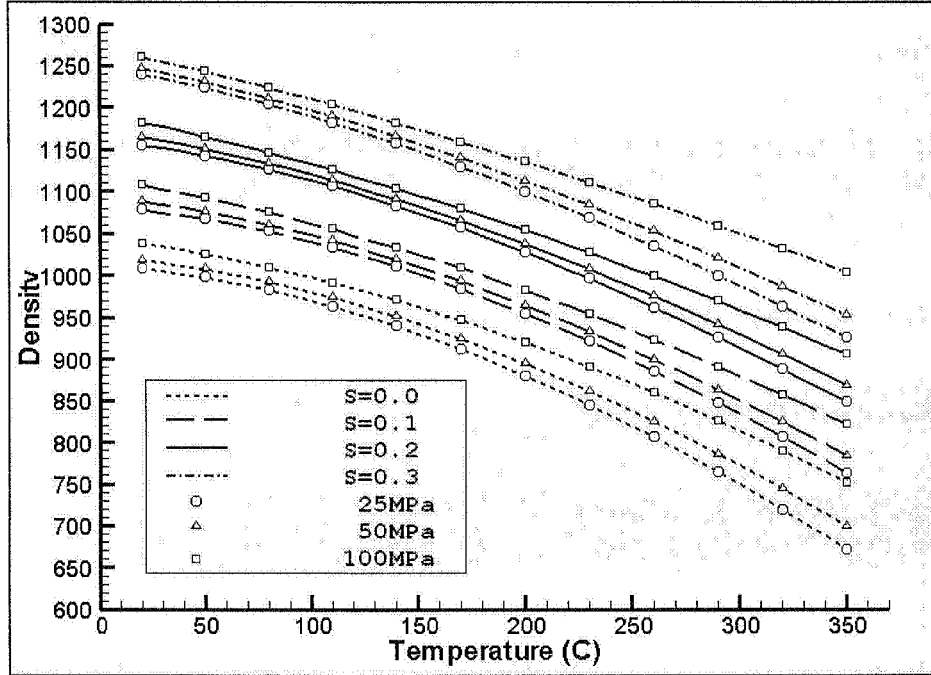


**Figure 2.2 Calculated by formulas of Batzle andWang (1992) fluid density as function of temperature. Fluid density is in ( $kg/m^3$ ).**

Analysing the calculated fluid density data, one can see that the major effect on fluid density is temperature: 260-340($kg/m^3$) over the temperature range 20-350($^oC$). Then follows salinity: for the pressure interval considered, at the temperature of 350($^oC$), the salinity change from fresh-water condition ($S$=0.0) to the value proper to saturated brine ($S$=0.3) produces average density variation of 255($kg/m^3$). Pressure has the least effect: at temperature 350($^oC$), the pressure increase from 5MPa to 100MPa causes density variation around 76-102($kg/m^3$) for different NaCl concentrations.

*Fluid viscosity*

In selecting an equation of state for pore fluid viscosity, the comparison of different algorithms given in (Adams and Bachu, 2002) was carefully considered. They stated that, in general, it is difficult to conclusively select a preferred algorithm for calculating brine viscosity due to the lack of measured field data. The widest range of conditions is covered by the algorithm by (Palliser and McKibbin, 1998c), see Table 2.2. However, according to the review authors, the algorithm increasingly underpredicts brine viscosity for salinity greater than 19wt% NaCl. Therefore, we chose between two alternatives: the algorithm developed by (Phillips et al., 1981) and the one by (Batzle and Wang, 1992). Their applicability ranges are sufficient for the purposes of the present study (Table 2.2).

| Study | Pressure (MPa) | Temperature (C) | Salinity (NaCl mass fraction) |
|---|---|---|---|
| Batzle and Wang (1992) | - | $\leq 250$ | $\leq 0.46$ |
| Phillips et al. (1981) | - | 10-350 | $\leq 0.42$ |
| Palliser and McKibbin (1998c) | 0.1-300 | <800 | $\leq 1.0$ |

**Table 2.2 Applicability range of various algorithms for calculating of brine viscosity.**

The (Phillips et al., 1981) algorithm is used in various models of flow in sedimentary basins (Raffensperger and Vlassopoulos, 1999), (Simms and Garven, 2004). But we gave preference to the algorithm of (Batzle and Wang, 1992). The reason for this choice will be explored later. Here we provide some general remark.

The effect of temperature, salinity and pressure on the brine viscosity is similar to that on the brine density: viscosity is most sensitive to temperature changes (decreases with increasing temperature), less dependent on salinity (rises with the salinity increase). Its dependency on pressure is almost negligible (directionally similar to the effect of salinity).

(Batzle and Wang, 1992) do not consider the effect of pressure in the following expression, because even at 50 MPa the viscosity is increased only a few percent:

$$\mu_B = \mu_B(T,S) = 0.1 + 0.333S + $$
$$+ (1.65 + 91.9S^3)\exp\{-[0.42(S^{0.8} - 0.17)^2 + 0.045]T^{0.8}\}$$

,   **Equation 2.18**

where $\mu_B$ is the dynamic viscosity of brine in cP, S is in NaCl mass fraction, and T is in $^o C$.

(Phillips et al., 1981) use a correlation for the viscosity of freshwater, $\mu_W$, published by (Watson et al., 1980), then introduce an amendment to include dependence on brine salinity:

$$\mu_B = \mu_W[1 + 0.0816m - 0.0122m^2 + 0.000128m^3 + \\ + 0.000629T(1 - e^{-0.7m})]$$

, **Equation 2.19**

where $m$ is NaCl molality, T is in $^oC$.

According to (Watson et al., 1980), $\mu_W$ is presented as a function of water density and temperature:

$$\mu_W = \mu_W(\rho_W, T) = \mu_0(T)\exp\left[\rho * \sum_{i=0}^{5}\sum_{j=0}^{6} a_{ij}\left(\frac{1}{T*}-1\right)^i (\rho*-1)^j\right],$$  **Equation 2.20**

where

$$\rho* = \frac{\rho_W}{\rho_r}; \qquad T* = \frac{T}{T_r};$$

$\rho_r = 317.763(kg/m^3)$; $T_r = 647(^0K)$ are some reference values, and

$$\mu_0 = \mu_0(T) = 10^{-3}T*^{1/2}\left[\sum_{k=0}^{3}\frac{a_k}{T*^k}\right]^{-1}$$  **Equation 2.21**

Here $\mu_0$ is in cP, $T$ is in $^0K$, all density values are in ($kg/m^3$). Nineteen non-zero coefficients $a_{ij}$ and four coefficients $a_i$ are not quoted here but can be found in (Watson et al. 1980, p.1278).

We must note at this point, that, although this expression for $\mu_W$ (and hence for $\mu_B$) is not explicitly dependent on pressure, this parameter effects the viscosity value indirectly, through correlation for water density, $\rho_W$, if the latter is defined as a function of pressure, and it is so in our case (see equations (2.16), (2.17)). However, as was noted before, pressure effect on viscosity is negligible. In Figure 2.3 we show viscosity calculated by algorithm (Phillips et al., 1981) as a function of temperature under different conditions. It is quite clear that even substantial pressure variations do not result in significant viscosity value increase.

(a)



(b)
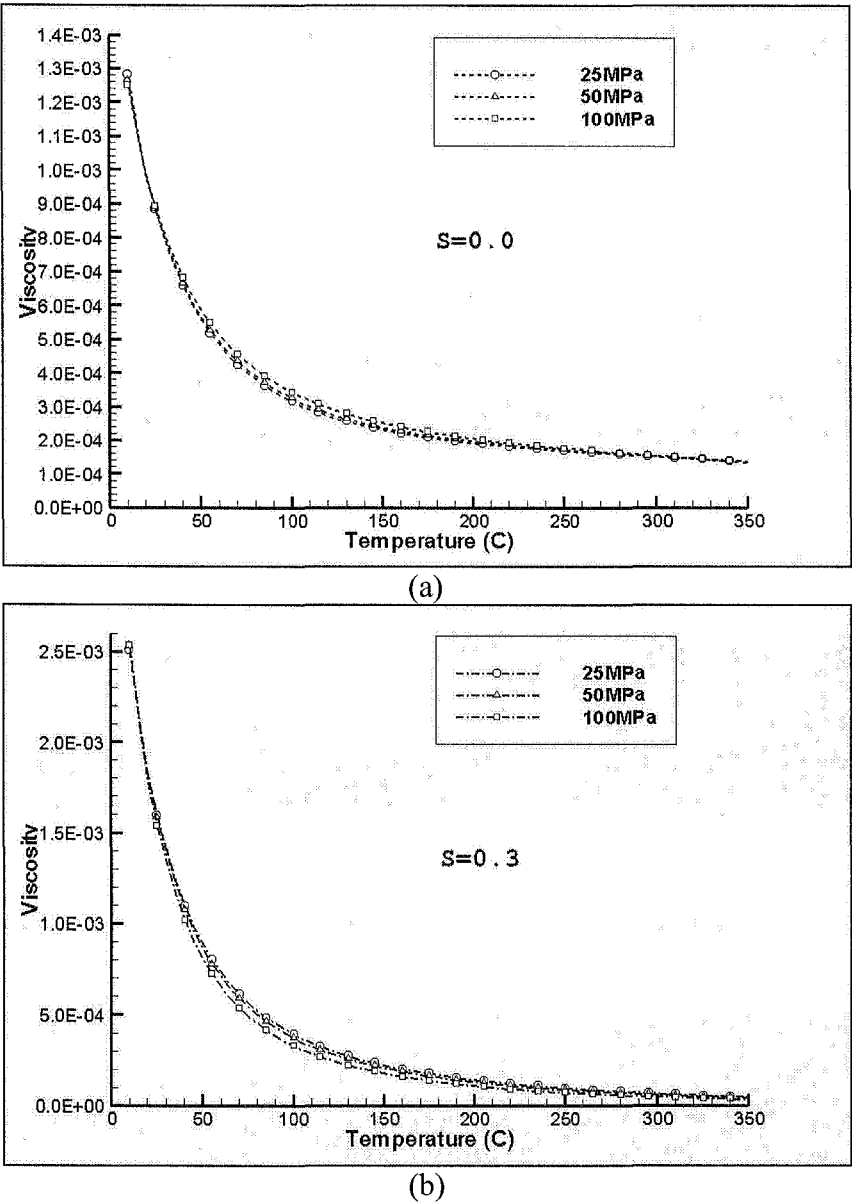
**Figure 2.3. Viscosity dependence on pressure at S=0.0 (a) and S=0.3 (b) (Phillips et al., 1981). Viscosity values are given in** $Pa \cdot s$ .

The algorithm has a shortcoming. As can be seen from Figure 2.4, at high temperatures, viscosity values correspondent to higher salinity appeared to be lower than ones correspondent to the lesser salinity value. Thus, at temperatures over $168\,^{\circ}C$, viscosity of brine containing NaCl at the level of $S$=0.2 (solid line) is lower than viscosity of less saline brine with $S$=0.1 (dashed line, long dashes). Moreover, at temperatures over $127\,^{\circ}C$, viscosity of the brine with $S$=0.3 (dash-dot line) is lower than the freshwater viscosity (dashed line, short dashes). This is at odds with reality, because at the same temperature, higher content of dissolved NaCl must result in high solute viscosity.
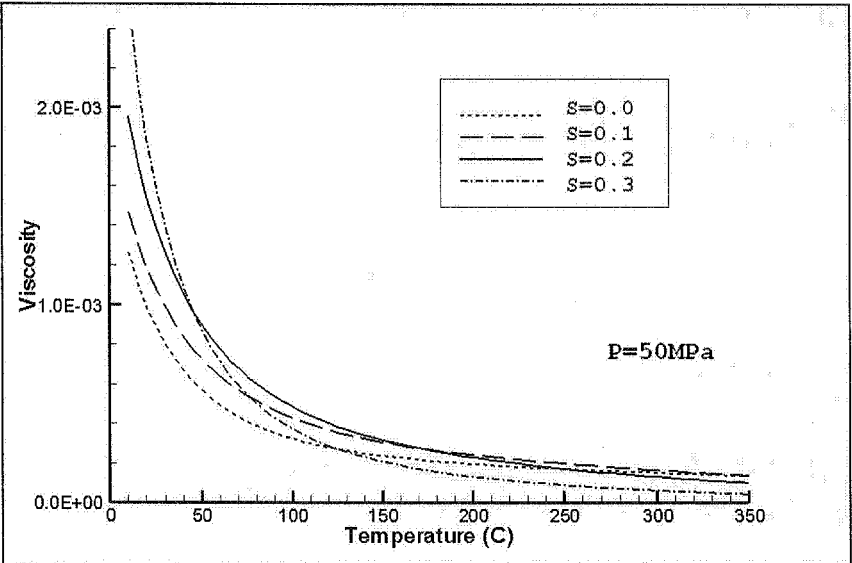
**Figure 2.4. Viscosity dependence on salinity (Phillips et al., 1981). Viscosity values are given in** $Pa \cdot s$ **and calculated by fluid density at P=50MPa.**

On the contrary, the algorithm by (Batzle and Wang, 1992), although overstating the viscosity values by up to 10% viscosity values for T<$120\,^{o}C$ (Adams and Bachu, 2002), avoids this undesirable feature (Figure 2.5).
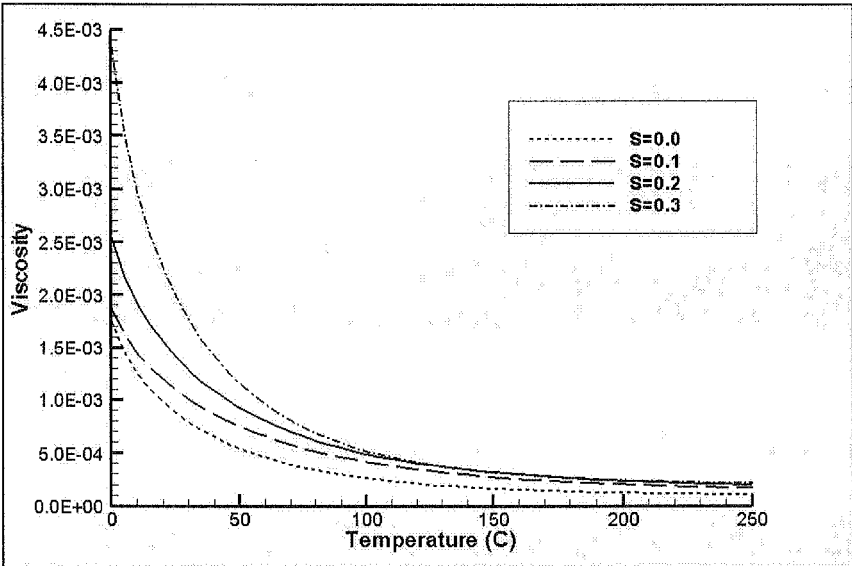


**Figure 2.5. Viscosity dependence on salinity (Batzle and Wang, 1992). Viscosity values are given in** $Pa \cdot s$ **.**

This overestimation is acceptable and as a result, we preferred to use the algorithm by (Batzle and Wang, 1992) (equation 2.18).

### Heat capacity of the brine

To calculate values of heat capacity of pore water, we use an empirical equation given in (Horne, 1969), which represents the specific heat as a function of temperature and salinity:

$$c_f = c_f(T,S) = 4186.8\{1.0049 - 0.0016210S + 3.5261 \cdot 10^{-6} S^2 -$$
$$-10^{-4}(3.2506 - 0.14795S + 7.7765 \cdot 10^{-4} S^2)T +$$
$$+10^{-6}(3.8013 - 0.12084S + 6.1210 \cdot 10^{-4} S^2)T^2\}$$

, **Equation 2.22**

where $S$ is dimensionless, $T$ is given in $^{o}C$ and $c_f$ is in J/(kg$^{o}C$).

The expression summarizes experimental data for sea water within the temperature interval from $0^{o}C$ to $40^{o}C$ and salinity up to 0.04. This range of parameters is not sufficient for our study, so we investigated using the extrapolation of this algorithm for higher temperatures (up to $350^{o}C$) and salinity (up to 0.3). We compared the extrapolation with another correlation for temperature-dependent heat capacity of water reported in (Holzbecher, 1998):

$$c_f = c_f(T) = 4186.8\{3.3774 - 1.12665 \cdot 10^{-2}(T + 273.15) +$$
$$+1.34687 \cdot 10^{-5}(T + 273.15)^2\}$$

, **Equation 2.23**

where $T$ is given in $^{o}C$ and $c_f$ is in J/(kg$^{o}C$).

Figure 2.6 shows a comparison of these two algorithms.

The polynomial expression (2.23) is applicable for temperature between $100^{o}C$ and $320^{o}C$, but disregards the salinity effect. It also cannot be used at temperatures below $100^{o}C$, because it produces non-realistic high values (Figure 2.6, dotted line).
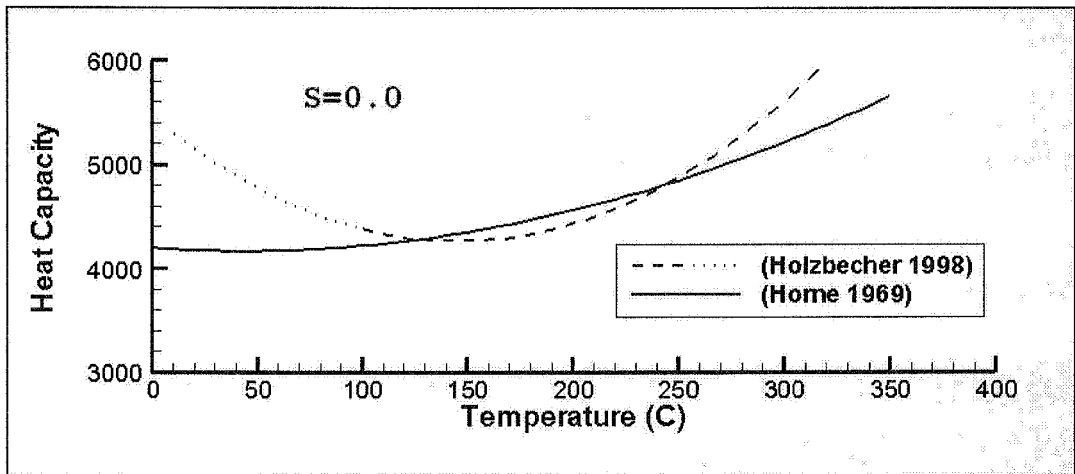


**Figure 2.6 Specific heat of water [J/(kg$^{o}C$)] as a function of temperature at S=0.0.**

Although (2.22) underestimats the heat capacity at temperatures over $240\,^oC$, this formulation produces reasonable heat capacity values for the range of lower temperatures (Figure 2.6, solid line). It also incorporates the salinity effect, though this effect is of much less significance (Figure 2.7). So ultimately, the preference was given to this correlation.
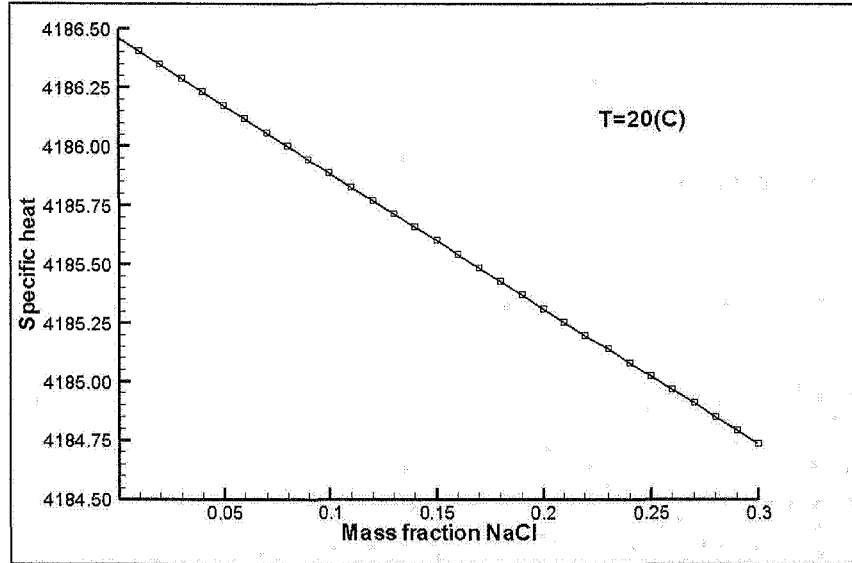


**Figure 2.7 Heat capacity of water [J/(kg $^o C$ )], as a function of salinity at T=20 $^o C$ .**

***Thermal conductivity of the brine***

Following (Holzbecher, 1998), we use the dependence of thermal conductivity of water on temperature, as presented below:

$$\lambda_f = \lambda_f(T) = 10^{-3}[-922.47 +$$
$$+ 2839.5T_r - 1800.7T_r^2 + 525.77T_r^3 - 73.44T_r^4]$$

, **Equation 2.24**

where $T_r = \dfrac{T}{T_0}$, $T$ is expressed in $^oK$, $T_0 = 273.15^0 K$, $\lambda_f$ is in W/(m$^0 K$).

$\lambda_f$ dependence on temperature is shown in Figure 2.8.
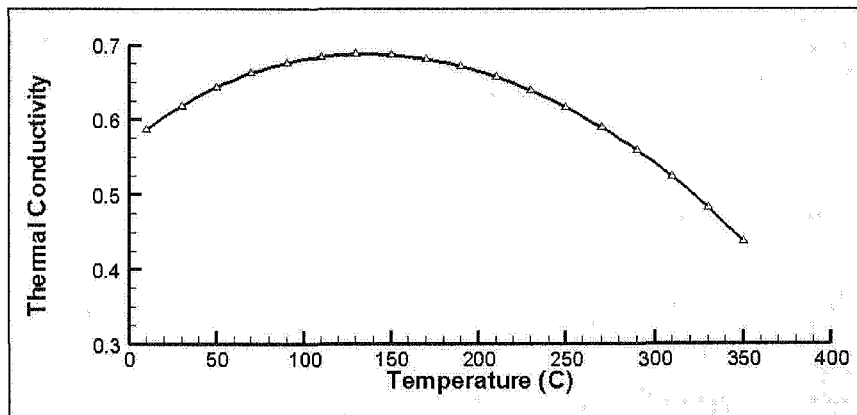


**Figure 2.8 Thermal conductivity of water [W/(m $^o C$ )].**

### Physical properties of the solid matrix

In the model presented here we disregard temperature effect on properties of the solid matrix. Density, compressibility, heat capacity and thermal conductivity are considered as time-independent constants. However, they vary spatially, that reflects the heterogeneity of a complex sedimentary structure. Besides that, thermal conductivities of the solid matrix parallel and perpendicular to rock bedding are deemed to be different as sedimentary rocks were proved to be anisotropic with respect to their thermal properties (Popov et al., 2003).

## 2.2 Boundary conditions

The three partial differential equations for the hydraulic head, temperature and salinity, (2.3), (2.12), (2.14) must be supplemented by the set of boundary and initial conditions. For equations of this kind, the following types of boundary conditions are permissible (Tyn, 1973):

1) the *first type (Dirichlet)* boundary condition: when the value of the unknown function (head, temperature, salinity) is prescribed on the boundary:

$$f = \bar{f}(\vec{x},t), \quad \vec{x} \in \partial D \; ; \qquad \qquad \text{Equation 2.25}$$

Here $f$ is an unknown function sought for ($\varphi_0$, $T$ or $S$); $\bar{f}$ is a prescribed function on the boundary $\partial D$ of the domain $D$;

2) the *second type (Neumann)* boundary condition:

$$\frac{\partial f}{\partial n} = \bar{f}_n(\vec{x},t), \quad \vec{x} \in \partial D \; ; \qquad \qquad \text{Equation 2.26}$$

Here $\dfrac{\partial f}{\partial n}$ denotes the directional derivative of $f$ along the outward normal to the boundary $\partial D$, $\bar{f}_n$ defines the prescribed flux across the boundary;

3) the *third type (Cauchy)* boundary condition:

$$\frac{\partial f}{\partial n} = \bar{h}(\vec{x},t)(f - \vartheta(\vec{x},t)), \quad \vec{x} \in \partial D \; ; \qquad \qquad \text{Equation 2.27}$$

Here $\bar{f}$, $\bar{f}_n$, $\bar{h}$, and $\vartheta$ are known functions.

We note here, that the model permits boundary conditions of different types applied over fragments of the domain boundary (mixed boundary value problem).

This concerns not just segments of $\partial D$ which we will designate as 'bottom', 'top', left, or 'right' by virtue of the way of the domain discretization, but also smaller sections of these four boundaries.

## 2.2.1 Hydraulic head

For the hydraulic head the following conditions on the segments of the domain boundary can be imposed by certain physical situations:

a) prescribed head:

$$\varphi_0(\vec{x},t) = \overline{\varphi}_0(\vec{x},t), \quad \vec{x} \in \partial D_{\varphi};$$
<div align="right">**Equation 2.28**</div>

A boundary condition of this kind occurs whenever the flow domain is adjacent to a body of a liquid continuum (Bear, 1972). We note here, that for a majority of the presented simulations, a special case of (2.28), when $\overline{\varphi}_0 = const$ (equipotential surface), will be set over the top domain boundary that represents the bottom of palaeo-ocean;

b) prescribed flux:

$$q_n = \vec{q} \cdot \vec{n} = \overline{q}_n(\vec{x},t), \quad \vec{x} \in \partial D_q.$$
<div align="right">**Equation 2.29**</div>

This is a type of boundary with a known influx (or outflow) rate $\overline{q}_n$;

c) the impermeable to flow boundary, a special case of (2.29), when $\overline{q}_n \equiv 0$:

$$q_n = \vec{q} \cdot \vec{n} = 0, \quad \vec{x} \in \partial D_q^0;$$
<div align="right">**Equation 2.30**</div>

In the last case, fluid velocity component in the direction of the normal to the boundary equals to zero.

Here

| | |
|---|---|
| $\partial D_{\varphi}$ | is the part of the boundary on which the Dirichlet boundary condition for the hydraulic head is prescribed; |
| $q_n$ | is the Darcy flux projection on the outward normal to the boundary; |
| "·" | denotes scalar product; |
| $\vec{n} = (n_1, n_2, n_3)$ | is the vector of the outward normal to the boundary; |
| $\partial D_q^0$ | is the part of the boundary on which the homogeneous Neumann boundary condition is prescribed; |
| $\partial D_q$ | is the part of the boundary on which the non-zero Neumann boundary condition is prescribed |

## 2.2.2 Temperature

For the temperature, we may prescribe following boundary conditions:

1) known temperature values at the points of the domain boundary:

$$T = \overline{T}(\vec{x},t), \quad \vec{x} \in \partial D_T;$$                    **Equation 2.31**

2) prescribed heat flux through the boundary:

$$W_n = \vec{W} \cdot \vec{n} = \overline{W}_n(\vec{x},t), \quad \vec{x} \in \partial D_W;$$                    **Equation 2.32**

where $\vec{W} = -\Lambda grad T$ is the vector of the heat flux density, $\Lambda$ denotes the thermodispersion tensor, and $\overline{W}_n(\vec{x},t)$ are known values of the projection of the heat flux vector onto the outer normal to the domain boundary.

A special case of this condition is heat-insulated boundary:

$$W_n = \vec{W} \cdot \vec{n} = 0, \quad \vec{x} \in \partial D_W^0.$$                    **Equation 2.33**

4) heat exchange with the environment of known temperature $\vartheta_T$ (Tihonov and Samarskiy, 1999):

$$W_n = \overline{h}_T(\vec{x},t)(T - \vartheta_T(\vec{x},t)), \quad \vec{x} \in \partial D_{HE}.$$                    **Equation 2.34**

Here

| | |
|---|---|
| $\partial D_T$ | is the part of the domain boundary on which the known temperature is prescribed; |
| $\partial D_W^0$ | is the part of the boundary that supposed to be insulated to heat flow; |
| $\partial D_W$ | is the segment of the boundary through which heat flux with the known rate is assigned; |
| $\partial D_{HE}$ | is the segment of the boundary on which heat exchange with the environment of known temperature is given; |
| $\overline{h}_T(\vec{x},t)$ | is the heat exchange coefficient. |

## 2.2.3 Salinity

The set of boundary conditions for the salinity can be set very similarly to the temperature:

1) known salinity values at the points of the domain boundary:

$$S = \overline{S}(\vec{x},t), \quad \vec{x} \in \partial D_S;$$                    **Equation 2.35**

2) no salt transfer across the boundary:

$$M_n = \vec{M} \cdot \vec{n} = 0, \quad \vec{x} \in \partial D_M^0;$$                    **Equation 2.36**

where $\vec{M} = -\Psi grad S$ is the vector of the mass flux and $\Psi$ denotes the dispersion tensor.

3) prescribed mass flux through the boundary:

23

$$M_n = \overline{M}_n(\vec{x}, t), \quad \vec{x} \in \partial D_M ;$$

<div align="right">**Equation 2.37**</div>

where $\overline{M}_n(\vec{x}, t)$ are known values of the salinity influx rate;

4) mass exchange with the environment of known salinity $\vartheta_S$ :

$$M_n = \overline{h}_S(\vec{x}, t)(S - \vartheta_S(\vec{x}, t)), \quad \vec{x} \in \partial D_{ME}.$$

<div align="right">**Equation 2.38**</div>

Here

$\partial D_S$     is the part of the domain boundary on which the known salinity is prescribed;

$\partial D_M^0$     is the part of the boundary that is impermeable to the mass transport;

$\partial D_M$     is the segment of the boundary through which mass flux with the known rate is assigned;

$\partial D_{ME}$     is the segment of the boundary on which mass exchange with the environment of known salinity is given;

$\overline{h}_S(\vec{x}, t)$     is the mass exchange coefficient.

## 2.3 Initial conditions

To complete the problem formulation, in addition to governing equations and boundary conditions, a set of initial conditions must be specified at the particular instant of time $t_0$ :

$$\varphi_0(\vec{x}, t_0) = \widetilde{\varphi}_0(\vec{x}) ;$$

<div align="right">**Equation 2.39**</div>

$$T(\vec{x}, t_0) = \widetilde{T}(\vec{x}) ;$$

<div align="right">**Equation 2.40**</div>

$$S(\vec{x}, t_0) = \widetilde{S}(\vec{x}).$$

<div align="right">**Equation 2.41**</div>

Here $\widetilde{\varphi}_0$, $\widetilde{T}$, and $\widetilde{S}$ represent known distributions of the hydraulic head, temperature and salinity at the moment of time $t_0$ respectively.

## 2.4 Final form of the system of governing equations and supplementary conditions

In the final analysis, the system of governing equations comprises of

- Equation for the hydraulic head (2.3):

$$S_0 \frac{\partial \varphi_0}{\partial t} + \frac{\partial}{\partial x_i}(q_i) = 0 \, ;$$

- Darcy's law (2.5):

$$q_i = -K_{ij}\left[\frac{\partial \varphi_0}{\partial x_j} + \rho_r \frac{\partial z}{\partial x_j}\right];$$

- Heat transport equation (2.12):

$$c_e \frac{\partial T}{\partial t} + \rho_f c_f q_i \frac{\partial T}{\partial x_i} = \frac{\partial}{\partial x_i}\left(\{(\lambda_e)_{ij} + (\lambda_{disp})_{ij}\}\frac{\partial T}{\partial x_j}\right) + Q_T \, ;$$

- Salinity transport equation (2.14):

$$\frac{\partial S}{\partial t} + V_i \frac{\partial S}{\partial x_i} = \frac{\partial}{\partial x_i}\left(\{k_s \delta_{ij} + D_{ij}\}\frac{\partial S}{\partial x_j}\right) + Q_S \, ;$$

- and four equations of state (2.17), (2.18), (2.22), (2.24):

$$\rho_f = \rho_f(T,P,S); \qquad \mu_f = \mu_f(T,S); \qquad c_f = c_f(T,S); \qquad \lambda_f = \lambda_f(T) \, .$$

The system of equations is accompanied by the boundary and initial conditions:

- ○ *Hydraulic head:* expressions (2.28), (2.29), (2.39):

$$\varphi_0(\vec{x},t) = \overline{\varphi}_0(\vec{x},t), \quad \vec{x} \in \partial D_\varphi \, ;$$

$$q_n = \vec{q} \cdot \vec{n} = \overline{q}_n(\vec{x},t), \quad \vec{x} \in \partial D_q \, ;$$

$$\varphi_0(\vec{x},t_0) = \widetilde{\varphi}_0(\vec{x}) \, ;$$

- ○ *Temperature:* expressions (2.31), (2.32), (2.34), (2.40):

$$T = \overline{T}(\vec{x},t), \quad \vec{x} \in \partial D_T \, ;$$

$$W_n = \vec{W} \cdot \vec{n} = \overline{W}_n(\vec{x},t), \quad \vec{x} \in \partial D_W \, ;$$

$$W_n = \overline{h}_T(\vec{x},t)(T - \vartheta_T(\vec{x},t)), \quad \vec{x} \in \partial D_{HE} \, ;$$

$$T(\vec{x},t_0) = \widetilde{T}(\vec{x}) \, ;$$

- ○ *Salinity:* expressions (2.35), (2.37), (2.38), (2.41):

$$S = \overline{S}(\vec{x},t), \quad \vec{x} \in \partial D_S \, ;$$

$$M_n = \overline{M}_n(\vec{x}), \quad \vec{x} \in \partial D_M \, ;$$

$$M_n = \overline{h}_S(\vec{x},t)(S - \vartheta_S), \quad \vec{x} \in \partial D_{ME} \, ;$$

$$S(\vec{x},t_0) = \widetilde{S}(\vec{x}) \, .$$

# 3 Numerical Method

To solve the system of governing equations analytically, strict simplifying limitations are required, like homogeneity and isotropy of the porous matrix, no fluid density variations etc. No complex sedimentary structure undergoing hydrothermal alteration can meet such requirements. So the problem is to be solved approximately, employing a numerical technique.

The finite element method is employed to build a numerical solution of the problem (Section 3.1). Bilinear shape functions for four-node quadrilateral finite elements are used. To handle complex geometry, an isoparametric transformation of the coordinates is applied within each element. This allows distortion of the elements (Section 1.1).

The option to switch to the more general Petrov-Galerkin formulation with non-symmetrical 'upwinding' weighting functions is embedded (Section 1.1). It suppresses some undesirable numerical effects that appear in advection-dominated areas, like highly permeable faults. We adapted the general procedure of calculating the parameters, which control the degree of upwinding, to our particular case of nonlinear heat and mass transport equations in porous media.

An implicit time-stepping scheme with 'weightings' is employed with an iterative procedure within each time step. The latter handles the nonlinearity of the problem (Section 3.5).

At the ultimate stage, discretization of the continuum problem by the finite element method leads to solving a system of linear algebraic equations with a sparse matrix at each iteration step. The chosen type of shape functions and domain discretization give the advantage that the matrix of the system is strictly ordered. A direct algorithm modified for this type of matrix is used to significantly reduce computing time (Section 1.1).

## 3.1 Weighted residual method. Approximation of the governing equations

The stratigraphic architecture of the section of interest has a complex geometry. For one thing, the laminated structure of the profile is distorted by multiple shifts along the rift planes, so the layers are not aligned strictly horizontally. For another, the geometry is complicated by the network of interconnected permeable fault zones, which play a significant role in defining major fluid pathways (Figure 3.1)

Choosing a numerical method and considering the way of the problem domain discretization, we were bound to satisfy the following two requirements: firstly, grid nodes must be placed in such a way as to trace the interface of laminary stratigraphic units. Secondly, they are to be structured so that the respective node numbering would lead to the effective matrix structure at the ultimate stage of the solution.

It is quite clear that no rectangular numerical grid can meet both of these requirements, hence employment of a finite difference scheme seemed inadequate for this problem. The finite element method, on the contrary, has the facility to handle complex geometry (Section 1.1).

Another consideration is the choice of shape and weight functions, the type of finite elements. In the case of using shape functions on the base of triangular elements, the matrix of the system is sparse but not ordered. This means that to take advantage of the matrix sparsity in reducing computing time, a special sophisticated procedure is to be used (Duff et al., 1986). The use of quadrilateral elements solves this problem more simply. Element corners, being nodes of a numerical grid, are merely numbered by columns (or rows). In this case, the resulting matrix of the system has a structure that can be interpreted either as block tridiagonal with each block tridiagonal in its turn, or as a banded matrix. In both cases, the algorithms for solving the system are not complicated, while being effective in the sense of computing time (Golub and Van Loan, 1989).

We use a mesh of distorted quadrilateral elements. Figure 3.1 demonstrates an example of the numerical grid superimposed onto the hydrostratigraphy of the ZCB section. One can see that this kind of mesh copes well, both with the task of representing the layered structure of a sedimentary formation and with the necessity to trace the complex geometry of the network of faults.
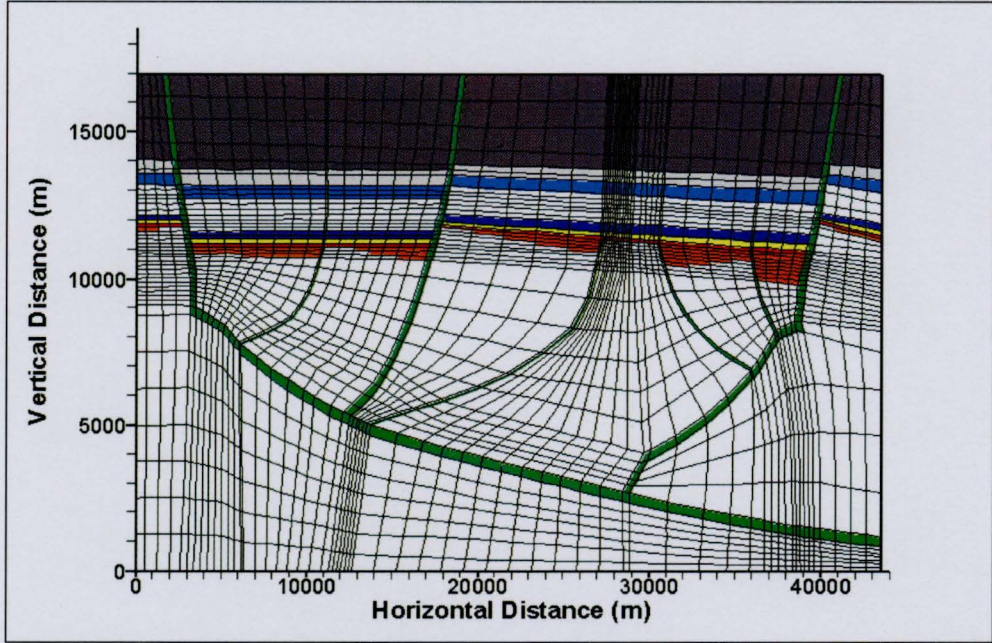
**Figure 3.1 Finite element grid superimposed onto the hydrostratigraphy of the ZCB section.**

Below we describe the construction of the numerical solution of the problem, with the final formulation given in Section 2.4. Without going into a detailed discussion of the methodology of the finite element method (as it is widely presented in special publications (Zienkiewicz, 1977), (Fletcher 1984), (Zienkiewicz and Taylor, 2000)), we show the principal steps of the procedure.

## 3.1.1 Equation for the hydraulic head

**Step1.** The starting point is the *differential form of the equation*, (2.3):

$$S_0 \frac{\partial \varphi_0}{\partial t} + \frac{\partial}{\partial x_i}(q_i) = 0 \quad ;$$

**Step2.** Then we pass on to the *weak (integral) form* of the equation (Zienkiewicz, 1977). As (2.3) must be valid at each point of the domain $D$, hence

$$\iint_D \left( S_0 \frac{\partial \varphi_0}{\partial t} + \frac{\partial q_x}{\partial x} + \frac{\partial q_z}{\partial z} \right) v \, dxdz = 0, \qquad \text{Equation 3.1}$$

for any arbitrary function $v$.

To simplify the further expounding, we denote:

$$I_t = \iint_D S_0 \frac{\partial \varphi_0}{\partial t} v dxdz \, ; \qquad \text{Equation 3.2}$$

28

$$I_x = \iint\limits_D \frac{\partial q_x}{\partial x} v \, dx dz \; ;$$

**Equation 3.3**

$$I_z = \iint\limits_D \frac{\partial q_z}{\partial x} v \, dx dz \; .$$

**Equation 3.4**

So equation (3.1) can be now rewritten as:

$$I_t + I_x + I_z = 0 \; .$$

**Equation 3.5**

Equations (3.3), (3.4) can be integrated by parts:

$$I_x = \iint\limits_D \frac{\partial q_x}{\partial x} v \, dx dz = -\iint\limits_D q_x \frac{\partial v}{\partial x} dx dz + \oint\limits_{\partial D} q_x v n_x \, dS \; ;$$

**Equation 3.6**

$$I_z = \iint\limits_D \frac{\partial q_z}{\partial x} v \, dx dz = -\iint\limits_D q_z \frac{\partial v}{\partial x} dx dz + \oint\limits_{\partial D} q_z v n_z \, dS \; .$$

**Equation 3.7**

Taking into account the Darcy's law (2.5) in adding (3.6) and (3.7), we obtain:

$$I_x + I_z = -\iint\limits_D q_x \frac{\partial v}{\partial x} dx dz + \oint\limits_{\partial D} q_x v n_x \, dS - \iint\limits_D q_z \frac{\partial v}{\partial x} dx dz + \oint\limits_{\partial D} q_z v n_z \, dS =$$

$$= \iint\limits_D K_{xx} \frac{\partial \varphi_0}{\partial x} \frac{\partial v}{\partial x} dx dz + \iint\limits_D K_{xz} \left( \frac{\partial \varphi_0}{\partial z} + \rho_r \right) \frac{\partial v}{\partial x} dx dz +$$

$$+ \iint\limits_D K_{xz} \frac{\partial \varphi_0}{\partial x} \frac{\partial v}{\partial x} dx dz + \iint\limits_D K_{zz} \left( \frac{\partial \varphi_0}{\partial z} + \rho_r \right) \frac{\partial v}{\partial z} dx dz + \oint\limits_{\partial D} q_n v \, dS$$

**Equation 3.8**

As boundary of the domain $\partial D = \partial D_\varphi \cup \partial D_q$, therefore

$$\oint\limits_{\partial D} q_n v \, dS = \oint\limits_{\partial D_\varphi} q_n v \, dS + \oint\limits_{\partial D_q} q_n v \, dS$$

**Equation 3.9**

Since $v$ is an arbitrary function, we can specify, without loss of generality, that

$$v\big|_{\partial D_\varphi} = 0$$

**Equation 3.10**

Thus, first term in the right-hand side of (3.9) becomes zero, and ultimately we have:

$$\oint\limits_{\partial D} q_n v \, dS = \oint\limits_{\partial D_\varphi} q_n v \, dS + \oint\limits_{\partial D_q} q_n v \, dS = 0 + \oint\limits_{\partial D_q} \overline{q}_n v \, dS$$

**Equation 3.11**

Having in mind (3.8) and (3.11), we can rewrite (3.5) as:

$$I_t + I_x + I_z = \iint_D S_0 \frac{\partial \varphi_0}{\partial t} v \, dx dz +$$

$$+ \iint_D K_{xx} \frac{\partial \varphi_0}{\partial x} \frac{\partial v}{\partial x} dx dz + \iint_D K_{xz} \left( \frac{\partial \varphi_0}{\partial z} + \rho_r \right) \frac{\partial v}{\partial x} dx dz +$$

$$+ \iint_D K_{xz} \frac{\partial \varphi_0}{\partial x} \frac{\partial v}{\partial x} dx dz + \iint_D K_{xz} \left( \frac{\partial \varphi_0}{\partial z} + \rho_r \right) \frac{\partial v}{\partial \mathfrak{n}} dx dz +$$

$$+ \oint_{\partial D_q} \overline{q}_n v \, dS = 0$$

<div align="right"><strong>Equation 3.12</strong></div>

Equation (3.12) is the weak (or integral) form of the differential equation (2.3).

**Step 3.** Now we proceed to the approximation to integral formulation using _the weighted residual method._

We seek so-called trial solution, which is the approximation, $\widetilde{\varphi}_0$, of the unknown function, $\varphi_0$, in the form of expansion:

$$\varphi_0(x,z,t) \approx \widetilde{\varphi}_0(x,z,t) = \sum_{l=1}^{Nn} \alpha_l(t) \psi_l(x,z), \qquad \textbf{Equation 3.13}$$

where $\{\psi_l(x,z) \mid l = 1,2,...Nn\}$ is the set of known analytic functions (shape functions), and the $\alpha_l$'s are coefficients to be determined (Fletcher, 1984).

In place of an arbitrary function $v$, we put a finite set of prescribed functions (weighting functions) (Zienkiewicz, 1977):

$$v = \omega_k(x,z), \quad k=1,2,...,Nn \qquad \textbf{Equation 3.14}$$

where $Nn$ is the number of unknown parameters $\alpha_l$.

Substitution (3.13) and (3.14) into (3.12), yields:

$$\sum_{l=1}^{Nn} \left( \iint_D S_0 \psi_l \omega_k dx dz \right) \alpha_l'(t) +$$

$$+ \sum_{l=1}^{Nn} \left\{ \iint_D K_{xx} \frac{\partial \psi_l}{\partial x} \frac{\partial \omega_k}{\partial x} dx dz + \iint_D K_{xz} \frac{\partial \psi_l}{\partial z} \frac{\partial \omega_k}{\partial x} dx dz + \right.$$

$$\left. + \iint_D K_{xz} \frac{\partial \psi_l}{\partial x} \frac{\partial \omega_k}{\partial z} dx dz + \iint_D K_{zz} \frac{\partial \psi_l}{\partial z} \frac{\partial \omega_k}{\partial z} dx dz \right\} \alpha_l(t) +$$

$$+ \left[ \iint_D \rho_r \left( K_{xz} \frac{\partial \omega_k}{\partial x} + K_{zz} \frac{\partial \omega_k}{\partial z} \right) dx dz + \oint_{\partial D_q} \overline{q}_n \omega_k dS \right] = 0, \qquad \forall k = \overline{1,Nn}$$

<div align="right"><strong>Equation 3.15</strong></div>

<div align="right">30</div>

To simplify the appearance of (3.15), we denote the expressions in round brackets, braces, and square brackets as $R_{kl}$, $C_{kl}$, and $s_k$ correspondingly/respectively. So (3.15) becomes:

$$\sum_{l=1}^{Nn} R_{kl}\alpha_l'(t) + \sum_{l=1}^{Nn} C_{kl}\alpha_l(t) + s_k = 0, \qquad \forall k = \overline{1, Nn} \qquad \textbf{Equation 3.16}$$

where $\alpha_l'(t) = \dfrac{d\alpha_l}{dt}$.

(3.16) represents a system of ordinary differential equations, where the set of unknowns $\{\alpha_l(t) \mid l = 1,2,...Nn\}$ is to be found. As long as fluid density and viscosity are assumed not constant but governed by the equations of state (2.17), (2.18), $S_0, K_{xx}, K_{xz}, K_{zz}, \rho_r, \overline{q}_n$ are functions of (x,z,t). Hence the coefficients $R_{kl}$, $C_{kl}$, and right-hand side vector $(s_k)_{k=1}^{Nn}$ will be time-dependent. Moreover, the problem becomes non-linear, as the coefficients are dependent on the unknown temperature and salinity.

## 3.1.2 Heat and mass transport equations

Similar steps should be accomplished in the way of constructing the numerical solution of the equations defining fluid temperature and salinity.

__Step1.__ *Differential form of the equation.*

Both equation of heat (2.12) and mass (2.14) transport have the form of the advective-diffusion equation, which can be generalized, as:

$$C(x,z,t)\frac{\partial\phi}{\partial t} + F(x,z,t)q_i(x,z,t)\frac{\partial\phi}{\partial x_i} = \frac{\partial}{\partial x_i}\left(\lambda_{ij}(x,z,t)\frac{\partial\phi}{\partial x_j}\right) + Q(x,z,t)$$

$$\textbf{Equation 3.17}$$

Where

| in the case of heat transport: | in the case of mass transport: |
|---|---|
| $\phi = \phi(x,z,t) = T(x,z,t)$; | $\phi = \phi(x,z,t) = S(x,z,t)$; |
| $C(x,z,t) = c_e(x,z,t)$ | $C(x,z,t) \equiv 1$; |
| $F(x,z,t) = \rho_f(x,z,t)c_f(x,z,t)$; | $F(x,z,t) = 1/n(x,z)$; |
| $\lambda_{ij}(x,z,t) = (\lambda_e)_{ij}(x,z,t) + n(\lambda_{disp})_{ij}(x,z,t)$; | $\lambda_{ij}(x,z,t) = k_S(x,z)\delta_{ij} + D_{ij}(x,z,t)$; |
| $Q(x,z,t) = Q_T(x,z,t)$; | $Q(x,z,t) = Q_S(x,z,t)$; |

**Table 3.1 Coefficients of the advective-diffusion equation (3.17) in the case of heat or mass transport considered.**

Therefore, the procedure of the numerical solution construction is common for both equations. Below we carry the procedure out for the unknown $\phi$ , that can represent either temperature or salinity with due coefficients from Table 3.1.

**Step2.** _Weak (integral) form of the equation._
Similarly to Section 3.1.1, we consider first:

$$\iint_D \left( C\frac{\partial \phi}{\partial t} + Fq_i \frac{\partial \phi}{\partial x_i} - \frac{\partial}{\partial x_i}\left( \lambda_{ij} \frac{\partial \phi}{\partial x_j} \right) - Q \right)v dx dz = 0 , \qquad \text{Equation 3.18}$$

which must be valid for any arbitrary function $v$.

Introducing the notations (notice they are different from ones defined in (3.2)-(3.4))

$$I_t = \iint_D C(x,z,t)\frac{\partial \phi}{\partial t} v dx dz ; \qquad \text{Equation 3.19}$$

$$I_x = \iint_D F(x,z,t)q_x(x,z,t)\frac{\partial \phi}{\partial x} v dx dz ; \qquad \text{Equation 3.20}$$

$$I_z = \iint_D F(x,z,t)q_z(x,z,t)\frac{\partial \phi}{\partial z} v dx dz ; \qquad \text{Equation 3.21}$$

$$I_{xx} = \iint_D \frac{\partial}{\partial x}\left( \lambda_{xx}(x,z,t)\frac{\partial \phi}{\partial x} \right)v dx dz ; \qquad \text{Equation 3.22}$$

$$I_{xz} = \iint_D \frac{\partial}{\partial x}\left( \lambda_{xz}(x,z,t)\frac{\partial \phi}{\partial z} \right)v dx dz ; \qquad \text{Equation 3.23}$$

$$I_{zx} = \iint_D \frac{\partial}{\partial z}\left( \lambda_{xz}(x,z,t)\frac{\partial \phi}{\partial x} \right)v dx dz ; \qquad \text{Equation 3.24}$$

$$I_{zz} = \iint_D \frac{\partial}{\partial z}\left( \lambda_{zz}(x,z,t)\frac{\partial \phi}{\partial z} \right)v dx dz ; \qquad \text{Equation 3.25}$$

$$\tilde{Q} = \iint_D Q(x,z,t)v dx dz , \qquad \text{Equation 3.26}$$

we can rewrite (3.18) in the form:

$$I_t + I_x + I_z - I_{xx} - I_{xz} - I_{zx} - I_{zz} = \tilde{Q} . \qquad \text{Equation 3.27}$$

Performing the integration by parts in the integrals $I_{xx}$, $I_{xz}$, $I_{zx}$, $I_{zz}$, yields:

$$I_{xx} = -\iint_D \lambda_{xx}(x,z,t)\frac{\partial \phi}{\partial x}\frac{\partial v}{\partial x} dx dz + \oint_{\partial D} \lambda_{xx}(x,z,t)\frac{\partial \phi}{\partial x} v n_1 dS ; \qquad \text{Equation 3.28}$$

$$I_{xz} = -\iint_D \lambda_{xz}(x,z,t)\frac{\partial \phi}{\partial z}\frac{\partial v}{\partial x} dx dz + \oint_{\partial D} \lambda_{xz}(x,z,t)\frac{\partial \phi}{\partial z} v n_1 dS ; \qquad \text{Equation 3.29}$$

$$I_{zx} = -\iint\limits_{D} \lambda_{xz}(x,z,t) \frac{\partial \phi}{\partial x} \frac{\partial v}{\partial z} dxdz + \oint\limits_{\partial D} \lambda_{xz}(x,z,t) \frac{\partial \phi}{\partial x} vn_2 dS ;$$    **Equation 3.30**

$$I_{zz} = -\iint\limits_{D} \lambda_{zz}(x,z,t) \frac{\partial \phi}{\partial z} \frac{\partial v}{\partial z} dxdz + \oint\limits_{\partial D} \lambda_{zz}(x,z,t) \frac{\partial \phi}{\partial z} vn_2 dS .$$    **Equation 3.31**

The domain boundary,

$$\partial D = \partial D_1 \cup \partial D_2 \cup \partial D_3 ,$$    **Equation 3.32**

where $\partial D_1, \partial D_2, \partial D_3$ denote the segments, on which boundary conditions of the first, second, and third type are respectively specified:

$$\phi = \bar{\phi}, \quad \vec{x} \in \partial D_1 ;$$    **Equation 3.33**

$$\Phi_n = \vec{\Phi} \cdot \vec{n} = \bar{\Phi}_n, \quad \vec{x} \in \partial D_2 ;$$    **Equation 3.34**

$$\Phi_n = \bar{h}(\phi - \vartheta), \quad \vec{x} \in \partial D_3 ,$$    **Equation 3.35**

Here $\vec{\Phi}$ is the flux of the variable $\phi$, $\bar{h}$ is the exchange coefficient, $\vartheta$ is the value of $\phi$ in the outside of the domain $D$.

Taking into account (3.32) and remembering that we are free to set the arbitrary function $v$ so that $v|_{\partial D_1} = 0$, we obtain the weak form of the advective-diffusion equation (3.17):

$$I_t + I_x + I_z - I_{xx} - I_{xz} - I_{zx} - I_{zz} =$$

$$= \iint\limits_{D} C \frac{\partial \phi}{\partial t} vdxdz + \iint\limits_{D} Fq_x \frac{\partial \phi}{\partial x} vdxdz + \iint\limits_{D} Fq_z \frac{\partial \phi}{\partial z} vdxdz +$$

$$+ \iint\limits_{D} \lambda_{xx} \frac{\partial \phi}{\partial x} \frac{\partial v}{\partial x} dxdz + \iint\limits_{D} \lambda_{xz} \frac{\partial \phi}{\partial z} \frac{\partial v}{\partial x} dxdz + \iint\limits_{D} \lambda_{xz} \frac{\partial \phi}{\partial x} \frac{\partial v}{\partial z} dxdz +$$

$$+ \iint\limits_{D} \lambda_{zz} \frac{\partial \phi}{\partial z} \frac{\partial v}{\partial z} dxdz + \oint\limits_{\partial D_2} \bar{\Phi}_n vdS + \oint\limits_{\partial D_3} k(\phi - \vartheta)dS = \tilde{Q}$$

**Equation 3.36**

**<u>Step 3.</u>** *The weighted residual method.*

Similarly to Section 3.1.1, the approximation $\tilde{\phi}$ of the unknown $\phi$ is sought in the form:

$$\phi(x,z,t) \approx \tilde{\phi}(x,z,t) = \sum_{l=1}^{Nn} \beta_l(t)\psi_l(x,z) ,$$    **Equation 3.37**

Where $\{\psi_l(x,z) \,|\, l = 1,2,...Nn\}$ are known analytical functions (shape or trial functions), $\beta_l$'s are the coefficients to be defined.

As before, setting $v = \omega_k(x,z)$ and substituting (3.37) into (3,36), we obtain:

$$\sum_{l=1}^{Nn}\left(\iint_{D}C\psi_{l}\omega_{k}dxdz\right)\beta_{l}'(t)+$$

$$+\sum_{l=1}^{Nn}\left\{\iint_{D}Fq_{x}\frac{\partial\psi_{l}}{\partial x}\omega_{k}dxdz+\iint_{D}Fq_{z}\frac{\partial\psi_{l}}{\partial z}\omega_{k}dxdz+\iint_{D}\lambda_{xx}\frac{\partial\psi_{l}}{\partial x}\frac{\partial\omega_{k}}{\partial x}dxdz\right.$$

$$+\iint_{D}\lambda_{xz}\frac{\partial\psi_{l}}{\partial z}\frac{\partial\omega_{k}}{\partial x}dxdz+\iint_{D}\lambda_{xz}\frac{\partial\psi_{l}}{\partial x}\frac{\partial\omega_{k}}{\partial z}dxdz+\iint_{D}\lambda_{zz}\frac{\partial\psi_{l}}{\partial z}\frac{\partial\omega_{k}}{\partial z}dxdz+$$

$$\left.+\oint_{\partial D_{3}}\overline{h}\,\psi_{l}\omega_{k}dS\right\}\beta_{l}(t)+$$

$$+\left[\oint_{\partial D_{2}}\overline{\Phi}_{n}\omega_{k}dS-\iint_{D}Q\omega_{k}dxdz-\oint_{\partial D_{3}}\overline{h}\,\vartheta\omega_{k}dS\right]=0,\qquad\forall k=\overline{1,Nn}$$

<div align="right">**Equation 3.38**</div>

Denoting the expressions in round brackets, braces, and square brackets as $\widetilde{R}_{kl}$, $\widetilde{C}_{kl}$, and $\widetilde{s}_{k}$ respectively, we rewrite (3.38) as:

$$\sum_{l=1}^{Nn}\widetilde{R}_{kl}\beta_{l}'(t)+\sum_{l=1}^{Nn}\widetilde{C}_{kl}\beta_{l}(t)+\widetilde{s}_{k}=0,\qquad\forall k=\overline{1,Nn}\qquad\qquad\text{**Equation 3.39**}$$

where $\beta_{l}'(t)=\dfrac{d\beta_{l}}{dt}$.

(3.39) is a system of ordinary differential equations, with unknowns $\{\beta_{l}(t)\,|\,l=1,2,...Nn\}$ to be found. The problem is non-linear, as the coefficients are dependent on the unknown functions: temperature, salinity, and fluid velocities (which are calculated using Darcy's law from the hydraulic head distribution).

Combining (3.16) and the system (3.39) written for the unknown $\phi=T$ and the one written for $\phi=S$, we obtain the non-linear system of ordinary differential equations providing the approximate solution of the coupled problem of heat and mass transport in a porous medium.

## *3.2   Shape functions. Isoparametric transformation*

The main idea of the finite element method consists in the specific choice of shape functions, $\psi_l$, due to which the unknowns $\alpha_l$ and $\beta_l$, $l = \overline{1, Nn}$, are the nodal values of the functions to be defined (head, temperature and salinity); and the number of unknown parameters, $Nn$, is the total number of nodes in the problem domain.

To do this, the spatial problem domain is subdivided into elements (quadrilateral in our case). A shape function, $\psi_l$, is built so that it equals 1 at the node it is associated with (l-th grid node in "global" nodes numbering), is a bounded continuous differentiable function on each of the elements surrounding the given node, and equals 0 everywhere else in the domain $D$. In Figure 3.2 we illustrate this idea for a mesh of square elements: a chosen node (circled red) is surrounded by four elements (e1, e2, e3, e4), Figure 3.2(a). A bilinear shape function associated with the node is shown in Figure 3.2(b)



|       (a)       |        (b)        |
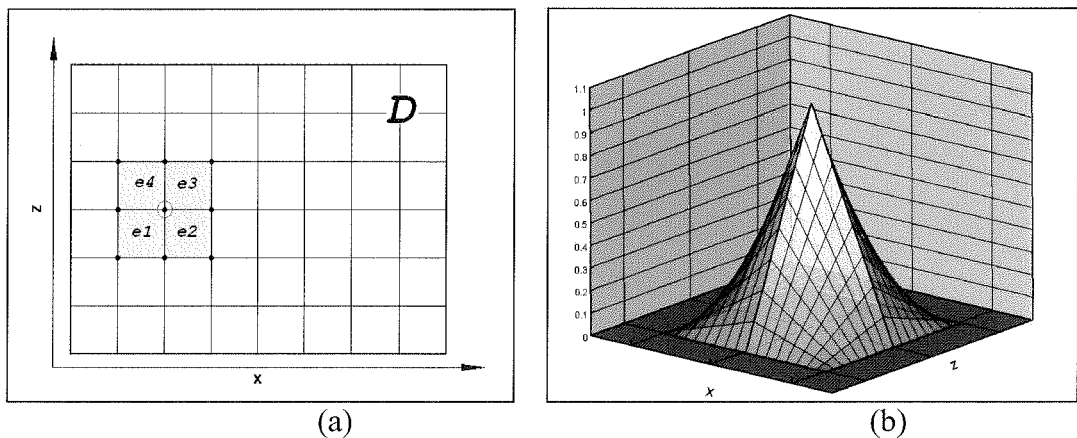
**Figure 3.2 An example of a bilinear shape function for the four-node rectangular element.**

The bilinear shape function for four-node rectangular elements, which we use in the model, is 'assembled' from four 'pieces', each defined over one of the four elements having the l-th node as one of corners, *e1, e2, e3, e4* . For a quadrilateral element of an arbitrary shape, these four parts are defined not in the physical (global) coordinates (x,z), but in local (element) coordinates, $(\xi, \eta)$. Then a one-to-one mapping of the archetypal square $\{(\xi, \eta) \mid -1 \le \xi \le 1, -1 \le \eta \le 1\}$ onto the quadrilateral element in physical coordinates (x,z) is established through a coordinate transformation. The transformation is specified in the way that corner nodes of the quadrilateral correspond to corner nodes of the square (Figure 3.3).
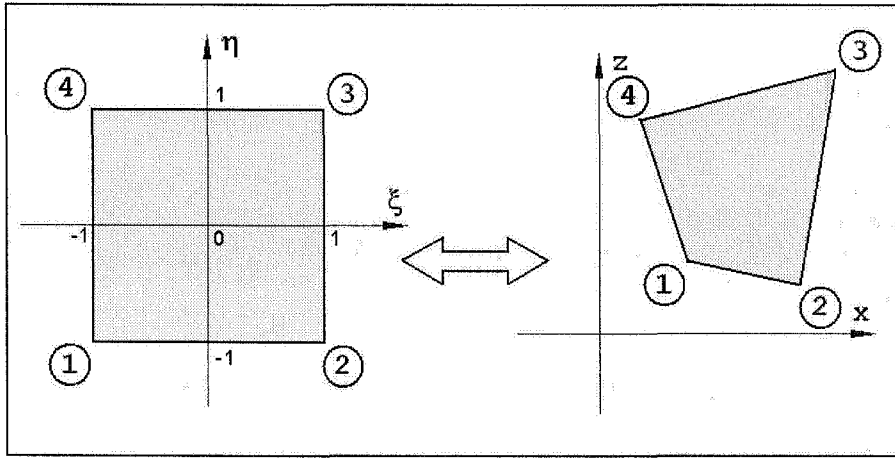
**Figure 3.3 Coordinate transformation of a two-by-two square in the element space into a quadrilateral element in physical space**

The coordinate transformation between physical space *(x,z)* and element space $(\xi, \eta)$ is defined by the expressions:

$$x = \sum_{i=1}^{4} \varphi_i(\xi, \eta)\bar{x}_i ,$$                                 **Equation 3.40**

$$z = \sum_{i=1}^{4} \varphi_i(\xi, \eta)\bar{z}_i ,$$                                 **Equation 3.41**

where

$$\varphi_1(\xi, \eta) = N_1(\xi)N_1(\eta) = \frac{1}{4}(1-\xi)(1-\eta) ,$$          **Equation 3.42**

$$\varphi_2(\xi, \eta) = N_2(\xi)N_1(\eta) = \frac{1}{4}(1+\xi)(1-\eta) ,$$          **Equation 3.43**

$$\varphi_3(\xi, \eta) = N_2(\xi)N_2(\eta) = \frac{1}{4}(1+\xi)(1+\eta) ,$$          **Equation 3.44**

$$\varphi_4(\xi, \eta) = N_1(\xi)N_2(\eta) = \frac{1}{4}(1-\xi)(1+\eta) ,$$          **Equation 3.45**

$$N_1(\xi) = \frac{1}{2}(1-\xi)$$                                                    **Equation 3.46**

$$N_2(\xi) = \frac{1}{2}(1+\xi)$$                                                    **Equation 3.47**

and

$\{(\bar{x}_i, \bar{z}_i) \mid i = \overline{1,4}\}$ are coordinates of the four element corners in physical space.

$\{\varphi_i(\xi, \eta) \mid i = \overline{1,4}\}$ are the *element basic functions*. They are associated with four corners of the archetypal square: $\varphi_i$ equals to 1 at the i-th element corner (the numbering order as shown in Figure 3.3). Their graphs are presented in Figures

3.4(a)-(c). A *"global" basic function*, $\psi_l$, correspondent to the l-th node of the grid covering the problem domain (like one shown in Figure 3.2(b)), consists of $\varphi_1$ defined over the element *e3*, $\varphi_2$ defined over *e4*, $\varphi_3$ defined over *e1*, and $\varphi_4$ defined over *e2*, converted to the physical space coordinates (x,z).
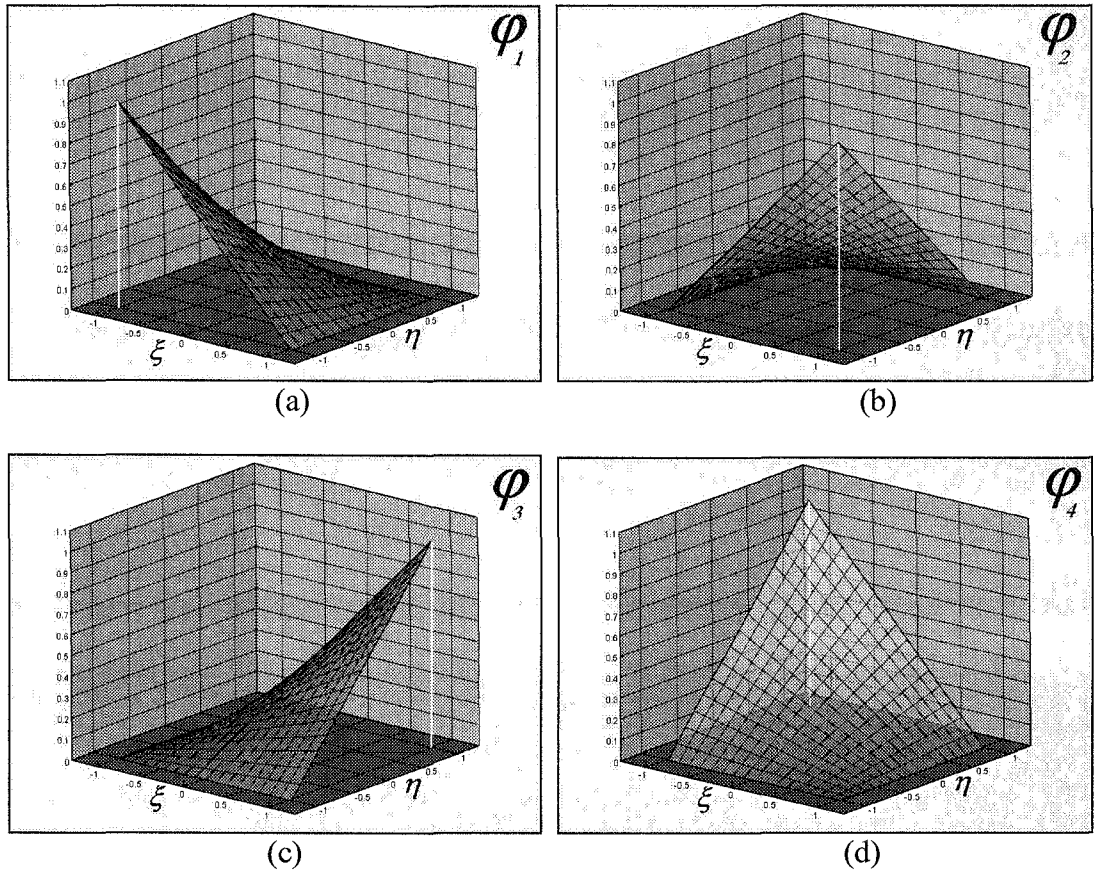


**Figure 3.4. The element basic functions, $\varphi_1$ (a), $\varphi_2$ (b), $\varphi_3$ (c), $\varphi_4$ (d).**

Thus, the basic functions $\{\varphi_i(\xi,\eta)\,|\,i=\overline{1,4}\}$ that define the trial solution over the archetypal square also specify the coordinate transformation (Wang and Anderson, 1982)

## 3.3   Weighting functions. 'Upwind' weighting

To solve the equation for the hydraulic head, which does not have advection terms, we use the original shape functions as weighting functions – standard Galerkin weighting procedure (in some sources, the Bubnov – Galerkin method):

$$\omega_k(x,z) = \psi_k(x,z), \quad k = \overline{1, Nn}.$$                     **Equation 3.48**

A different approach, the Petrov – Galerkin method, is used for the numerical solution of the advective-diffusion equation. This generalization of the standard Galerkin procedure implies the use of weighting (test) functions different from those originally used as shape functions (Zienkiewicz, 1977):

$$\omega_k(x,z) \neq \psi_k(x,z)$$                                         **Equation 3.49**

A special choice of non-symmetrical form of $\omega_k$'s helps to overcome a typical problem peculiar to the standard Galerkin procedure, which produces oscillatory solutions, when the problem is dominated by advection (Heinrich J.C. et al., 1977). By analogy with the finite difference schemes, in some literature the method is called 'upwinding'.

Similarly to the shape functions, first we set the element weight functions associated with its corners and defined in local (element) coordinates over the archetypal square (Zienkiewicz and Heinrich, 1978):

$$w_1(\xi,\eta) = [N_1(\xi) + \tilde{\alpha}_2 F(\xi)][N_1(\eta) + \tilde{\alpha}_1 F(\eta)] = L_1(\xi)L_1(\eta),$$     **Equation 3.50**

$$w_2(\xi,\eta) = [N_2(\xi) - \tilde{\alpha}_2 F(\xi)][N_1(\eta) + \tilde{\alpha}_3 F(\eta)] = L_2(\xi)L_1(\eta),$$     **Equation 3.51**

$$w_3(\xi,\eta) = [N_2(\xi) - \tilde{\alpha}_4 F(\xi)][N_2(\eta) - \tilde{\alpha}_3 F(\eta)] = L_2(\xi)L_2(\eta),$$     **Equation 3.52**

$$w_4(\xi,\eta) = [N_1(\xi) + \tilde{\alpha}_4 F(\xi)][N_2(\eta) - \tilde{\alpha}_1 F(\eta)] = L_1(\xi)L_2(\eta),$$     **Equation 3.53**

where the modifying function, $F$:

$$F(\xi) = -\frac{3}{4}(1-\xi)(1+\xi),$$                                 **Equation 3.54**

$\tilde{\alpha}_k$ are the four parameters that govern the degree of upwinding along the sides of a quadrilateral element. In our notation, $\tilde{\alpha}_1$ is associated with the element side, correspondent to the left side of the archetypal square between 1st and 4th nodes, $\tilde{\alpha}_2$ - with the bottom side (1st and 2nd), $\tilde{\alpha}_3$ - with the right side (2nd and 3rd), and $\tilde{\alpha}_4$ - with the top side (4th and 3rd), see Figure 3.5.
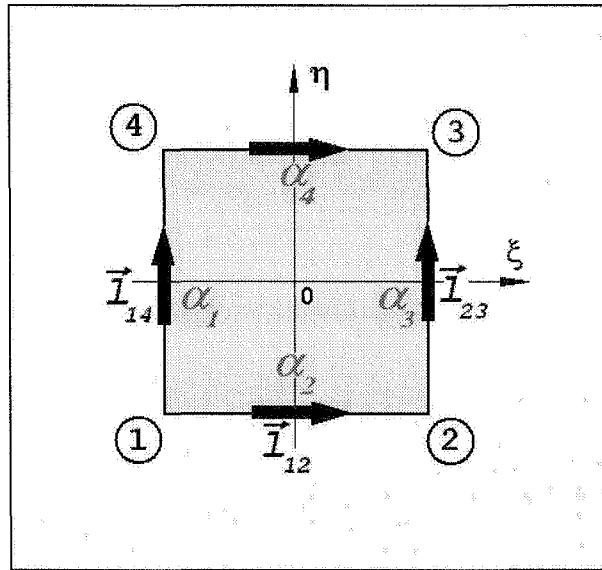
**Figure 3.5 The sign convention adopted for the 'upwinding' parameers.**

$\tilde{\alpha}_k$'s absolute values range from 0 (no upwinding, when the weigh functions coincide with the shape functions) to 1 (full upwinding) and signs are made dependent on the direction of the velocity vector (Heinrich J.C. et al., 1977). We omit here the theoretical reasoning of $\tilde{\alpha}_k$'s definition, as they can be found in (Zienkiewicz and Heinrich, 1978: p.3) or (Heinrich J.C. et al., 1977: pp.135-138). We present here only the algorithm of their calculation that was adapted for to our particular case of non-linear heat and mass transport equations in porous media.

$\tilde{\alpha}_k$'s absolute value is defined based on the local Reynolds number, $\gamma_k$, computed for a chosen direction $\vec{l}_{ij}$. Here, $\vec{l}_{ij}$ is the vector specifying the direction of an element side between nodes i and j, a unit vector in the positive direction, which coordinates are calculated from coordinates of the i-th and j-th nodes in physical space (x,z). 'Positive direction' is chosen in the direction of increase of the local variables $(\xi,\eta)$ (Figure 3.5).

In our case,

$$\gamma_k = \frac{coeff\ n\ V_{ij}\ h_{ij}}{D_a},$$                                      **Equation 3.55**

where

$k$ is the number of the element side (numbering order as the one adopted for $\tilde{\alpha}_k$'s)

$$coeff = \begin{cases} \rho_f c_f, & \text{for the heat transport equation} \\ 1, & \text{for the mass transport equation} \end{cases}$$

$V_{ij}$ is the component of the average velocity vector along the element side $ij$,

$$V_{ij} = \frac{1}{2}(\vec{V_i} + \vec{V_j}) \cdot \vec{l_{ij}},$$                    **Equation 3.56**

where $\vec{V_i}$ and $\vec{V_j}$ are the fluid velocity vectors at the nodes $i$ and $j$ respectively,

$h_{ij}$ is the length of the element side $ij$ in physical space,

$D_a$ is the dispersion (thermodispersion) coefficient averaged over the element.

Since we assume the porous medium anisotropic, the dispersion coefficients can be different in the lengthwise and crosswise to the bedding plane directions, therefore

$$D_a = \begin{cases} D_{lengthwise}, & \text{if calculating } \alpha_2 \text{ or } \alpha_4 \\ D_{crosswise}, & \text{if calculating } \alpha_1 \text{ or } \alpha_3 \end{cases}$$      **Equation 3.57**

Where $D_{lengthwise}$ and $D_{crosswise}$ are computed by the formulas inverse to (2.6):

$$D_{lengthwise} = \frac{\lambda_{xx} + \lambda_{zz}}{2} + \frac{\lambda_{xx} - \lambda_{zz}}{2}\cos 2\theta - \lambda_{xz}\sin 2\theta,$$

**Equation 3.58**

$$D_{crosswise} = \frac{\lambda_{xx} + \lambda_{zz}}{2} - \frac{\lambda_{xx} - \lambda_{zz}}{2}\cos 2\theta + \lambda_{xz}\sin 2\theta.$$

Since $\gamma_k$'s have been defined, we calculate $\alpha_k$'s by formulas:

$$\alpha_k = \begin{cases} \alpha_o = \coth\left(\dfrac{\gamma_k}{2}\right) - \dfrac{2}{\gamma_k}, & \gamma_k \leq 10 \\ \alpha_c = 1 - \dfrac{2}{\gamma_k}, & \gamma_k > 10 \end{cases}$$      **Equation 3.59**

where $\alpha_o$ is an *optimal value* of the parameter at which the exact solution of the one-dimensional problem can be obtained, $\alpha_c$ is the *critical value*, the minimum value of $\alpha$, at which the problem solution is oscillation free (Christie et al., 1976). Graphs of $\alpha_o$ and $\alpha_c$ are shown in Figure 3.6. In general, the optimal value of the parameter, $\alpha_o$, has to be computed for each element side. But for large values of $\gamma$, $\alpha_o$ calculation would introduce difficulties in evaluating the exponential. However,

the asymptotic behaviour of $\alpha_o$ for large $\gamma$ allows to replace it with $\alpha_c$ (Zienkiewicz and Heinrich, 1978). Thus for example, for $\gamma=10$, $\alpha_o - \alpha_c < 10^{-4}$, so using the critical value does not effect the accuracy of calculation.
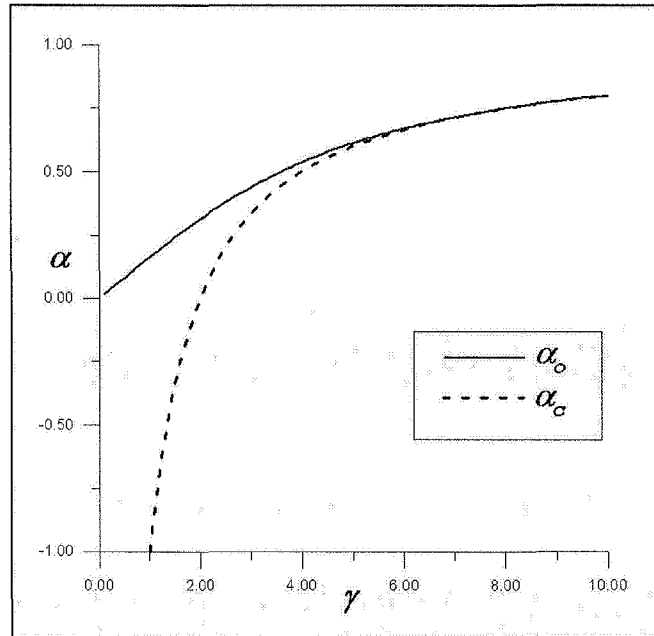


**Figure 3.6 'Upwinding' parameters depending on the local Reynolds number.**

Thus, to construct a weight function, the four parameters $\tilde{\alpha}_k$ must be computed for each element, as the element size, fluid velocity, values of dispersion (thermodispersion) coefficients vary from element to element. Then four element weight functions are built with the use of (3.50)-(3.53). Afterwards, the 'global' weight function, $\omega_k$, is constructed in a similar way as the shape functions $\psi_l$ (Section 1.1).

The effectiveness of the employment of the 'upwind' finite element scheme was supported by one of the preliminary runs of the model. It appeared that in case of application of the standard Galerkin method, an undesirable numerical effect appears at the outlets of highly permeable faults, where fluid velocities are high. Figure 3.7 illustrates this problem. In Figure 3.7(a) we show the fluid velocity field superimposed over the section hydrostratigraphy. The permeable faults are marked green. One can see that in these areas fluid velocities have maximal values. Figure 3.7(b) shows fluid temperature distribution with the problem areas circled red (temperature scale is in $^o C$).
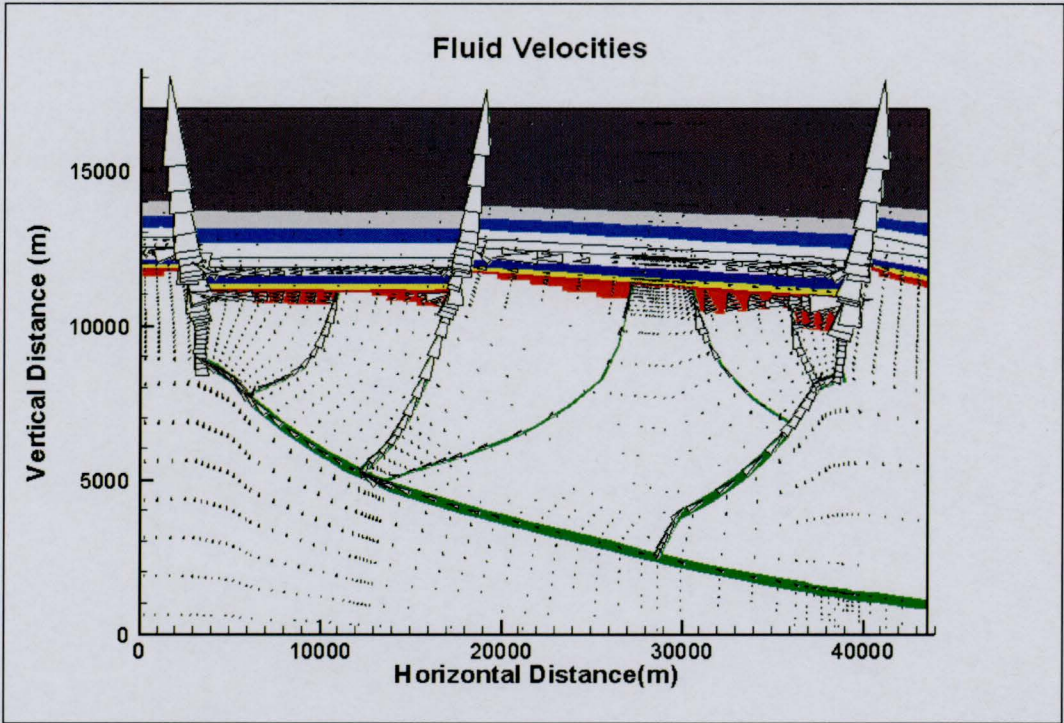
(a)
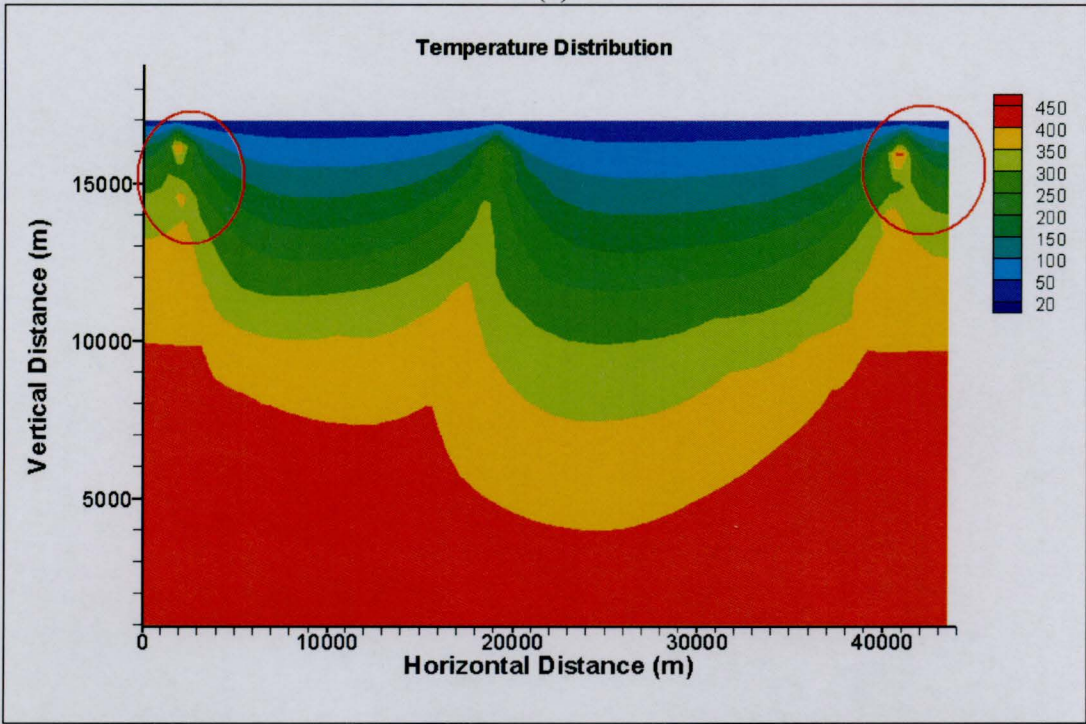


(b)

**Figure 3.7 Illustration of a numerical error appearing if the standard Galerkin method is applied. (a) Fluid velocity field (maximum velocities are at the outlets of the discharge faults); (b) fluid temperature distribution (circles mark zones, where strong numerical perturbations appear).**

The numerical error manifests itself as isolated hot water spots at the top outlets of the discharge faults, although there is no physical reason for this.

In Figure 3.8 we show the result of the model application under the same conditions but with 'upwinding' involved.

42

**Temperature Distribution**
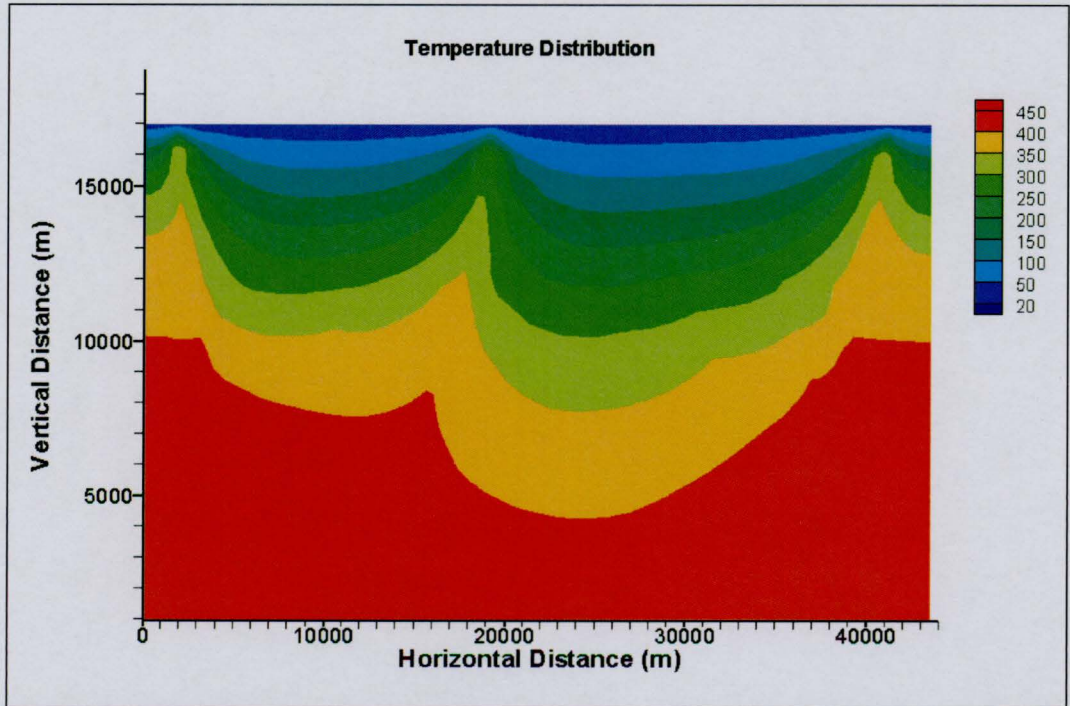


**Figure 3.8 An example of the Petrov-Galerkin method application, which handles the numerical error in the advection-dominative areas.**

One can see that the 'upwinding' procedure does not affect the temperature distribution all over the domain, it just removes the non-physical effects at the fault outlets.

## 3.4 Integrals evaluation

To calculate coefficients and right-hand side terms of the systems of ordinary differential equations (3.16), (3.39) that were obtained as a result of the weighted residual method application, $R_{kl}$, $C_{kl}$, $S_k$ , $\tilde{R}_{kl}$, $\tilde{C}_{kl}$, and $\tilde{S}_k$, we need to evaluate the integrals of such forms:

$$\iint_D coeff(x,z,t)\psi_l(x,z)\omega_k(x,z)dxdz , \qquad \textbf{Equation 3.60}$$

$$\iint_D coeff(x,z,t)\frac{\partial\psi_l(x,z)}{\partial x_m}\frac{\partial\omega_k(x,z)}{\partial x_n}dxdz , \qquad \textbf{Equation 3.61}$$

$$\iint_D coeff(x,z,t)\frac{\partial\omega_k(x,z)}{\partial x_n}dxdz , \qquad \textbf{Equation 3.62}$$

$$\iint\limits_{D} coeff(x,z,t)\frac{\partial \psi_l(x,z)}{\partial x_m}\omega_k(x,z)dxdz \, , \qquad\qquad \text{Equation 3.63}$$

$$\iint\limits_{D} coeff(x,z,t)\omega_k(x,z)dxdz \, , \qquad\qquad \text{Equation 3.64}$$

where $l,k=\overline{1,Nn}$ ; $n,m=1,2$ (see equations (3.15), (3.38)).

As both shape and test functions are non-zero only on four elements surrounding the node the functions are associated with, instead of the integral over the region D we will have a sum of the integrals evaluated over the elements, on which both $\psi_l$ and $\omega_k$ are non-zero. Thus, the integrals of (3.60)-(3.64) forms, but over a finite element $e$ must be evaluated.

An integral over a finite element $e$ is computed in local (element) coordinates $(\xi,\eta)$, using formula of change of coordinates in a double integral (Campbell and Dierker, 1976):

$$\iint\limits_{e} f(x,z)dxdz = \int\limits_{-1}^{1}\int\limits_{-1}^{1} f(x(\xi,\eta),z(\xi,\eta))\left|\det J\right| d\xi d\eta \, , \qquad \text{Equation 3.65}$$

where

$$J = \begin{pmatrix} \dfrac{\partial x}{\partial \xi} & \dfrac{\partial z}{\partial \xi} \\[2mm] \dfrac{\partial x}{\partial \eta} & \dfrac{\partial z}{\partial \eta} \end{pmatrix}, \qquad\qquad \text{Equation 3.66}$$

$$\det J = \frac{\partial x}{\partial \xi}\frac{\partial z}{\partial \eta} - \frac{\partial z}{\partial \xi}\frac{\partial x}{\partial \eta} = \frac{\partial(x,z)}{\partial(\xi,\eta)}, \qquad\qquad \text{Equation 3.67}$$

and $\dfrac{\partial(x,z)}{\partial(\xi,\eta)} = \begin{pmatrix} \dfrac{\partial x}{\partial \xi} & \dfrac{\partial x}{\partial \eta} \\[2mm] \dfrac{\partial z}{\partial \xi} & \dfrac{\partial z}{\partial \eta} \end{pmatrix}$ is the Jacobian of the coordinate transformation

defined by (3.40)-(3.41).

Let us consider an integral which includes a shape (test) function derivative, like for example following:

$$\iint\limits_{e} coeff(x,z,t)\frac{\partial \varphi_i}{\partial x_m}\frac{\partial w_j}{\partial x_n}dxdz \, , \qquad\qquad \text{Equation 3.68}$$

The change of coordinates in this integral leads to the representation:

$$\iint\limits_{e} coeff(x,z,t)\frac{\partial \varphi_i}{\partial x_m}\frac{\partial w_j}{\partial x_n}dxdz = \int\limits_{-1}^{1}\int\limits_{-1}^{1} coeff(\xi,\eta,t)\frac{\partial \varphi_i}{\partial x_m}(\xi,\eta)\frac{\partial w_j}{\partial x_n}(\xi,\eta)\left|\det J\right| d\xi d\eta$$

$$\text{Equation 3.69}$$

So we need to express the derivatives $\dfrac{\partial \varphi_i}{\partial x_m}(\xi,\eta)$ and $\dfrac{\partial w_j}{\partial x_n}(\xi,\eta)$ in the local

element coordinates $(\xi,\eta)$.

For an arbitrary function, $f = f\big(x(\xi,\eta), z(\xi,\eta)\big)$,

$$\frac{\partial f}{\partial \xi} = \frac{\partial f}{\partial x}\frac{\partial x}{\partial \xi} + \frac{\partial f}{\partial z}\frac{\partial z}{\partial \xi},$$

<div align="right">**Equation 3.70**</div>

$$\frac{\partial f}{\partial \eta} = \frac{\partial f}{\partial x}\frac{\partial x}{\partial \eta} + \frac{\partial f}{\partial z}\frac{\partial z}{\partial \eta}$$

<div align="right">**Equation 3.71**</div>

or in the matrix form:

$$\begin{pmatrix} \dfrac{\partial f}{\partial \xi} \\ \dfrac{\partial f}{\partial \eta} \end{pmatrix} = \begin{pmatrix} \dfrac{\partial x}{\partial \xi} & \dfrac{\partial z}{\partial \xi} \\ \dfrac{\partial x}{\partial \eta} & \dfrac{\partial z}{\partial \eta} \end{pmatrix}\begin{pmatrix} \dfrac{\partial f}{\partial x} \\ \dfrac{\partial f}{\partial z} \end{pmatrix} = J\begin{pmatrix} \dfrac{\partial f}{\partial x} \\ \dfrac{\partial f}{\partial z} \end{pmatrix}$$

<div align="right">**Equation 3.72**</div>

Hence

$$\begin{pmatrix} \dfrac{\partial f}{\partial x} \\ \dfrac{\partial f}{\partial z} \end{pmatrix} = J^{-1}\begin{pmatrix} \dfrac{\partial f}{\partial \xi} \\ \dfrac{\partial f}{\partial \eta} \end{pmatrix} = \frac{1}{\det J}\begin{pmatrix} \dfrac{\partial z}{\partial \eta} & -\dfrac{\partial z}{\partial \xi} \\ -\dfrac{\partial x}{\partial \eta} & \dfrac{\partial x}{\partial \xi} \end{pmatrix}\begin{pmatrix} \dfrac{\partial f}{\partial \xi} \\ \dfrac{\partial f}{\partial \eta} \end{pmatrix}$$

<div align="right">**Equation 3.73**</div>

or

$$\frac{\partial f}{\partial x} = \frac{\partial f}{\partial x}(\xi,\eta) = \frac{1}{\det J}\left( \frac{\partial z}{\partial \eta}\frac{\partial f}{\partial \xi} - \frac{\partial z}{\partial \xi}\frac{\partial f}{\partial \eta} \right),$$

<div align="right">**Equation 3.74**</div>

$$\frac{\partial f}{\partial z} = \frac{\partial f}{\partial z}(\xi,\eta) = \frac{1}{\det J}\left( -\frac{\partial x}{\partial \eta}\frac{\partial f}{\partial \xi} + \frac{\partial x}{\partial \xi}\frac{\partial f}{\partial \eta} \right).$$

<div align="right">**Equation 3.75**</div>

The integrals over the archetypal square $\{(\xi,\eta)\,|-1\le\xi\le1,\,-1\le\eta\le1\}$ are

calculated numerically by the Gaussian quadrature formula:

$$\int_{-1}^{1}\int_{-1}^{1} g(\xi,\eta)d\xi d\eta \approx \sum_{i=1}^{NGss}\sum_{j=1}^{NGss} a_i a_j g(\varsigma_i,\varsigma_j),$$

<div align="right">**Equation 3.76**</div>

where $a_i$ is the required weighting factor at the Gauss point $\varsigma_i$. In the code, the

option to chose $NGss=2,3,4$ or $5$ is embedded. $a_i$ and $\varsigma_i$ values are taken from (Korn

and Korn, 1961) and are shown in Table 3.2

| NGss | Abscissas $\varsigma_i$ | Weight factors $a_i$ |
|------|------------|---------------|
| 2 | $\pm 0.577350$ | 1 |
| 3 | 0 | 8/9 |
|   | $\pm 0.774597$ | 5.9 |
| 4 | $\pm 0.339981$ | 0.652145 |
|   | $\pm 0.861136$ | 0.347855 |
| 5 | 0 | 0.568889 |
|   | $\pm 0.538469$ | 0.478629 |
|   | $\pm 0.906180$ | 0.236927 |

**Table 3.2 Abscissas and weight factors for Gauss quadrature formulae.**

## 3.5 Time-stepping scheme

The procedure of semi-discretization of transient problems (2.3) and (3.17) has led to the coupled non-linear systems of ordinary differential equations (3.16), (3.39). As both of the systems have the same type, we unify the presentation, considering (3.16), written in the matrix form:

$$\mathbf{R}\vec{\alpha}' + \mathbf{C}\vec{\alpha} + \vec{s} = 0 \qquad \text{Equation 3.77}$$

where

$\mathbf{R} = (R_{kl})_{k,l=1}^{Nn}$, $\mathbf{C} = (C_{kl})_{k,l=1}^{Nn}$ are capacitance and thermal conductance matrixes,

$\vec{s} = (s_k)_{k=1}^{Nn}$ is the vector of heat loads (Tamma et al., 1999).

Following (Zienkiewicz, 1977) we adopt a weighted residual approach to the time discretization in the transient problem.

Specifying a set of time instants $\{t_i \mid i = \overline{1, Nt}\}$ which divide the time interval of interest $[0,T]$, we consider

$$\vec{\alpha} \approx \tilde{\vec{\alpha}} = \sum_{i=1}^{Nt} M_i \vec{\alpha}_i \qquad \text{Equation 3.78}$$

where

$\tilde{\vec{\alpha}}$ is the approximation to the unknown ("approximation to the problem") $\vec{\alpha}$; $\vec{\alpha}_i$ stands for a nodal set $\vec{\alpha}$ at the time instant $t_i$; the shape functions, $M_i$'s, are the same for each component of the vector $\vec{\alpha}$ and hence scalar.

Substituting (3.78) into (3.77), we obtain:

$$\sum_{i=1}^{Nt} \mathbf{R} M_i' \vec{\alpha}_i' + \sum_{i=1}^{Nt} \mathbf{C} M_i \vec{\alpha}_i + \vec{s} = 0.$$

Equation 3.79

As equation (3.77) is of first order, the lowest order of polynomial is necessary for $M_i$ (its graph is shown in figure 3.9):

$$M_i(t) = \frac{t_{i+1} - t}{t_{i+1} - t_i} = \frac{t_{i+1} - t}{\Delta t},$$

Equation 3.80

$$M_{i+1}(t) = \frac{t - t_i}{t_{i+1} - t_i} = \frac{t - t_i}{\Delta t}.$$

Equation 3.81
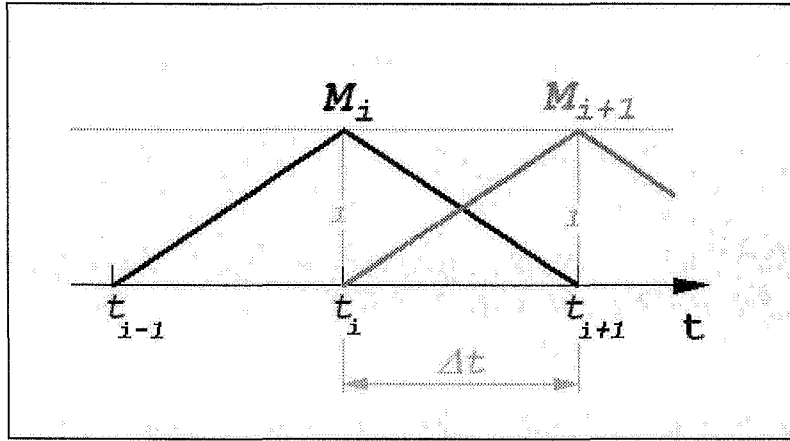


**Figure 3.9 Shape function for two point recurrence time scheme.**

Considering a typical time element of length $\Delta t$, we introduce the local element coordinate $\varsigma$. Now the interpolation, shape functions and their derivatives can be expressed in terms of the variable $\varsigma$. The transformation, mapping $\{t \mid t \in [t_i, t_{i+1}]\}$ to $\{\varsigma \mid \varsigma \in [0,1]\}$ is:

$$\varsigma = \frac{t - t_i}{t_{i+1} - t_i} = \frac{t - t_i}{\Delta t}.$$

Equation 3.82

Now in the time element coordinates:

$$M_i(\varsigma) = 1 - \varsigma; \qquad M_{i+1}(\varsigma) = \varsigma$$

Equation 3.83

and

$$M_i' = \frac{dM_i}{dt} = \frac{dM_i}{d\varsigma} \frac{d\varsigma}{dt} = \frac{dM_i}{d\varsigma} \frac{1}{\Delta t} = \dot{M}_i \frac{1}{\Delta t}.$$

Equation 3.84

Assuming that the full domain of interest corresponds with that of one element, taking into account (3.79) and (3.84) we may write the weighted residual equation:

$$\int_0^1 \left[ \mathbf{R}(\vec{\alpha}_i \dot{M}_i + \vec{\alpha}_{i+1} \dot{M}_{i+1}) + \mathbf{C}(\vec{\alpha}_i M_i + \vec{\alpha}_{i+1} M_{i+1}) + \vec{s} \right] W_j d\varsigma = 0, \quad j=1$$

Equation 3.85

or

$$\left[\frac{1}{\Delta t}\int_0^1 \mathbf{R}W_j d\varsigma + \int_0^1 \mathbf{C}\varsigma W_j d\varsigma\right]\vec{\alpha}_{i+1} + \left[-\frac{1}{\Delta t}\int_0^1 \mathbf{R}W_j d\varsigma + \int_0^1 \mathbf{C}(1-\varsigma)W_j d\varsigma\right]\vec{\alpha}_i +$$

$$+ \int_0^1 \vec{f}W_j d\varsigma = 0$$

**Equation 3.86**

In theory, the full integration should be performed in (3.86). But the procedure is not straightforward due to the non-linearity of the problem: the integration can only be carried out numerically with iteration within each time step, which makes it costly.

We substitute dependent on $\varsigma$ $\mathbf{R}$, $\mathbf{C}$, and $\vec{f}$ with their interpolations $\overline{\mathbf{R}}$, $\overline{\mathbf{C}}$, $\overline{\vec{f}}$ within the interval [0,1]. The interpolation is constructed by $\mathbf{R}^i$, $\mathbf{C}^i$, $\vec{f}^i$, the result from the previous time step that corresponds to $\varsigma = 0$, and yet unknown $\mathbf{R}^{i+1}$, $\mathbf{C}^{i+1}$, $\vec{f}^{i+1}$ corresponding to $\varsigma = 1$. Now (3.86) can be rewritten:

$$\left[\frac{1}{\Delta t}\overline{\mathbf{R}}\int_0^1 W_j d\varsigma + \overline{\mathbf{C}}\int_0^1 \varsigma W_j d\varsigma\right]\vec{\alpha}_{i+1} + \left[-\frac{1}{\Delta t}\overline{\mathbf{R}}\int_0^1 W_j d\varsigma + \overline{\mathbf{C}}\int_0^1 (1-\varsigma)W_j d\varsigma\right]\vec{\alpha}_i +$$

$$+ \overline{\vec{f}}\int_0^1 W_j d\varsigma = 0$$

**Equation 3.87**

If we denote

$$\sigma = \frac{\int_0^1 \varsigma W_j d\varsigma}{\int_0^1 W_j d\varsigma},$$

**Equation 3.88**

(3.87) becomes:

$$\left[\frac{1}{\Delta t}\overline{\mathbf{R}} + \sigma\overline{\mathbf{C}}\right]\vec{\alpha}_{i+1} + \left[-\frac{1}{\Delta t}\overline{\mathbf{R}} + (1-\sigma)\overline{\mathbf{C}}\right]\vec{\alpha}_i + \overline{\vec{f}} = 0$$ **Equation 3.89**

It is logical and convenient to use the following interpolation for $\overline{\vec{f}}$ :

$$\overline{\vec{f}} = \sigma\vec{f}^{i+1} + (1-\sigma)\vec{f}^i$$ **Equation 3.90**

$\overline{\mathbf{R}}$ and $\overline{\mathbf{C}}$ can be evaluated in the similar way but with the independent weight factors, $\sigma_c$ and $\sigma_{cR}$ :

$$\overline{\mathbf{C}} = \mathbf{C}^{\sigma c} = \sigma_c\mathbf{C}^{i+1} + (1-\sigma_c)\mathbf{C}^i,$$ **Equation 3.91**

$$\overline{\mathbf{R}} = \mathbf{R}^{\sigma cR} = \sigma_{cR}\mathbf{R}^{i+1} + (1-\sigma_{cR})\mathbf{R}^i.$$ **Equation 3.92**

Now substitution (3.91)-(3.92) into (3.89) yields:

$$\left[\frac{1}{\Delta t}\mathbf{R}^{\alpha R}+\sigma\mathbf{C}^{\alpha c}\right]\vec{\alpha}_{i+1}=\left[\frac{1}{\Delta t}\mathbf{R}^{\alpha R}-(1-\sigma)\mathbf{C}^{\alpha c}\right]\vec{\alpha}_i-\left(\sigma\vec{f}^{i+1}+(1-\sigma)\vec{f}^i\right)$$

**Equation 3.93**

As $\mathbf{R}^{\alpha R}$, $\mathbf{C}^{\alpha c}$, and $\vec{f}^{i+1}$ depend on yet unknown $\vec{\alpha}_{i+1}$, the iterative procedure should be involved:

$$\left[\frac{1}{\Delta t}\overset{(s)}{\mathbf{R}^{\alpha R}}+\sigma\overset{(s)}{\mathbf{C}^{\alpha c}}\right]\overset{(s+1)}{\vec{\alpha}}_{i+1}=\left[\frac{1}{\Delta t}\overset{(s)}{\mathbf{R}^{\alpha R}}-(1-\sigma)\overset{(s)}{\mathbf{C}^{\alpha c}}\right]\vec{\alpha}_i-\left(\sigma\overset{(s)}{\vec{f}^{i+1}}+(1-\sigma)\vec{f}^i\right),$$

**Equation 3.94**

where $s$ and $s+1$ denote two successive iterations,

$$\overset{(s)}{\mathbf{C}^{\alpha c}}=\sigma_c\overset{(s)}{\mathbf{C}^{i+1}}+(1-\sigma_c)\mathbf{C}^i,$$

**Equation 3.95**

$$\overset{(s)}{\mathbf{R}^{\alpha R}}=\sigma_{cR}\overset{(s)}{\mathbf{R}^{i+1}}+(1-\sigma_{cR})\mathbf{R}^i.$$

**Equation 3.96**

(3.94) is a system of linear algebraic equations that must be solved at each iterative step.

Different variants of (3.94) are reported to be used. Thus, the simplest one is when all the coefficients, $C_{kl}$ and $R_{kl}$ are evaluated at the previous time step (the scheme itself still can remain implicit if $\sigma\neq0$) (Zienkiewicz, 1977: p.595). (Holzbecher, 1998) used in his model $\sigma_{cR}=1$, while $\sigma_c=1$ in the left-hand side of (3.94) and $\sigma_c=0$ in the right-hand side.

We found that the way of weighting $\mathbf{C}$ and $\mathbf{R}$ scarcely influences the result, especially for complex profile configurations. In most simulations, we used fully implicit scheme ($\sigma=1$) as it permits a higher time step and therefore reduces the time of computations.

## 3.6   *System of linear equations with a sparse matrix*

System of linear algebraic equations (3.94) can be rewritten in the form:

$$\mathbf{A}\vec{y} = \vec{b}$$                                          **Equation 3.97**

where

$$\mathbf{A} = \frac{1}{\Delta t}\overset{(s)}{\mathbf{R}^{\alpha R}} + \sigma\overset{(s)}{\mathbf{C}^{\alpha}},$$                                 **Equation 3.98**

$$\vec{y} = \overset{(s+1)}{\vec{\alpha}}_{i+1},$$                          **Equation 3.99**

$$\vec{b} = \left[\frac{1}{\Delta t}\overset{(s)}{\mathbf{R}^{\alpha R}} - (1-\sigma)\overset{(s)}{\mathbf{C}^{\alpha}}\right]\vec{\alpha}_i - \left(\sigma\overset{(s)}{\vec{f}^{i+1}} + (1-\sigma)\vec{f}^i\right).$$   **Equation 3.100**

Matrix of the system, $\mathbf{A}$, and the right-hand side vector, $\vec{b}$, are recalculated at each iteration step.

We adopt the grid node numeration order in columns starting from the below moving from the left to right. If $N_z$ is the number of nodes in a column, and $N_x$ – in a row, then the total number of nodes in the finite element grid of quadrilateral elements, $N_n = N_x N_z$.

Matrix $\mathbf{A}$ of the system has structure shown in Figure 3.10.
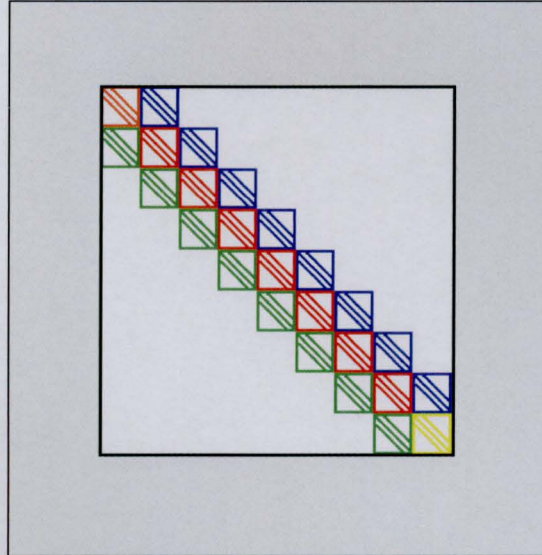


**Figure 3.10 Structure of the matrix of the system.**

This is a block tridiagonal matrix with each block being tridiagonal in its turn too. Matrix dimension, $\dim \mathbf{A} = N_n$, while the dimension of a block equals to $N_z$. In

another way, the matrix can be interpreted as banded with the lower and upper bandwidth $N_z + 1$.

As for the system of linear equations that provides the numerical solution for the hydraulic head, its matrix is symmetrical, because we use the shape functions by way of weight functions. The symmetry is broken only if the boundary condition of the first type is prescribed at a node (forced boundary condition in terminology of (Zienkiewicz, 1977)). In this case, the equation correspondent to the node is substituted by

$$y_l = y_l^0,$$                                                                          **Equation 3.101**

where $l$ is the node number $y_l^0$ is the specified value of the variable at this boundary node. (3.101) leads to zeroing all the matrix elements except the diagonal, which equals to 1, and substituting the correspondent right-hand side vector component by $y_l^0$.

Matrix of the system for the advective-diffusion equation is non-symmetrical due to the presence of advection terms. If upwinding involved, there is no symmetry even in the hypothetical case, if no advective fluid motion present.

We unify the procedure of the linear system solution for all the equations and employ the direct LU-decomposition (Duff et al., 1986) modified for a banded matrix. Even if this method is not the best in the sense of storing and processing unused inner zero diagonals, it nevertheless gives an advantage comparatively to the classical Gauss elimination procedure. Thus, the latter needs $\dfrac{2n^3}{3}$ operations ($n$ is the matrix dimension), which in our case is $\dfrac{2N_x^3 N_z^3}{3}$, while the algorithm for a banded matrix – about $2npq$ ($p$ is the lower bandwidth, $q$ – the upper bandwidth), that in our case is $2N_x N_z (N_z + 1)^2$ (Golub and Van Loan, 1989). We used the finite element grid with $N_x = 61$, $N_z = 44$. In this situation, our algorithm needs approximately 1186 times fewer operations than the standard procedure.

In (Golub and Van Loan, 1989) we found justification of the Block LU Factorization method being even more effective, especially taking into account the tridiagonal structure of each block, this modification can be the subject of further improvement of the model.

# 4  Model Validation

The validation of the model was carried out in several steps. First, the numerical results were compared with the analytical solutions obtained under restrictive simplifying assumptions (Section 4.1). Some properties of the numerical method were investigated in the process.

Second, the model was applied to several problems of free convection in a porous media (Section 4.2). The model output was compared both with the published results of several numerical studies and experimental data. Although the published results themselves do not lack contradiction, the model output was found to be physically correct and for some case studies is quantitatively consistent with the reported data.

The third step undertaken was a set of tests performed for a more complex structure, the faulted sedimentary section of the McArthur Basin, Northern Territory, Australia (Section 4.3). Although not all results are purely non-contradictory, the model has been proven to be applicable to this type of problem as well. An interesting result obtained in the process is that in some cases not a steady-state but a periodical solution can be obtained. The hydrothermal system showed an 'auto-oscillatory' regime: a sequence of states that repeat cyclically.

The last section of this chapter (Section 4.4) compares the results of the coupled heat-mass transport simulation with the numerical study of the thermohaline convection by Rosenberg and Spera (1992). The developed model showed the ability to reproduce the results obtained by an independent algorithm for a wide range of boundary and initial conditions and model parameters.

## 4.1  Comparison with the analytical solutions for simplified problems

As the coupled problem cannot be solved analytically, we consider the equation for the hydraulic head (Section 4.1.1) and the advective diffusion equation (Section 4.1.2) separately. The analytic solutions are constructed for a one-dimensional problem that has its physical interpretation. Different types of boundary conditions analogous to ones that can be posed in the simulations are considered.

It is shown that in all cases, the numerical model provides a numerical solution that is in good agreement with the analytical one. The necessary accuracy can be acquired by the manipulation with the time step value and the time-stepping scheme used.

## 4.1.1 Equation for the hydraulic head

We consider equation (2.3) and, taking into account the Darcy's law (2.5), rewrite it in the form:

$$S_0 \frac{\partial \varphi_0}{\partial t} + \frac{\partial}{\partial x_i}\left(-K_{ij}\left[\frac{\partial \varphi_0}{\partial x_j} + \rho_r \frac{\partial z}{\partial x_j}\right]\right) = 0.$$                     **Equation 4.1**

First simplification done is that an isotropic horizontal layer of a homogeneous porous medium is considered. In this case:

$$K_{xz} = 0,$$                                                                                       **Equation 4.2**

$$K_{xx} = K_{zz} = K = const.$$

Taking into account that $\rho_r = \dfrac{\rho_f - \rho_0}{\rho_0}$ we obtain:

$$S_0 \frac{\partial \varphi_0}{\partial t} - \frac{\partial}{\partial x}\left(K \frac{\partial \varphi_0}{\partial x}\right) - \frac{\partial}{\partial z}\left(K \frac{\partial \varphi_0}{\partial z}\right) = \frac{\partial}{\partial z}\left(\frac{K(\rho_f - \rho_0)}{\rho_0}\right)$$     **Equation 4.3**

As $K$ and $\rho_0$ are considered constant, the latest equation becomes:

$$S_0 \frac{\partial \varphi_0}{\partial t} - \frac{\partial}{\partial x}\left(K \frac{\partial \varphi_0}{\partial x}\right) - \frac{\partial}{\partial z}\left(K \frac{\partial \varphi_0}{\partial z}\right) = \frac{K}{\rho_0}\frac{\partial \rho_f}{\partial z}$$          **Equation 4.4**

Now we pass on to the one-dimensional problem, that can be interpreted as a problem of vertical infiltration: a horizontal layer of porous material of thickness $H$ is topped with a layer of water of thickness $H_w$ (Figure 4.1). If at the initial time moment pore fluid pressure is assumed hydrostatic ($\varphi_0(z) \equiv H$), its higher value at the top boundary forces water to infiltrate downwards until equilibrium is achieved. In one case study, the lower boundary is considered impervious, but a different type of boundary condition is also tested.
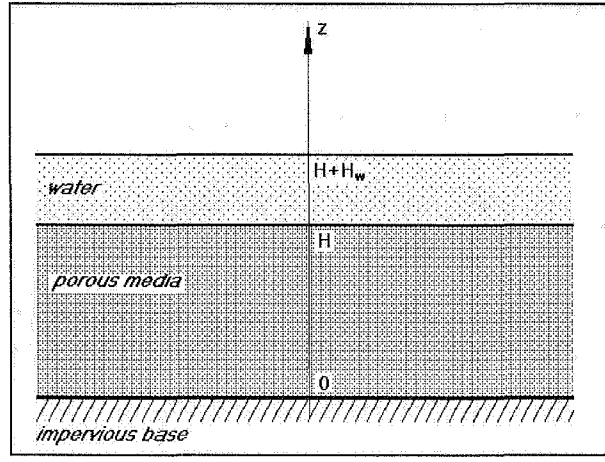
**Figure 4.1 1-D problem of vertical infiltration.**

The hydraulic head, which is now a function of two variables, (z,t), is described by the equation:

$$S_0 \frac{\partial \varphi_0}{\partial t} - \frac{\partial}{\partial z}\left( K \frac{\partial \varphi_0}{\partial z}\right) = \frac{K}{\rho_0}\frac{\partial \rho_f}{\partial z}, \quad z \in (0,H),\ t>0.$$   **Equation 4.5**

If we prescribe $\dfrac{\partial \rho_f}{\partial z} = const = C$, (4.5) becomes:

$$S_0 \frac{\partial \varphi_0}{\partial t} - \frac{\partial}{\partial z}\left( K \frac{\partial \varphi_0}{\partial z}\right) = \frac{KC}{\rho_0}$$   **Equation 4.6**

We consider three following initial-boundary value problems:

I) $\varphi_0(0,t) = \varphi_b = const,$

$\varphi_0(H,t) = \varphi_t = const,$

$\varphi_0(z,0) = \tilde{\varphi}_0(z);$

No source term: $C=0$.

II) $\dfrac{\partial \varphi_0}{\partial z}(0,t) = q_b = 0,$

$\varphi_0(H,t) = \varphi_t = cons,$

$\varphi_0(z,0) = \tilde{\varphi}_0(z);$

No source term: $C=0$.

III) $\varphi_0(0,t) = \varphi_b = const,$

$\varphi_0(H,t) = \varphi_t = const;$

$\varphi_0(z,0) = \tilde{\varphi}_0(z)$

The buoyancy term included: $C \neq 0$

Here $\varphi_b$ and $\varphi_t$ are hydraulic head values at the bottom and top boundaries respectively, $q_b$ is the Darcy's flux at the lower boundary.

The numerical solution was obtained on the uniform mesh with the resolution of 1000m. Parameter values used in the calculations are shown in Table 4.1.

| Parameter | Value | Unit |
|---|---|---|
| specific volumetric storativity, $S_0$ | $10^{-6}$ | $m^2$ |
| hudraulic conductivity, $K$ | $8.7732 \cdot 10^{-8}$ | $m/s$ |
| fluid density, $\rho_0$ | $10^3$ | $kg/m^3$ |
| gravitational acceleration, $g$ | $10$ | $m/s^2$ |
| $\varphi_b$ | $11000$ | $m$ |
| $\varphi_t$ | $15000$ | $m$ |
| $q_b$ | $0$ | $m/s$ |

**Table 4.1 Parameter values for the hydraulic head equation testing.**

### *Initial-boundary value problem (I)*

The general solution of the equation (4.6) satisfying the set of supplementary conditions (I) is assumed in the form:

$$\varphi_0(z,t) = \bar{u}(z) + v(z,t)$$

Equation 4.7

where $\bar{u}(z)$ is the solution of the boundary value problem:

$$\begin{cases} \bar{u}''(z) = 0, & z \in (0,H) \\ u(0) = \varphi_b, \\ u(H) = \varphi_t, \end{cases}$$

Equation 4.8

The stroke denotes $\dfrac{d}{dz}$, and $v(z,t)$ is the solution of the initial-boundary value problem with homogeneous boundary conditions:

$$\begin{cases} \dfrac{\partial v}{\partial t} = a^2 \dfrac{\partial^2 v}{\partial z^2}, & a^2 = \dfrac{K}{S_0}, & z \in (0,H), & t > 0 \\ v(0,t) = 0, & t > 0 \\ v(H,t) = 0, & t > 0 \\ v(z,0) = \tilde{\varphi}_0(z) - \bar{u}(z) = \varphi_1(z), & z \in (0,H) \end{cases}$$

Equation 4.9

We only present here the final result, remarking that the method of separation of variables was used to built the solution of (4.9):

$$\bar{u}(z) \equiv \dfrac{\varphi_t - \varphi_b}{H} z + \varphi_b;$$

Equation 4.10

$$v(z,t) = \sum_{n=1}^{\infty} C_n \sin\left(\frac{\pi n}{H} z\right) \exp\left[-\left(\frac{\pi n}{H}\right)^2 a^2 t\right],$$

**Equation 4.11**

where the Fourier's coefficients, $C_n$:

$$C_n = \frac{2}{H} \int_0^H \varphi_1(z) \sin\left(\frac{\pi n}{H} z\right) dz$$

**Equation 4.12**

If we specify the initial condition: $\widetilde{\varphi}_0(z) \equiv \varphi_b$, in this case

$$C_n = (-1)^n \frac{2(\varphi_t - \varphi_b)}{\pi n}$$

**Equation 4.13**

Over time, the solution evolves to the steady state linear distribution.

Comparison of the exact (solid line) and numerical (dashed line) solutions is presented in Figure 4.2. Figures (a) and (b) relate to the simulation performed with the time step $10^3$ days, while (c) and (d) - $10^2$ (days) for different time-weighting coefficient values.

For the time steps considered, the explicit scheme ($\sigma = 0$) produces oscillatory solutions, which therefore are not shown. To get an acceptable result for this time-stepping scheme, further reduction of the time step is required. For higher time steps, the fully implicit scheme with $\sigma = 1$ provides a better result than the more accurate symmetrical one (Figure 4.2 (a), (b), $\Delta t = 10^3$), still producing the notable numerical error differentiating the numerical solution from the analytic one. For the smaller time step, $\Delta t = 10^2$ days, the symmetrical scheme proves to be more accurate (see graphs correspondent to the 40th time step in Figure 4.2 (c), (d)).

Thus, for long term simulations, when the use of a larger time step can reduce computing time, preference may be given to the fully explicit scheme, of course, with the cost of some loss of accuracy.

(a)

(b)

(c)

(d)
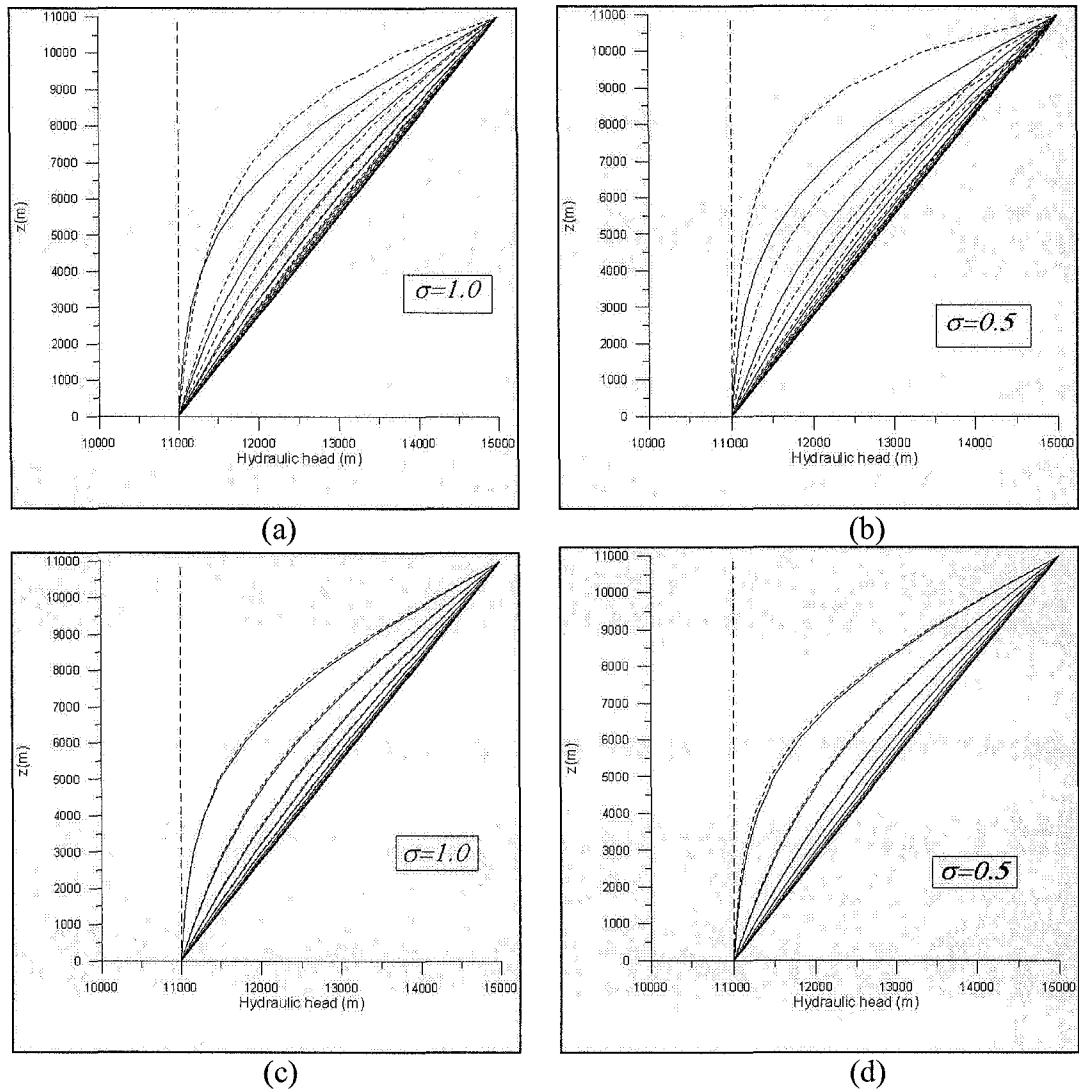
**Figure 4.2 Comparison of the analytic (solid lines) and numerical (dashed lines) solutions for initial-boundary value problem (I). Dash-dot line marks the initial state. (a) time step $10^3$ days, fully implicit scheme ($\sigma$=1), from left to right, time steps 1,2,...,10; (b) time step $10^3$ days, symmetrical scheme ($\sigma$=0.5), from left to right, time steps 1,2,...,10; (c) time step $10^2$ days, fully implicit scheme ($\sigma$=1), from left to right time, steps 10,20,...,100; (d) time step $10^2$ days, symmetrical scheme ($\sigma$=0.5) , from left to right, time steps 10,20,...,100.**

### *Initial-boundary value problem (II)*

A general solution of the equation (4.6) satisfying the set of supplementary conditions (II) is sought in the form (4.7), but now $\bar{u}(z)$ is the solution of a different boundary value problem:

$$\begin{cases} \bar{u}''(z) = 0, & z \in (0, H), \\ \quad \bar{u}'(0) = q_b, \\ \quad u(H) = \varphi_t, \end{cases}$$

Equation 4.14

and *v(z,t)* is the solution of the initial-boundary value problem with the following/next boundary conditions:

$$\begin{cases} \dfrac{\partial v}{\partial t} = a^2 \dfrac{\partial^2 v}{\partial z^2}, & z \in (0, H), \quad t > 0, \\ \dfrac{\partial v}{\partial z}(0, t) = 0, & t > 0, \\ v(H, t) = 0, & t > 0, \\ v(z, t) = \tilde{\varphi}_0(z) - \bar{u}(z) = \varphi_1(z), & z \in (0, H). \end{cases}$$

Equation 4.15

Skipping the detailed expounding, the final result is:

$$\bar{u}(z) \equiv \varphi_t \, ;$$

Equation 4.16

$$v(z, t) = \sum_{n=0}^{\infty} C_n \cos\left( \frac{\pi(2n+1)}{2H} z \right) \exp\left[ -\left( \frac{\pi(2n+1)}{2H} \right)^2 a^2 t \right],$$

Equation 4.17

where the Fureje's coefficients, $C_n$ :

$$C_n = \frac{2}{H} \int_0^H \varphi_1(z) \cos\sqrt{\lambda_n} \, z \, dz \, .$$

Equation 4.18

Here

$$\lambda_n = \left( \frac{\pi(2n+1)}{2H} \right)^2 .$$

Equation 4.19

If the initial condition is $\tilde{\varphi}_0(z) \equiv \varphi_b$, then

$$C_n = (-1)^n \frac{2(\varphi_b - \varphi_t)}{H} \frac{1}{\sqrt{\lambda_n}} \, .$$

Equation 4.20

As time progresses, the solution must approach the steady-state uniform distribution, $\bar{u}(z) \equiv \varphi_t$.

Comparison of the analytic and numerical solutions for the initial-boundary value problem (II) is presented in Figure 4.3. Similarly to the previous case study,

Figures (a) and (b) relate to the simulation performed with the time step $10^3$ days, while (c) and (d) - $10^2$ (days) for two different time-weighting coefficient values.



(a)    (b)

(c)    (d)
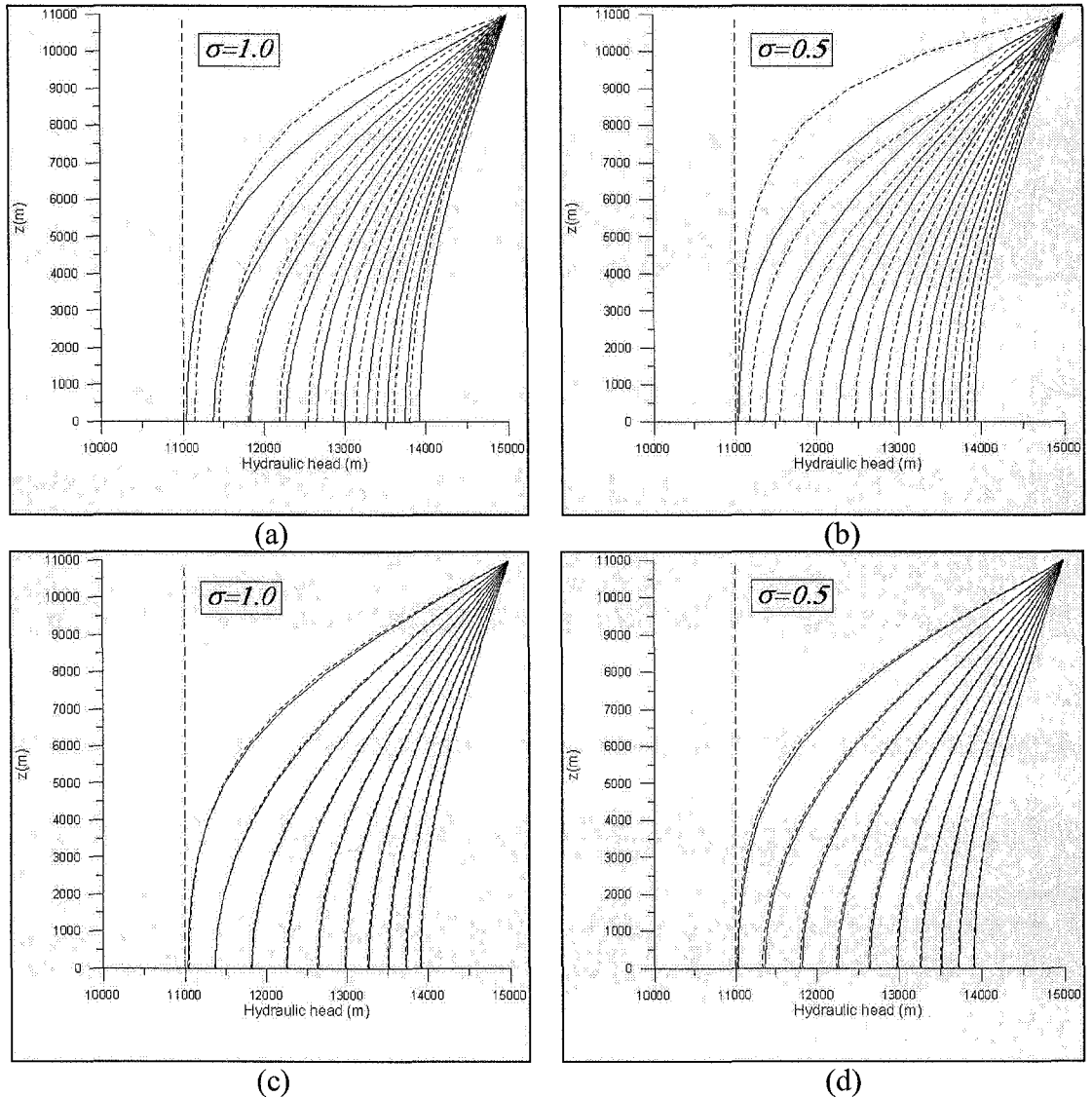
**Figure 4.3 Comparison of the analytic (solid lines) and numerical (dashed lines) solutions for initial-boundary value problem (II). Dash-dot line marks the initial state. (a) time step $10^3$ days, fully implicit scheme ($\sigma$ =1), from left to right, time step=1,2,...,10; (b) time step $10^3$ days, symmetrical scheme ($\sigma$ =0.5), from left to right, time step=1,2,...,10; (c) time step $10^2$ days, fully implicit scheme ($\sigma$ =1), from left to right, time step=10,20,...,100; (d) time step $10^2$ days, symmetrical scheme ($\sigma$ =0.5) , from left to right, time step=10,20,...,100.**

The numerical effect similar to the previous case study is observed for the time-step $\Delta t = 10^3$ : the fully explicit scheme seems to produce values closer to the exact solution comparatively to the symmetrical scheme, especially in the vicinity of the impervious boundary. For a smaller time step, the difference is scarcely distinguishable.

### *Initial-boundary value problem (III)*

The difference of this case study from two previous ones lies in the presence of the constant source term, which can be interpreted as a buoyancy force under the assumption that a constant density gradient is maintained.

As before, we seek the general solution of equation (4.6) satisfying the set of supplementary conditions (III) in the form (4.7), but now $\bar{u}(z)$ is the solution of the boundary value problem with the non-homogeneous equation:

$$\begin{cases} -\bar{u}''(z) = \dfrac{C}{\rho_0}, & z \in (0,H), \\ \bar{u}'(0) = \varphi_b, \\ u(H) = \varphi_t, \end{cases}$$

**Equation 4.21**

and $v(z,t)$ is the solution of the initial-boundary value problem (4.9).

In this case,

$$\bar{u}(z) = -\frac{C}{2\rho_0}z^2 + \left( \frac{\varphi_t - \varphi_b}{H} + \frac{CH}{2\rho_0} \right)z + \varphi_b$$

**Equation 4.22**

The $v(z,t)$ is expressed by (4.11). The Fureje's coefficients, calculated by (4.12) under the condition $\widetilde{\varphi}_0(z) \equiv \varphi_b$, have the form:

$$C_n = \frac{2}{\pi n}(-1)^n \left[ \frac{C}{\rho_0}\left(\frac{H}{\pi n}\right)^2 + \varphi_t - \varphi_b \right] - \frac{2C}{H\rho_0}\left(\frac{H}{\pi n}\right)^3.$$

**Equation 4.23**

In Figure 4.4 we present the comparison of the exact and numerical solutions of the initial-boundary value problem (III) calculated for C=0.035(kg/$m^4$). This value of the density gradient has physical meaning: if the fluid density is considered dependent only on the temperature variations, and the related equation of state is

$$\rho_f = \rho_0(1 - \beta T),$$

**Equation 4.24**

with $\beta = 8 \cdot 10^{-4}(1/^0 C)$, this value of $C$ corresponds to the linear vertical temperature profile with $20\,^0C$ at the top boundary and $501.25\,^0C$ at the lower one. The temperature gradient value in this case, $gradT$=43.75($^0C$ /km), that agrees with the reported geothermal gradient of $25\text{-}50\,^0C$ per km (Bear, 1972: p.641).

The numerical solution calculations were carried out with the time step $10^2$ days with the use of the fully implicit scheme ($\sigma$ =1.0). Vertical profile of the hydraulic head graphs at the early simulation stage is marked blue (time steps 1,2,...,10), the later moments of time (time steps 20,30,...,100) are presented with

black lines. Over time, the curve evolves form initially uniform state (the vertical dash-dot line) to the steady state solution (the outermost black line on the right).

Figure 4.4 shows that for this case study as well, the model appears to reproduce the analytic solution with the adequate/sufficient accuracy.
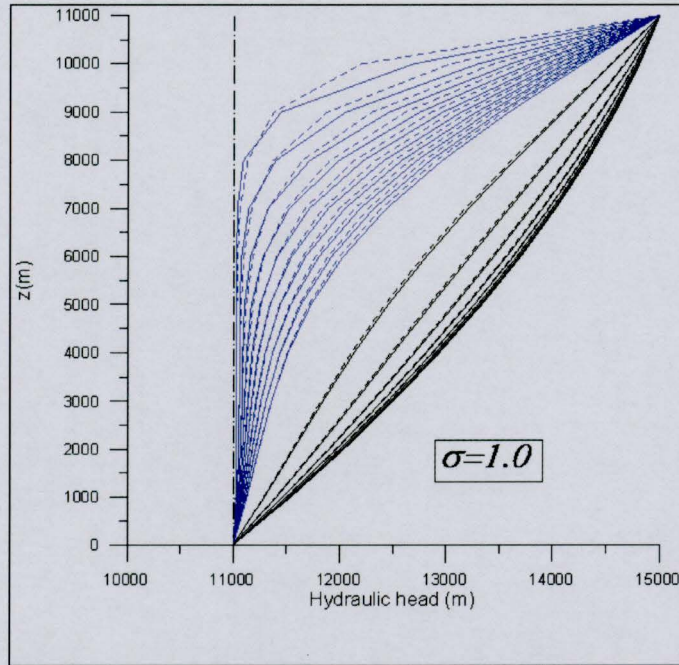


**Figure 4.4 Comparison of the analytic (solid lines) and numerical (dashed lines) solutions for initial-boundary value problem (III). Dash-dot line marks the initial state. The time step equals $10^2$ days. Blue marks the solutions at the time steps 1,2,…,10 (from left to right), black corresponds to the time steps 20,30,…,100. After 60th time step both analytic and numerical solutions are rapidly approaching to the steady state and almost indistinguishable from it.**

## 4.1.2  Advective diffusion equation

We tested the effectiveness of the numerical model for the solution of the advective diffusion equation in two stages: first, advective terms were not taken into account, as an analytic solution can easily be obtained in this case; second, we 'turned off' the diffusive term checking the advective displacement of the initial perturbation in the steady fluid velocity field.

### *Heat conduction equation*

We carried out a set of tests for the one-dimensional heat transport problem under assumption of the absence of advective fluid motion and heat sinks/sources. Under conditions described, equation (2.12) takes form:

$$c_e \frac{\partial T}{\partial t} - \lambda \frac{\partial^2 T}{\partial z^2} = 0$$

**Equation 4.25**

61

Two initial-boundary value problems were considered:

IV) $T(0,t) = T_b = const,$

$T(H,t) = T_t = const,$

$T(z,0) = \widetilde{T}(z) \equiv T_t \, ;$

V) $\dfrac{\partial T}{\partial z}(0,t) = q_b = 0,$

$T(H,t) = T_t = const,$

$T(z,0) = \widetilde{T}(z) \equiv T_b \, ;$

Here $T_b$ and $T_t$ are temperature values at the bottom and top boundaries respectively, $q_b$ is the heat flux at the bottom boundary.

These problems are analogous to initial-boundary value problems (I) and (II) described in Section 4.1.1. The difference consists only in the physical meaning of the unknown and coefficients, but the expressions of the analytic solutions have the same forms.

The exact solution of the initial-boundary value problem (IV) is:

$$T(z,t) = \frac{T_t - T_b}{H} z + T_b + \sum_{n=1}^{\infty} C_n \sin\left(\frac{\pi n}{H} z\right) \exp\left[-\left(\frac{\pi n}{H}\right)^2 a^2 t\right] \qquad \textbf{Equation 4.26}$$

with $C_n$ described by (4.12) and $a^2 = \dfrac{\lambda}{c_e}$.

For the initial-boundary value problem (V), the analytic solution is expressed as:

$$T(z,t) = T_t + \sum_{n=0}^{\infty} C_n \cos\left(\frac{\pi(2n+1)}{2H} z\right) \exp\left[-\left(\frac{\pi(2n+1)}{2H}\right)^2 a^2 t\right] \qquad \textbf{Equation 4.27}$$

with $C_n$ defined by (4.18)

The comparison of the numerical and analytical solutions of the initial-boundary value problems (IV) and (V) are presented in Figure 4.5 (a) and (b) respectively. The effect of the time-weighting coefficient on the numerical solution appeared to be similar to one described in detail in Section 4.1.1. Therefore, here we only show results of the application of the symmetrical scheme ($\sigma = 0.5$) with the time step $10^6$ days. The entry parameters used in the computations were:

$T_b = 144.27(^0C),$

$T_t = 20(^0C),$

$\lambda = 2.5(J/(m\ s\ ^0C),$

$c_e = 2.725 \cdot 10^6 (J/(m^3\ ^0C)).$

Numerical solutions are presented with dashed lines, analytic ones – with solid. For the initial-boundary value problem (IV) (Figure 4.5 (a)), initially uniform temperature distribution (dash-dot line) rapidly evolves to the steady-state linear distribution. The difference between numerical and analytic solutions is hardly distinguishable after 400th time step.

It takes longer to achieve the steady state for problem (V) comparatively to (IV), around $4 \cdot 10^9$ days (4000 time steps if $\Delta t = 10^6$ (days))

4000 time steps with their value of $10^6$ days. However, as in the previous case, the numerical and analytic solutions are close.



(a)                                                 (b)
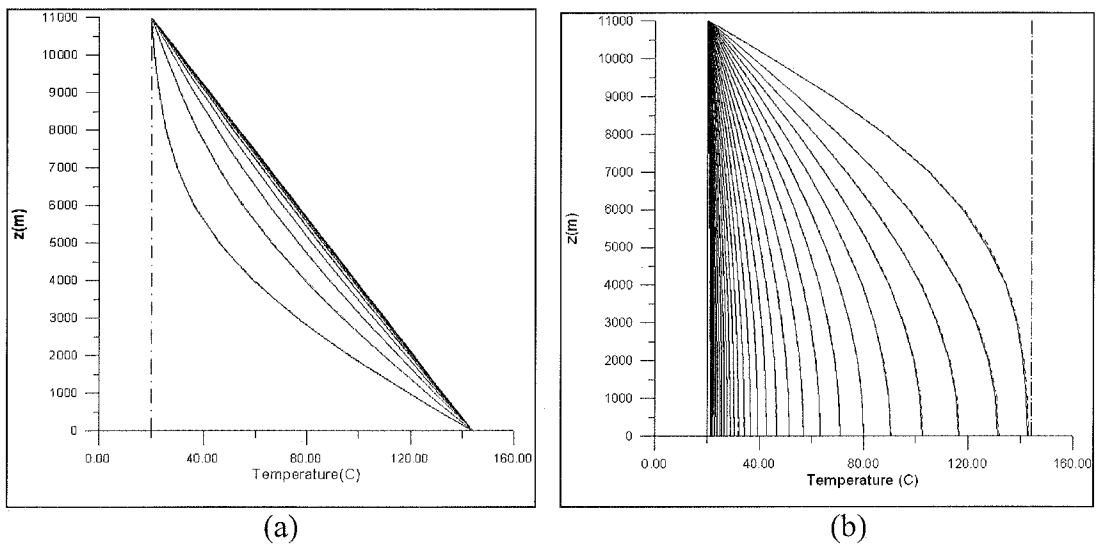
**Figure 4.5 Comparison of the analytic (solid lines) and numerical (dashed lines) solutions for (a) initial-boundary value problem (IV) and (b) initial-boundary value problem (V). Dash-dot line marks the initial state. Graphs show temperature profiles for time steps 100,200,...,3000 starting from the initial state.**

### *Advection test*

The aim of the set of tests described below was to ensure of the valid representation by the numerical model of the advective transport processes. Particular attention has been paid to this problem because of the exclusive role of the advection dominating zones, like aquifers and highly permeable faults. They mainly control the fluid flow pattern in the section, defining main fluid pathways.

Ehe equation (2.12 ) in the absence of the conduction, dispersion and inner sinks/sources can be written:

$$c_e \frac{\partial T}{\partial t} + \rho_f c_f q_x \frac{\partial T}{\partial x} + \rho_f c_f q_z \frac{\partial T}{\partial z} = 0 .$$

**Equation 4.28**

We assume no heat flux through all boundaries and set the initial condition as:

$$T(x,z,t) \big|_{t=0} = \widetilde{T}(x,z) ,$$

**Equation 4.29**

where $\widetilde{T}$ is the initial temperature perturbation.

Prescribing $q_z=0$ and $q_x=const>0$, we set in this way the unidirectional pore fluid flow oriented in the positive direction of the x-axis.

Then, at an arbitrary time moment, t>0

$$T(x,z,t) = \widetilde{T}(x - q_x t, z, t)$$

**Equation 4.30**

In other words, the initial temperature distribution is simply progressing to the right with the velocity $q_x$.

The numerical experiments have been performed involving a square domain of a homogeneous porous medium which is 11km long covered with the finite element mesh of square elements 500m wide. The boundary conditions for the hydraulic head at the vertical boundaries were set so that:

$\varphi_0$ *(0,z,t)=11000(m),*

$\varphi_0$ *(11000,z,t)=0(m),*            *z∈ [0,11000], t>0.*

No fluid flow was allowed through the horizontal boundaries.

The hydraulic conductivity value used for the simulation was $K=8.7732 \cdot 10^{-8}$ *(m/s)*. In this case, $q_x=8.7732 \cdot 10^{-8}$ *(m/s)*, $q_z=0$.

The initial temperature perturbation set was:

$$\widetilde{T}(x,z) = 20 + 100 \exp\left( -\frac{(x-5000)^2}{10^6} \right),$$

**Equation 4.31**

which is uniform in z-direction.

The graph of the function $\widetilde{T}(x,z)$ is shown in Figure 4.6. The initial temperature distribution has its maximum values aligned along the line x=5000. Upon the given value of the Darcy's flux, the displacement in 1000m of the initial temperature distribution must be achieved in approximately $1.3193 \cdot 10^5$ days.
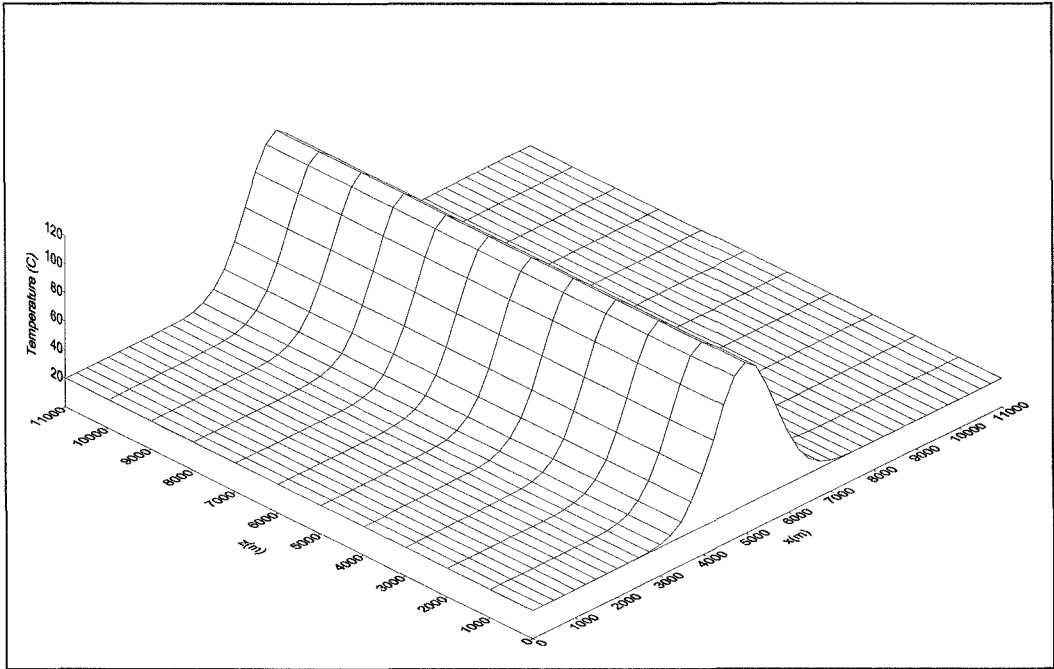
**Figure 4.6 Advection test. Uniform in z-direction initial temperature distribution.**

In Figure 4.7 we present the results of the numerical simulation carried out with the time step of $1.3193 \cdot 10^4$ days by the fully implicit scheme (a) and the symmetrical Crank-Nicolson type scheme (b). It was expected that every 10 steps the initial temperature profile must be displaced by 1000m to the right. Both time-stepping schemes realize this correctly. But the fully implicit scheme ($\sigma$ =1.0) produces significant numerical diffusion (Figure 4.7 (a)), while the symmetrical one ($\sigma$ =0.5) does not have this shortcoming (Figure 4.7 (b)). Decreasing the time step diminishes the numerical diffusion (Figure 4.7 (c), (d)), but the same effect can be achieved by much less computing time cost, simply by using a different time-marching algorithm with $\sigma$ =0.5.

(a)

(b)

(c)

(d)
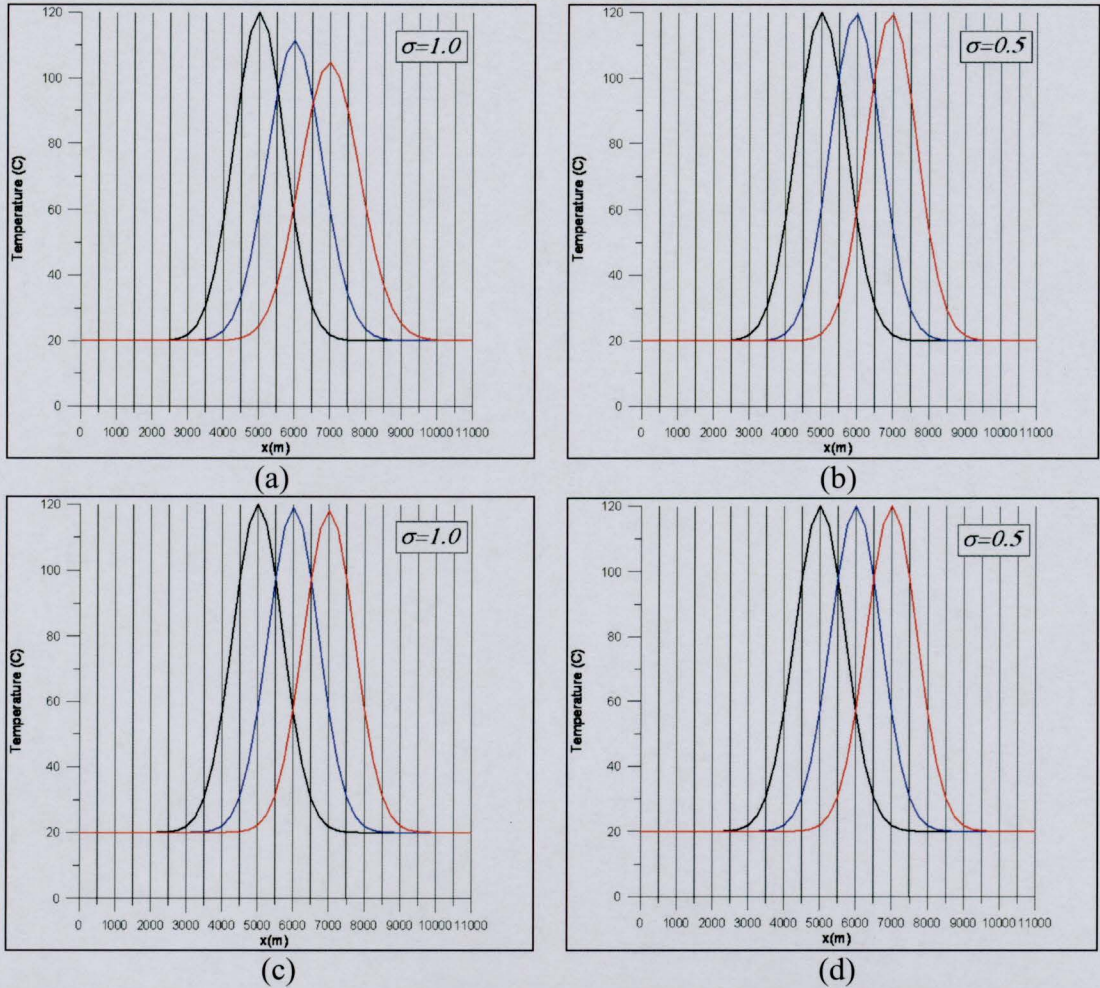
**Figure 4.7 Advection test. Displacement of the uniform in z-direction initial temperature perturbation. (a) and (b) correspond to** $\Delta t \approx 1.3 \cdot 10^4$ **(days); (c) and (d) correspond to** $\Delta t \approx 1.3 \cdot 10^3$ **(days). (a) and (c) relates to the fully implicit time-scheme (** $\sigma$ **=1.0), (b) and (d) – to the symmetrical one (** $\sigma$ **=0.5). The black line marks the initial state, blue and red – time steps 10 and 20 in Figures (a) and (b), 100 and 200 in Figures (c) and (d).**

The next consideration was to investigate the directional character of the numerical diffusion in the case if the initial temperature distribution is not uniform in one direction. For this purpose, $\widetilde{T}(x,z)$ was defined by the expression:

$$\widetilde{T}(x,z) = 20 + 100\exp\left(-\frac{(x-5000)^2 + (z-5000)^2}{10^6}\right)$$
     **Equation 4.32**

$\widetilde{T}(x,z)$ 3-D graph and x-z-plane representation are shown in Figure 4.8



(a)                (b)
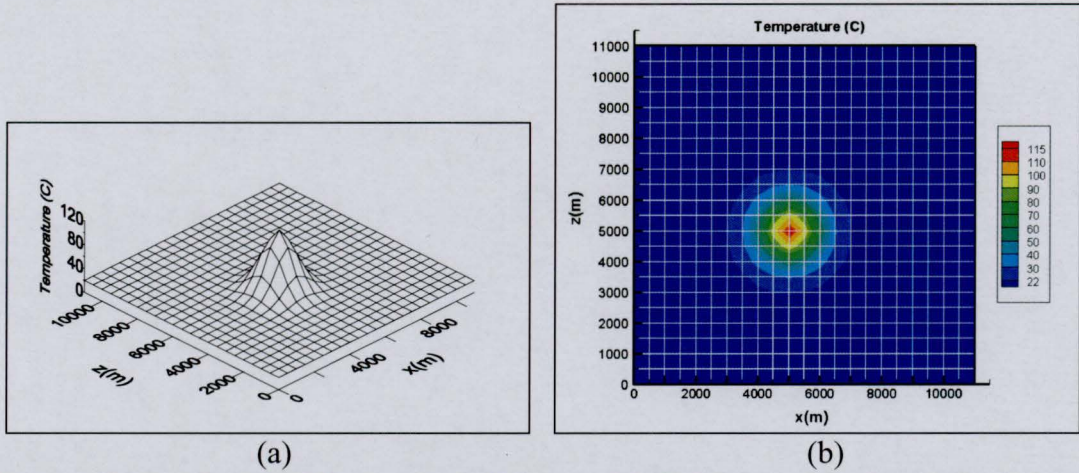
**Figure 4.8 Advection test. 2-D numerical diffusion test. Initial temperature distribution. (a) – 3-D graph, (b) – planar representation.**

The perturbation maximum was initially placed at the point with coordinates (5000,5000). As all the model setting is the same as in the previous test, the temperature maximum must be moved for 1000m every $1.3193 \cdot 10^5$ days.

In Figure 4.9 we show the results of the numerical simulations. Figures (a) and (b) relate to the calculation performed with the fully implicit scheme and the time step, $\Delta t \approx 1.3 \cdot 10^4$ (days). It can be seen, that the initial perturbation maximum (Figure 4.8 (b)) is displaced into the position (6000,5000) in 10 time steps (Figure 4.9 (a)) and to the position (7000,5000) in 20 time steps (Figure 4.9 (b)), as expected. But the numerical diffusion in the direction of flow affects the temperature distribution (no noticeable diffusion across the flow direction was observed). This undesirable effect is far less appreciable, if the symmetrical time-marching scheme is employed (Figure 4.9 (c), (d)). The numerical diffusion, however, can be decreased to a comparable degree in the case of the fully implicit scheme too, but this needs a significantly smaller time step. Figure 4.9 (e), (f) illustrate this (10 times less time step, $10^3$ days, was used). The latter approach is obviously much more costly with respect to the computing time.

(a)                                                              (b)



(b)                                                              (d)



(e)                                                              (f)
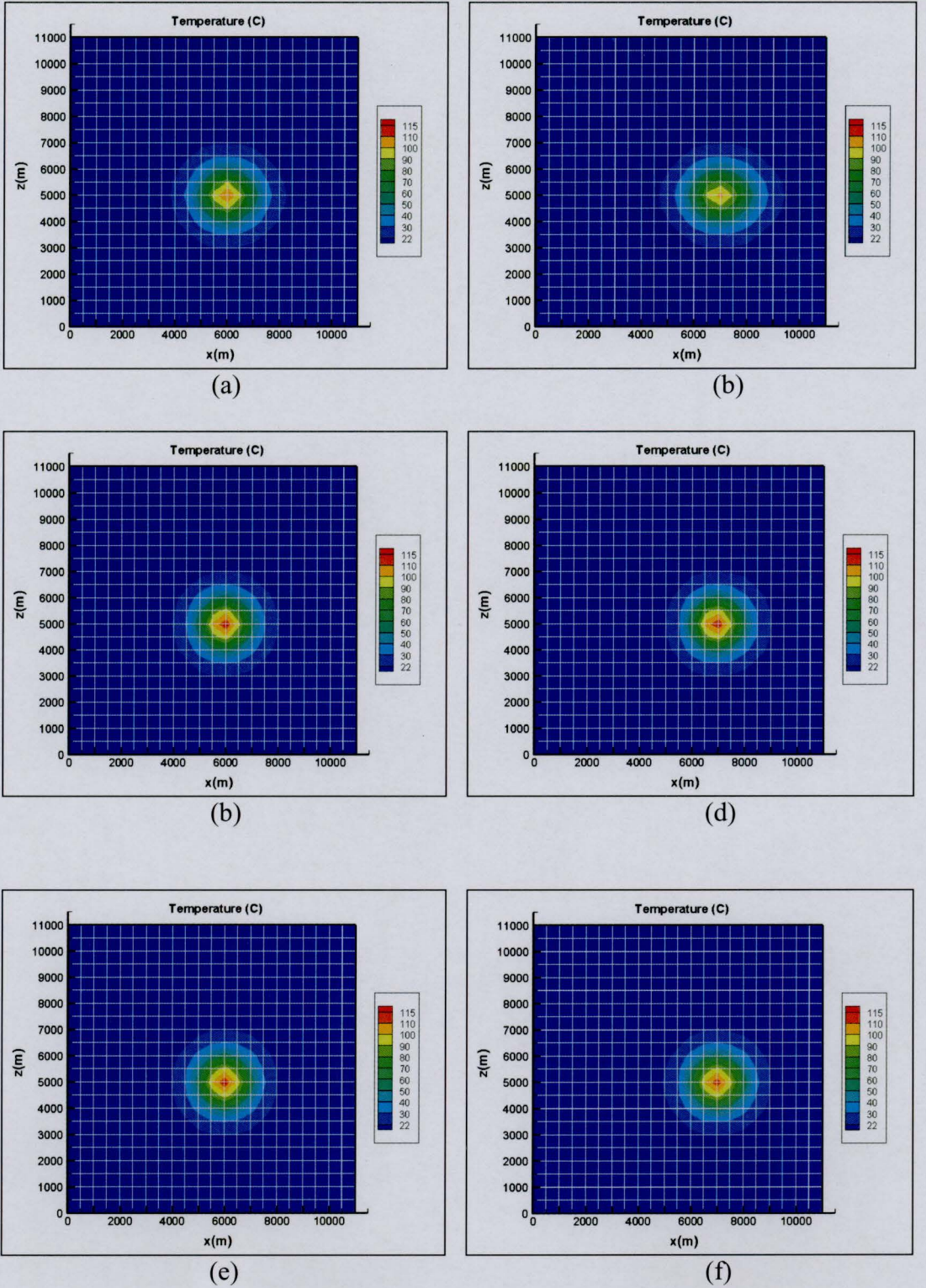
**Figure 4.9 Advection test. Non-uniform in z-direction initial temperature perturbation displacement.**

(a), (b): $\Delta t \approx 1.3 \cdot 10^4$ **(days)**, $\sigma$ **=1.0, time steps – 10, 20 respectively.**

(c), (d) : $\Delta t \approx 1.3 \cdot 10^4$ **(days)**, $\sigma$ **=0.5, time steps – 10, 20 respectively.**

(e), (f): $\Delta t \approx 1.3 \cdot 10^3$ **(days)**, $\sigma$ **=1.0, time steps – 100, 200 respectively.**

Another effect observed was that at these boundary conditions, if no upwinding is used, the temperature perturbation, having reached the outflow boundary, tends to

'reappear' at the inflow one. Figure 4.10 shows successive displacements of the initial perturbation (the first snap shot) every 10 time steps. The calculations were performed with the more accurate symmetrical scheme and $\Delta t \approx 1.3 \cdot 10^4$ (days). One can see that after the 30th time step, the temperature perturbation spot should have left the simulation area, yet it 'reenters' the domain from the left continuing to be transferred by the flow.
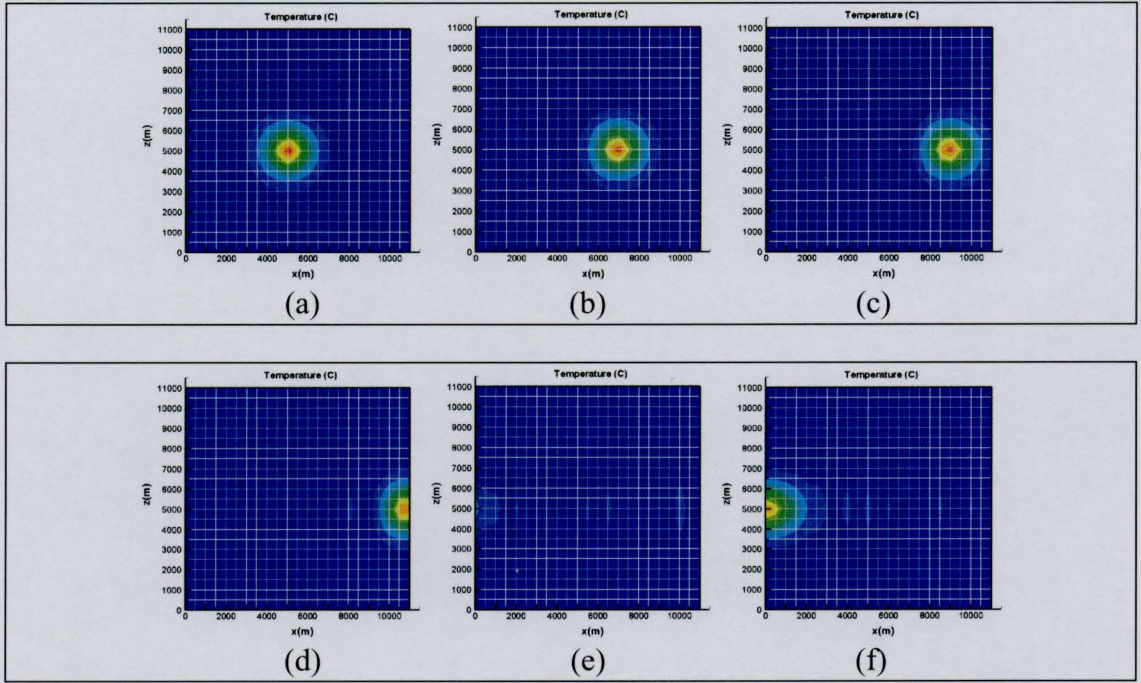


**Figure 4.10 Advection test. Effect of open to flow boundaries. Bubnov-Galerkin scheme (no upwinding), $\Delta t \approx$ 1.3D+04 (days), $\sigma$ =0.5. Time steps: (a) 0, (b) 20, (c) 40, (d) 60, (e) 80, (f) 100.**

This effect occurs because the symmetrical approximation of the advective term allows transmission of the numerical error upstream (Bradford and Katopodes, 2000).

In Figure 4.11 we present the results of the similar numerical experiment but now with the use of non-symmetrical weighting functions. All other settings of the model, including time-marching scheme, parameter values, were the same. One can see, that the numerical solution, although being more dissipative in this case (the temperature pick becomes lower as the perturbation is being moved towards the right boundary), does not 'recreate' the hot spot at the inflow boundary after it has left the domain through the outflow boundary.
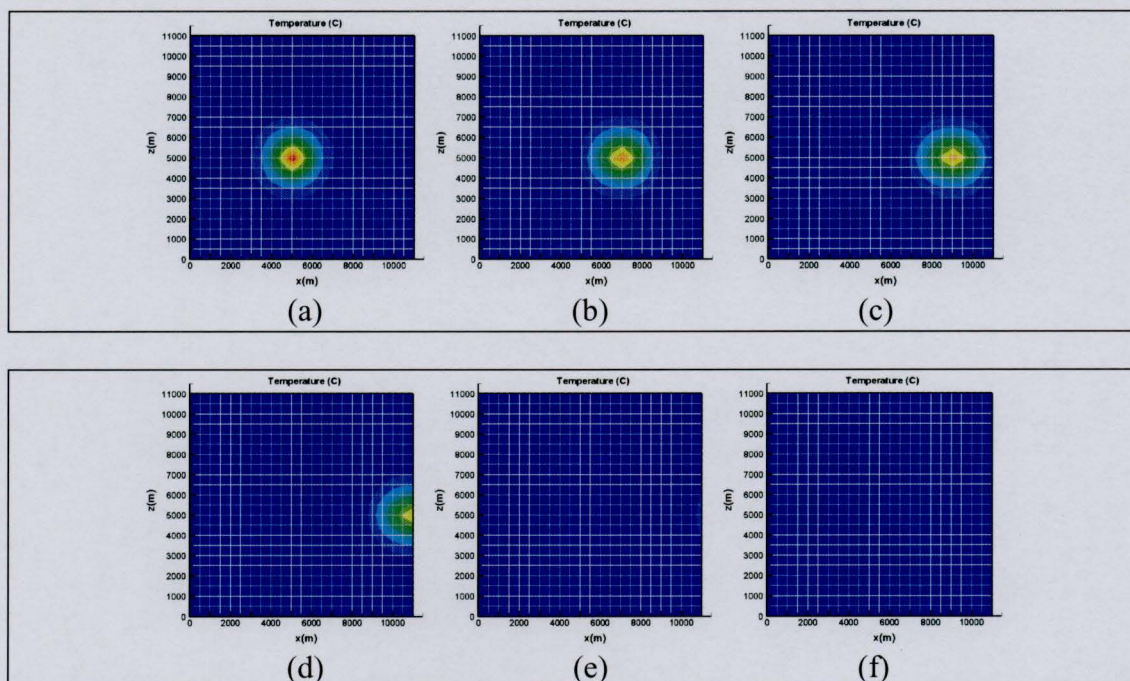
**Figure 4.11 Advection test. Effect of open to flow boundaries. Petrov-Galerkin scheme (upwinding),** $\Delta t \approx 1.3D+04$ **(days),** $\sigma = 0.5$. **Time steps: (a) 0, (b) 20, (c) 40, (d) 60, (e) 80, (f) 100.**

In the modeling of the hydrothermal fluid flow in a vertical cross-section of a sedimentary structure, the boundary conditions of no heat flux through the side boundaries are usually set. As can be seen, in this case, if the side boundaries are open to flow and fluid flux is predominantly directed in a horizontal direction, the standard Bubnov-Galerkin technique can cause an undesirable numerical effect. And it can be left undetected, concealed by the complex interplay of other factors, if complex domain architecture is involved. This should be taken into consideration when specifying the model setting.

The conclusions reached after carrying out the set of tests described in the Section 4.1 are:

1)    The built numerical model appears to produce numerical solutions which are in good agreement with analytical ones that are possible to construct for simplified problems.

2)    Preference should be given to the symmetrical time-marching scheme as less diffusive one, unless a drastic shortening of the computing time is needed.

3)    An 'Upwinding' scheme is preferable in the case of domain boundaries open to flow.

## 4.2 Free thermal convection

Prior to the model application to a complex hydrostratigrafic structure, the set of tests modeling the onset of free thermal convection in a uniform porous layer was carried out. The problem of the Rayleigh-Darcy instability has been studied theoretically, experimentally and numnerically over years (Elder, 1967; Palm et al., 1972; Combarnous and Bories, 1975; Ribando and Torrance, 1976; Schubert and Straus, 1979; Phillips, 1991; Lein and Tankin, 1992; Raffensperger and Vlassopoulos, 1999). The results of the studies provide an extensive base to check the validity of the present model in the simulation of this physical effect.

We consider a horizontal slab of a homogeneous water-saturated porous material which is not exposed to a pressure gradient. The basement is uniformly heated from below maintaining a constant temperature gradient across the porous layer: at the upper boundary, $z=H$ ($H$ is the porous layer thickness), $T=T_0$ , while the temperature of the lower boundary is higher by the amount $\Delta T$ : $T=T_0 + \Delta T$ , $z=0$. In this case, the fluid motion is supposed to be generated only by density variation due to variations in temperature. The porous material is generally considered as anisotropic with $k_H$ and $k_V$ being the permeability coefficients in the horizontal and vertical directions respectively. $k_H$ and $k_V$ are uniform but not necessarily equal. The uniformly heated from below interstitial fluid can remain at rest in the conductive state unless the Rayleigh-Darcy number reaches its critical value (Phillips, 1991). A modified Rayleigh-Darcy number, $Ra*$, is defined by:

$$Ra* = \frac{g\alpha\Delta TH}{\nu\kappa} \frac{k_H k_V}{\left(k_H^{1/2} + k_V^{1/2}\right)^2}$$
**Equation 4.33**

where

| | |
|---|---|
| $g$ | is the acceleration of gravity; |
| $\alpha$ | is the thermal expansion coefficient (it is assumed that the fluid density linearly depends on the temperature: $\rho = \rho_0(1 - \alpha T)$ ); |
| $\nu$ | is the kinematic viscosity; |
| $\kappa$ | is the thermal diffusivity coefficient, defined as $\kappa = \lambda_e /(\rho_f c_f)$ |

If $Ra*$ exceeds the critical value, the buoyancy forces, which now dominate viscous effects, initiate cellular convective motion of the interstitial fluid. In the case

when both lower and top domain boundaries are impermeable to flow, the critical value is

$$Ra_c{}^* = \pi^2.$$                  **Equation 4.34**

The initial conditions of the simulation correspond to a disturbed hydrostatic state: temperature linearly increases with depth, hydraulic head is assumed uniform all over the domain. As the rotation direction depends on the initial disturbance, we prescribe $+0.2\,^0C$ temperature deviation at the right lower corner of the rectangular computing domain. This will force fluid mass adjacent to the right boundary to rotate in the anticlockwise direction.

### 4.2.1 Anisotropy effect

Accordingly to (Phillips, 1991), when $Ra^*$ just exceeds $Ra_c{}^*$, the horizontal width of a convective cell, $L$, can be evaluated as:

$$L = \left(\frac{k_H}{k_V}\right)^{1/4} H.$$           **Equation 4.35**

To make sure of the model ability to reproduce this effect, we performed numerical experiments for:

a) $k_H = k_V = 10^{-14}\,(m^2)$ – isotropic case;

b) $k_V > k_H$, with $k_H = 10^{-14}\,(m^2)$, $k_V = 16 \cdot 10^{-14}\,(m^2)$;

c) $k_V < k_H$, when $k_H = 16 \cdot 10^{-14}\,(m^2)$, $k_V = 10^{-14}\,(m^2)$.

The correspondent aspect ratio of a convective cell, $L/H$, is:

a) *L/H=1* ;

b) *L/H=1/2*;

c) *L/H=2*.

The computing domain used in the simulation was 22000m long with the depth of the porous layer 11000m. Hence, in case (a) the fluid flow pattern will consist of two square convective cells; in case (b), the model should produce four vertically elongated convective cells; in case (c) the computing domain will accommodate one horizontally elongated cell. Model parameters used in the simulation are listed in Table 4.2. Figure 4.12 shows results on the three case studies described above. The flow pattern is visualized by fluid velocity vectors. One can see that the convective flow produced by the model agrees with the expected result.

| Parameter | Value | Units |
|---|---|---|
| $Ra^*$ | 10 | - |
| $H$ | 11000 | $m$ |
| $g$ | 10 | $m/s^2$ |
| $\rho_0$ | $10^3$ | $kg/m^3$ |
| $\lambda_e$ | 2.5 | $J/(m \cdot s \cdot^0 C)$ |
| $c_f$ | 4174 | $J/(kg \cdot^0 C)$ |
| $\alpha$ | $8 \cdot 10^{-4}$ | $(^0 C)^{-1}$ |
| $\Delta T$ | a) 31.03176 <br> b) 12.12178 <br> c) 12.12178 | $^0 C$ |

**Table 4.2 Model parameters for testing the anisotropy effect on the free convection pattern in a uniform porous layer.**



(a)



(b)



(c)
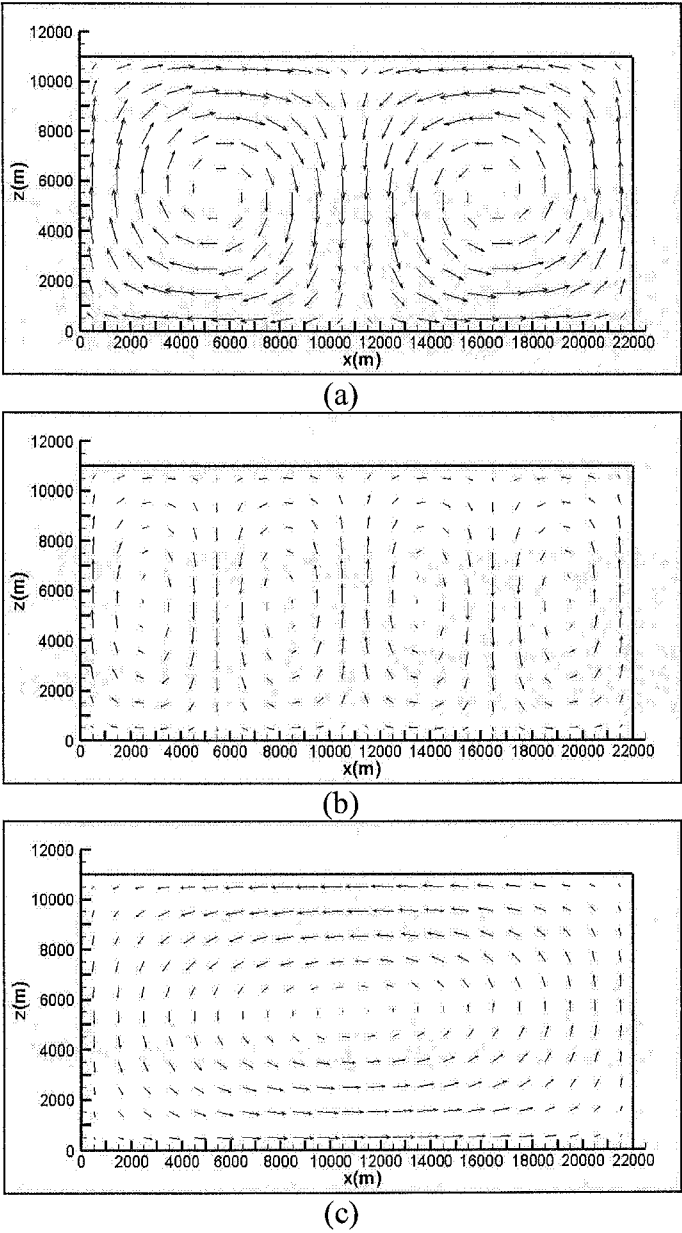
**Figure 4.12 Free thermal convection. Anisotropy effect at $Ra^*=10$ slightly exceeding the critical value: (a) $k_H = k_V = 10^{-14} (m^2)$, L/H=1; (b) $k_H = 10^{-14} (m^2)$, $k_V = 16 \cdot 10^{-14} (m^2)$, L/H=1/2; (c) $k_H = 16 \cdot 10^{-14} (m^2)$, $k_V = 10^{-14} (m^2)$, L/H=2.**

## 4.2.2 Convective cell aspect ratio as a function of the Rayleigh number

The following group of tests aimed to trace the changes that the fluid velocity field and temperature distribution undergo as the Rayleigh number increases. The tests were carried out under the assumption that the porous layer is isotropic. When $k_H = k_V = k$, the modified Rayleigh number:

$$Ra^* = \frac{g\alpha\Delta T H}{\nu\kappa}\frac{k}{4}.$$

Equation 4.36

Therefore

$$Ra = \frac{g\alpha\Delta T H k}{\nu\kappa}$$

Equation 4.37

rather than $Ra^*$ is considered as the control parameter of the porous system. The critical value marking the onset of free convection is now:

$$Ra_c = 4\pi^2.$$

### *Comparison with (Combarnous and Bories, 1975)*

The authors, studying numerically heat transfer induced by free thermal convection, deduced that for a bidimensional convective roll, the Nusselt number, *Nu*, is a function of the Raleigh number and of the reduced size of the roll, *H/L* (where *H* stands for the convective sell heights and *L* denotes its width). The graphs of *Nu* versus *H/L* were plotted for $Ra \le 40$, $Ra=60$, 100, 200 and 350 (Figure 4.13).
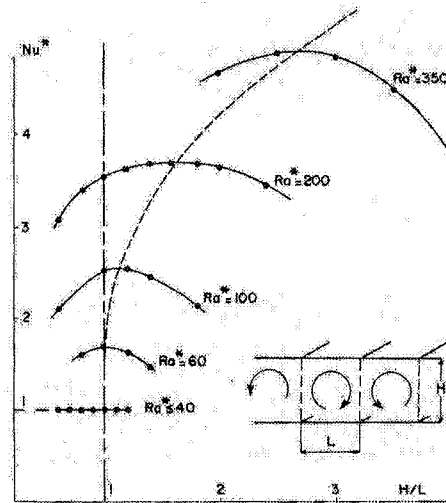


**Figure 4.13 The Nusselt number as a function of the Rayleigh number and of the reduced size of the convective roll. Numerical results for the heat transfer (from Combarnous and Bories, 1975).**

It is stated in the paper that the maximum of the curve corresponds to the greatest overall heat transfer and also to the real size of the convective cells in the infinite porous layer. From the plot presented there, we evaluated approximate *H/L* values correspondent to the maximums and compared them with the results produced by our model. The model was run successively for the listed *Ra* values to investigate its response to the increase in this controlling parameter. Physical properties of the medium were the same as in the previous section (see Table 4.2), the porous matrix is supposed to be isotropic with $k_H = k_V = 10^{-14}(m^2)$ and porosity 0.3. As the simulation can not be done for a porous layer of infinite length, to diminish the influence of side boundaries, we increased the horizontal extent of the domain to 55000m. All boundaries were assumed to be impermeable to the fluid flow. No heat flux was allowed through the side boundaries, horizontal ones were considered as isothermal: $20^0 C$ at the top, while the lower boundary temperature was varied to obtain the correspondent *Ra* value (see Table 4.3).

| Ra | 39.9 | 60 | 100 | 200 | 350 |
|---|---|---|---|---|---|
| Lower boundary temperature ($^0 C$) | 50.9542 | 66.5476 | 97.5794 | 175.1588 | 291.5279 |

**Table 4.3 Simulation parameters: Ra values and correspondent temperature of the lower boundary.**

In all cases, the system ultimately comes to the steady state, fitting an integer number of convective cells of equal size into the computing domain (Figure 4.14 (a) –(c) and Figure 4.15 (a)-(b)). The model responses to the increase in *Ra*, intensifying convection (what is reflected in the growth of the absolute value of pore velocities, see Table 4.4) and increasing the number of convective cells.

| Ra | 39.9 | 60 | 100 | 200 | 350 |
|---|---|---|---|---|---|
| Maximum pore velocity value (m/s) | $3.82 \cdot 10^{-17}$ | $1.80 \cdot 10^{-9}$ | $3.72 \cdot 10^{-9}$ | $8.15 \cdot 10^{-9}$ | $1.43 \cdot 10^{-8}$ |

**Table 4.4 Maximum values of pore velocities in steady state at different Rayleigh number values.**
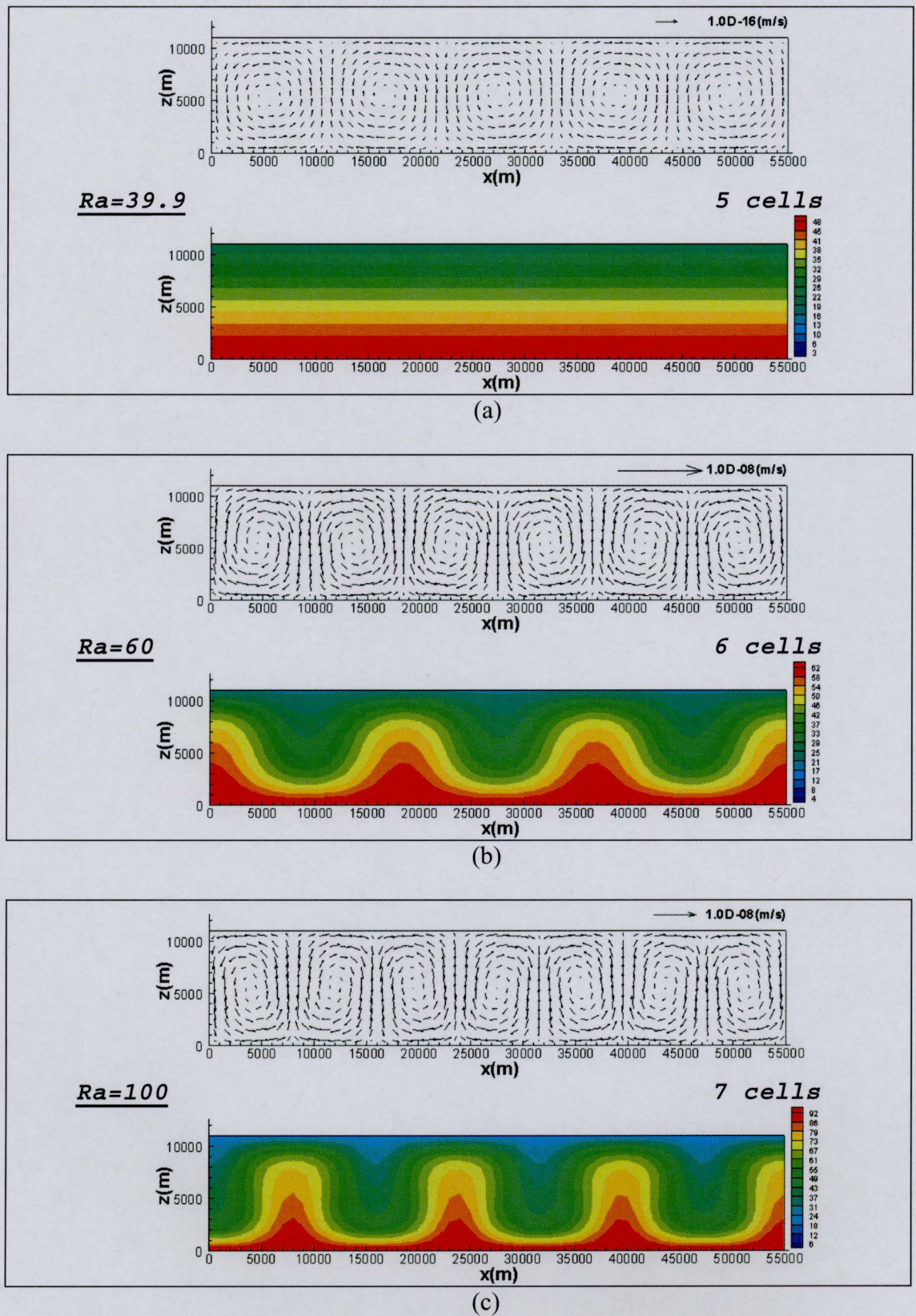
**Figure 4.14 Fluid velocity field and temperature distribution at (a) Ra=39.9; (b) Ra=60; (c) Ra=100**
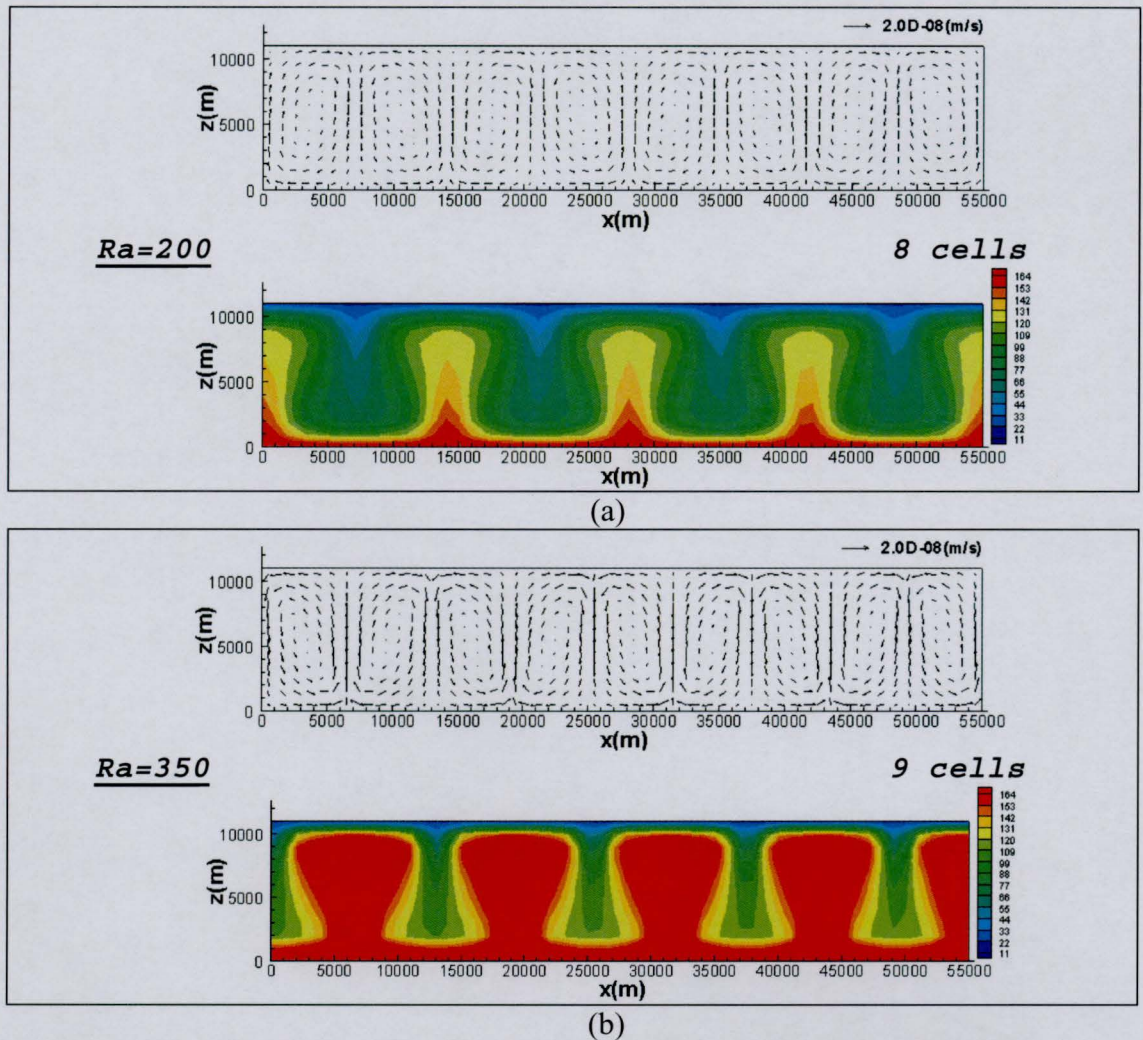
Figure 4.15 Fluid velocity field and temperature distribution at (a) Ra=200; (b) Ra=350.

Similar to the authors of the paper under discussion, we obtained that the cell aspect ratio, *L/H*, is a decreasing function of *Ra*. In Table 4.5 we present the computed by the model values of the reduced size of the convective cell and the values obtained from Combarnous and Bories's data. The results are comparable.

| *Ra* | | 39.9 | 60 | 100 | 200 | 350 |
|------|------|------|-----|-----|-----|-----|
| *H/L* | this model | 1.0 | 1.2 | 1.4 | 1.6 | 1.8 |
| | (Combarnous and Bories, 1975) | 1.0 | 1.0 | 1.2 | 1.6 | 2.6 |

Table 4.5 Reduced size of a convective cell at different Rayleigh number values.

For the lower *Ra* value, the results are comparable. However, when *H/L* values versus *Ra* were plotted and compared with the graph built on the base of Combarnous and Bories data (Figure 4.16), a discrepancy in the character of the curves was found.
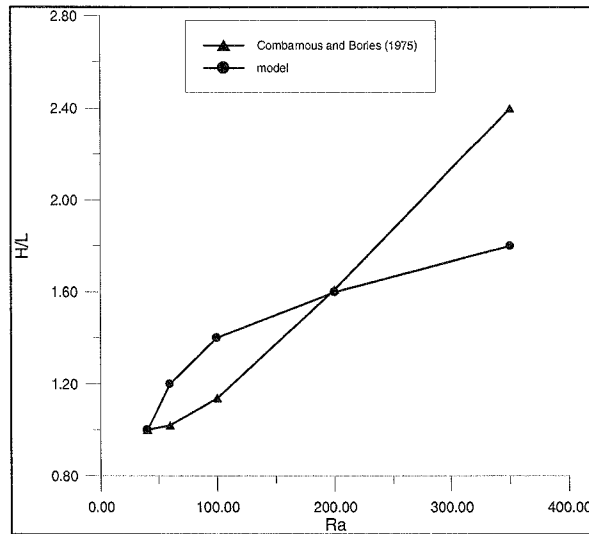
**Figure 4.16 Reduced size of a convective cell as a function of Ra.**

A possible explanation of this fact may be that Combarnous and Bories results represent the generalization made for the infinite porous layer, while the model had to deal with a test section of finite length (although the length of the domain exceeds its depth significantly). In this case, the system has to 'squeeze' an integer number of convective cells increased due to more intense heating, and no asymmetry or non-uniformity in their size seems to be justified. Besides that, the authors were evaluating the overall heat transfer using *H/L* as a control parameter along with *Ra*. We may suggest that the computing domain aspect ratio was varied to achieve this. In our case, we left the system to adjust itself within the invariable domain affecting only the intensity of buoyancy forces manipulating *Ra*.

Combarnous and Bories show also the results of the numerical simulation obtained with a convective roll divided into a 20x20 field for *Ra*=60 and 200 (we assume that in this case simulation was performed in a square domain), see Figure 4.17.
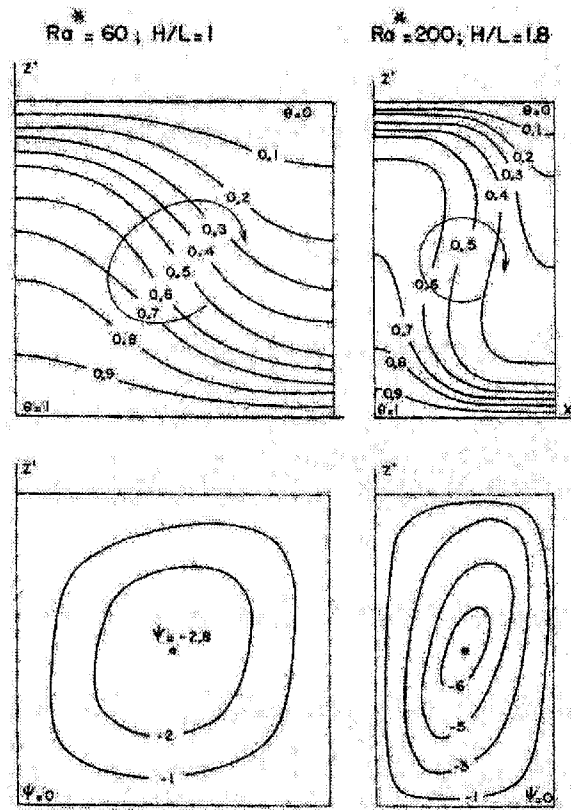
**Figure 4.17 Temperature and stream function distributions in a free convection roll for (*Ra*=60; *H/L*=1) and (*Ra*=200; *H/L*=1.8) (from Combarnous and Bories, 1975).**

A similar numerical experiment was fulfilled with the use of the model being presented. The convective cell size was proved to be dependent on the aspect ratio of the computing domain and the results seem to agree with ones reported in the publication. Thus, when *Ra*=60, if a square computing domain (11km x 11km) is used for the simulation, *H/L*=1 (Figure 4.18 (a)). This result is in agreement both with the value correspondent to the *Nu* curve maximum and the plots of the temperature and stream function distributions presented by the authors (in the case of the long domain (55km x 11km), *H/L* equals approximately 1.2).

For *Ra*=200, the square section calculation gives *H/L*=2, (Figure 4.18 (b). Combarnous and Bories report 1.8 (when the computation is performed on the long section, *H/L*=1.6; Combarnous and Bories's value of *H/L* corresponding to Nu maximum is also 1.6).

**Ra=60**



(a)

**Ra=200**



(b)
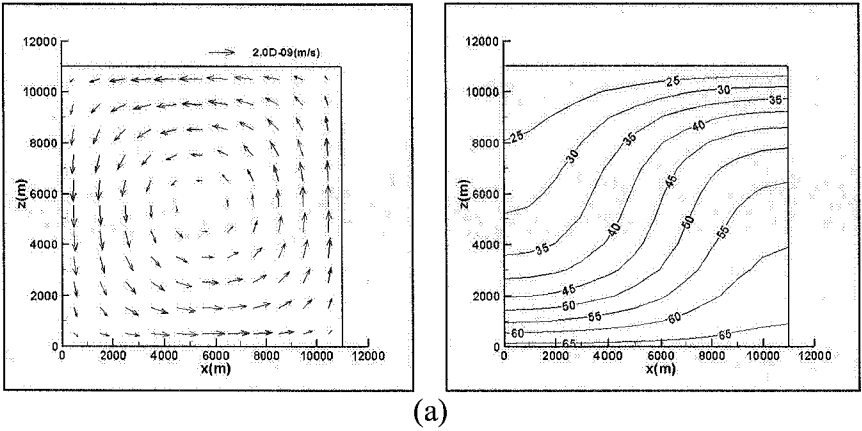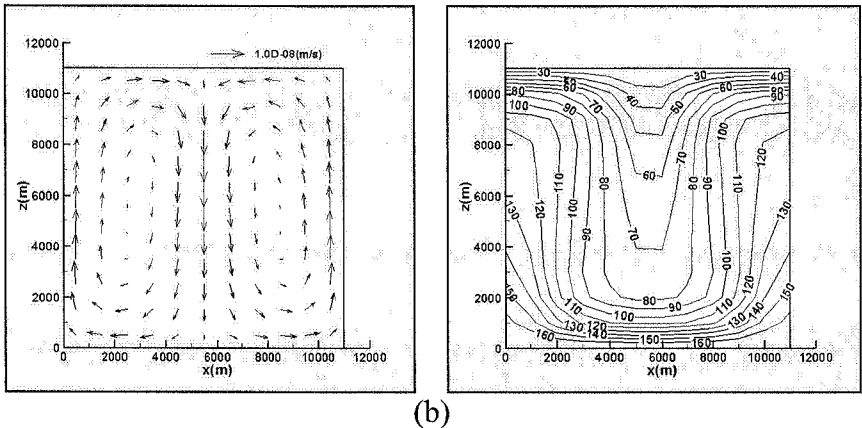
**Figure 4.18 Fluid flow pattern and temperature distribution in a square domain for (a) *Ra*=60 and (b) *Ra*=200.**

## Comparison with (Lein and Tankin, 1992)

Lein and Tankin (1992) presented results of the experimental and numerical studies of natural convection in a horizontal slab of porous material for the Rayleigh number range 39.9 – 72.5. The temperature field in the porous layer was visualized with the use of the Christiansen filter concept that allowed us to see the configuration of the isotherms and to evaluate the aspect ratio of the convective cells. The results of the experiment were compared with the output of a numerical model. The numerical model, they used, is based on the stream function approach and employs a finite difference method with the upwind differences involved to ensure numerical stability.

The aim was to investigate Ra – aspect-ratio dependency with our model for two different settings (permeable to flow upper boundary and impermeable upper boundary) and to compare the obtained results with Lein and Tankin's data. As the control parameter in this porous system of the fixed length is the Rayleigh number, we did not reproduce exactly their experimental setting (which was done for the ethyl

salicylate). Our model was run for pure water: as in the previous section, fluid density linearly depends on temperature and viscosity is assumed constant. Thermal boundary conditions were set so that the correspondent Ra would be comparable with the values the authors used.

### *Impermeable upper boundary*

Plots comparing the numerical and experimental results for impermeable horizontal boundaries are presented in the publication for $Ra$=39.9, $Ra$ =45.4, $Ra$=51.4, $Ra$ =58.3, $Ra$=64.2 and $Ra$=72.5 (Figure 4.19).
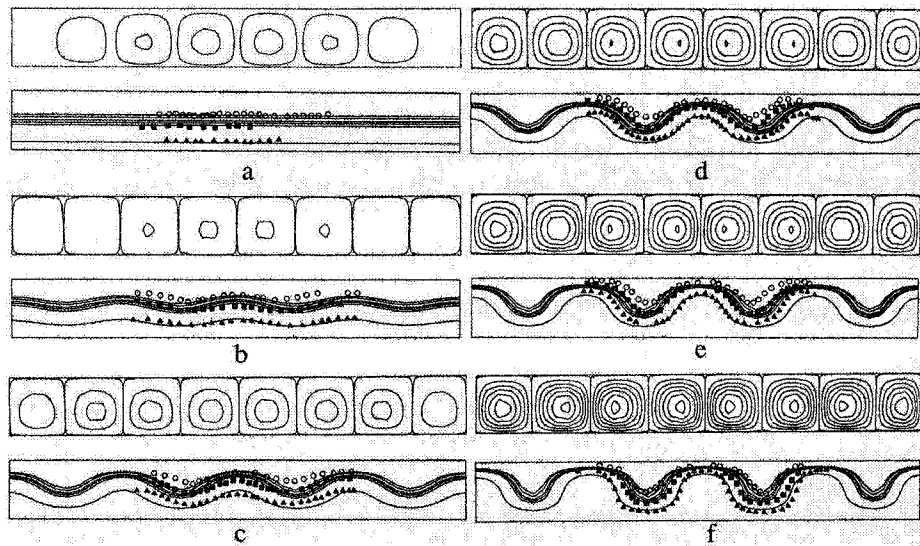


**Figure 4.19 Plots comparing the numerical and experimental results for impermeable boundaries: (a) *Ra*=39.9; (b) *Ra*=45.4; (c) *Ra*=51.4; (d) *Ra*=58.3; (e) *Ra*=64.2; (f) *Ra*=72.5. The theoretical isotherms (solid lines) are as follows: 18.6, 20.5, 22.6, 24.1, and 38.2 $^0C$. The experimental isotherms – 18.6, 26, and 38.2$^0C$ are represented by $\bigcirc$, $\blacksquare$, and $\blacktriangle$, respectively. Streamlines are also shown. (From Lein and Tankin, 1992)**

For comparison, we used our numerical results obtained for $Ra$=39.9, $Ra$=60 (Figure 4.14 (a), (b)) and $Ra$=70 (Figure 4.20)
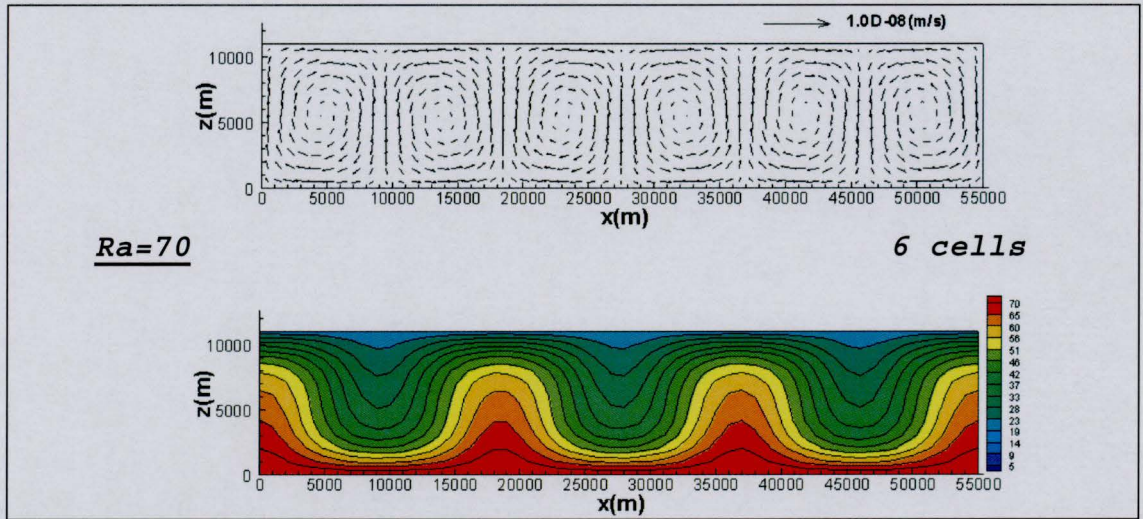
**Figure 4.20 Fluid velocity field and temperature distribution at Ra=70. Impermeable top boundary.**

Similar to Lein and Tankin (1992) at *Ra*=39.9, which is slightly above the critical value, $Ra_c = 4\pi^2$, we found that the isotherms are nearly straight (Figure 4.14 (a)). With an increase in *Ra,* the isotherms deform, in our opinion, very like the picture shown in the publication (Figure 4.14 (b) and Figure 4.20). However, the authors assert that the cell size does not change over the range of the Rayleigh numbers in their experiments, regardless of the glass bead size (which constitute the porous medium) and aspect ratio of the test section (Lein and Tankin, 1992: p.182). This contradicts Combarnous and Bories's results. In a different experiment set up, when the test section aspect ratio and the size of glass beads were varied, the convective cell aspect ratio remained within the range 0.7 – 1.2. As one can see, in our numerical experiments, the aspect ratio decreases from 1.0 at *Ra*=39.9 (Figure 4.14 (a)) to approximately 0.83 at *Ra*=70 (Figure 4.20) nevertheless remaining within the *L/H* limits determined by the experimental study.

It was also found that the aspect ratio of the test domain does not affect the aspect ratio of the convective cells for these particular boundary conditions. The section length was doubled, which led to a doubling of the number of convective cells. In Figure 4.21 the results of the simulation for *Ra*=39.9 and *Ra*=60 are presented.
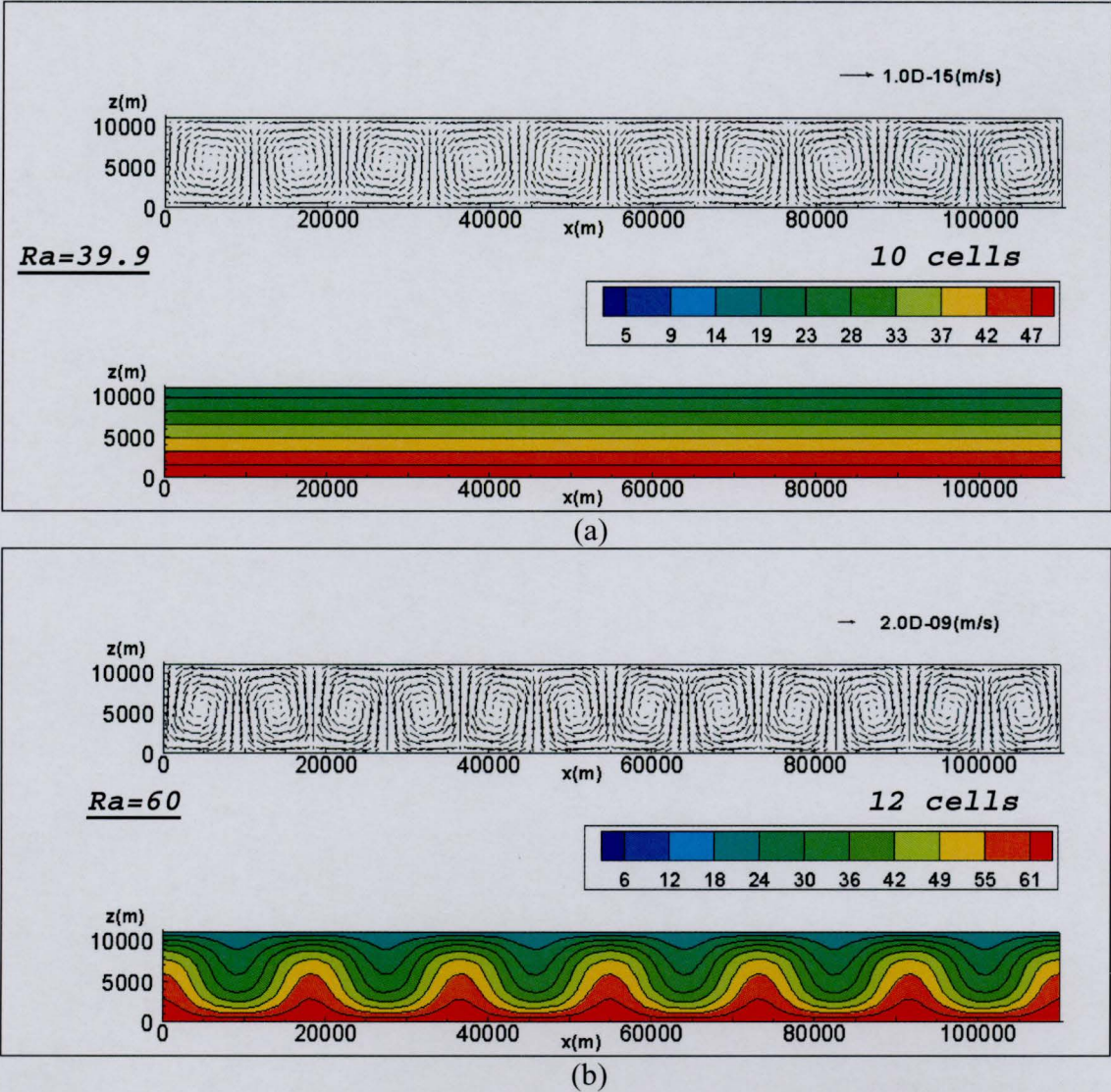
Figure 4.21 Fluid velocity field and temperature distribution at (a) *Ra*=39.9 and (b) *Ra*=60. Impermeable top boundary, expanded test section.

Thus, at *Ra*=39.9, the expanded test section (110km length) accommodates 10 cells (Figure 4.21 (a)), while the one of length 55km contains 5 cells (Figure 4.14 (a)). Correspondingly, at *Ra*=60, we have 12 cells within the long section (Figure 4.21 (b)) and 6 cells if the domain is two times shorter (Figure 4.14 (b)).

### *Permeable upper boundary*

In the publication of Lein and Tankin (1992), the next set of tests is reported to be carried out when a uniform liquid layer was imposed between the beads and the top plate. This liquid layer changes the hydrodynamic boundary to a permeable condition. The numerical model used by the authors does not yield a change in cell spacing with the Rayleigh number. They suggest, this possibly occurs due to the simplifying assumption in the numerical simulation that pressure and temperature are

constant along the interface (Lein and Tankin, 1992: p.182). However, the experimental results showed the cell width/height ratio increase with the Rayleigh number. The plots comparing the numerical and experimental results are presented for *Ra*=30.6, *Ra*=40.3, *Ra*=50.7 and *Ra*=61.7 (Figure 4.22).
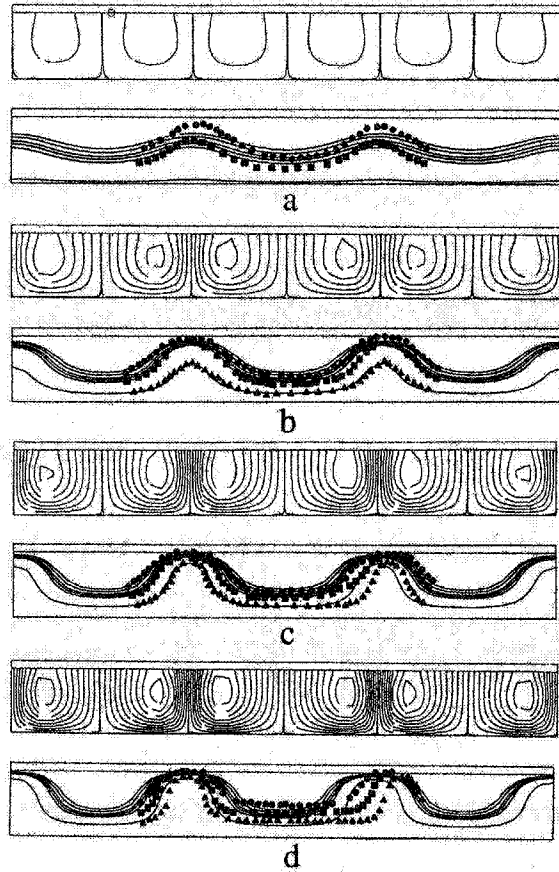


**Figure 4.22 Plots comparing the numerical and experimental results for the permeable top boundary: (a) *Ra*=30.6; (b) *Ra*=40.3; (c) *Ra*=50.7; (d) *Ra*=61.7. The theoretical isotherms (solid lines) are as follows: 18.6, 20.5, 22.6, 24.1, and 38.2 $^0C$. The experimental isotherms – 18.6, 26, and 38.2$^0C$ are represented by ●, ■, and ▲, respectively. Streamlines are also shown. (From Lein and Tankin, 1992)**

With the use of the model being presented, the simulation was carried out for the same *Ra* values for two settings: for the test section with the aspect ratio equal 5 and for the domain with the aspect ration equal 10. In the first case (the test section is 55km long), the same number of convective cells appears in the domain for all *Ra* (Figure 4.23 (a), (b), (c) respectively).

(a)



(b)



(c)
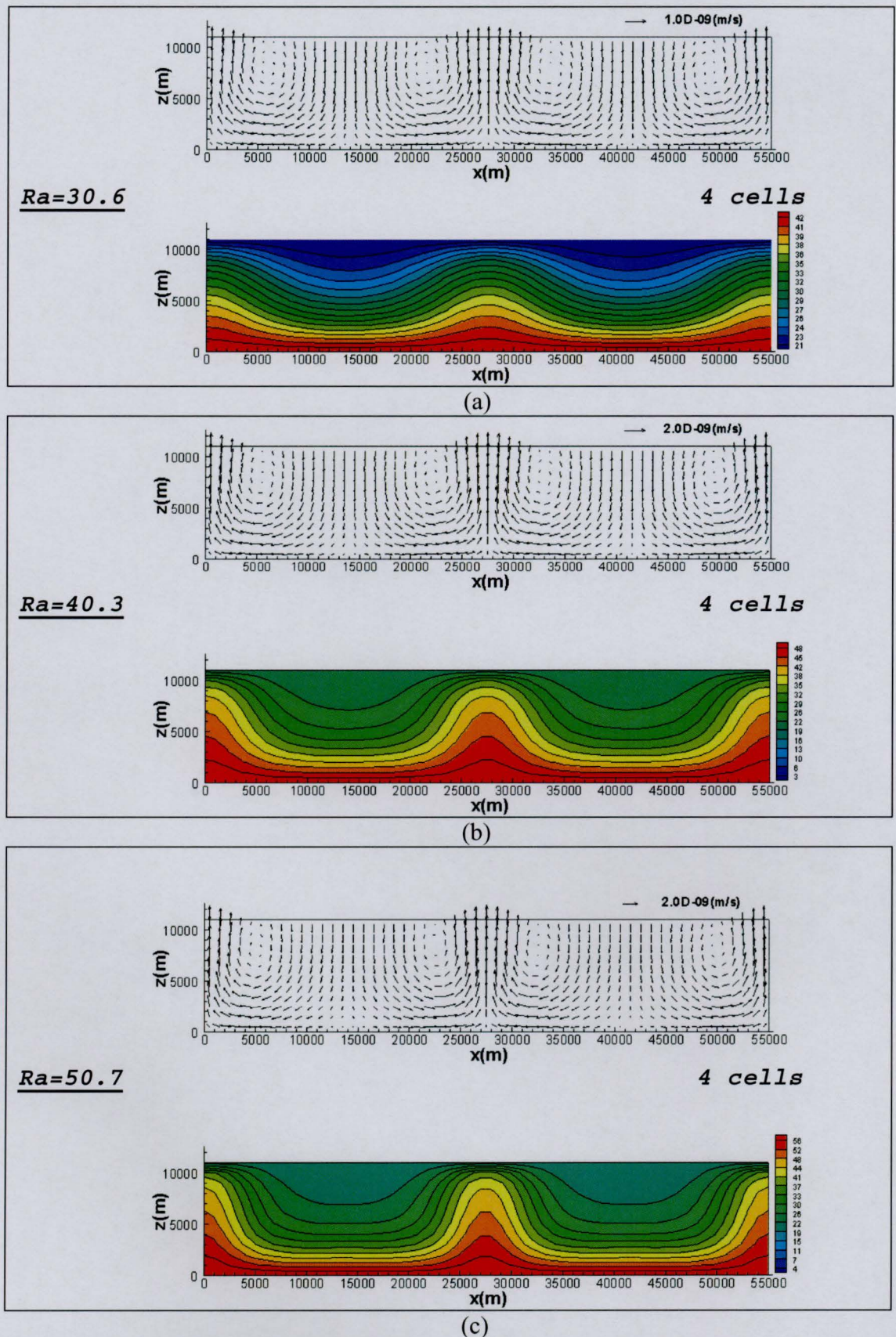
**Figure 4.23 Fluid velocity field and temperature distribution at (a) *Ra*=30.6, (b) *Ra*=40.3, (c) *Ra*=50.7. Permeable to flow top boundary.**

We have four contrarotating cells and three equally spaced isotherm picks. This is similar to the numerical results obtained by Lein and Tankin. However, having

done a similar simulation in the section of the double length, it was found that at $Ra$=39.9 and $Ra$=40.3, 8 cells are formed (double quantity), but at the higher Rayleigh number value, $Ra$=50.7, we have 9 of them (Figure 4.24 (a)-(c)).



(a)

(b)

(c)
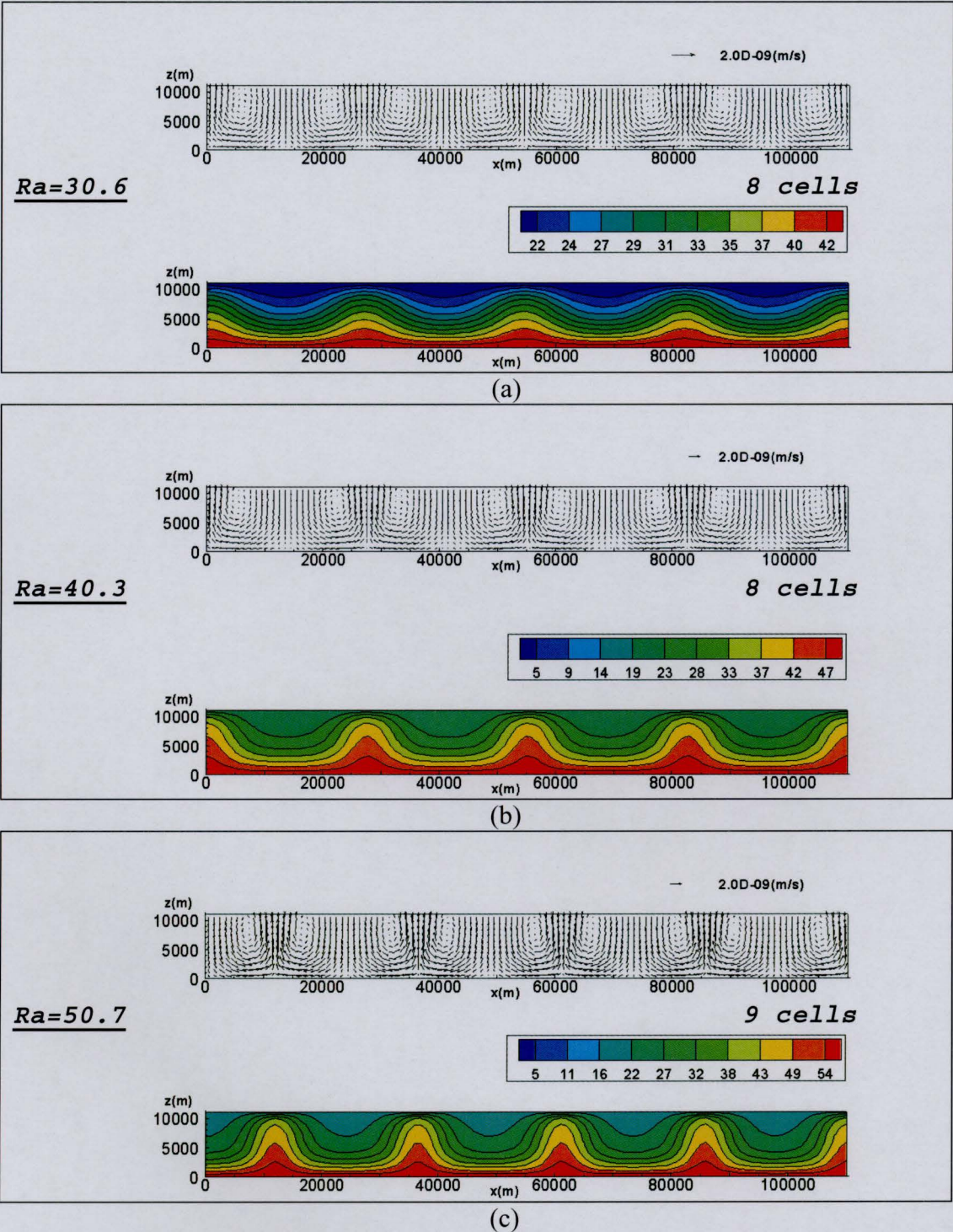
**Figure 4.24 Fluid velocity field and temperature distribution at (a) *Ra*=30.6, (b) *Ra*=40.3, (c) *Ra*=50.7. Permeable to flow top boundary; expanded test section.**

It was found that the reason for the discrepancy in the results is the simplification that the fluid viscosity is constant. The similar simulations were

performed with the dynamic viscosity coefficient dependent on temperature (equation (2.18) at S=0.0). In this case, we evaluated *Ra* similarly to Raffensperger and Vlassopoulos (1999) as

$$Ra = \frac{gHk(\overline{\rho}_{top} - \overline{\rho}_{bottom})}{\overline{\mu}\kappa},$$      **Equation 4.38**

where $\overline{\rho}_{top}, \overline{\rho}_{bottom}$ are the mean fluid density at the top and bottom of the porous layer, $\overline{\mu}$ is the mean fluid viscosity within then layer. As $\rho = \rho_0(1 - \alpha T)$ in these tests, hence

$$Ra = \frac{gHk\alpha\rho_0(T_{bottom} - T_{top})}{\overline{\mu}\kappa}.$$      **Equation 4.39**

Here $T_{top}$ and $T_{bottom}$ are temperature values at the top and bottom of the porous layer respectively. $\overline{\mu}$ was evaluated as an average of $\overline{\mu}(T_{top})$ and $\overline{\mu}(T_{bottom})$. The result of the numerical experiment is shown in Figure 4.25 (a), (b).



(a)



(b)
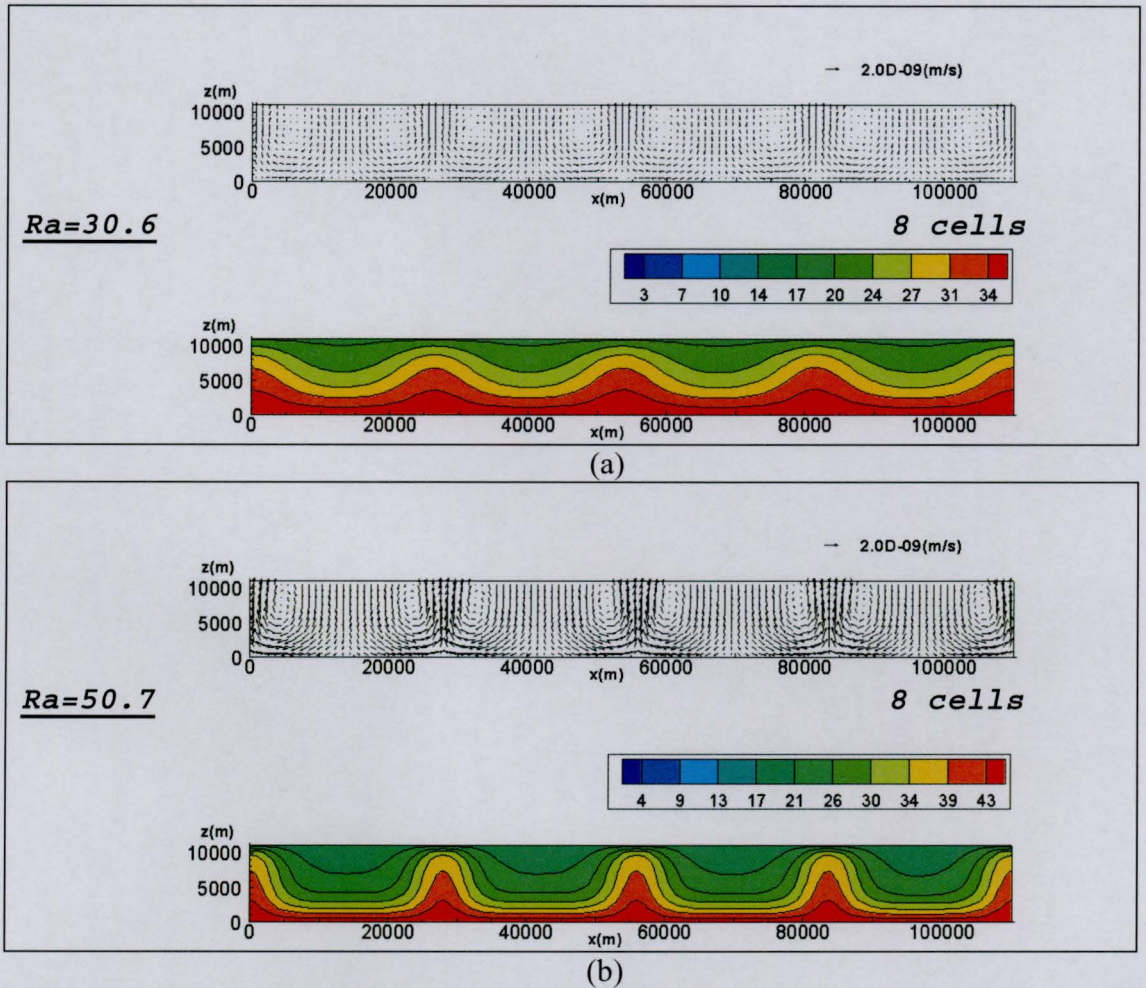
**Figure 4.25 Fluid velocity field and temperature distribution at (a) *Ra*=30.6, (b) *Ra*=40.3, (c) *Ra*=50.7. Permeable to flow top boundary; expanded test section; viscosity dependent on temperature.**

In both cases, eight convective cells formed, meaning that the cell aspect ratio remains the same over this Rayleigh number range which agrees with Lain and Tankin's results.

However, the model does not reproduce the experimentally established increase in the cell aspect ratio with *Ra* rise, as well as the code the authors used. The discrepancy can be caused by the interplay of several factors. First, as we have shown, the result is sensitive to the equation of state for the fluid viscosity. The switch from the constant coefficient to the expression as a function of temperature affects the aspect ratio. Further, both in the case of the impermeable top boundary and in the case of a liquid film superimposed over the porous layer, the controlling factor was the temperature of the horizontal plates bounding the system. But the presence of the liquid film may affect the actual thermal boundary condition on the top of the porous layer, especially if its thickness is about 10% of the porous system. If, for example, the temperature at the interface 'liquid layer-porous system' is lower than of the top plate, it affects the controlling parameter, *Ra* value. Another option, if the convection occurs in the film (the roughly evaluated Rayleigh number for the liquid layer appeared to exceed significantly the critical value), one may expect some periodicity in the temperature distribution in the immediate vicinity of the interface.

In other words, in our opinion, the discrepancy with the experiment is acceptable, since to reproduce this 'liquid film-porous layer' system more accurately, one needs a more accurate consideration of the liquid layer dynamics.

### *Comparison with Elder (1967)*

This paper has become a classical benchmark for variable-density transport models. Comparing our model output with the results presented in the publication, we had two goals:

    1)  to recheck the consistency of our free convection results;

    2)  to examine the validity of the free discharge simulation (Section 4.2.3).

The output of the free convection simulations for *Ra*=60, 80, 100 and 120 is presented in Figure 4.26. Figure 4.26 (a) includes the results obtained within the square test section 11*km* x 11*km* (12 nodes in each direction). To present the results in the format similar to one used in (Elder, 1967), see Figure 4.27, we show the fragment of the temperature distribution field within 3000m long section containing a convective cell centre.

In the square domain, one convective cell is formed when $Ra$=60, 80 and 100. The isotherm configurations are very similar to ones shown by Elder for this Rayleigh number range. However, at $Ra$=120, the model being presented produces two cells and therefore the isotherm pattern is quite different from Elder's. To clarify this discrepancy, the analogous numerical tests were performed on the mesh of the double length but with the same spatial resolution (Figure 4.26 (b)).



(a)



(b)
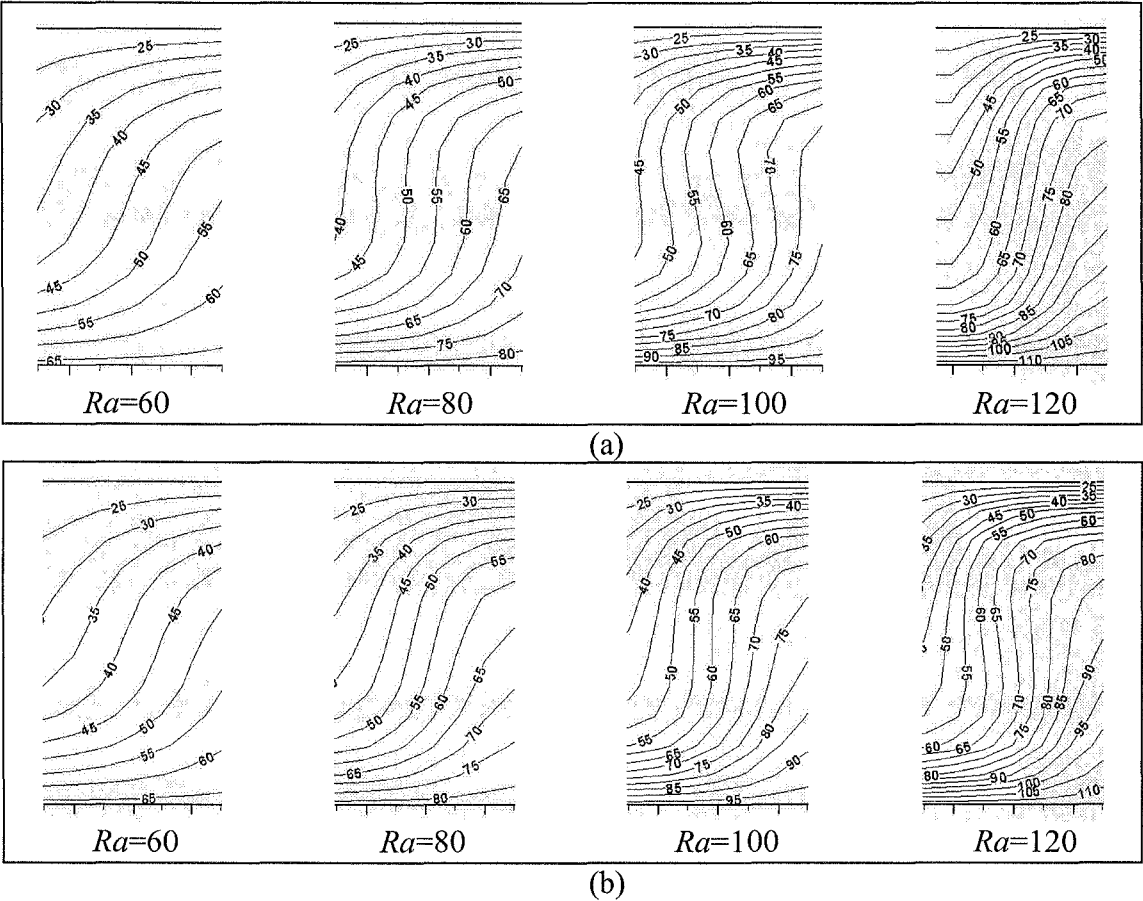
**Figure 4.26 Temperature distribution at $Ra$=60, 80, 100, 120. (a) test section 11 $km$ x 11 $km$; (b) test section 22 $km$ x 11 $km$.**
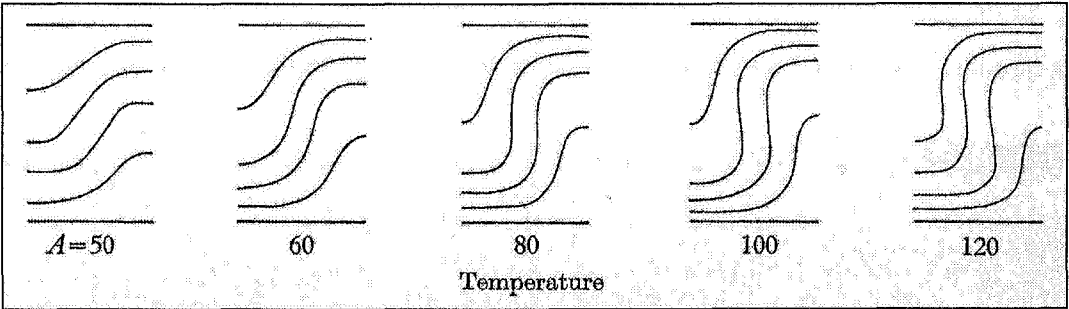


**Figure 4.27 Temperature distribution in a half-cell calculated at Rayleigh number $A$=50, 60, 80, 100, 120. Isotherms drawn at intervals 0 (0.2) 1. Mesh 21 x 21 (from Elder, 1967).**

It was observed, that the convective cell aspect ratio is shown to be dependent not only on the Rayleigh number value, but also on the aspect ratio of the test

section. Thus, in the test section of double length, at $Ra$=60, two contrarotating cells are formed, while for $Ra$=80, 100 and 120, three cells are contained in the domain. Similar to Elder, we found that the isotherms steepen as $Ra$ increases, the result for $Ra$=120 is also consistent with the published graph. The only confusing discrepancy with the published data is that Elder's results were calculated on the mesh of 21 x 21 nodes (see Elder, 1967: p.38), we assume, a square test section was used for the simulation. For this kind of mesh, our model produces a different result at $Ra$=120.

However, the resent study of Graf (2004) revealed a high sensitivity of the Elder results to flow parameters used (equivalent freshwater head or streamfunction), fluid density relationship (linear, nonlinear) as well as the numerical method. The author states that the quantitative conformity of the results can be achieved if both the flow parameters and the model approach of the two codes are identical. Taking into account the fact that Elder's model used the stream function to describe fluid flow and a finite difference method for the numerical solution of the problem, we attribute the described discrepancy in the results to this.

### 4.2.3 Free discharge

#### *Elder (1967)*

As has been mentioned, another object of interest in Elder (1967) was the natural discharge simulation. The latest has a key importance for this research since the discharge zones are considered as possible locations of ore deposits and the discharge regime (fluid velocities, thermal characteristics) accounts for mineral precipitation.

The numerical experiment was set up similar to one described in Elder (1967, paragraph 6.2):

- Test section aspect ratio equals 5 (a domain 55 $km$ x 11 $km$ is used);
- The pressure is maintained at zero on the top boundary;
- Side and lower boundaries are assumed impermeable to flow;
- The centrally located section of the lower boundary of length 11km is held at temperature $T_{top} + \Delta T$, while all other sections of the domain boundary are kept at temperature $T_{top}$.

Figure 4.28 (a) shows the temperature distribution and stream lines at $Ra$=50, which are very similar to ones given in (Elder 1967), Figure 4.28 (b).

(a)



(b)
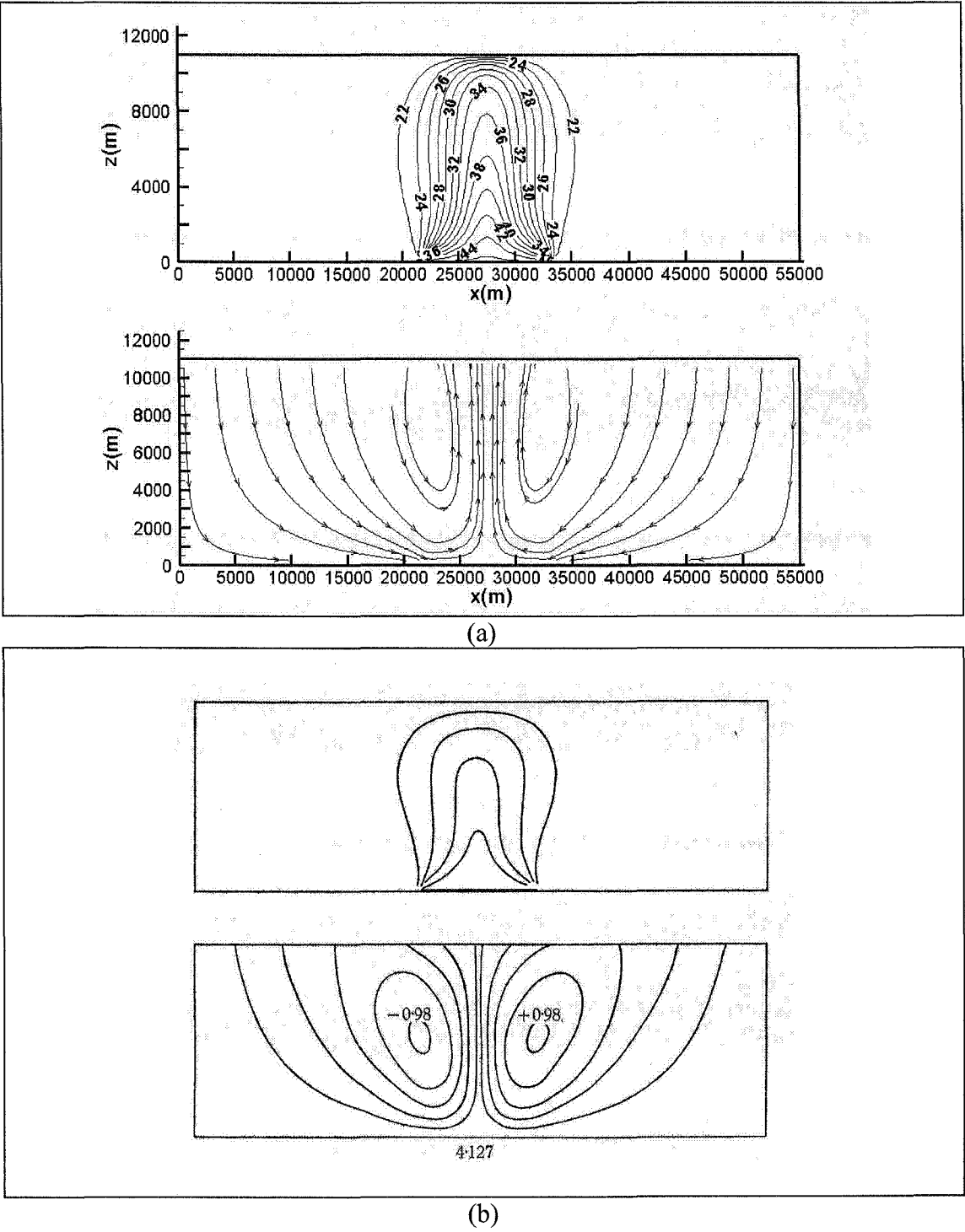
**Figure 4.28 Free discharge. (a) Calculated isotherms and streamlines at *Ra*=50. (b) Natural discharge, calculated isotherms and stream function at *Ra*=50, mesh 101 x 21 (from Elder, 1967).**

In Figure 4.29 (a) the vertical component of fluid velocities through the upper surface is plotted. Similar to (Elder, 1967), the velocity values are normalized by $\kappa / H$ to obtain a dimensionless characteristic.

<center>(a)                                                    (b)</center>
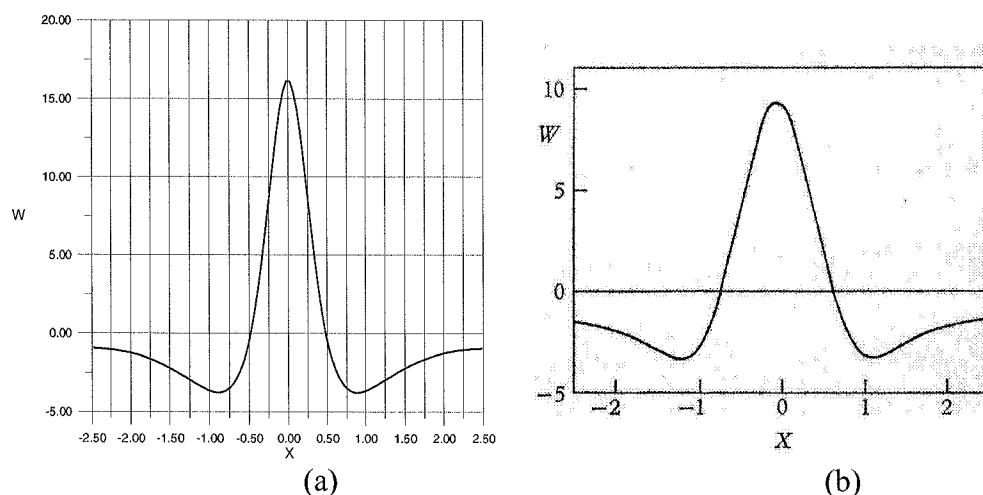
**Figure 4.29 Free discharge. (a) Calculated dimensionless velocity of the fluid flow through the upper surface. (b) Natural discharge, velocity through the upper surface (from Elder, 1967).**

The appearance of the graph is very similar to that of (Elder, 1967), see Figure 4.29 (b). However, we obtained higher dimensionless discharge velocities than in the publication, and the discharge area is narrower in our case (1.0 against 1.4 in Elder's data). As above, based on the conclusions by Graf (2004), we relate the discrepancy in the quantitative characteristics to the differences in the description and numerical solution of the problem.

## 4.3 Density driven flow in a complex faulted sedimentary basin (McArthur Basin, Northern Territory, Australia)

The examples of the model application to different aspects of free convection (Section 4.2) have shown a good capability of the model to simulate density driven flows in the uniform porous media. The architecture of the Zambian Copperbelt (discussed in the next chapter) is, however, incomparably more complicated than the considered case studies; and so the natural next step was to apply the model to a more complex though not very intricate structure. For this purpose, we made an attempt to reproduce the results of the numerical simulation of hydrothermal fluid flow in a section of the McArthur Basin, Australia, reported in (Garven et al., 2001).

The section hydrostratigraphy was reconstructed from the diagram presented in the publication as accurately as possible (Figure 4.30 (a)). The finite element mesh was built so as to mimic the one used in the reported simulation: it contained 89

quadrilateral elements in the horizontal direction and 39 elements in the vertical direction (Figure 4.30 (b)).



(a)



(b)
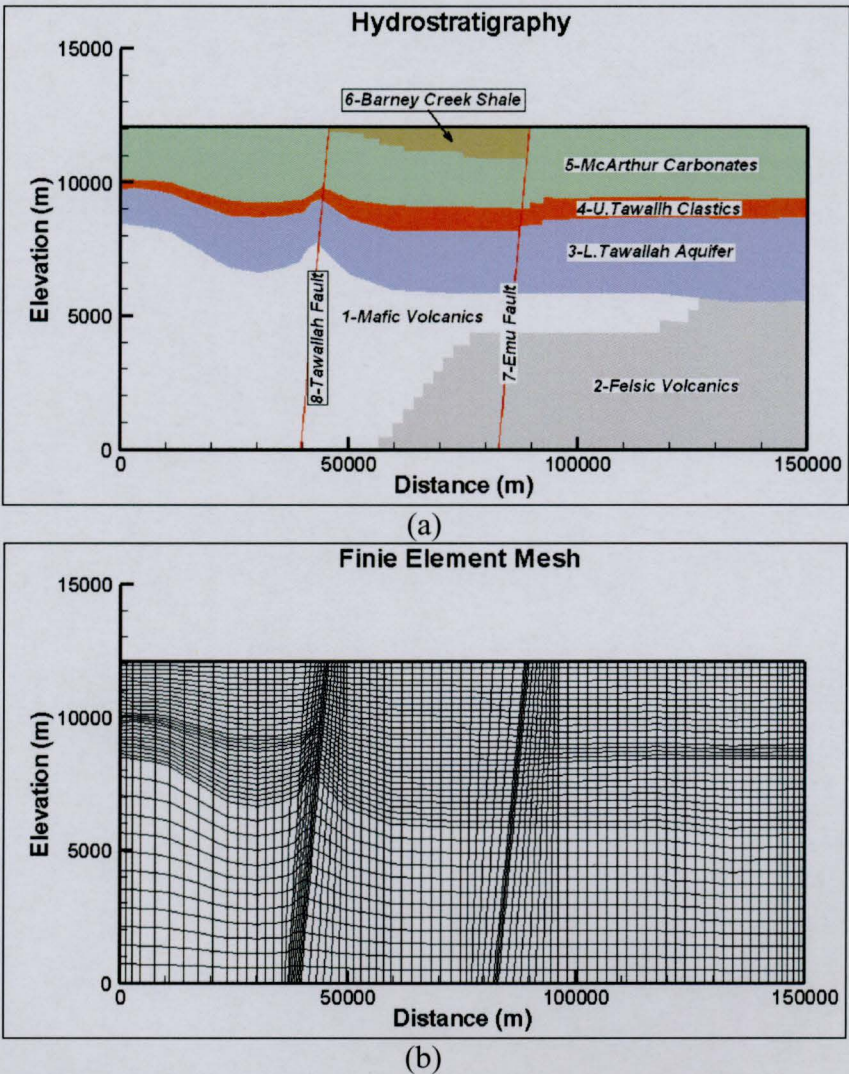
**Figure 4.30 McArthur Basin. (a) hydrostratigraphy of the section; (b) finite element mesh used in the simulation of the density driven flow.**

The first of the numerical experiments described in the publication (Garven et al., 2001: p.298) was reproduced. In this scenario, the Upper Tawallah Aquifer (unit 4) and the Lower Tawallah Group Package (unit 3) are considered as a single aquifer. Physical properties of the rock units comprising the section are shown in Table 4.6.

| Hydrologic unit | Permeability | | Porosity, $n$ (fraction) | Compressibility, $\alpha_c$ $(m \cdot s^2 / kg)$ | Thermal conductivity of the saturated porous medium, $\lambda_e$ $(Wm^{-1}\,{}^0C^{-1})$ |
| --- | --- | --- | --- | --- | --- |
| | $k_x(m^2)$ | $k_z(m^2)$ | | | |
| 1-Mafic Volcanics | $3.143701 \cdot 10^{-16}$ | $3.143701 \cdot 10^{-18}$ | 0.01 | $9.673101 \cdot 10^{-11}$ | 3.0 |
| 2-Felsic Volcanics | $9.431103 \cdot 10^{-16}$ | $9.431103 \cdot 10^{-18}$ | 0.01 | $9.673101 \cdot 10^{-11}$ | 3.0 |
| 3-L.Tawallah Aquifer | $9.431103 \cdot 10^{-14}$ | $9.431103 \cdot 10^{-16}$ | 0.15 | $1.099684 \cdot 10^{-9}$ | 3.0 |
| 4-U.Tawallah Clastics | $9.431103 \cdot 10^{-14}$ | $9.431103 \cdot 10^{-16}$ | 0.15 | $1.099684 \cdot 10^{-9}$ | 3.0 |
| 5-McArthur Carbonates | $9.431103 \cdot 10^{-15}$ | $9.431103 \cdot 10^{-17}$ | 0.10 | $1.064041 \cdot 10^{-9}$ | 2.5 |
| 6-Barney Creek Shale | $9.431103 \cdot 10^{-16}$ | $9.431103 \cdot 10^{-18}$ | 0.30 | $1.237165 \cdot 10^{-9}$ | 2.0 |
| 7-Emu Fault | $9.431103 \cdot 10^{-14}$ | $9.431103 \cdot 10^{-14}$ | 0.05 | $8.151523 \cdot 10^{-11}$ | 3.0 |
| 8-Tawallah Fault | $9.431103 \cdot 10^{-14}$ | $9.431103 \cdot 10^{-14}$ | 0.05 | $8.151523 \cdot 10^{-11}$ | 3.0 |

**Table 4.6 McArthur Basin. Properties of hydrologic units comprising the section.**

Permeability values were calculated by the hydraulic conductivities given in the publication (Garven et al., 2001: p.297, Table 1), assuming the reference fluid density $\rho_0$=1016.22 $(kg/m^3)$ and $\mu_0$=1.1398338$\cdot 10^{-3}$ $(kg\,m^{-1}\,s^{-1})$. Solid matrix density and heat capacity were assumed constant and uniform throughout the profile: $\rho_s$=2630$(kg/m^3)$, $c_s$=800$(J \cdot kg^{-1} \cdot {}^0C^{-1})$; so were fluid properties such as compressibility, heat capacity and thermal conductivity: $\beta_c$=4.581057742$\cdot 10^{-10}$ $(m \cdot s^2 / kg)$, $c_f$=4200$(J \cdot kg^{-1} \cdot {}^0C^{-1})$, $\lambda_f$=0.6$(Wm^{-1}\,{}^0C^{-1})$.

### Boundary conditions.

Lower and lateral boundaries of the domain are assumed to be impermeable to flow. Uniform hydraulic head value (15000$m$) is prescribed on the top section boundary.

Lateral boundaries are impermeable to heat flow. The bottom boundary is subjected to constant heat flux at a rate of $70mW/m^2$. The upper boundary is maintained at a uniform temperature $(20^0C)$ except for fault outlets, where no temperature gradient condition is assumed to allow fluid discharge at the temperature of the underlying media.

_**Initial conditions.**_

At the initial instant of time, the hydraulic head is assumed uniform ($15000m$) corresponding to the hydrostatic state. The temperature increases linearly with depth from $20^0 C$ on the top to $300^0 C$ on the bottom of the section.

The only unclear point is what in particular equation of state relating fluid density and viscosity to pressure, temperature and salinity should be used for this scenario. The simulations reported in the paper were performed with the use of the OREGEN model. Two references to this model, which are given in the publication, were considered to clarify the question. However, in (Garven, 1989), it is stated that density and viscosity are functions of pressure, temperature and salinity (Garven, 1989: p.122), but no explicit equations were found. Another reference to this model, (Garven et al., 1993), refers in its turn to (Kestin et al., 1981) which contains several pages of tabulated data. Thus, the simulations presented below were performed based mainly on the expressions by (Batzle and Wang, 1992) introduced in Section 2.1.5 with the gradual increase of complexity of the equations of state.

_**Test 1.**_ For this case study, a simplest linear dependence of the water density on temperature, $\rho_f = \rho_f (T) = \rho_0 (1 - \alpha T)$, was used with $\alpha = 8 \cdot 10^{-4} (1/^0 C)$. Fluid viscosity was assumed constant: $\mu = 5 \cdot 10^{-4} (kg\, m^{-1}\, s^{-1})$. The results of the simulation, fluid velocity field and temperature distribution at steady state, are shown in Figure 4.31 (a) and (b) respectively.

(a)



(b)
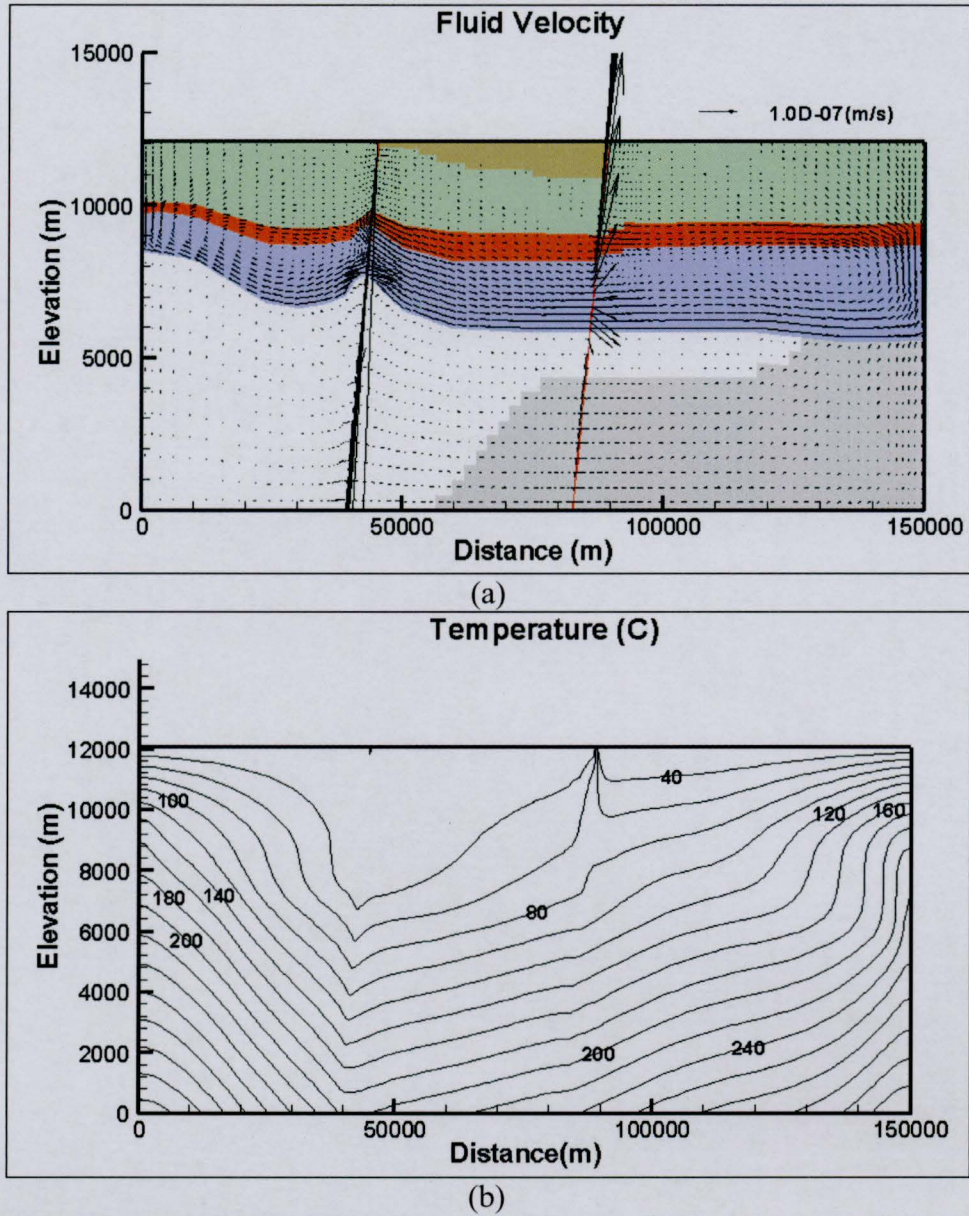
**Figure 4.31 McArthur Basin. _Test 1_. (a) Steady state fluid velocity field and (b) temperature distribution calculated under the assumption** $\rho_f = \rho_f(T) = \rho_0(1 - \alpha T)$**,** $\alpha$ **=8·10$^{-4}$ (1/$^0$C ),** $\rho_0$ **=1016.22(kg/$m^3$ ),** $\mu$ **=const=5·10$^{-4}$ (kg m$^{-1}$ s$^{-1}$ ).**

One can see that both fluid velocity field and temperature distribution are very similar to those presented in the publication (compare with Figure 4.32 (a) and (b)). The only difference that can be pointed out is that the peak of the isotherm at $80^0 C$ in the Emu fault area does not approach the surface.

(a)



(b)
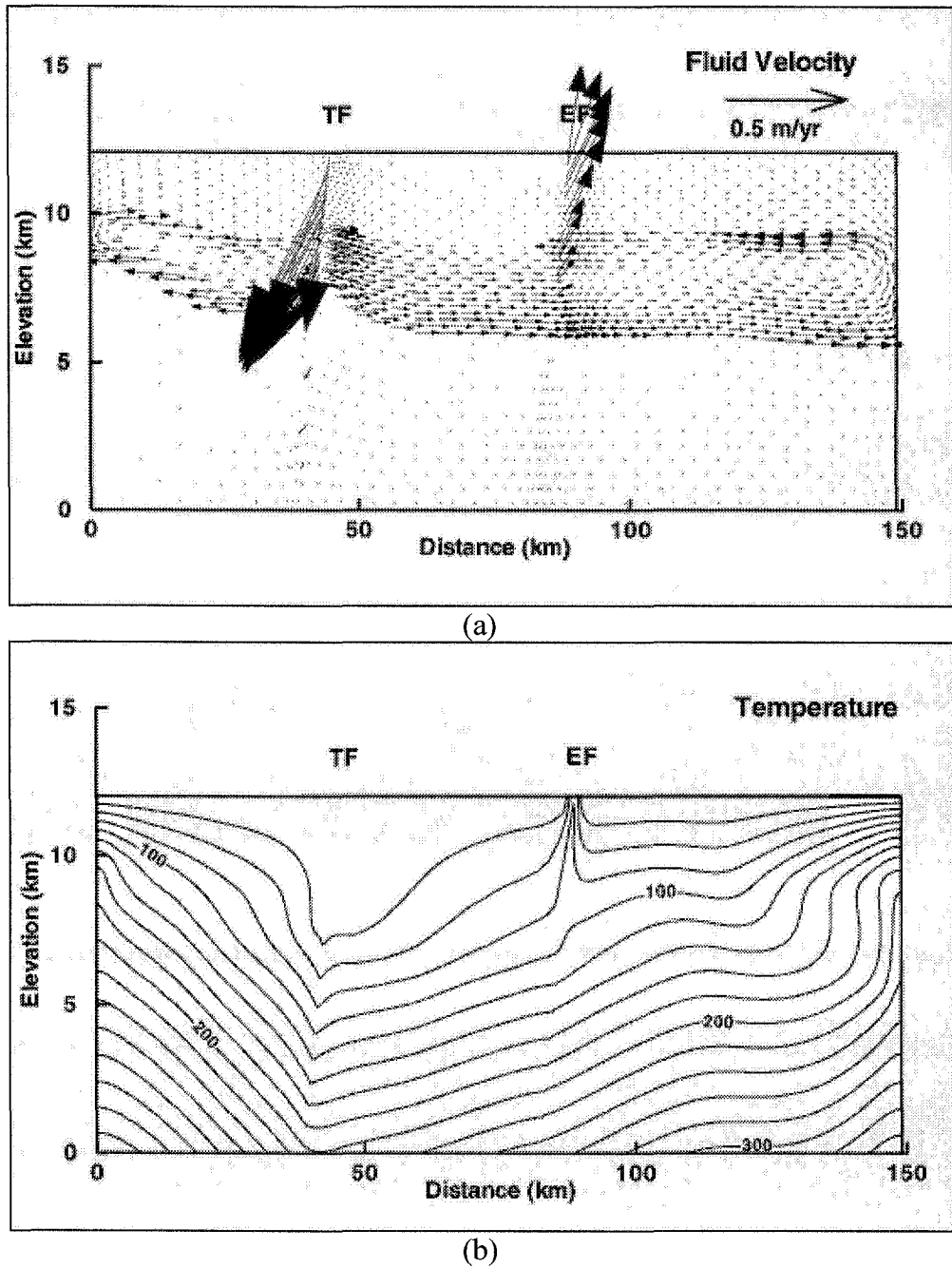
Figure 4.32 McArthur Basin. *Test 1*. (a) Fluid velocity vectors, assuming 'thick' Tawallah Group aquifer (combining hydrologic units 3 and 4) and that both faults act as permeable conduits for flow. TF, Tawallah Fault; EF, Emu Fault. (b) Temperature field assuming a basal heat flux of 70 mW m$^{-2}$. (From Garven et al., 2001).

*Test 2* was performed assuming $\rho_f = \rho_W(T, P)$ (equation (2.16)) and $\mu = const = 5 \cdot 10^{-4} (kg\,m^{-1}\,s^{-1})$. Similarly to the previous case study, the solution reaches steady state in this experiment. Figure 4.33 (a) and (b) show the resulting velocity field and temperature distribution.

(a)



(b)
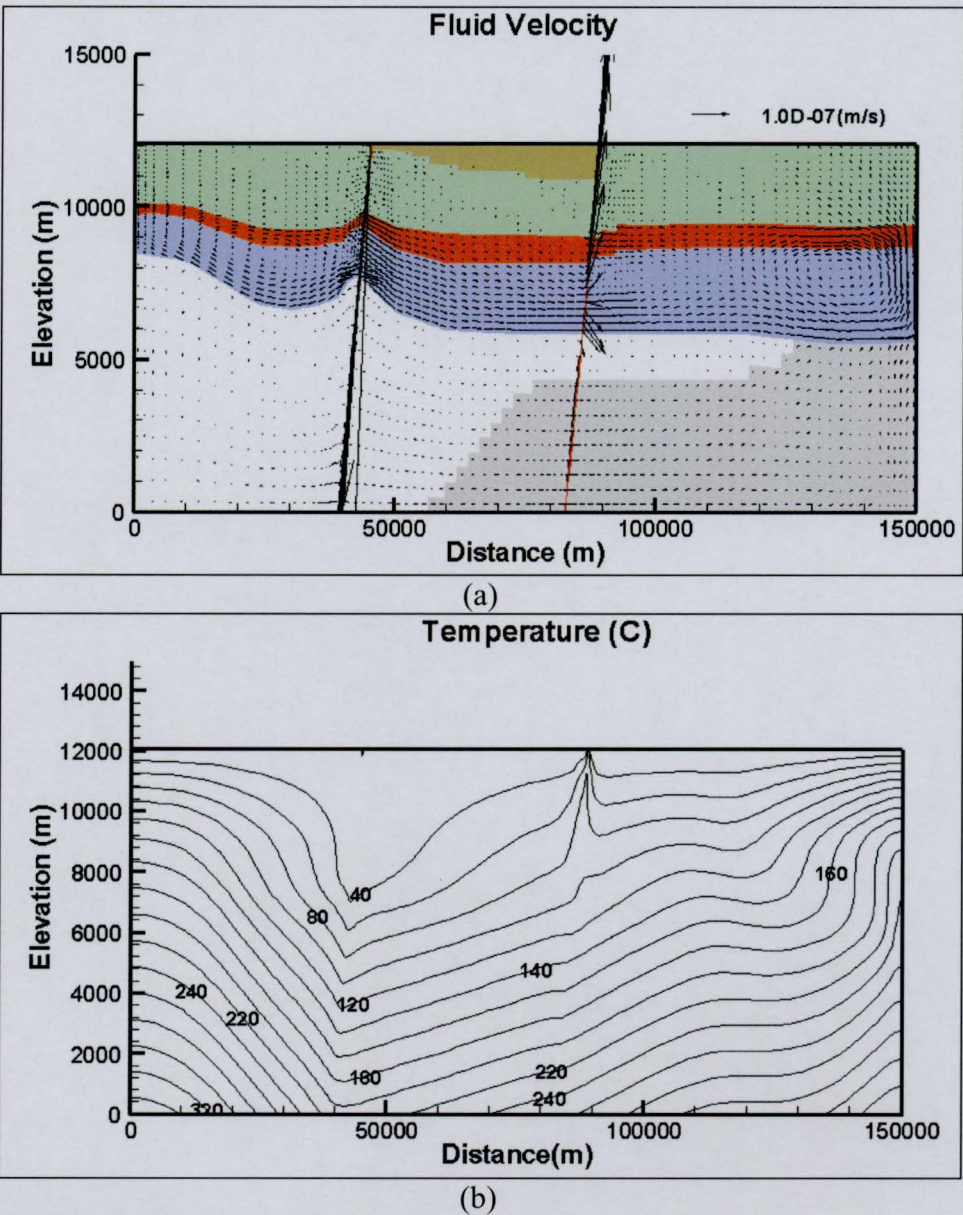
**Figure 4.33 McArthur Basin. _Test 2_. (a) Steady state fluid velocity field and (b) temperature distribution calculated under the assumption** $\rho_f = \rho_W(T,P)$ **according to (Batzle and Wang, 1992),** $\mu = const = 5 \cdot 10^{-4} (kg\, m^{-1}\, s^{-1})$ **.**

In this case, the temperature distribution seems identical to the one shown in the publication (compare with Figure 4.32 (b)).
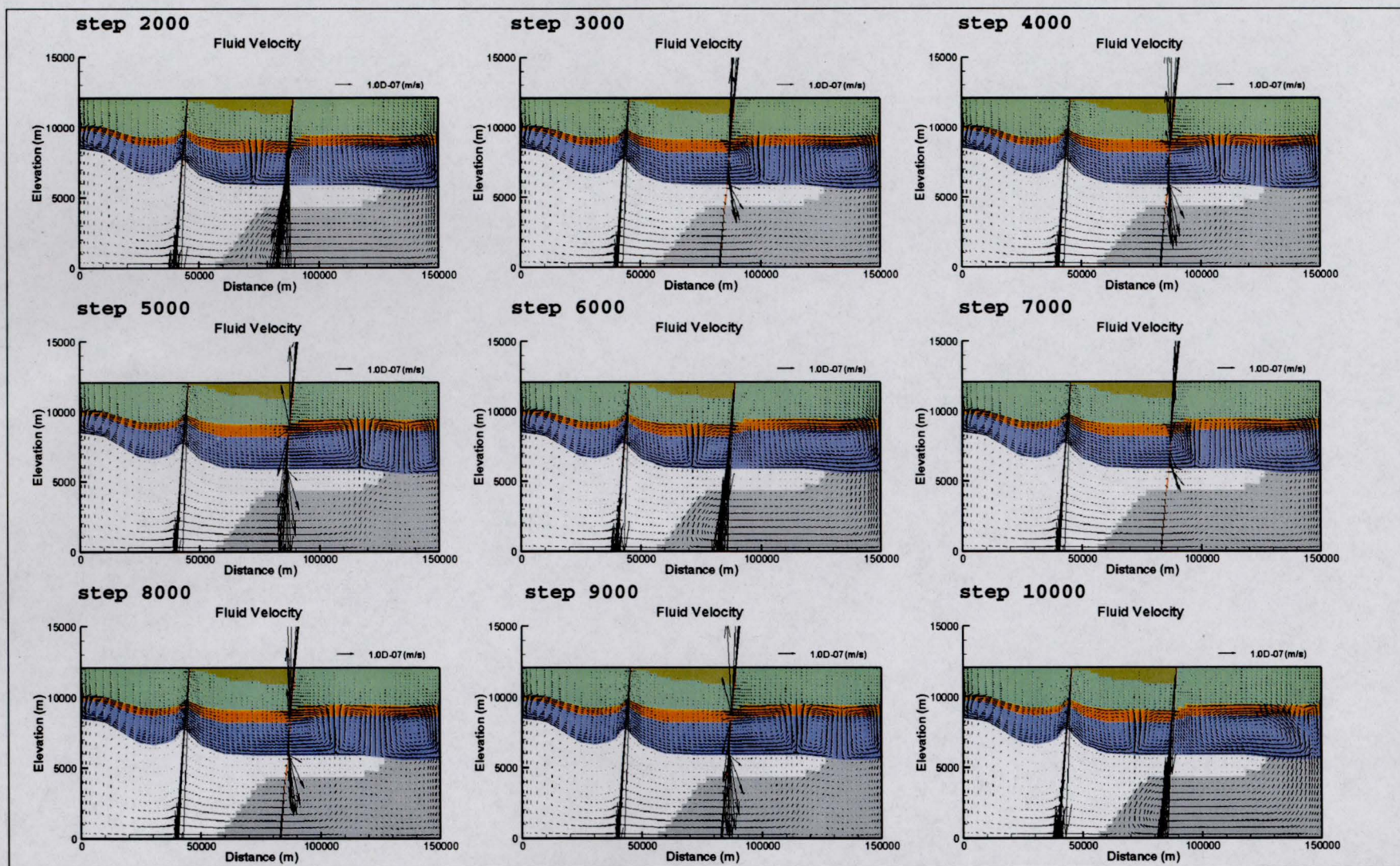
**Figure 4.34 McArthur Basin. _Test 3_. Fluid velocity field calculated under the assumption $\rho_f = \rho_w(T, P)$, $\mu = \mu(T)$ according to (Batzle and Wang, 1992).**

*Test 3*. In this scenario, in addition to the water density being a function of pressure and temperature, the dependence of fluid viscosity on temperature was also included: $\mu$ is described by equation (2.18), assuming $S=0$.

The system does not come to a steady state in this scenario. The long term simulation (10000 steps with $\Delta t = 10^6$ (days)) showed a periodicity in the groundwater flow. Thus, the fluid flow pattern in the section on the left of the Tawallah Fault, as well as the recharge-discharge regime of this fault, remains the same throughout the simulation. However, the fluid flow direction in the Emu Fault and the number of the convective cells on the right of the Tawallah Fault changes cyclically. Figure 4.34 shows the fluid flow field after every 1000 steps of the simulation.

The schematic picture of the fluid flow direction in the Emu Fault (Figure 4.35) prompted the suggestion that the whole picture of the groundwater circulation, including its thermal regime, changes periodically.
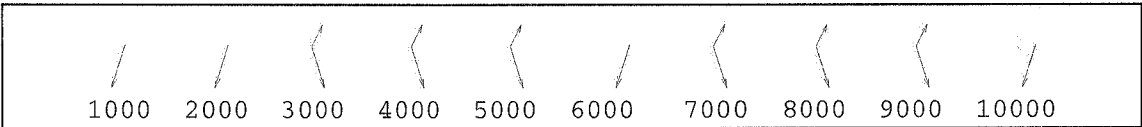


**Figure 4.35 McArthur Basin. *Test 3*. Schematic direction of the groundwater flow in the Emu Fault every 1000 time steps of the simulation,**

To verify the supposition, the simulation was rerun for a longer period of time (15100 steps) with more frequent output (every 100 steps). The simulation has shown that the fluid flow field, as well as the temperature distribution, does change cyclically repeating itself practically precisely with the period approximately equal to 4300 steps. In Figure 4.36 (a) we show the superimposition of the temperature fields correspondent to time levels with numbers 1600, 5900, 10200, and 14500 (4300 time steps between each successive output) and the fluid velocity pattern which is the same for all these time instants (Figure 4.36 (b)).

(a)



(b)
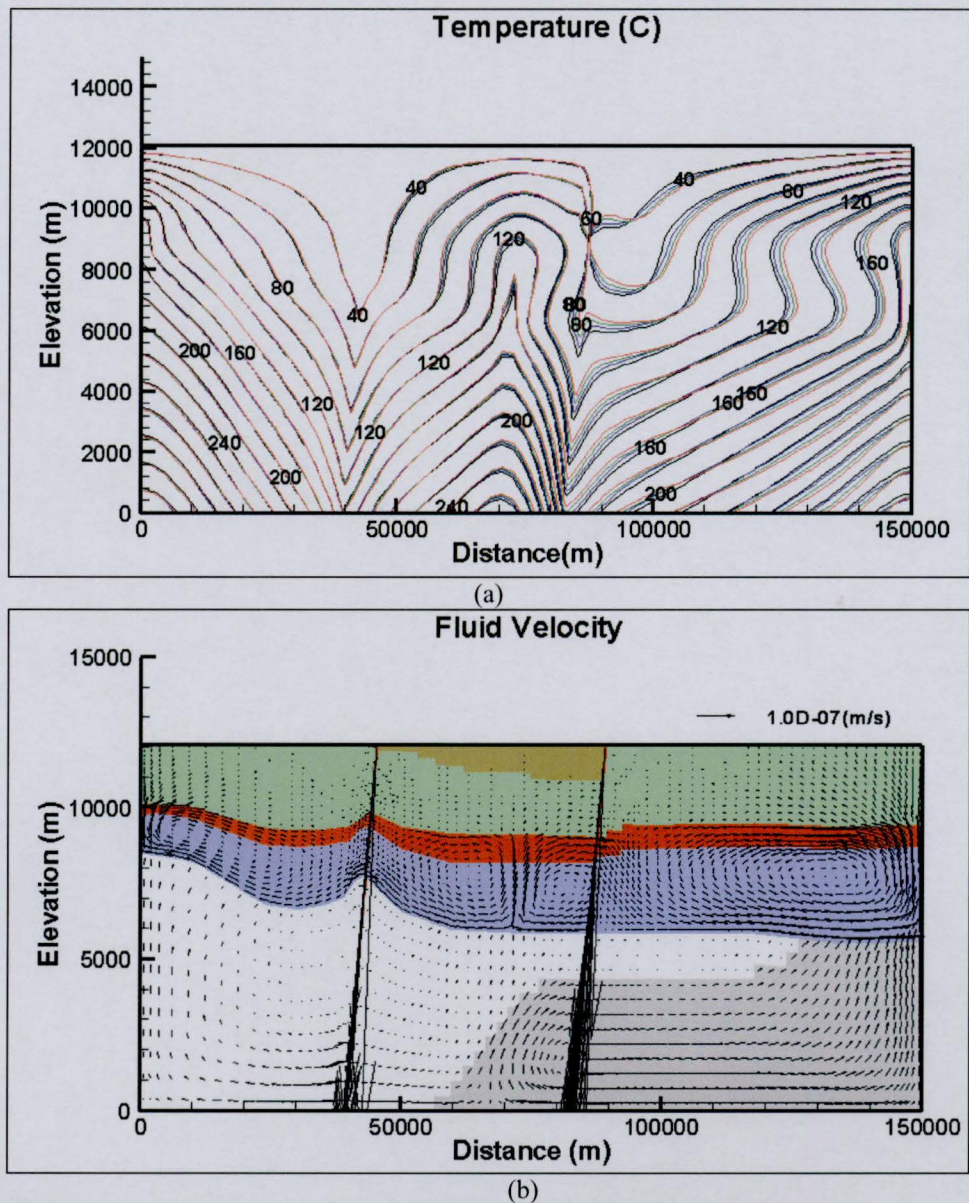
**Figure 4.36 McArthur Basin. _Test 3_. (a) Temperature distribution for time level numbers 1600 (black), 5900 (blue), 10200 (green), and 14500 (red). (b) Fluid velocity field common for all these time levels.**

One can see that the isotherms practically retrieve themselves. A very similar picture is observed for any other phase of the cycle: Figure 4.37 shows the superimposed temperature distributions and correspondent fluid flow pattern for time level numbers 2200, 6500, 10800, and 15100, when the Emu Falt acts as a discharge zone. The slight discrepancy in the isotherms can be attributed to the accuracy of the estimation of the auto-oscillation period.
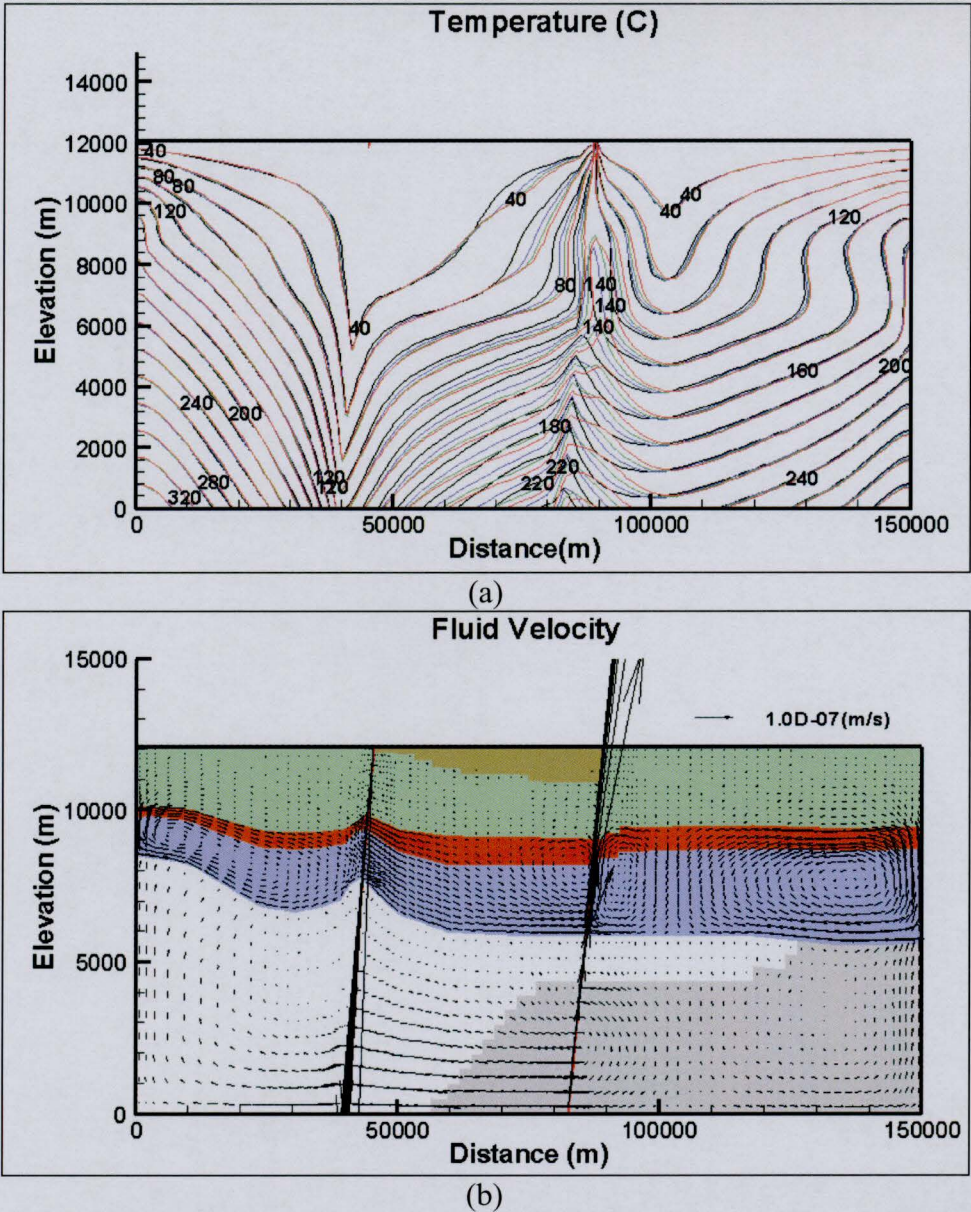
**Figure 4.37 McArthur Basin.** *Test 3*. **(a) Temperature distribution for time level numbers 2200 (black), 6500 (blue), 10800 (green), and 15100 (red). (b) Fluid velocity field common for all these time levels.**

The periodic character of this hydrothermal system is even more evident when the flow characteristics at a paricular point are considered. Thus, in Figure 4.38 the time dynamic of the vertical component of the fluid velocity and fluid temperature at the outlet of the Emu Fault are shown; both quantities are clearly periodical. This figure also allows us to evaluate the duration of the discharge regime of the fault (about 8.21 million years) which is 3 times longer than the period of recharge (2.74 million years). Thus, most part of the period the fault works as a discharge zone with the peak of temperature (about $63\,^{0}C$) falling at the moment when the fault switches from recharge to discharge.
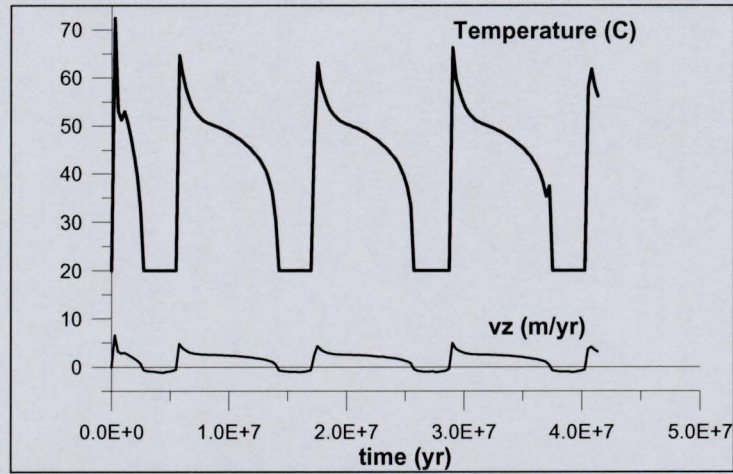
**Figure 4.38 McArthur Basin.** *Test 3*. **Vertical component of the fluid velocity and fluid temperature at the outlet of the Emu Fault.**

The next three tests were performed under the assumption, that $\rho_f = \rho_B(P, T, S)$ (equation (2.17)). In line with the publication, the salinity field was assumed not to be affected by the fluid flow and to maintain the initial distribution, which increases linearly with depth reaching 20wt% at 5*km*. The salinity below this level was set uniformly equal at 20wt% (Figure 4.39).
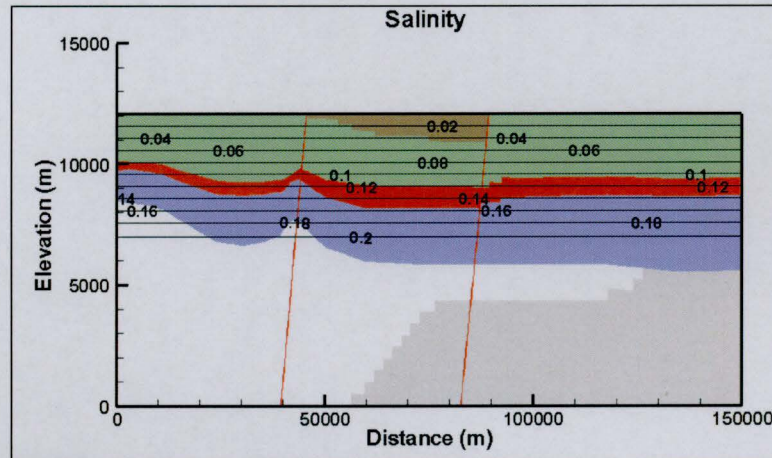


**Figure 4.39 McArthur Basin.** *Tesst 4, 5, and 6*. **Salinity distribution which is presumed not to be affected by fluid flow during simulation.**

**Test 4** was performed with the constant fluid viscosity coefficient: $\mu = const = 5 \cdot 10^{-4} (kg\, m^{-1}\, s^{-1})$.

**Test 5** involved the dependence of $\mu$ on temperature: $\mu = \mu_B(T, S)\big|_{S=0}$ (equation (2.18)).

In **Test 6**, viscosity was considered as a function of both temperature and salinity, expressed by equation (2.18).

Figure 4.40 shows fluid velocity fields and temperature distributions obtained for these case studies. Solutions in Test 4 and Test 5 come to the steady state, so the steady-state flow pattern and temperature field are shown. In Test 6, the steady state is not achieved, although the flow pattern in the whole section on the right of the Tawallah Fault is practically unchanged. Only the flow in the section of the aquifer on the left of the Tawallah Fault changes cyclically affecting the value of the velocity vectors in the fault to a very slight degree.

The pattern of the flow obtained in tests 4-6 disagree with the one presented in the publication, however, as has already been mentioned, it is not quite clear if the fluid viscosity was affected by temperature and salinity and the fluid density dependence on salinity was taken into consideration for this particular scenario.

However the fulfilled tests allowed us to make an observation. One can see that in the last three case studies, the presence of the saline layer drastically changed the pattern of the flow, actually reversing its direction. The picture is the same, no matter what parametrization of the viscosity is used. It means that the immovable saline layer has a major influence first of all on the fluid density which seems to be the factor controlling the fluid flow pattern in the section with the rock properties shown in Table 4.6. To make more accurate conclusions about the salinity effect on the groundwater flow in this profile, it is necessary to eliminate the simplifying assumption about the immobility of the dissolved salt, which is beyond the scope of this numerical study.

## Test 4

**Fluid Velocity**

**Temperature (C)**

## Test 5

**Fluid Velocity**

**Temperature (C)**

## Test 6
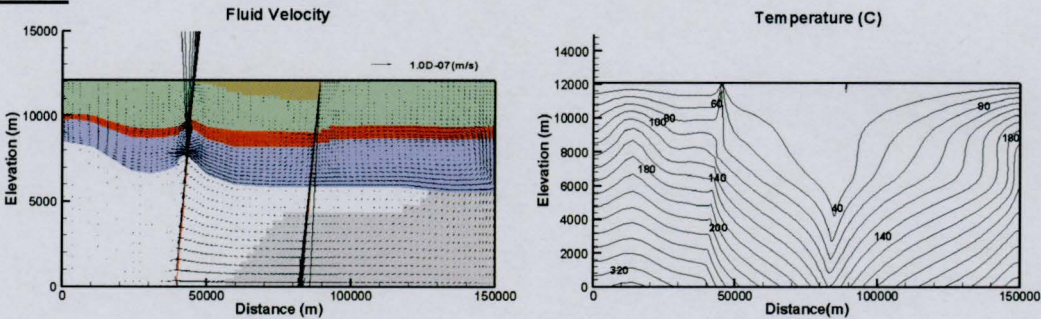
**Fluid Velocity**
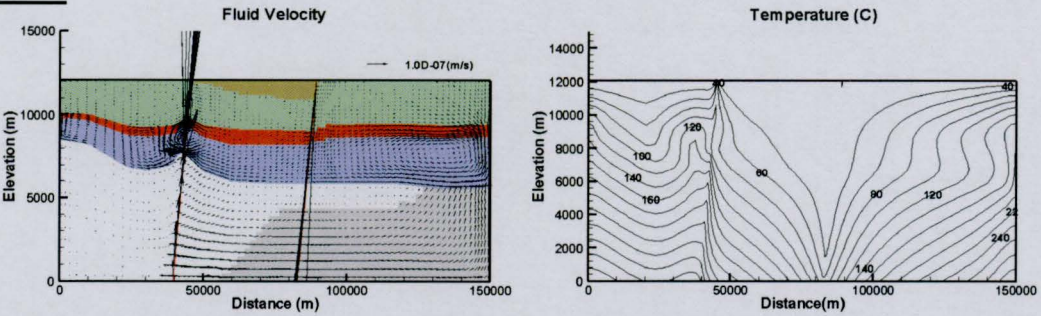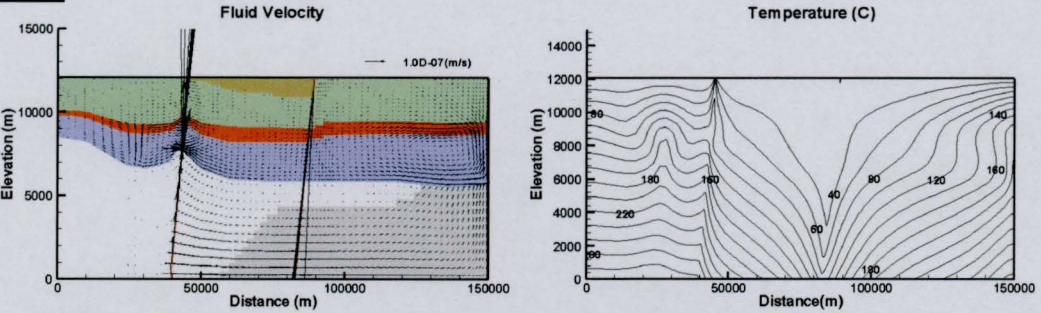
**Temperature (C)**

**Figure 4.40 McArthur Basin. _Test 4, 5, and 6_. Fluid velocity field and temperature distribution.**

## 4.4 Coupled heat and mass transport (free thermohaline convection)

Dense brines formed by dissolution of salt-rich layers in a sedimentary basin introduce an additional source of density variation, which, along with the double advective/diffusive phenomena (Phillips, 1991) significantly affects heat and mass transfer and groundwater flow.

The last group of tests presented in this section aimed to verify the validity of simulation of coupled heat-mass transport by the developed model. For this purpose, the results of experimental and numerical studies on different aspects of double-diffusive convection in porous media were examined (Nield, 1968; Griffiths, 1981; Trevisan and Bejan, 1987; Trevisan and Bejan, 1990; Evans et al., 1991; Rosenberg and Spera, 1992; Sarkar et al., 1995; Schoofs et al., 1999; Simmons et al., 2001; Malki-Epshtein et al., 2004). From the point of view of the model testing, the paper by Rosenberg and Spera (1992) seemed to be the most useful, as it reports, in detail, results of the numerical simulation for a range of different initial and boundary conditions and model parameters.

Rosenberg and Spera studied numerically free convection in porous media heated from below with two opposing sources of buoyancy. The fluid density is assumed to be affected both by temperature, $T$, and concentration of the dissolved substance, $S$ expressed as the mass fraction of the solute in the solution. The equation of state for fluid density is expressed as:

$$\rho = \rho_0 (1 - \alpha T + \beta S),$$

<div align="right">Equation 4.40</div>

where the coefficient of thermal expansion, $\alpha = 8 \cdot 10^{-4} (^0 C^{-1})$ and the coefficient of chemical expansion, $\beta = 0.8$ (*mass fraction*$^{-1}$). In this set of numerical experiments, dispersion effects are not taken into account, therefore $\alpha_L$, $\alpha_T$, $\alpha_L^S$, and $\alpha_T^S$ are considered zero.

The convective dynamics of the thermohaline system is governed by four dimensionless parameters: the thermal Rayleigh number ($Ra_T$), the Lewis number ($Le$), $\phi^*$, and the buoyancy ratio ($R_\rho$). The parameters are defined as:

$$Ra_T = \frac{g\alpha\Delta THk\rho_0}{\mu\kappa}$$

<div align="right">Equation 4.41</div>

$$Le = \frac{\kappa}{nk_S}$$                                                                                                      Equation 4.42

$$\phi^* = \frac{n}{\sigma}$$                                                                                                          Equation 4.43

$$R_\rho = \frac{\beta \Delta S}{\alpha \Delta T}$$                                                                                                       Equation 4.44

Here $\kappa = \dfrac{\lambda_e}{\rho_f c_f}$ is the effective thermal diffusivity and $\sigma = n + (1-n)\dfrac{\rho_s c_s}{\rho_f c_f}$

represents the ratio of the heat capacities of the saturated porous medium and the fluid.


The results of the simulations by Rosenberg and Spera, which we attempted to reproduce here, are reported to be performed in a square domain with $Ra_T = 600$, $Le$ =20, and $\phi^* = 1$ at different $R_\rho$. The value of $\phi^* = 1$, however, seems not to be physically justified, as it implies either porosity, $n$, equals to 1 or $\rho_s c_s = 0$. In the first case, when no solid matrix is present, the equation of motion in the form of Darcy's law is not applicable. The second option means that either the solid matrix density or heat capacity is zero, which, strictly speaking, is not so. However, from the point of view of comparison of the numerical algorithm output with one produced by an independent code, this arguable value of the parameter can still be used.

We reproduced three blocks of the tests for the time-dependent problem; these tests are classified by different types of boundary and initial conditions for the dissolved substance. Keeping the nomenclature of the conditions adopted by the authors, the blocks are:

Block 1:

'Salted from below' boundary condition: the top and bottom boundaries are kept at a constant composition (zero at the surface and $S_b$ at the bottom); no salt flux is allowed through the side walls.

'Empty box' initial condition: the initial salinity distribution is assumed to be uniformly equal to the value at the top boundary, which has been set zero.

Block 2:

'Salted from below' boundary condition.

'Layered box' initial condition: the lower half of the domain has uniform salinity $S_b$, while the salinity in the upper half is zero.

Block 3:

'No flux' boundary condition: all four boundaries are impermeable to the flux of the dissolved substance.

'Layered box' initial condition.

Thermal boundary and initial conditions are common to all the numerical experiments: no heat flux is allowed through the side boundaries, while horizontal boundaries are kept at constant temperature: $T_t = 20\,^0 C$ at the top and $T_b = 485.49\,^0 C$ at the bottom. For the physical constants listed in Table 4.7, $T_t$ and $T_b$ correspond to $Ra_T = 600$.

| Parameter | Value | Unit |
|---|---|---|
| thermal expansion, $\alpha$ | $8 \cdot 10^{-4}$ | $^0 C^{-1}$ |
| chemical expansion, $\beta$ | 0.8 | $mass\ fraction^{-1}$ |
| dynamic viscosity, $\mu$ | $1.1398338 \cdot 10^{-3}$ | $kg/(m \cdot s)$ |
| porous layer depth, $H$ | 11000 | $m$ |
| reference value of fluid density, $\rho_0$ | 1000 | $kg/m^3$ |
| heat capacity of the fluid, $c_f = c_{f,0} = const$ | 4174 | $J/(m^3 \cdot\,^0 C)$ |
| effective thermal conductivity of the saturated porous medium, $\lambda_e$ | 2.5 | $J/(m \cdot s \cdot\,^0 C)$ |
| effective thermal diffusivity $\kappa = \dfrac{\lambda_e}{\rho_0 c_{f,0}}$ | 5.99 | $m^2/s$ |
| permeability, $k$ | $10^{-14}$ | $m^2$ |
| porosity, $n$ | 0.3 | - |
| molecular diffusivity, $k_s$ | $9.98 \cdot 10^{-8}$ | $m^2/s$ |

**Table 4.7 Free thermohaline convection test: model parameters**

All four boundaries are impermeable to flow; the initial distribution of the hydraulic head is uniformly equal to $H$.

## 4.4.1  'Salted from below' boundary conditions, 'empty box' initial condition

*Low* $R_\rho$

Rosenberg and Spera (1992) found that 'for low $R_\rho$ values, the systems evolve to a convective steady-state consisting of four side-by-side convection cells' ( see Rosenberg and Spera, 1992: p.1267).  Figure 4.41 shows the fluid velocity field and the temperature distribution at convective steady-state calculated by our model for $R_\rho$ =0.25.  $S_b$ was set at 0.1141 for this test.  Our result confirms the result of Rosenberg and Spera.
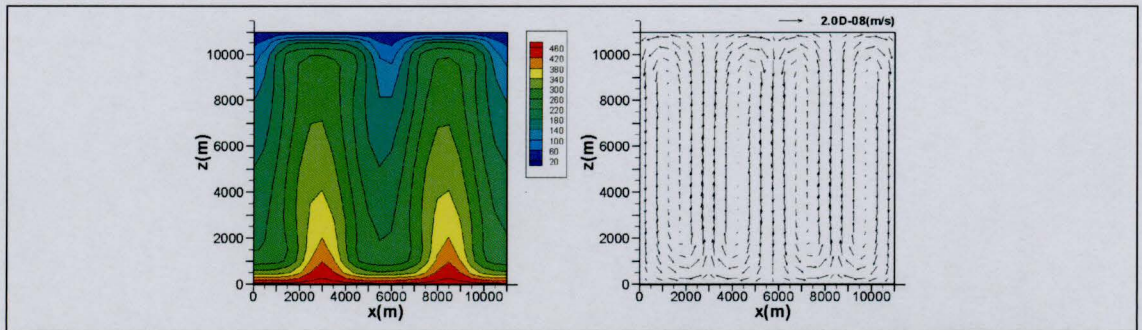


**Figure 4.41 Free thermohaline convection test. 'Salted from below' boundary conditions, 'empty box' initial condition. $R_\rho$ =0.25. Steady-state temperature distribution and fluid velocity field.**

*Intermediate* $R_\rho$

Numerical experiments showed that at intermediate $R_\rho$ values (simulations were performed for $R_\rho$ =0.5 and $R_\rho$ 0.75), the flow remains unsteady: temperature fields change periodically. The result is consistent with Rosenberg and Spera's (1992: p. 1268): 'For intermediate $R_\rho$ , convection evolves to a chaotic state in which regions of sharp temperature and salinity gradient are highly mobile in time and space'.

### High $R_\rho$

The next numerical experiment was run with $R_\rho = 3.0$. For this high $R_\rho$ value, $S_b$ was set equal to 0.3 with the consequent change in the thermal boundary condition at the lower boundary, $T_b = 120\,^0 C$ (to have $Le=20$), and the permeability value, $k=4.6548 \cdot 10^{-14}\ m^2$ (to keep $Ra_T = 600$).

The authors of the paper under discussion state that 'at high $R_\rho$, convection is characterized at early time by flow confined to the upper part of the domain. The system eventually evolves to a steady-state where the velocity is zero everywhere and the temperature and salinity fields are conductive' (Rosenberg and Spera, 1992: p.1268). Figure 4.42 shows our results: the fluid velocity field superimposed onto the salinity distribution at consecutive time instants outputted every 200 time steps (the simulation was performed with the time step, $\Delta t = 10^5$ days). One can see that the flow does take place in the upper part of the domain where the fluid is less saline. The figure also shows that the fluid circulation is gradually dying away.
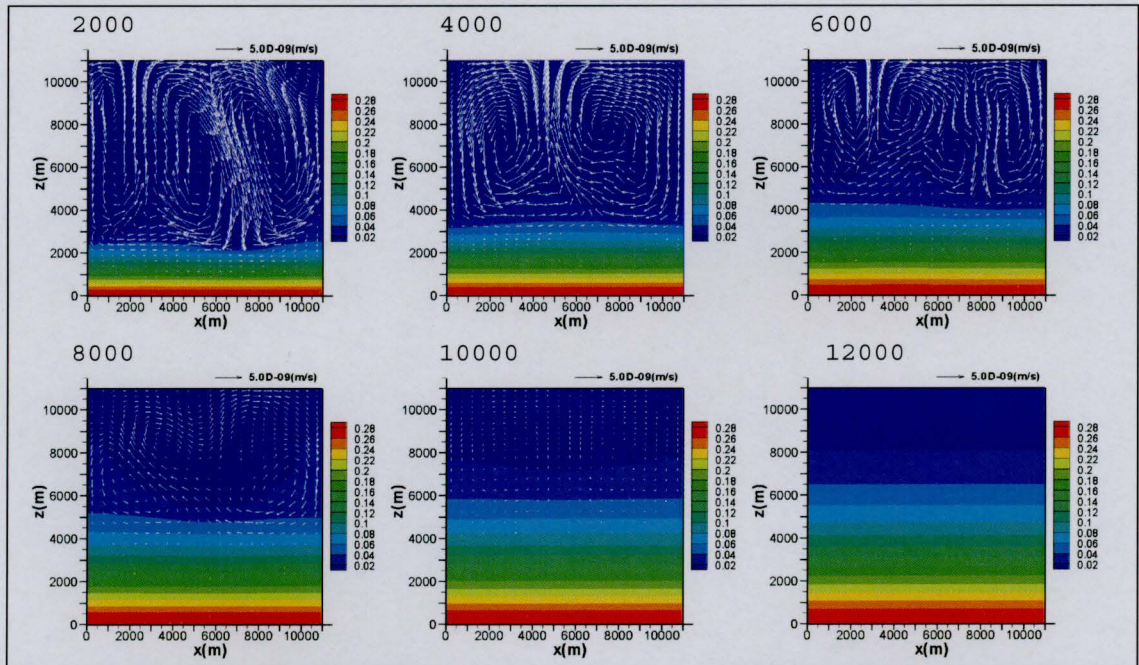


**Figure 4.42 Free thermohaline convection test. 'Salted from below' boundary conditions, 'empty box' initial condition.** $R_\rho = 3.0$. **Temporal salinity distribution and fluid velocity field. At early times, the fluid flow is confined to the upper part of the domain, it gradually dies away with the salinity distribution becoming conductive. The numbers denote the time level number (the time step used for the simulation, $\Delta t = 10^5$ days).**

Figure 4.43 represents the temperature field transition to the conductive state.
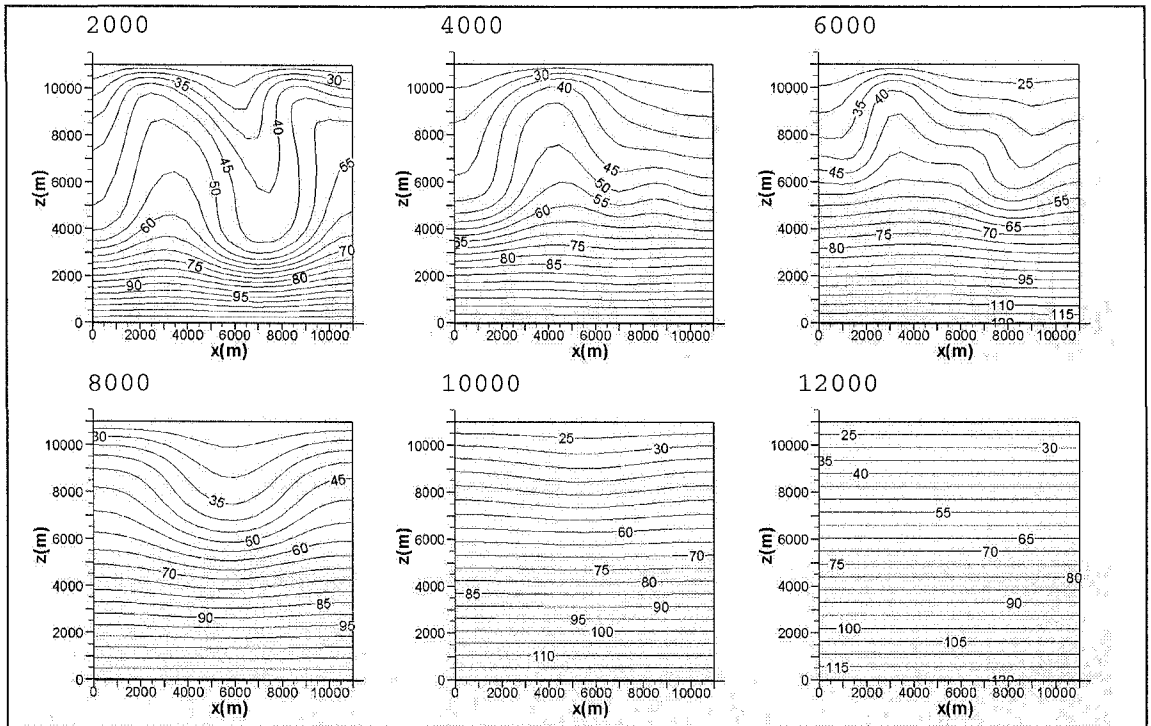


**Figure 4.43 Free thermohaline convection test. 'Salted from below' boundary conditions, 'empty box' initial condition.** $R_\rho$ **=3.0. Temperature field transition to the conductive steady state. The numbers denote the time level number (the time step used for the simulation,** $\Delta t = 10^5$ **days).**

It can also be noted that temperature reaches the conductive state earlier than salinity (compare Figure 4.42 and Figure 4.43 at time level 12000), which is natural, as the thermal diffusivity is higher than the diffusivity of salt.

## 4.4.2 'Salted from below' boundary conditions, 'layered box' initial condition

*Low* $R_\rho$

The numerical experiment performed at $R_\rho$ =0.25 revealed that the thermohaline system comes to the convective steady-state. This result is similar to one obtained by Rosenberg and Spera (see Rosenberg and Spera, 1992: p.1268).

*Intermediate* $R_\rho$

On p.1268 (Rosenberg and Spera, 1992) we find: 'At intermediate $R_\rho$ values, the system is characterized at early time by oscillatory convection in each

composition layer. These layers are separated by a highly mobile interface which oscillates between concave up and concave down… At later time, this interface becomes highly distorted, and convection becomes chaotic'. In Figure 4.44 we show our result which supports this statement. The simulation was run with $R_\rho$ =0.5 ( $S_b$ =0.2282, $T_b$ =485.49 $^0C$ , $k$=10$^{-14}$ $m^2$ ). The fluid velocity field is superimposed onto the salinity distribution to show the fluid flow disposition relatively to the composition layers. The calculation was performed with the time step, $\Delta t$ =10$^5$ days. The snapshots were outputted every 100 steps, starting from the initial state.
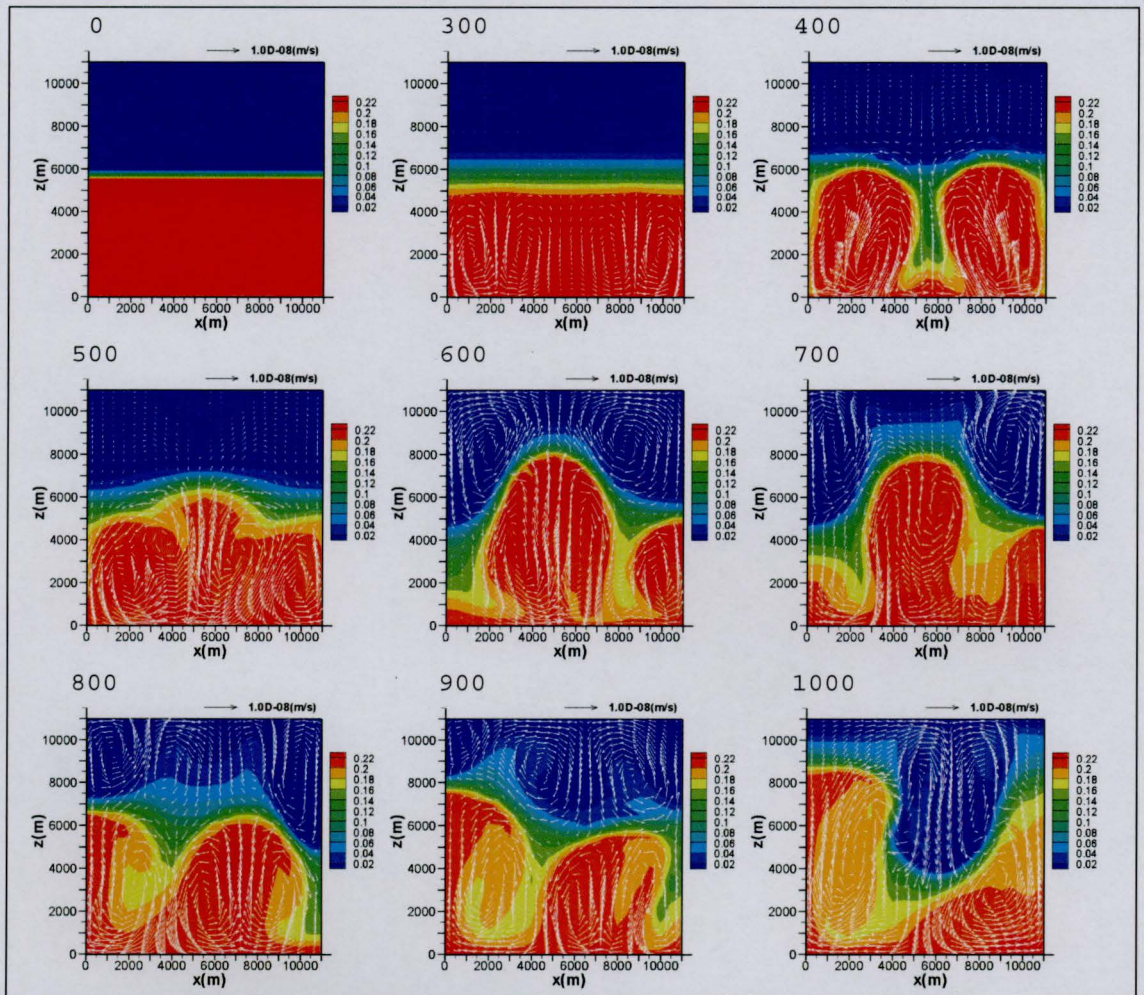


**Figure 4.44 Free thermohaline convection test. 'Salted from below' boundary conditions, 'layered box' initial condition.** $R_\rho$ **=0.5. Temporal salinity distribution and fluid velocity field at early time. Convection takes place in each composition layer; the interface between the layers becomes distorted. The numbers denote the time level number (the time step used for the simulation:** $\Delta t$ **=10$^5$ days).**

In the publication (Rosenberg and Spera, 1992), the authors present the result of the simulation performed with $R_\rho$ =0.75 showing dimensionless velocities,

temperature and salinity field plots for three consecutive time instants (see Figure 4.45). We also ran the simulation for this $R_\rho$ value, and

Figure 4.46 contains the result presented in the format similar to one adopted in the paper. It is clear that the fluid flow pattern, temperature and salinity distributions are very similar to ones shown by Rosenberg and Spera, even though we used a coarser grid (748 elements against 1120 reported in the paper under discussion).
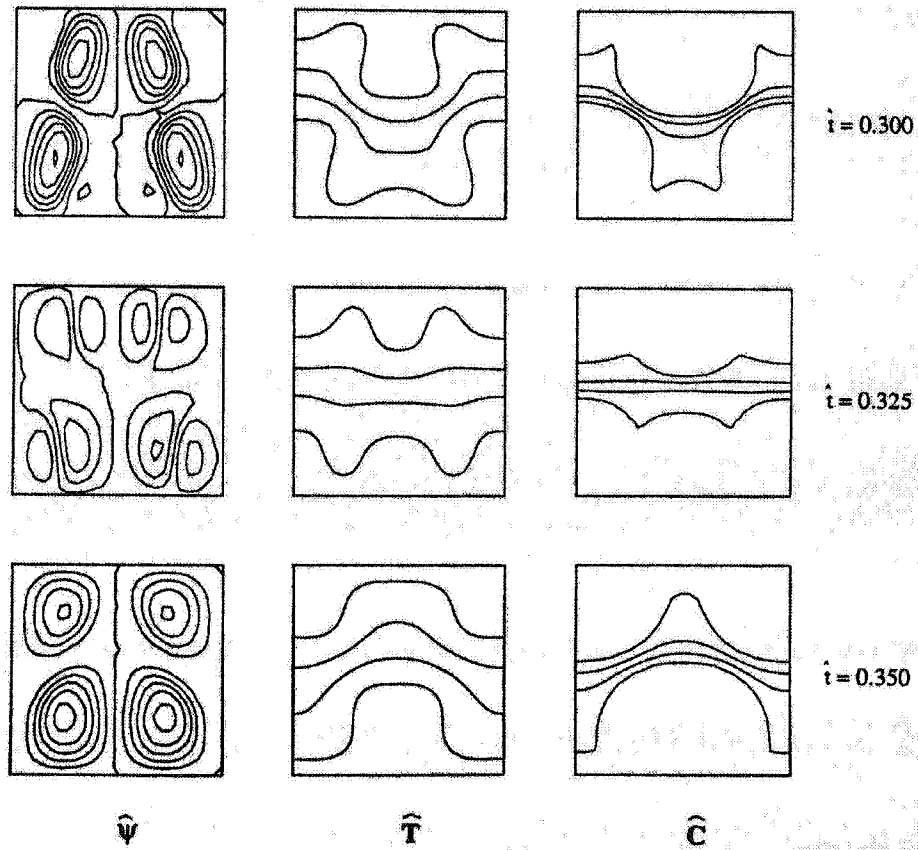


Figure 4.45 Free thermohaline convection test. (a) Velocity, (b) temperature, and (c) salinity field plots at $\hat{t}$ =0.3-0.35 for porous media heated from below with the 'salted from below' boundary condition and 'layered box' initial condition on composition. The parameters for this problem are $Ra$=600, $Le$=20, $\sigma$ =1 and $R_\rho$ =0.75. The contour interval is 2 for $\hat{\psi}$ and 0,2 for $\hat{T}$ and $\hat{C}$ (dimensionless streamfunction, temperature and concentration of dissolved species respectively). (From Rosenberg and Spera, 1992).
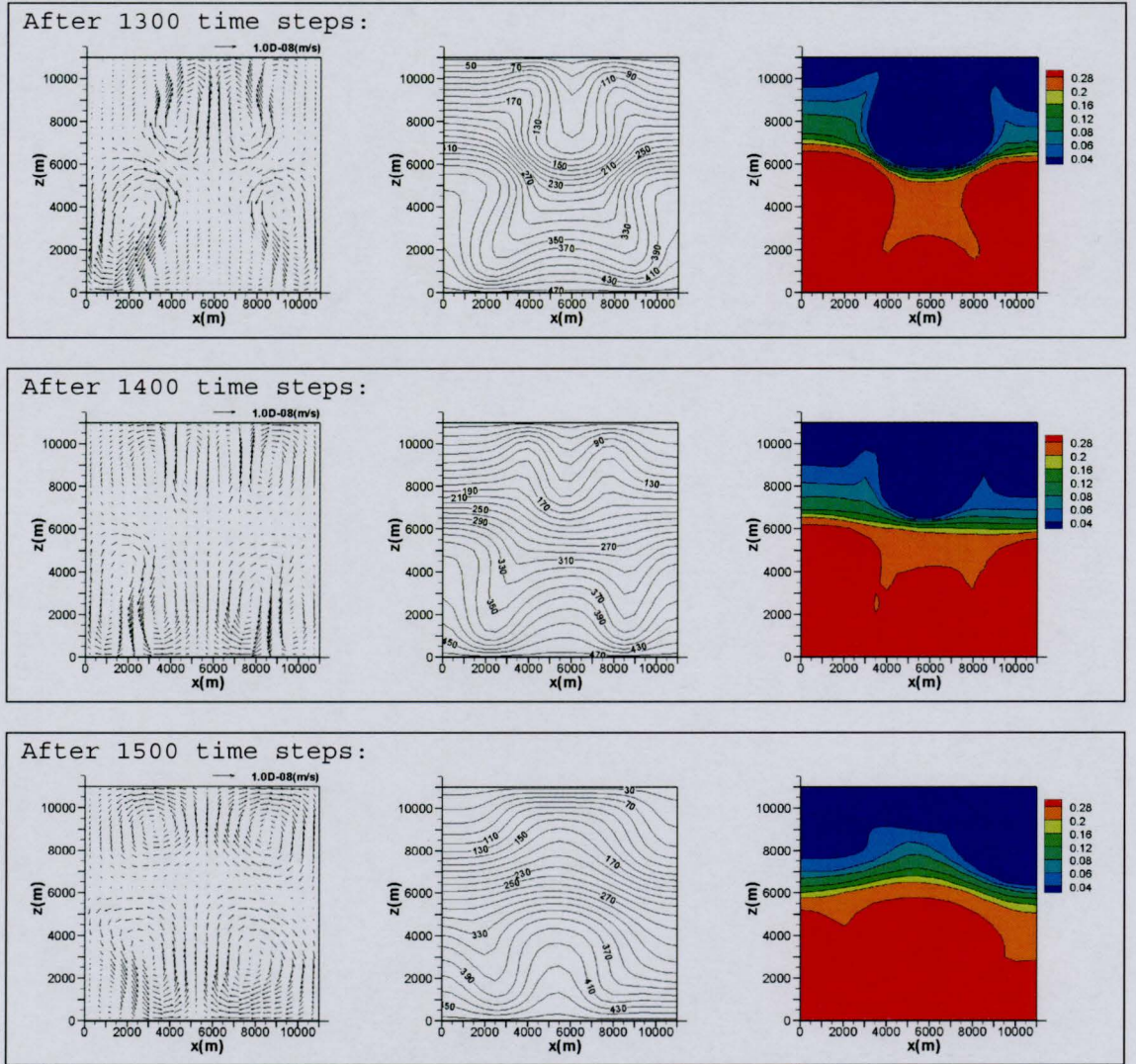
**Figure 4.46 Free thermohaline convection test. 'Salted from below' boundary conditions, 'layered box' initial condition.** $R_\rho$ **=0.75. Calculated elocity, temperature and salinity fields, comparison with (Rosenberg and Spera, 1992). The numbers denote the time level number (the time step used for the simulation was** $\Delta t = 10^5$ **days).**

### High $R_\rho$

This test was run for $R_\rho$ =1.0 (Rosenberg and Spera report the range from 0 to 1.5 for this set of boundary and initial conditions). We obtained that the system comes to a static steady-state (no fluid motion, conductive temperature and salinity), which agrees with the paper result.

### 4.4.3 'No flux' boundary conditions, 'layered box' initial condition

As in the previous cases, at low $R_\rho$ value ($R_\rho$ =0.25), the system comes to the convective steady-state. The picture is similar to Figure 4.41, so it is not repeated here. This result is in agreement with the publication under discussion.

According to the paper (see Rosenberg and Spera, 1992: p.1270), at $R_\rho$ >1, the system evolves to a static quasi-steady-state: first, temperature and salinity fields become conductive with no fluid motion observed; then, after the salinity field homogenizes, the system evolves to the convective steady-state. Supporting this observation, Figure 4.47 shows the temperature field evolution. It does come to the conductive state, when the temperature is a linear function of the vertical coordinate and isotherms are horizontal. Then, the lines become deformed and the field achieves the steady-state showing a sequence of vertically elongated convective cells.

This numerical test was run for $R_\rho$ =1.25 and slightly lower $Ra_T$ and *Le* values ($Ra_T$ =592.06 and *Le*=19.88) which resulted in a lesser number of the convective cells formed (three against four in the previous case studies which led to the convective steady-state). The reason for that was that at high $Ra_T$ values, fluid velocities significantly increase drastically raising the grid Peclet number, especially for salinity. In the current case study, when salinity gradient is high, it causes numerical instability. No flux boundary conditions at all four boundaries also contribute to that demanding the grid detalization in the boundary layers. However, the grid condensation needs decrease in the time step (to keep the Courant number within the stability range) and would result in the significant increase in computing time which we tried to avoid.
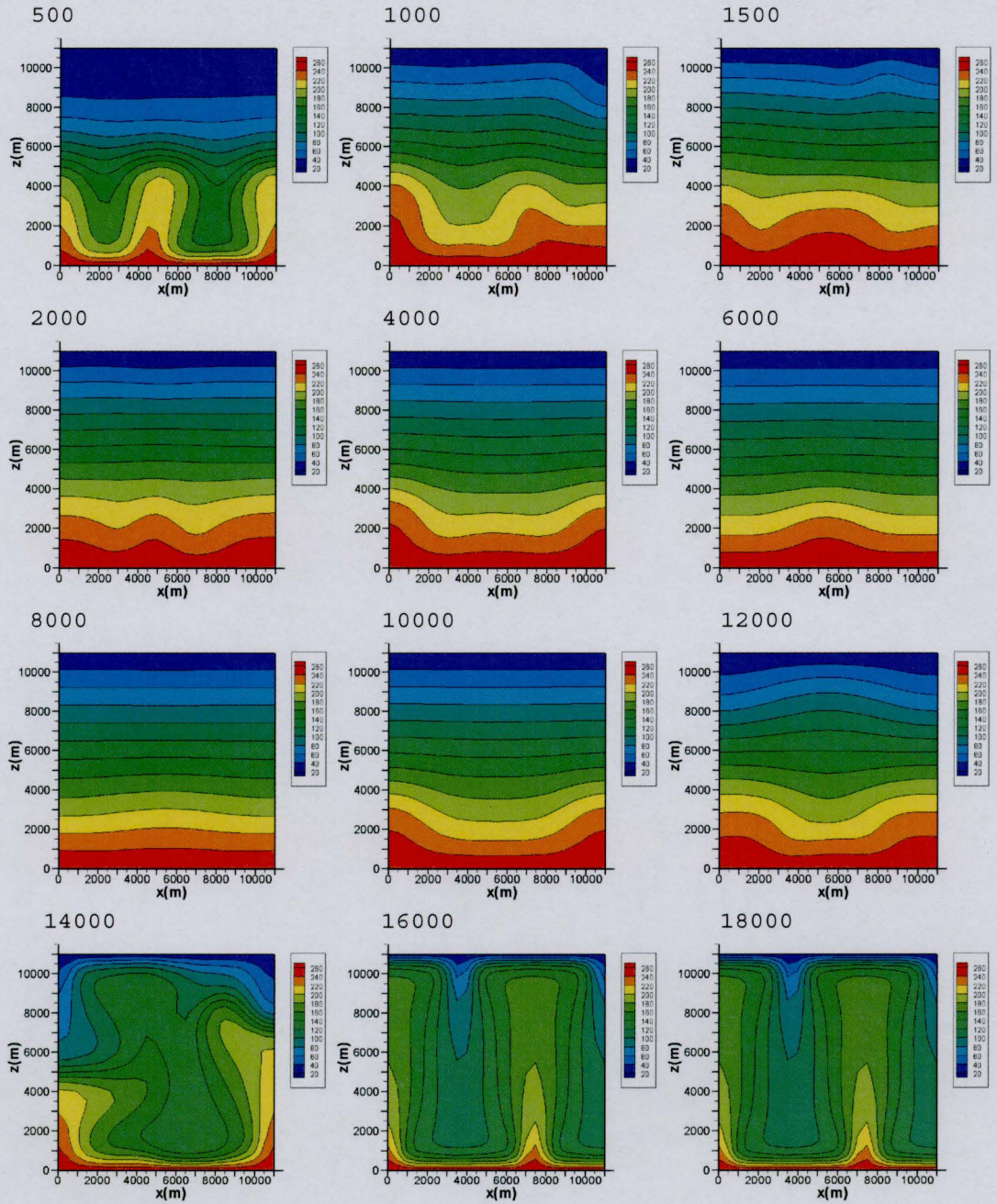
**Figure 4.47 Free thermohaline convection test. 'No flux' boundary conditions, 'layered box' initial condition.** $R_\rho$ =1.25. **Temporal temperature distribution. System evolves to a static quasi-steady-state: first, the temperature and salinity fields become conductive, then, the system evolves to the convective steady-state. The numbers denote the time level number (the time step used for the simulation was** $\Delta t = 10^5$ **days).**

# 5 Zambian Copper Belt. Geology

The ZCB is one of the world's largest sediment-hosted stratiform copper systems. It forms the southern portion of the Central Africa Copperbelt (Figure 5.1) and contains numerous deposits, many of them giant (Hitzman et al., 2005) (Figure 5.2).
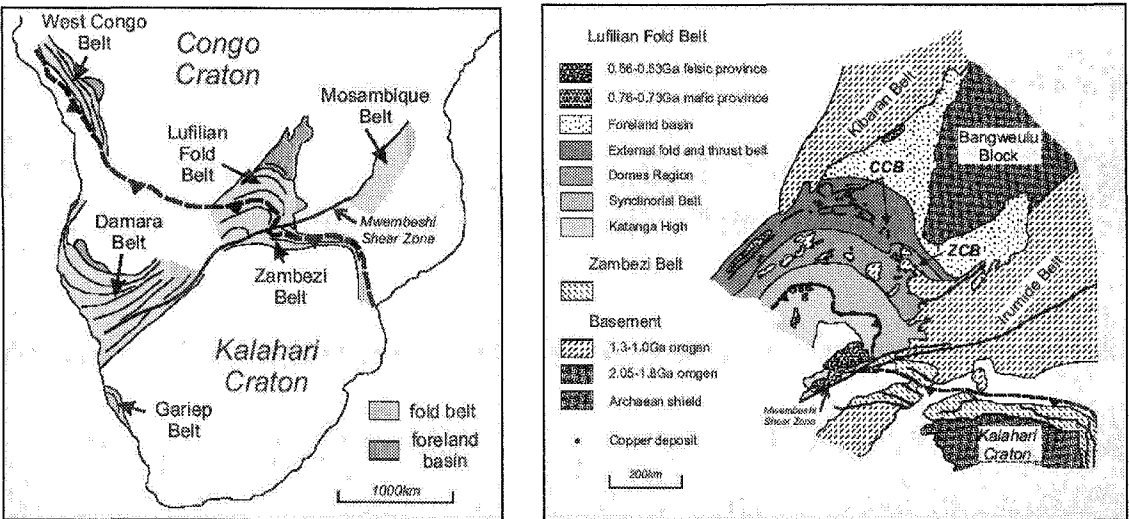


**Figure 5.1 Tectonic setting and structural architecture of the LFB. Shown in the heavy dashed lines is the trace of a suture zone between the Congo and Kalahari cratons, as interpreted by Porada and Berhorst (2000). (a) Pan-African system of central and southern Africa (modified from Kampunzu and Cailteux, 1999; Porada and Berhorst, 2000). (b) Tectonic zoning in the LFB. This map differs from those previously published in that basement inliers of the ZCB are included within the Domes Region, rather than the External Fold and Thrust Belt (modified from Kampunzu and Cailteux, 1999) (from Selley et al., 2005).**
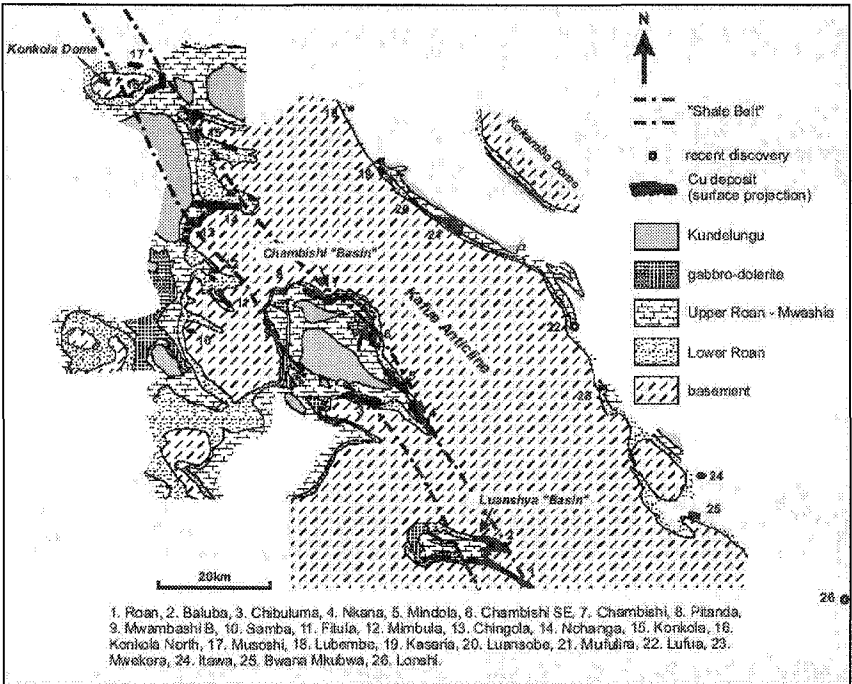


**Figure 5.2 Geology and ore distribution in the ZCB. Modified from Darnley (1960), Mendelsohn (1961), Annels (1984), Fleischer (1984), Sweeney and Binda (1989) (from Selley et al., 2005).**

117

These have been commonly recognized to be a diagenetic product of a large-scale (basin- or sub-basin-scale) fluid flow system. However, there is still no unified opinion on some aspects of ore formation. Thus, the sources of metals, sulfur, and metal-bearing fluid, paths of the fluid delivering metals and sulfur to deposition sites, the mechanism impelling fluid flow, the mechanism of sulfide precipitation are still debated. The problem is accentuated by the fact that the ZCB shares distinctive elements common for all sediment-hosted stratiform copper deposits, but also has some unique characteristics. One of the fundamental differences is a significantly smaller volume of red-bed sediments (compared to well-studied Polish Kupferschiefer and White Pine deposits) to be accountable for such considerable copper accumulation in the economic zones of the ZCB deposits. Another feature distinguishing the African Copperbelt is the wide range of styles and stratigraphic locations of deposits, which could, according to Hitzman et al. (2005), be a result of a long history of mineralization and also of the massive size of the hydrological framework.

This suggests that the model of ore formation in the ZCB would differ from those proposed for better studied sediment-hosted stratiform copper deposits. Thus, for example, for the White Pine district, Swenson et al. (2004) modeled a scenario of early diagenetic copper deposition by compaction-driven fluid flow in a hydrologically open basin. In this model, the cupriferous brine, formed within the basal red-bed aquifer, is focused towards the thinning portion of the basin fill in response to mechanical loading during deposition of overlying sequences. This model cannot be directly transferred to the ZCB for several reasons. Firstly, the small volume of the red-bed aquifer requires an alternative metal source; cupriferous components of the metamorphic basement, for example. If so, we should also envisage a mechanism transporting copper from this source to a trap site. Secondly, the variability in ore body locations must be a result of a more intricate pattern of fluid flow. And finally, the compaction-driven discharge cannot account for late diagenetic to early orogenetic mineralization recorded at various stratigraphic levels. Considering this reasoning, it was decided to investigate the potential of density-driven flow as an ore-forming mechanism in the ZCB. The fluid density variations are considered to be caused by dissolution of halite bodies, the former presence of which is argued below, and the existing geothermal gradient. Magmatism is discounted as a thermal driver as there is no evidence for syn-extensional volcanic or intrusive activity. The one exception is an episode of mafic intrusives into the hangingwall succession that are too limited in extent to have significant hydrological implications (Selley et al., 2005).

The ZCB is hosted by the Neoproterozoic Katangan basin. As with other deposits of this type, the Kupferschiefer (the Permian basin of Europe (Vaughan et al., 1989)), Kodaro-Udokan (the Paleoproterozoic basin of Siberia (Volodin et al., 1994)), Dzhezkazgan (the Devonian to Carboniferous Chu-Sarysu basin of Kazakhstan (Gablina, 1997)), White Pine (the Middle Proterozoic Mid-Continent Rift of the United Stattes (Mauk et al., 1992)), three main litho-stratigraphic architectural elements can be distinguished: (1) a basal red-bed sequence; (2) evaporites, including thick bedded massive salt; (3) reduced shales and carbonates. The stratigraphic arrangement of these units varies from deposit to deposit (Hitzman et al., 2005); in the ZCB, the coarse-grained red-beds are overlain by a marine sequence with mixed permeability and oxidation state (a detailed description of the ZCB stratigraphy follows in Section 5.1).

The conceptual model is based on the western ZCB, where the Roan basin architecture is best constrained (Section 5.1.1) and Ore Shale facies are best developed (Selley et al., 2005). The section inherits its configuration from early rift geometry and is basically oriented normal to the axis of main depocentres. Though the key elements of the basin geometry, compartmentalized fault bounded Lower Roan sedimentation, layer cake configuration of the overlying marine strata, are justifiable (Sections 5.1.1 - 5.1.3), the section is schematic: the architecture and thickness of the Upper Roan and Kundelungu (Section 5.1.4) units are conjectural: positioning and thickness of former salt horizons is mainly based on the distribution of polylithic breccia bodies attributed to salt dissolution/mobilization (Annels, 1984; Selley et al., 2005).

Section 5.2 explains the choice of rock property values: permeability, degree of anisotropy, porosity, density, compressibility, heat capacity, thermal conductivity and dispersivity. It should be noted that only the primary values are considered and chemically enhanced changes in the characteristics are ignored for simplicity.

As discussed in Section 5.1.2, the presence of large volumes of breccia within the Roan Group is interpreted to reflect the former presence of halite bodies. Section 5.3 covers some aspects of the envisaged evolution of Roan Salt, and the way salt dissolution is parametrized in the model.

## 5.1 Hydrostratigraphy

The stratigraphic architecture of the ZCB is consistent with its development as an intra-continental rift basin (Miller, 1983; Munyanyiwa et al. 1997) and initial sedimentation was closely linked to the evolution of syn-depositional fault arrays. The interpreted hydrostratigraphy of the section, shown in Figure 5.3, was used for most of the simulations presented in the next chapter, with slight modification for particular case studies.

The Archaean-Mesoproterozoic basement, represented by a multiply reworked assemblage of metagranite, migmatite, metavolcanic and metasedimentary units is overlain by the Katangan Supergroup, the preserved remnants of Neoproterozoic supracrustal rocks. A four-fold stratigraphic subdivision of the Katangan Supergroup is commonly accepted (Mendelsohn, 1961; van Eden and Binda, 1972; Garlick and Fleischer, 1972; Binda and Mulgrew, 1974; Clemmey, 1976; Lefebvre, 1989; Cailteux, 1994; Cailteux and Kampunzu, 2002). This includes (from base to top): (1) Lower Roan Group; (2) Upper Roan Group; (3) Mwashia Group; (4) Lower and Middle Kundelungu Group.

In summary, the Katangan succession records a transition from fluvial/alluvial to restricted marine or large-scale lacustrine deposition environments; basically, coarse-grained terrigeneous units are succeeded by progressively finer-grained strata (Selley et al., 2005). Carbonates and evaporates are abundant in the upper Lower Roan through the Upper Roan and into the lower Mwashia.

### 5.1.1 Lower Roan Group

The initial unit of the Lower Roan Group, the **Mindola Clastic Formation** (orange unit in Figure 5.3), records the _"rift initiation"_ stage. The sub-arkosic sandstones, conglomerates and rare siltstones which constitute this unit are accumulated in a series of narrow troughs and interpreted to record a distributed syn-depositional rift system (Selley et al., 2005). At the onset of sedimentation, these small fault-bounded depocenters were filled by material deposited in fluvial, alluvial, aeolian and fan-delta environments.

The *Copperbelt Orebody Member*, overlying the Mindola Clastic Formation, records abrupt transgression of the older compartmentalized subaerial deposits by layered marine sediments. The principal host to Co-Cu mineralization mainly consists of finely laminated dolomitic siltstone (Annels et al., 1983), but also includes facies variants such as carbonaceous shale, argillaceous sandstone and laminated dolomite (Garlick, 1961; Annels, 1974; Clemmey, 1974; Fleischer, 1984). The base of the Copperbelt Orebody Member records the *"rift climax"* stage (Sharp et al., 2000), when the evolution of extensive master faults caused an increase in the rate and the degree of subsidence and consequent interconnection of small isolated depocentres into a system of broader ones. This resulted in the layer-cake stratal configuration of the units overlying the Mindola Clastic Formation, which is typical for mature rift basins. From the point of view of the hydrological configuration of the basin, an important consequence of this stage was the sealing of the older fault network of secondary faults by fine-grained strata. To reflect the cyclicity within vertical profiles of the argillaceous facies of the Copperbelt Orebody Member (Clemmey, 1978; Sweeney and Binda, 1989), we distinguish two hydrostratigrafic units: "Ore Shale", marked red, and "Ore Shale/ Sandstone", colored yellow, which are characterized by different physical and hydrological properties.

## 5.1.2 Upper Roan Group

The Upper Roan Group shows a gradual accumulation of evaporitic carbonate strata at the stage of "post-rift" basin growth. At the beginning of this stage, reintroduction of coarse clastic supply followed by gradual depletion of source areas at the later periods (Prosser, 1993) are recorded by laterally extensive, upward-fining cycles of sandstone and siltstone followed by dolomite, algal dolomite, and local anhydrite. Dolomitic members were precipitated in evaporitic, sabkha conditions during a period of relative tectonic inactivity (Cailteux, 1994; Selley at al., 2005). Continued abating tectonism at the end of the cycle and resultant decreased rates of displacement along the master faults explain the sheet-like distribution of Upper Roan strata.

A distinguishing feature of the Upper Roan Group is the widespread presence of significant volumes of polylithic breccia. Breccia bodies occur not only within the Upper Roan strata but also at higher stratigraphic levels. Lack of bedding, the unsorted and ungraded character of the breccias and clast emplacements into overlying and

underlying stratigraphic levels suggest the former presence of significant evaporitic salt accumulation within the Upper Roan strata. Brecciation is attributed to salt dissolution/mobilization during post-depositopnal extension, rather than to deformation of the sequence during orogenesis (Selley at al., 2005). In the hydrostratigraphy, the Upper Roan Group is represented by two hydrological units: "Upper Roan Dolomites" (dark blue in Figure 5.3), which represents the carbonate strata, and, approximately 1km thick, "Upper Roan Salt" (white layer in Figure 5.3). Salt dissolution during breccia development would have generated a large volume of brine (Jackson et al., 2003), which, as it is shown later in Section 6.3, would dramatically affect the hydrothermal fluid flow in the basin.

### 5.1.3 Mwashia Group

In Zambia, the Mwashia Group is traditionally defined as a shale dominant sequence overlying the Upper Roan Group (Mendelsohn, 1961; Marjonen, 2000). It is subdivided into lower dolomitic and upper clastic sequences (Cailteux, 1994). To represent this subdivision, two hydrological units are assigned to the Mwashia Group: "Lower Mwashia Dolomitic Member" (colored light blue in Figure 5.3) and "Upper Mwashia Siliciclastic Member" (lilac layer).

### 5.1.4 Kundelungu Group

The Mwasia – Kundelungu contact is defined by the **Grand Conglomerate**, a glaciogenic diamictite containing interbeds of laminated siltstone and coarse lithic sandstone (Selley et al., 2005). The Grand Conglomerate stratigraphic layer is not shown in Figure 5.3, it was considered as part of the "Lower and Middle Kundelungu" unit.

The Kundelungu stratigraphy overlying the Grand Conglomerate is poorly known in ZCB, but generally consists of a sequence of carbonates and siltstones-mudstones separated into Lower and Upper Kundelungu by a diamictite marker termed the Petit Conglomerate. Due to lack of detailed information on this part of the stratigraphy a single "Lower-Middle Kundelungu" unit was ascribed to the hydrostratigraphy.

## 5.1.5 Faults

As mentioned before, the stratigraphic architecture of the rift basin was driven by the evolution of an array of syn-depositional faults. Two types of faults are distinguished in the hydrostratigraphy: master faults, which are about 300m wide and secondary faults, approximately 100m wide.

The secondary faults represent the older fault network which governed accumulation of the Mindola Clastic Formation. The master faults evolved during the "rift climax" stage as a result of further extension of the basin (Selley et al., 2005). The process resulted in linking of individual fault segments and further widening of these linked pre-existing faults. Therefore, primary faults are assumed to be three times wider. The chosen width for the primary conduits is consistent with (Garven et al., 2001; Simms and Garven, 2004).

To reflect the permeability loss with depth, the fault network is subdivided into 3 zones which decrease in permeability towards the base of the section. The boundary of the most permeable fault zone (green, Figure 5.3) corresponds to a depth of 7000m from the surface. The fault zone of intermediate permeability (light grey in Figure 5.3) has its lower boundary 12000m below the surface. Below this level, the fault permeability is practically indistinguishable from the permeability of the surrounding basement (dark grey zones). For the case studies simulating the effect of piercement structures cutting the Mwashia and Kundelungu stratigraphy, the green fault sections are extended upwards with more permeable segments (colored light green on the corresponding diagrams e.c. Figure 6.30).
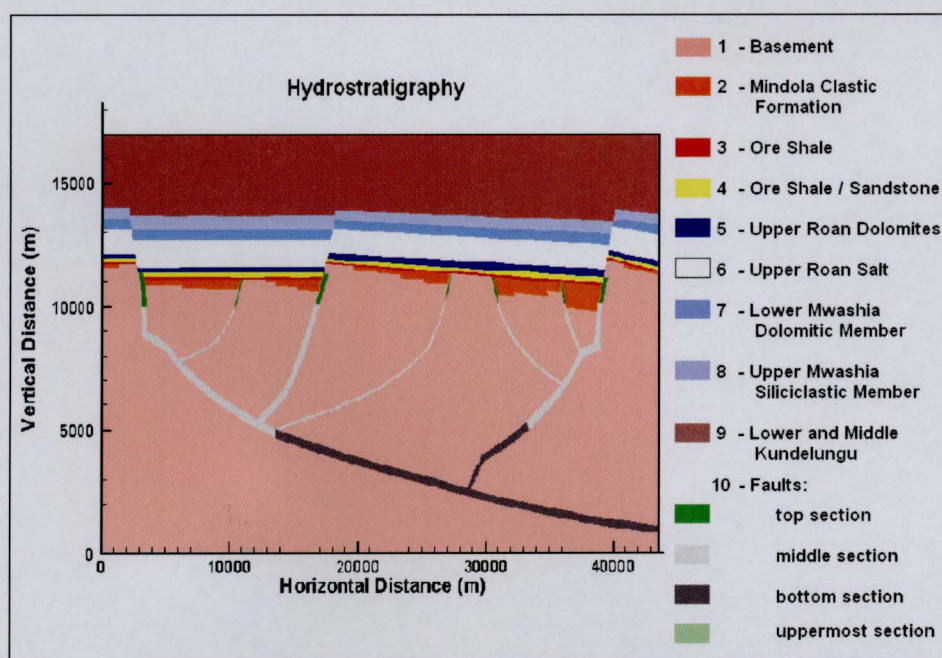


**Figure 5.3 Basic hydrostratigraphy of the ZCB.**

It should be noted here that the fault system geometry is conjectural. The width of master-fault bounded basins is based on Lufilian fold wavelengths of 10-15km along the western flank of the Kafue Anticline. Selley et al. (2005) have demonstrated that fold geometries are largely inherited from the early rift architecture, and thereby the wavelength of folds roughly equates to the width of basin compartments. This reasoning underlies the placement of master faults.

The fault architecture in the basement, shown as a linked system, is based partly on structural models by Daly et al (1984). However, in assuming the permeability of the lowermost section of the fault network (dark grey) was very low and the same as of the basement, we, in fact, ruled out the connectivity of the fault segments at depths of more than 12km.

## 5.2 Rock properties

The list of physical properties of stratigraphic components of the ZCB section is summarized in Table 5.1. A discussion of the values choice on each parameter follows.

### 5.2.1 Permeability (value)

When designating permeability values to the rock strata, several factors were taken into account:

1) depth of burial;

2) rock type;

3) degree of anisotropy.

Ingebritsen and Manning (2002) obtained a general permeability-depth dependency for average crustal rocks:

$$\log k = -14 - 3.2 \log z,$$ <span style="float:right">**Equation 5.1**</span>

Where permeability $k$ is in meters squared and depth, $z$, is in kilometers. The graph of $\log k$ versus $z$ is shown in Figure 5.4.
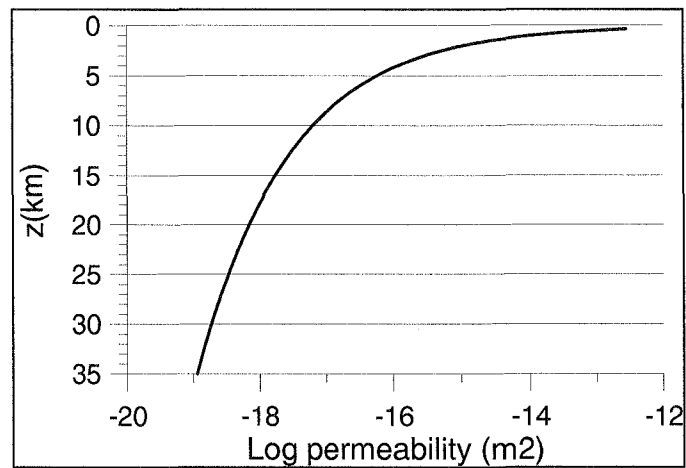
**Figure 5.4 Permeability-depth of burial dependency obtained by Ingebritsen and Manning (2002)**

As an alternative to using direct measurements, which are widely available only for the uppermost few kilometers of the Earth's crust, Ingebritsen and Manning used models of heat and mass transport constrained by geothermal data and the progress of metamorphic reactions driven by fluid flow. The authors showed a good coherence of the data to the obtained logarithmic curve.

The range of the permeability values calculated by formula (5.1) for the stratigraphic units of the Zambian Copper Belt depending on their depth of burial is shown in Table 5.2.
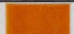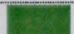
| Hydrogeologic unit | Colour on the map | Permeability, $k_x$ ($m^2$) | Coefficient of anisotropy, $k_x / k_z$ (-) | Porosity, $n$ (fraction) | Density, $\rho_s$ ($kg/m^3$) | Heat capacity, $c_s$ ($J/(kg\,{}^0C)$) | Thermal conductivity, $(\lambda_s)_x$ ($W/(m^0C)$) |
|---|---|---|---|---|---|---|---|
| 1 – Basement | | $10^{-16}$ | 1.0 | 0.1 | 2900 | 800 | 3.0 |
| 2 - Mindola Clastic Formation | | $10^{-14}$ | 100 | 0.2 | 2400 | 830 | 2.0 |
| 3 - Ore Shale | | $10^{-16}$ | 100 | 0.1 | 2400 | 850 | 2.5 |
| 4 - Ore Shale/ Sandstone | | $10^{-15}$ | 100 | 0.2 | 2400 | 850 | 2.5 |
| 5 - Upper Roan Dolomites | | $10^{-16}$ | 100 | 0.1 | 2600 | 850 | 2.3 |
| 6 - Upper Roan Salt | | $10^{-16}$ | 100 | 0.1 | 2400 | 850 | 5.0 |
| 7 - Lower Mwashia Dolomitic Member | | $10^{-16}$ | 100 | 0.1 | 2300 | 850 | 2.3 |
| 8 - Upper Mwashia Siliciclastic Member | | $10^{-15}$ | 100 | 0.1 | 2300 | 850 | 2.5 |
| 9 - Lower and Middle Kundelungu | | $10^{-14}$ | 100 | 0.1 | 2300 | 890 | 2.0 |
| 10 - Faults: | | | | | | | |
| top section | | $5\cdot10^{-15}$ | 1.0 | 0.3 | 2630 | 830 | 2.5 |
| middle section | | $10^{-15}$ | 1.0 | 0.3 | 2630 | 830 | 2.5 |
| bottom section | | $10^{-16}$ | 1.0 | 0.3 | 2630 | 830 | 2.5 |
| uppermost section | | $10^{-14}$ | 1.0 | 0.3 | 2630 | 830 | 2.5 |

**Table 5.1 Physical properties of the stratigraphyic components comprising the model section**

| Hydrogeologic unit | Depth of burial (km) | | $\log k$ | | $\log k_x$ used in the simulation |
|---|---|---|---|---|---|
| | min | max | min | max | |
| 1 – Basement | 5.2 | 17.0 | -17.93 | -16.29 | -16 |
| 2 - Mindola Clastic Formation | 5.2 | 7 | -16.70 | -16.29 | -14 |
| 3 - Ore Shale | 5.1 | 6 | -16.49 | -16.26 | -16 |
| 4 - Ore Shale/ Sandstone | 5.0 | 5.8 | -16.44 | -16.24 | -15 |
| 5 - Upper Roan Dolomites | 4.8 | 5.6 | -16.39 | -16.18 | -16 |
| 6 - Upper Roan Salt | 3.8 | 5.5 | -16.37 | -15.86 | -16 |
| 7 - Lower Mwashia Dolomitic Member | 3.4 | 4.3 | -16.03 | -15.70 | -16 |
| 8 - Upper Mwashia Siliciclastic Member | 3.0 | 3.8 | -15.86 | -15.53 | -15 |
| 9 - Lower and Middle Kundelungu | 0 | 3.2 | -15.62 | -- | -14 |
| 10 - Faults: | | | | | |
| top section | 5.7 | 7.0 | -16.70 | -16.42 | -14.30 |
| middle section | 7.0 | 12.0 | -17.45 | -16.70 | -15 |
| bottom section | 12.0 | 16.0 | -17.85 | -17.45 | -16 |
| uppermost section | 0 | 5.7 | -16.42 | -- | -14 |

Table 5.2 Permeability ranges of the hydrogeologic elements subject to depth of burial.

One can see that horizontal permeability coefficients used in the simulations for "Basement", "Ore Shale", "Upper Roan Dolomites", "Lower Mwashia Dolomitic Member" and "Lower and Middle Kundelungu" units correlate well with the calculated values.

However, it should be noted that Ingebritsen and Manning's formula (5.1) reflects the permeability-depth dependency for average crustal rocks, without distinguishing specific rock types. It was therefore ensured that $k_x$ values do not contradict the results of laboratory measurements. Thus, for bedded organogenic limestones taken from a depth 1859 - 1948m, Popov et al. (2003) give the permeability range $9.87 \cdot 10^{-18}$ - $6.99 \cdot 10^{-14} (m^2)$ with the average value of $5.23 \cdot 10^{-16} (m^2)$, while algal limestones (depth interval of 2797-3444m) show permeabilities from $9.87 \cdot 10^{-19}$ - $1.53 \cdot 10^{-12} (m^2)$ with the average $1.04 \cdot 10^{-13} (m^2)$. The reported permeability of intercalated siltstones and shale siltstones lies in the interval $3.95 \cdot 10^{-17}$ - $3.36 \cdot 10^{-15} (m^2)$ with the average of $6.12 \cdot 10^{-16} (m^2)$ (Popov et al., 2003). Thus, permeability prescribed for the dolomitic members and shales of the ZCB also fit well the measurement data.

To introduce the permeability contrast for more permeable "Mindola Clastic Formation", "Ore Shale/ Sandstone", and "Upper Mwashia Siliciclastic Member", the chosen $k_x$ values exceed those governed by their depth of occurrence according

127

to average from (Ingebritsen and Manning, 2002). Nevertheless, they are comparable with the available laboratory results. Popov et al. (2003) report $9.87 \cdot 10^{-18}$ - $1.97 \cdot 10^{-13} (m^2)$ for polymictic, arkose, and mica-quartz sandstones taken from a depth interval of 1968-3005m, and the permeability range for fine-grained and slightly bedded quartz sandstones from a depth 1637 – 2572(m) is $1.09 \cdot 10^{-14}$ - $1.92 \cdot 10^{-12} (m^2)$.

In sedimentary sequences, halite crystals are frequently well-cemented (Yechieli et al., 1995). Within the first 10m of burial, cementation reduces the porosity of halite crusts to less than 10%. The remaining pore spaces are completely filled by a burial depth of approximately 45m (Casas and Lowenstein, 1989: p.724). The laboratory measurements of permeability of halite give the range $10^{-9}$ to $10^{-6}$ darcy (Bredehoeft, 1988; Yaramanci, 1994), which is equivalent approximately to $10^{-21}$ - $10^{-18} (m^2)$. However, there is some conflicting stable isotope evidence that deeply buried salt actually participates in considerable rock-water interaction (Knauth et al., 1980; Land et al., 1988). Lewis and Holness (1996) demonstrated, via the experimental determination of the halite-brine dihedral angle which controls pore-fluid connectivity and hence permeability, that in sedimentary basins with normal geothermal gradients, halite bodies at depths exceeding 3 km will contain a stable interconnected brine-filled porosity, resulting in permeabilities comparable to those of sandstones (Lewis and Holness, 1996: p.431). The authors report the permeability range for halite at these depths $10^{-1}$ to $10^{-4}$ darcy, which is equivalent to $10^{-13}$ - $10^{-16} (m^2)$.

As a result, for most of the simulations, the permeability of the "Upper Roan Salt" was assumed low, $k_x = 10^{-16} (m^2)$, comparable with the permeability of the crystalline basement and the salt layer was considered anisotropic. However, a set of numerical tests was performed with different values from the range: isotropic salt layer with permeability $10^{-16} (m^2)$, then $10^{-18} (m^2)$; anisotropic salt sheet with the higher $k_x = 10^{-14} (m^2)$ (Sections 6.2.2 – 6.2.3).

The permeability of fault zones is, in general, a function of a suite of factors: the fault structure (the proportion between a fault core and an associated damage zone (Caine et al., 1996)), fault width and throw (Bense and Person, 2006), clay content in the core and lithology of flanking rock (Rawling et al., 2001; Sperrevik et al., 2002; Yielding, 2002), depth of burial (Bethke and Corbet, 1988), deformation

style and history, fluid chemistry, etc. (Smith et al., 1990). In the presented simulation, taking into account a conjectural geometry of the studied section and the lack of detailed data, we adopted the simplest model. The faults are assumed to act as conduits with roughly one order of magnitude higher permeability than the surrounding strata. As previously mentioned, one of the goals of this numerical study was to investigate whether the basement can act as a source of metals. In this content, one of the aims of this research was to see how strongly the faults facilitate convection through the basement and whether they are necessary at all to assure fluid flow across the basin/basement boundary.

### 5.2.2 Permeability (degree of anisotropy)

Rock mass permeability is often significantly anisotropic (Lee and Farmer, 1993). In stratified sediments, permeability has been found to be greater parallel to the bedding than perpendicular to it (Pettijohn, 1975). In Table 5.3 we summarize the data on anisotropy coefficient available from (Lee and Farmer, 1993).

**Laboratory scale**

| *Rock* | $k_{horizontal} / k_{vertical}$ | *Orientation of principal permeability* |
|---|---|---|
| Shales and clays | 0.5 - 10 | parallel to the preferred orientation of the clay particles |
| Sandstones | 1 - 4 | parallel to the bedding |
| Granite | 2.5 | parallel to the principal jointing |
| Slate and gneiss | - | parallel to foliation |

***In situ* investigations**

| *Rock* | $k_{horizontal} / k_{vertical}$ | *Orientation of principal permeability* |
|---|---|---|
| Fractured rocks whose joint are primarily vertical | $10^{-2}$ | parallel to the principal faults orientation |
| Intact layered sedimentary strata | up to $10^3$ | parallel to the layer plane |
| Salt formations | approximately 1 | almost isotropic |
| Bedded salt | $10^2 - 10^3$ | horizontal |
| Basaltic rock mass | 5-50 but two values exceeding 1000 were also obtained | horizontal |

**Table 5.3 Anisotropy coefficient and orientation of principal permeability by (Lee and Farmer, 1993).**

One of Lee and Farmer's conclusions, which is clearly illustrated by Table 5.3, is that the results of *in situ* tests may be 1 to 3 orders of magnitude above laboratory

values. Taking into account large linear scales of the simulations presented here, the values of the anisotropy coefficient were chosen from the reported *in situ* diapason. For all sedimentary units, $k_{horizontal}/k_{vertical}$ is $10^2$ (see Table 5.1). The crystalline basement is assumed isotropic ($k_{horizontal}/k_{vertical}$=1.0). The anisotropy coefficient of the salt layer was assumed: $k_{horizontal}/k_{vertical}$=$10^2$, which agrees with the value of Lee and Farmer's for bedded salt, however, a simulation based on an isotropic salt unit was also conducted (Section 6.2.2)

According to (Cain et al., 1996), the bulk two-dimensional permeability and, therefore, the degree of anisotropy, of a fault zone is controlled by lithology, fault scale, fault type, deformation style and history, fluid chemistry, P-T history, percentage, permeability and anisotropy of the fault zone components (core and damage zone). In this study, it was assumed that fault zones are isotropic (similar to (Garven et al., 2001)). The first reason for doing this is the lack of data on faults in the ZCB. Secondly, the intention was to avoid fluid forcing through the basin/basement boundary resulting from a higher permeability assigned along the fault plane.

## 5.2.3 Porosity

Porosity does not correlate directly with permeability (Lee and Farmer, 1993). Some beds may have a medium to high porosity but extremely low permeability (Conybeare, 1979). Nevertheless, it is quite reasonable to presume more permeable units to have higher porosity. For that reason, porosity of the "Mindola Clastic Formation" and "Ore Shale/Sandstone" units was set higher (0.2) than that of surrounding rocks (0.1). The highest porosity (0.3) was assigned to the fault zones.

## 5.2.4 Density

To assign the density of the rock units, the average values for the generic rock types from (Telford et al, 1990: p.16, Table 2.2) were used. Higher densities were prescribed to more compacted, deeper buried rock units. Rock filling the fault space was assumed to have a crystalline structure; therefore, its density was set to be higher than of the sedimentary rocks but lower than of the basement.

## 5.2.5 Compressibility

With respect to compressibility, the whole profile was considered homogeneous: compressibility of the porous medium, $\alpha_c$, was assumed uniformly equal to $10^{-11}$ ($m^2/N$), which is within the admissible range for sound rock.

## 5.2.6 Heat capacity

The values of heat capacity of the rock matrix were set close to the average by data from Bear (1972). This parameter gradually decreases with depth. It was assumed that a more deeply buried and more compacted rock should have lower heat capacity.

## 5.2.7 Thermal conductivity

Solid matrix thermal conductivity is heterogeneous depending to the rock type (Table 5.1). The values used here were set by data from (Popov et al., 2003) close to the average values for dry samples (see Popov et al., 2003: p.1142-1143, Table 1), as the effective thermal conductivity of the saturated porous medium is calculated in the model by the conductivity of the solid matrix and the conductivity of the fluid saturating the void space of the porous medium domain (Section 2.1.3).

Since the thermal conductivity of salt at room temperature is up to three times that of adjacent shales (Warren, 1999: p.54), this parameter for the "Upper Roan Salt" layer was prescribed a maximum value (5.0 $W/(m^0C)$) compared to all other sedimentary units (2.0-2.5 $W/(m^0C)$).

From the data presented in (Popov et al., 2003), it is clear, that the thermal anisotropy coefficient (the ratio of thermal conductivity component parallel to rock bedding to one perpendicular to it) is close to unity for the majority of the samples analyzed. Therefore, with respect to thermal conductivity, all rock units comprising the ZCB section were assumed isotropic though heterogeneous.

## 5.2.8 Dispersivity

The effect of dispersive mixing is taken into account in the model (Section 2.1.4). As the model is two-dimensional, two parameters, longitudinal ($\alpha_L^S$) and transversal ($\alpha_T^S$) dispersivities must be defined. Gelhar et al. (1992) presented a comprehensive review of available dispersivity observations from 59 field sites. In their investigation, the authors:

- found that field-scale dispersivities are several orders of magnitude greater than laboratory-scale suggesting laboratory measurements of dispersivity cannot be used to predict field values of dispersivity;
- documented the evidence of the scale effect;
- thoroughly assessed the reliability of the data.

The authors attributed the majority of large-scale tests to the low reliability category. They also state that at any given scale, "the preponderance of evidence favors the use of dispersivity values in the lower half of the range" (Gelhar et al., 1992: p.1972). To assess this range, in Table 5.4 we gathered the $\alpha_L^S$ values for large-scale studies.

| Reference | Scale of test (m) | $\alpha_L^S$ (m) |
|---|---|---|
| Ahlstrom et al. (1977) | 20000 | 30.5 |
| Grove (1977) | 20000 | 91 |
| Cupta et al. (1975) | 50000 | 80-200 |
| Rabinowitz and Gross (1972) | 32000 | 20-23 |
| Robertson (1974) Robertson and Barraclough (1973) | 20000 | 910 |
| Vaccaro and Bolke (1983) | 43400 | 91.4 |
| Wood (1981) | $10^5$ | 5600-40000 |

**Table 5.4 Summary on dispersivity data for large-scale observations accordingly to (Gelhar et al., 1992).**

The scatter of $\alpha_L^S$ values is extremely wide: from 20m to 40000m. Based on the conclusion of Gelhar et al. (1992), the longitudinal dispersivity was set close to the lower limit of the range: $\alpha_L^S$ =200m.

Another important finding by Gelhar et al. (1992) is that despite the popularity of using in numerical simulations a horizontal transversal dispersivity being about one third of the longitudinal dispersivity, this does not appear to have any real

justification (Gelhar et al., 1992: p.1970). According to the authors, horizontal transverse dispersivities are typically an order of magnitude smaller than the longitudinal dispersivity, whereas vertical transverse dispersivities are another order of magnitude lower. This means that $\alpha_T^S = 0.01 \, \alpha_L^S$.

For the present simulation, it has been assumed that $\alpha_L^S = 200$m, therefore, $\alpha_T^S$ should equal about 2m.

## 5.3 Role of the Upper Roan Salt in the sediment-hosted stratiform copper system

### 5.3.1 Effect of the salt layer on basin evolution

As was discussed in Section 5.1.2, the voluminous and widespread breccias in the Upper Roan Group suggest the former presence of significant salt accumulation at this level. We envisage, the presence of this salt layer would have influenced the hydrological development of the basin in several ways:

1) Dense brine, formed as a result of the salt dissolution, would have provided a source of chloride ions which facilitate Cu transport;

2) Salinity enhanced buoyancy effects would have influenced fluid and heat flow. It is demonstrated in Chapter 6 how significantly dissolution of the salt layer, its geometry and physical characteristics, affect flow structure and the temperature field;

3) Salt, being a highly unstable and mobile facies, would have impacted the hydrostratigraphy of the basin, not only by changing its own geometry, but also by facilitating the formation of more permeable brecciated zones due to dissolution/mobilization processes.

Breccia bodies can result from various scenarios within the context of the local evolution of the salt layer. On the one hand, they may originate from caving of the overburden above the location, where the salt layer is thinned (the left part of Figure 5.5 (a), (b)), either due to dissolution or laterally directed viscous salt flow (Warren, 1999). On the other, they can be a consequence of brecciation around an ascending diapir (the right part of Figure 5.5 (a), (b)). Later, in Chapter 6, the effect of permeable zones of this origin on the flow system is studied.
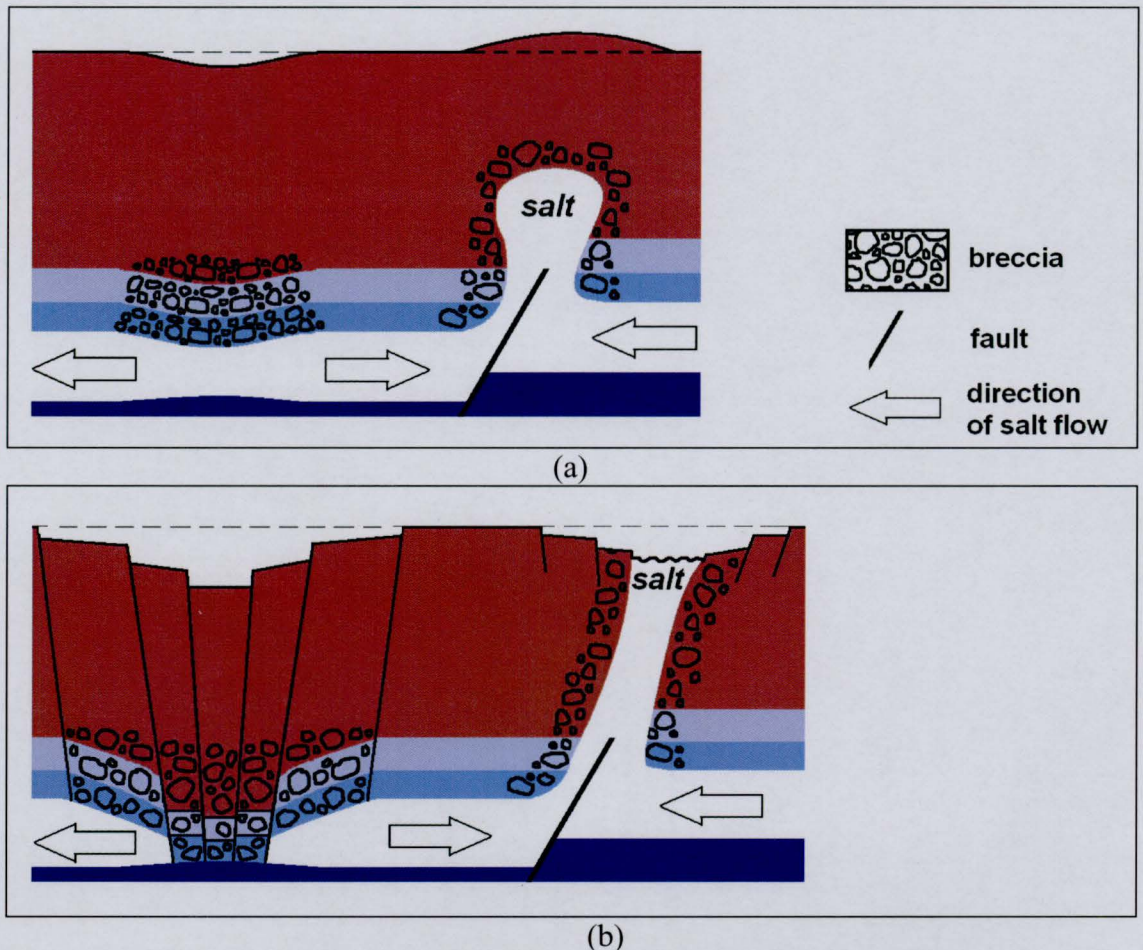
**Figure 5.5 Formation of breccia bodies by dissolution/mobilization of rock salt. (a) – early stage; (b) – late stage.**

## 5.3.2 Salt dissolution parametrization.

Previous studies showed a significant salinity impact on fluid migration, heat transport and mineralization (Yang et al., 2004). The specificity of the present numerical investigation is that it involves a constant salt influx into the system due to dissolution of the Upper Roan Salt. Sarkar et al. (1995) showed that the formation of dense brines by dissolution of salt sheets may induce free thermohaline convection of pore fluid beneath the salt layer. As salt dissolves, high concentrations change fluid density to such an extent that a significant density gradient becomes the primary mechanism driving groundwater flow (Herbert et al., 1988; Evans et al., 1991; Simmons et al., 2001).

Three options for the salt dissolution formalization are envisaged in the model. The first implies the parametrization of the source term, $Q_S$, in Equation (2.14). $Q_S$ characterizes the rate of salt dissolution, as an increase in salinity per unit of time. However, it was found difficult to estimate the numerical value of this natural "theoretical" parameter for a particular salt source. So, an alternative approach is also

134

adopted, in which it is assumed that any pore fluid coming into contact with the salt unit, acquires salinity at the saturation state, $S_{sat}$. In that way, in the grid nodes which are "ascribed" to the salt layer, salinity equals $S_{sat}$ throughout the indicated period of the simulation. $S_{sat}$ can be read from the input data file (second option of salt source parametrization), or it can be set as a function of halite dissolution temperature (third option). In the latter case,

$$S_{sat} = 0.01\,(26.242 + 0.4928\,\Psi + 1.42\,\Psi^2 - 0.223\,\Psi^3 + 0.04129\,\Psi^4 + \\ + 6.295 \cdot 10^{-3}\,\Psi^5 - 1.967 \cdot 10^{-3}\,\Psi^6 + 1.1112 \cdot 10^{-4}\,\Psi^7)$$     , **Equation 5.2**

where $\Psi = T(^0C)/100$ (Sterner et al., 1988; Bodnar, 2003). The graph of NaCl solubility in water from the peritectic temperature ($0.1\ ^0C$) to the NaCl triple point ($801\ ^0C$) is shown in Figure 5.3.
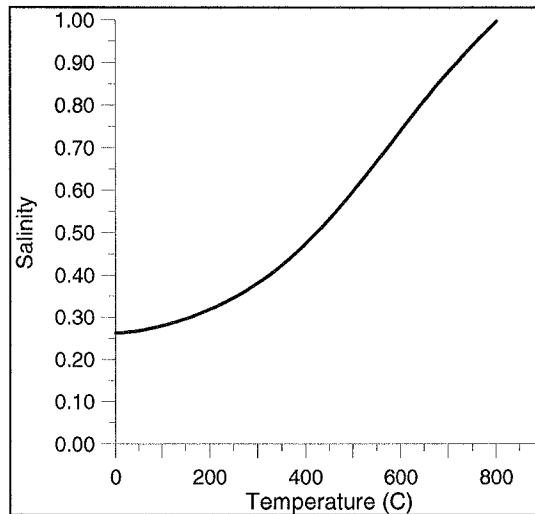


**Figure 5.6 Solubility of NaCl in water (mass fraction of salt in the solute) as a function of temperature calculated using Equation 5.2.**

# 6  Zambian Copper Belt. Numerical simulation results

The aim of the numerical simulations presented below is to study factors which affect the flow regime of the metal-bearing fluid and formation of ore bodies in the ZCB. For this purpose, a set of possible paleo-hydrologic scenarios have been tested.

The scenarios are grouped in the following way: first two case studies (Section 6.1.1) represent early stages of the basin development, "rift initiation" and "rift climax. The third scenario (Section 6.1.2) corresponds to the initial stage of the Kundelungu deposition, when the thickness of this stratigraphic unit constituted about one third of its ultimate thickness. In Section 6.2, the basic scenario is discussed. The hydrostratigraphy of the section used in this basic case study is described in detail in Chapter 5. An analysis of the model's sensitivity to the salt layer properties was then carried out. In Section 1.1, the effect of salt transport and Roan salt dissolution is studied by comparison of the basic scenario with the case study run under assumption that the interstitial water carries no salt. Further, the basic hydrostratigraphy of the section has been altered in order to investigate influence of different factors such as fault network configuration (Section 6.4), salt layer geometry (Section 6.5), piercement structures cutting low-permeable Upper Roan and Lower Mwashia strata (Section 6.6).

Local properties of the metal-bearing fluid and the amount of Cu that can be potentially deposited in the trap sites was evaluated based on the flow regimes of three scenarios representing consecutive stages of basin evolution (Section 6.8.1).

The simulations were performed with the use of a two-dimensional mesh built for the basic hydrostratigraphy of the ZCB section (Figure 5.1). The mesh is shown in Figure 6.1 (a). For the case studies involving some change of the basin geometry, like salt layer flattening (Section 6.5) or leveling of the upper boundary for the truncated section (early stages of the basin development), this basic grid was modified.

The *side boundaries* are assumed impermeable to fluid flow, heat and dissolved substance fluxes. At the *top boundary,* water temperature equals $20^0 C$, salinity is set at the average sea water value of 0.035 (which is equivalent to 3.5% or 35000ppm). The *bottom boundary* is considered impermeable to fluid flow and salt flux (which is natural as the volcanic basement has very low permeability and porosity). Temperature at the bottom boundary of the domain is calculated based on the

average geothermal gradient of $25\,^{0}C/km$ (Bear, 1972), thickness of the section, and temperature at the surface, $20\,^{0}C$.

Rock properties used in the simulations are listed in Table 5.1 (Section 5.2).

The coefficient of molecular diffusion for the dissolved substance is $5 \cdot 10^{-8}$ ($m^2/s$). The simulations were performed with the use of a fully implicit scheme: $\sigma = \sigma_c = \sigma_{cR} = 1.0$ (see Section 3.5 for the coefficient definitions), with the time step - $5 \cdot 10^4$ (days).

For the scenarios involving salt layer dissolution, it is assumed that the hydrothermal fluid, having come into contact with the Upper Roan Salt, acquires salinity at the saturation value, $S_{sat} = 0.3$.

All the simulations were run for the period of approximately 1.4 million years. The results are presented after 200 thousand years (to illustrate the system behavior at early stages) and at the end of the simulation. For simulations started from the 'zero state' (motionless fluid with the uniform hydraulic head, linear temperature distribution corresponding to geothermal gradient, seawater salinity everywhere but the Upper Roan Salt, where it equals to 30 weight %, see Figures 6.1(b-c)), T1 and T2 are further used to denote 200 thousand and 1.4 million years respectively. For some case studies, the final distributions of the hydraulic head, temperature and salinity calculated for the 'basic scenario' were taken as initial conditions. The intention here was to investigate the effect of changes in the basin structure considering the prehistory of the paleo-flow. The notation T1 and T2 for the output moments 200 thousand and 1.4 million years respectively is kept for these case studies, though T1 actually means 1.6 million years from the 'zero state' and T2, correspondingly, 2.8 million years.

## 6.1 Early stages of basin evolution

### 6.1.1 'Rift initiation' and 'rift climax'

According to (Selley et al. 2005), the Mindola Clastics Formation is considered to record "rift initiation" and the formation of the array of small fault-bounded depocentres. The "rift climax" stage is recorded by the abrupt transgression of older compartmentalized sub-basins, by expansive marine deposits (Sharp et al., 2000). In this connection, the basin stratigraphy at "rift initiation" and "rift climax" stages is modeled by two sections:

*__Case 1__*. At the "rift initiation" stage, the section consists only of the volcanic basement, cut by the faults, and the Mindola Clastics Formation accumulated in the array of half-grabens (Figure 6.2)

*__Case 2__*. For the "rift climax" stage, the section is amplified by two less permeable stratigraphic units representing the Copperbelt Orebody Member: "Ore Shale" and "Ore Shale/ Sandstone" (Figure 6.3(a)). The shale layers are pierced by three master faults, although they still seal the outlets of secondary faults.

Strictly speaking, at the early stages, when the deposition occurred in fluvial, alluvial, aeolian and fan-delta environments, the porous system can hardly be considered as fully saturated with water. It is also affected by the influx of meteoric fluid and other processes taking place in the subaerial depositional environment. So the purpose of performing these two simulations was principally to investigate the effect of the basin architecture in comparison with the later stages of the basin evolution.

Since at these stages, the pore fluid can only be of meteoric origin, the section is saturated with fresh water and salt transport is not involved in the simulation.

The initial finite-element grid (Figure 6.1(a)) was modified so as to level the upper boundary of the domain ('Mindola Clastic Formation' – 'Ore Shale' interface for Case 1, 'Ore Shale/Sandstone' - 'Upper Roan Dolomites' contact for Case 2). Figure 6.3(b) illustrates the modification. This was done to eliminate any effect of the initial topography of the stratigraphic units considered, as free convection is meant to be the only mechanism driving ground-water flow. The following boundary conditions are set for these case studies: at the top boundary, the hydraulic head is assumed equal to 11000m, the temperature is 20 $^0C$. At the bottom boundary, the temperature is set equal to $350^0C$ based on the thickness of the section, 11km, approximate geothermal gradient of $30^0C$/km and temperature at the surface:

$$T_{bottom} = 11km \cdot 30\frac{^0C}{km} + 20^0C = 350^0C$$

It should be noticed that for these two scenarios, a higher value of the geothermal gradient was used, while setting thermal boundary conditions ($30^0C$/km against $25^0C$/km in all other case studies). Preliminary runs showed extremely low flow rates, compared to the later stage scenarios, so the higher temperature gradient was used to facilitate free convection.

Results of the simulation for Cases 1 and 2 at T2 are shown in Figure 6.4-Figure 6.5 respectively.

In *Case 1*, the discharge-recharge processes takes place through the open top boundary (Figure 6.4(a)). Four convective cells are formed in the domain (Figure 6.4(b)). The fault network deviates the cell distribution from uniform providing more convenient pathways for the fluid flow. Both primary and secondary faults are actively involved into the fluid exchange at the surface. At the same time, the convective flow takes place through the low-permeable basement section. The flow rates are low: maximum velocity at T2 is about 4.4 cm/yr. As a result, isotherms are hardly deviated from the initial state, even after a long simulation period as 1.4 million years (Figure 6.4(c)).

Figure 6.5 shows the results of the simulation for *Case 2*. This case study illustrates the impact of the impermeable seal on the system. The cellular flow patterns within the basement are similar to Case 1 (Figure 6.5(b)). However, in the Mindola Clastics Formation, instead of the intense discharge-recharge, the flow is now redirected horizontally beneath the seal (Figure 6.5(a)). Flow rates are approximately half those in Case 1: maximum is 2.9cm/yr. As a consequence, the temperature field differs from the initial linear distribution even less than in the previous scenario (Figure 6.5(c)). This case study shows that the deposition of the shale (Copperbelt Orebody Member) significantly inhibits the system dynamics until the Upper Roan and younger sediments formed and additional driving mechanisms (like increased thickness of the section and density effects due to the dissolved salt presence) come into play.

## 6.1.2 The initial stage of the Kundelungu deposition

*Case 3* represents an intermediate scenario aimed to complete the chronological picture of the basin development. The results on the fluid flow regime are further used for evaluation of copper precipitation during the basin evolution.

At this stage, the model section is expanded by the Upper Roan and Mwashia members and a thinned Kundelungu layer constituting about one third of its ultimate thickness (Figure 6.6). Compared to preceding case studies, the increased thickness of the section (and, therefore, the temperature excess) together with the Upper Roan Salt dissolution intensified the convective flow in the section. Flow rates grew 1 order of magnitude: the maximum fluid velocity at T2 is now 35.2 cm/yr compared to 2.9cm/yr for Case 2. The results of the simulation at T1 and T2 are presented in

Appendix 1 (Figures A1.1 and A1.2 respectively), as there is a clear similarity with the basic scenario below.

## *6.2 Basic scenario*

<u>*Case 4*</u> is considered a basic scenario, because it takes into account all features of the ZCB geology discussed in Chapter 5. The effect of different hydrostratigraphy modifications are studied further by comparison with results from Case 4. In some of the following simulations the final distribution of temperature, salinity, and hydraulic head calculated for Case 1 will be taken as initial conditions, to simulate the consequent stages of the basin development, with the consideration of its past history (Section 6.6).

### 6.2.1 Simulation results

Figure 6.7-Figure 6.8 show fluid velocity field, temperature and salinity distributions at T1 and T2 respectively.

Thermal instability coupled with the formation of dense brine by dissolution of the Upper Roan Salt leads to establishment of the cellular flow beneath the salt sheet. The circulation involves more permeable fault zones and the Mindola aquifer (Figure 6.9(a)). At the same time, the simulation shows a significant convective flow through the low permeability basement (see the streamline diagram Figure 6.9(b)). It appears (Figure 6.7(c)) that spatially concentrated heavy brine plumes sink down the more permeable conduits, and continue into the underlying basement. On the other hand, fluid, heated in the lower part of the section, rises through the basement until it encounters a more convenient pathway, such as a fault zone. Oliver et al. (in press) for north Australian sedimentary basin, note that long lived stable convection is generated within the basement 'with $\leq 2$ order of magnitude permeability difference between basement and cover'. The simulation presented here shows a similar result, and the permeability difference between the basement and Mindola Clastic Formation is also 2 orders of magnitude in our case.

In the earlier period (Figure 6.7 (c)), we observe several downwelling solute plumes formed beneath the salt layer (double-diffusive fingering (Phillips, 1991)). More extensive and penetrating more deeply into the basin, salt "tongues" are associated with the vertical primary faults. The first and obvious reason of this effect

is the higher permeability of the fault zones. But also the edge effect recognized by Sarkar et al. (1995) takes place. The salt layer sections are displaced along the fault planes. Consequently, the vertical face of the salt layer segment is exposed and dissolution of the vertical face contributes to, and promotes, the extensive edge plume formation. This phenomenon is even more conspicuous in the later case study when there are no faults beneath the salt layer (Section 6.4). In the later periods (Figure 6.8(c)), higher fluid velocities in the permeable conduits and therefore higher rates of salt transport maintain the spatial association of the plumes with the fault zones.

A boundary effect is observed in the right section of the domain. In the earlier time (T1) the fluid flow at the right boundary is directed upwards. The up-flow is invoked by the hot, less saline fluid rising up. One can see two vertically elongated convective cells on the right-hand side of the model section (Figure 6.7(a)). The right one defines the upward direction of the flow in the vicinity of the boundary. After 1.4 million years, the heavy saline plume sinks down towards the right boundary (which is assumed to be impermeable) causing the fluid to descend to the base of the section.

There is no significant fluid flow in the upper part of the section above the salt layer. The dissolved salt rapidly diffuses upward into the Kundelungu sediments creating strong stable stratification of the pore fluid. Under these conditions, significant thermal instability is necessary to initiate convection in this upper section. However, the present thermal gradient is not sufficient for this. At the same time, the bedded salt, being impermeable itself, and the covering layer of dolomites, prevent the hot fluid from rising. Thus, there is no driving mechanism to activate significant fluid flow within the permeable Lower and Middle Kundelungu stratigraphy.

## 6.2.2 Effect of the salt layer isotropy/anisotropy

The degree of the anisotropy of the Upper Roan Salt permeability, $k_{horizontal} / k_{vertical}$, was assumed on the basis of data for bedded salt (Section 5.2.2): $k_{horizontal} / k_{vertical} = 100$ ($k_{horizontal} = 10^{-16}$ $m^2$; $k_{vertical} = 10^{-18}$ $m^2$). However, in some cases, salt formations are considered isotropic (Lee and Farmer, 1993).

To clarify, if the anisotropy of the salt layer has a significant impact on the system dynamics, two case studies were run:

*__Case 4A__*. The salt layer is isotropic with $k_{horizontal} = k_{vertical} = 10^{-18}$ ($m^2$), which is the value of the vertical permeability of the Upper Roan salt in the basic scenario, Case 4.

*__Case 4B__*. The salt layer permeability, $k_{horizontal} = k_{vertical} = 10^{-16}$ ($m^2$), which is the value of the horizontal permeability in the basic scenario.

In Figure 6.10-Figure 6.12 we compare fluid velocity field, temperature and salinity distributions respectively for Case 4, 4A, and 4B.

One can see, that in scenario *Case 4A* the decrease in horizontal permeability ($10^{-18}$ ($m^2$) comparatively to $10^{-16}$ ($m^2$) for Case 4) leads to:

1) drop in the flow rates within the salt layer;

2) slightly intensified circulation at the rightmost primary fault and adjacent Mindola Clastics Formation segment and secondary conduit;

3) slightly lower fluid salinity values as a consequence of a weaker fluid flux through the salt layer and therefore lesser salt influx into the system.

Nevertheless, in Case 4A, the fluid flow pattern, as well as the temperature distribution, is the same as in Case 4. The salinity field retains a similar structure, though with slightly lower absolute values. Thus, the fact that the salt layer is isotropic does not make a significant difference provided the vertical permeability of the layer remains the same.

In *Case 4B*, the picture is slightly different, we observe:

1) higher fluid flow rates within the Upper Roan Salt;

2) velocities in the middle primary fault and the top, most permeable, sections of the faults to the right are increased;

3) the salinities are slightly higher, especially in the centre of the basement;

4) the temperature distribution has changed in the left part of the section as a consequence of a different fluid flow pattern in this zone.

However, all the listed differences relate to the intensified circulation due to the increased vertical permeability of the salt layer, rather than to the fact that it is isotropic.

Thus, the general conclusion can be drawn, that the degree of anisotropy of the salt layer does not have a significant influence on the system as long as the vertical permeability of the layer is kept low.

## 6.2.3 Highly permeable salt layer

In Chapter 5, where the properties of the rock units comprising the section were discussed, it was pointed out that some researchers (Lewis and Holness, 1996; Land et al., 1998; Knauth et al., 1980) showed evidence of considerable rock-water interaction of deeply buried salt. Thus, Lewis and Holness (1996) report the permeability range for halite $10^{-1}$ to $10^{-4}$ darcy, which is equivalent to $10^{-13}$ - $10^{-16}$ $m^2$.

In **_Case 4C_**, the salt layer permeability was increased: $k_{horizontal} = 10^{-14}$ $m^2$ and $k_{vertical} = 10^{-16}$ $m^2$ (compared to $k_{horizontal} = 10^{-16}$ $m^2$, $k_{vertical} = 10^{-18}$ $m^2$ for the basic scenario, Case 4). The simulation shows that two orders of magnitude increase in the halite permeability drastically changes the system flow dynamics (Figure 6.13):

1) flow rates increase: the maximum at T2 reaches now 1.066 m/yr, which is 3 times higher than for the basic scenario, Case 4 (0.353 m/yr);

2) intensive horizontal fluid flow takes place through the salt layer. The maximum velocities at T2 are observed in the Roan Salt (Figure 6.13);

3) the horizontal scale of the convective cells is increased. For the basic scenario, Case 4, there are five convective cells below the Upper Roan Salt (Figure 6.14(a)), In Case 4C, one can see three widened convective cells and the salt layer becomes involved in the circulation (Figure 6.14(b));

4) the change in the pattern of the cellular flow causes differences in the temperature field. In Case 4C (Figure 6.15(b)), the plume of cooler water associated with the central master-fault penetrates deeper into the basement than in the basic Case 4 (Figure 6.15(a));

5) an extensive brine reservoir is formed deep in the central part of the basement (Figure 6.16(b)), which is significantly different from the basic scenario salinity distribution (three salt "fingers" associated with the master faults, Figure 6.16(a)).

These differences are caused by the increased salt input into the system as a result of the intensified fluid flow through the salt layer and, therefore, enhanced rock salt dissolution.

## 6.3 Fresh water scenario

*Case 5* was developed to show the difference in modeling results if NaCl transport and dissolution of the salt sheet present in the section is not taken into consideration. The scenario was run with the same setting (hydristratigraphy, rock properties, initial and boundary conditions) as the basic scenario, Case 4, only properties of the fluid saturating the section are not dependent on the NaCl concentration and the salt inflow into the system, due to Upper Roan Salt dissolution, is not simulated. In this case, the thermal gradient is the only mechanism driving convective flow.

At the early stages, the intensity of fluid flow is significantly lower in Case 5 compared to the basic scenario (Figure 6.17). At T1, the maximum value of fluid velocity is 0.079m/yr for Case 5 against 0.637m/yr for basic Case 4, which is almost one order of magnitude less. Since fluid velocities are low, the temperature field hardly differs from the initial linear distribution (Figure 6.18(b)). Later on, convection intensifies (Figure 6.19(b)), though the flow pattern is completely different from the saline fluid case study (Figure 6.19 (a)). Thus, in Case 5 at T2, there are three wide cellular structures (Figure 6.20(b)) compared to 5 vertically elongated convective cells in Case 4 (Figure 6.20(a)). Directions of the flow in permeable units are opposite (compare Figure 6.19 (a) and (b)), and the fluid mostly 'uses' the Mindola Clastic aquifer and fault zones: the circulation through the basement is less intensive, vertical velocity components within this unit are generally lower. As a result, at T2 the isotherms are more smoothed out in Case 5 (Figure 6.21(b)) besides their configuration is considerably different from Case 4 (Figure 6.21(a)). This leads to the different temperature regime in the same rock units. Thus, for example, at T2 temperature in the thin 'Ore Shale' and 'OreShale/Sandstone' layers in the center of the domain lies within the interval $160\text{-}170\,^{0}C$ for Case 5, while being $190\text{-}210\,^{0}C$ for the basic scenario. The difference is about $30\text{-}40\,^{0}C$.

Thus, the exclusion of the salt sheet dissolution as one of the driving mechanisms completely restructures the fluid flow, lowers vertical mixing throughout the basement, and, therefore, leads to lower average temperatures and fluid flow rates at the same stratigraphic levels.

## 6.4 Fault network effect

In all previous case studies, the network of permeable faults is shown to control the fluid flow in the upper third of the basement. A natural question emerges, what happens in a quite plausible situation, when the conduits are sealed with the precipitated matter. In **_Case 6_**, all the settings (hydrostratigraphy, rock properties, boundary and initial conditions) were kept the same as in the basic scenario with the only difference being that there are no permeable faults in the section (Figure 6.22).

It appears that the absence of the fault network drastically changes the system dynamics beneath the salt layer. First of all, fluid velocities are generally lower: at T1, the velocity maximum is observed in the Mindola Clastic Formation (Figure 6.22(a)) and equals approximately 0.290m/yr, which is about 2.2 times less than in the basic scenario, Case 4, (0.637m/yr). At the early period, the flow pattern below the Upper Roan Salt represents a system of narrow convective cells which, in contrast to Case 4, are not deformed by the guiding faults (compare Figure 6.22 (b) and (c)).

At the later time, T2, the velocities in the Mindola Clastic Formation are surprisingly higher for Case 6, than for Case 4 (0.490m/yr against 0.353 m/yr), as now it is only the Mindola Clastic unit which has a high permeability below the Roan Salt (as the faults are impermeable). The flow patterns are totally different: the scale of convection is larger, as the porous media below the salt layer is more uniform and not dissected by the permeable conduits. One can observe three cellular convective systems within the basement (Figure 6.23(b)), while in Case 4, there are five (Figure 6.23(c)). The temperature field also responds to this difference in flow patterns (Appendix 2, Figure A2.1).

At T1, the salinity field shows more pronounced "fingering" and the solute plumes are more spatially "concentrated" (Figure 6.24(b)), because the dispersive effect is diminished due to lower fluid velocities in Case 6. The common feature for Case 6 and the basic scenario is the spatial location of the salt "tongues" at the earlier stage (Figure 6.24 (a) and (b)). The plumes penetrating more deeply are associated with the places where the salt layer is broken and its segment subsides exposing the vertical face. It seems that the "edge effect" mentioned before, rather than the presence of the faults, defines the position of these plumes. The complete explanation of this effect is given in the following section, where the results of the simulation with the unbroken and perfectly flat salt layer are presented. Whereas at

the early period (T1), there is a similarity in the salinity distributions, after 1.4 million years (T2), the picture is completely different (Figure 6.25 (a) and (b)). In Case 4, we have solute "fingers" associated with the vertical master faults. In Case 6, there is an extensive brine reservoir created in the central part of the basement, mainly fed by the brine descending from the salt layer edge zone above. Apart from the geometry, the reservoir position is also promoted by flow through the Mindoal Clastics, which is directed towards the central edge zone.

Thus, sealing of the basement fault network beneath the Roan clastics totally restructures the flow pattern, temperature and salinity distributions. At the same time, the flow pattern for Case 6 shows similarity with the one for Case 4C (highly permeable salt layer). Comparing streamlines at T2, Figure 6.23(b) (Case 6) and Figure 6.14(b) (Case 4C), one can see that in both cases we have a three-cell structure within the basement (slightly deformed in Case 4C, as fluid fluxes are deviated by the permeable conduits). However, the mechanisms leading to this similarity seem to be different. In Case 4C, it is an inhanced salt flux from the Upper Roan Salt due to the increased permeability of this layer; in Case 6, it is the absence of the fault network beneath the salt layer.

## 6.5 Effect of the salt layer geometry

In **_Case 7_**, the Upper Roan Salt and overlying layers were flattened to exclude any non-uniformity in the salt layer geometry which could affect the flow regime below this layer. In Figure 6.26, the comparison of the salinity fields at T1 is presented for Case 4 (basic scenario), Case 6 (no permeable faults), and Case 7. It shows that at the early period (T1),

1) it is Mindola Clastic Formation segments that define salt 'finger' placement in the horizontal direction (Figure 6.26(a));

2) in the absence of the salt layer breaks and displacements along them, all the salt 'fingers' penetrate to the same depth into the basement (compare Figure 6.26 (b) and (c));

3) if the salt layer is broken and its segments are shifted and tilted, longer solute plumes are formed where the vertical face is exposed (the "edge effect") and towards the subsided end of a segment (Figure 6.26(b));

4) the fault network controls the fluid fluxes deviating a salt plume from the straight vertical sinking into the basement (Figure 6.26(a)).

At the later time, it seems that the presence of the fault network makes a crucial difference: by T2, a larger amount of vertically elongated convective cells are established within the basement dissected by the faults (compare Figure 6.27 (a) and (b)). In the absence of the faults, the flow patterns show more similarity, the convection is of a larger scale (Figure 6.27 (b) and (c)), though for the unbroken salt sheet the picture is more symmetrical, distorted only by enhancing flow Mindola Clastic segments. Comparison of the temperature and salinity fields for these three case studies makes the effect even more evident (Figure 6.28, Figure 6.29).

Thus, the breaks and shifts of the salt layer promote salt dissolution at these locations, and the inclination of a salt sheet segment leads to the formation, at the subsided end, of a more concentrated solute plume penetrating more deeply into the basement.

## 6.6 Effect of piercement structures cutting the Upper Roan Salt.

Simulation results presented in previous sections showed no substantial circulation in the uppermost part of the ZCB section above the Upper Roan Salt, because strong stable salinity stratification overpowers the effect of the existing geothermal gradient. Two supplementary case studies presented in Appendix 3 demonstrated that even if permeable interconnected structures exist above the Upper Roan Salt, they cannot facilitate any fluid flow in Mwashia and Kundelungu strata.

In this section, we investigate conditions under which the interaction of upper and lower parts of the basin separated by the Upper Roan Salt can be achieved. First, the low-permeable barrier was breached above the position of the middle primary fault (Section 6.6.1). Then, in Section 6.6.2, the extension of all three master faults is simulated. For each of the two settings, two scenarios are run with the fault extension successively reaching different stratigraphic levels: first – to the interface 'Upper Mwashia Siliciclastic Member' – 'Kundelungu', second - to the surface. Apart from piercement of the low permeability strata by faulting, the scenarios can be interpreted as progressive vertical brecciation due to diapirism.

There is a distinction in the following case studies from those presented before. The following simulations were run from the final state of the basic scenario: hydraulic head, temperature and salinity distributions after 1.4 million years calculated for Case 4 (Figure 6.8) were taken as the initial conditions. When a new simulation started, the hydrostratigraphy of the section is changed so that master faults penetrate further towards the surface. This setting models a situation when a fault is extended as a result of a short-term tectonic event; and the further basin evolution is simulated taking into account its prehistory.

## 6.6.1 Middle primary fault extension

In the following two case studies, the middle fault was successively extended towards the surface:

*Case 8*: to the contact 'Upper Mwashia Siliciclastic Member' – 'Kundelungu' (Figure 6.30 (a));

*Case 8A*: up to the surface (Figure 6.30 (b)).

In Figure 6.31-Figure 6.32 the results of the simulation for Case 8 are presented at T1 and T2 respectively. In the early stages, the behavior of the system is similar to that of the basic scenario at the end of the simulation (compare Figure 6.31 and Figure 6.8), which is natural, as final distributions for Case 4 were used as initial conditions. In particular, the salinity field maintains the 'three-finger' pattern. However, at the end of the simulation (after 1.4 million years), the system dynamics is rather close to one of Case 6 (no permeable faults). Thus, the obvious similarity in temperature fields for the current Case 8 and Case 6, Figure 6.33, suggests the comparison be done for the fluid velocities as well. It appears that in both case studies the fluid fluxes are directed similarly (Figure 6.34) (though, of course, velocities are higher in the permeable faults in Case 8). Moreover, the streamlines show (Figure 6.35) a three-cell flow pattern. Temporal dynamics of the salinity field (Figure 6.36) displays that with time, its pattern transfers from the 'three-finger' type, peculiar to the basic scenario, to the 'brine-reservoir' configuration of the no-faults case study. The comparison of salinity distributions at T2 for Case 6 and Case 8 (Figure 6.37) shows that although for Case 8 the salinity values are higher (the Roan Salt was being dissolved for 2.8 million years: 1.4 till the initial state (Case 4 at T2) plus 1.4 of the current simulation) the spatial distributions are very similar. This

suggests that when a continued salt influx is maintained for a substantial period of time, the permeability contrast, due to the presence of the fault network, plays a less significant role than does the geometry of the system.

In addition, the long-continued salt layer dissolution boosts the circulation of the hydrothermal fluid: while for the basic scenario the maximum fluid velocity at T2 is 0.353 m/yr, for these two case studies it is around 0.553 m/yr. The values are comparable only with scenarios with the increased permeability of the salt layer:

Case 4B, $k_{horizontal} = k_{vertical} = 10^{-16} \ m^2$ - maximum fluid velocity is 0.591m/yr;

Case 4C, $k_{horizontal} = 10^{-14} \ m^2 ; k_{vertical} = 10^{-16} \ m^2$ - 1.066m/yr.

In an attempt to initiate circulation above the salt sheet, it was expected that the piercement structure would link the two basins separated by the Upper Roan Salt, providing a way for the less dense fluid to rise up. However, this pathway becomes "engaged" straight away by the downwelling heavy brine formed within the salt layer. Even if the Kundelungu layer is ruptured by faulting to the surface, it does not have any significant influence onto the flow (see comparison of Cases 8 and 8A in Appendix 4, Figures A4.1 – A4.3). The only difference that can be identified is a response of the salinity field to the slight upflow in the uppermost part of the fault extension at the very end of the simulation for Case 8A, when the conduit reaches the surface (Figure A4.3(b)). As heat advects much slowly than dissolved salt, this small increase in the fluid velocity in the conduit cannot affect the temperature field, and temperature distributions in all three case studies look practically identical.

The main conclusion, on the basis of the results presented in this section, is that a single piercement structure cannot effectively interconnect the hydrological compartments above and below the Roan Salt in terms of establishing a convective flow between them. Even if different initial conditions are involved, the system behaves similarly to the previously considered case studies, responding to the long-continued salt sheet dissolution rather than to the presence of the permeable extension of the middle master fault.

## 6.6.2 Extension of all master faults towards the surface

Since the previous section showed that a single permeable conduit piercing the low-permeable barrier of Upper Roan and Lower Mwashia strata is insufficient to establish fluid circulation between the two hydrological compartments, in the following scenario, *Case 9*, all three master faults are extended to the contact 'Upper

Mwashia Siliciclastic Member – Kundelungu' (Figure 6.38). The simulation shows that, in this case, the flow dynamics changes profoundly. This is particularly apparent if a comparison with the previous Case 8 is done (Figure 6.39). It is necessary to note beforehand that these results are presented at earlier than the T2 moment, 550 thousand years ('T3' is used as a denotation in figures). When the circulation is triggered in the permeable Kundelungu, the fluid velocities start rising quickly; and towards T2 the numerical process becomes less stable and needs mesh refinement and time step adjustment.

Figure 6.39(b) shows that if the low-permeable Roan and Mwashia strata are ruptured at more than one location, the fluid starts circulating in the upper part of the basin: the fluid rises up the left and right master faults, flows horizontally above the Mwashia layer forming two 'streams' directed towards each other. Then the fluid descends down the central primary fault completing the circuit. At the same time, the interconnection of the upper and lower parts of the basin seems to only slightly affect the flow pattern below the Upper Roan Salt: on the right from the middle master fault, it is practically the same as in the previous scenario Case 8 and it is somewhat different in the left part (Figure 6.40).

Diagrams of temperature and salinity fields (Figure 6.41-Figure 6.42) display the reason causing the lateral fluid flow in the Kundelungu layer: one can see hot saline brine rising along left and right master faults (Figure 6.41 (b),Figure 6.42 (b)). This creates a horizontal density gradient triggering the lateral fluid lfow. From Figure 6.43 it is also visible that the saline plume having risen up the left fault is then drawn horizontally towards the central primary conduit. Thus, in Case 9, for the first time, the advective transport of the saline brine into the part of the basin above the Upper Roan Salt is observed; all previous case studies showed only diffusive transfer of the dissolved salt upwards.

The main result arising from the case study described here is that to obtain an effective interconnection of the upper and lower parts of the basin, the low permeable Upper Roan and Lower Mwashia strata should be ruptured in more than one location. If this happens, then fluid circulation is established in both the strata underlying and overlying the salt sheet and the faults provide pathways for hot saline brine access into the permeable Kundelungu strata.
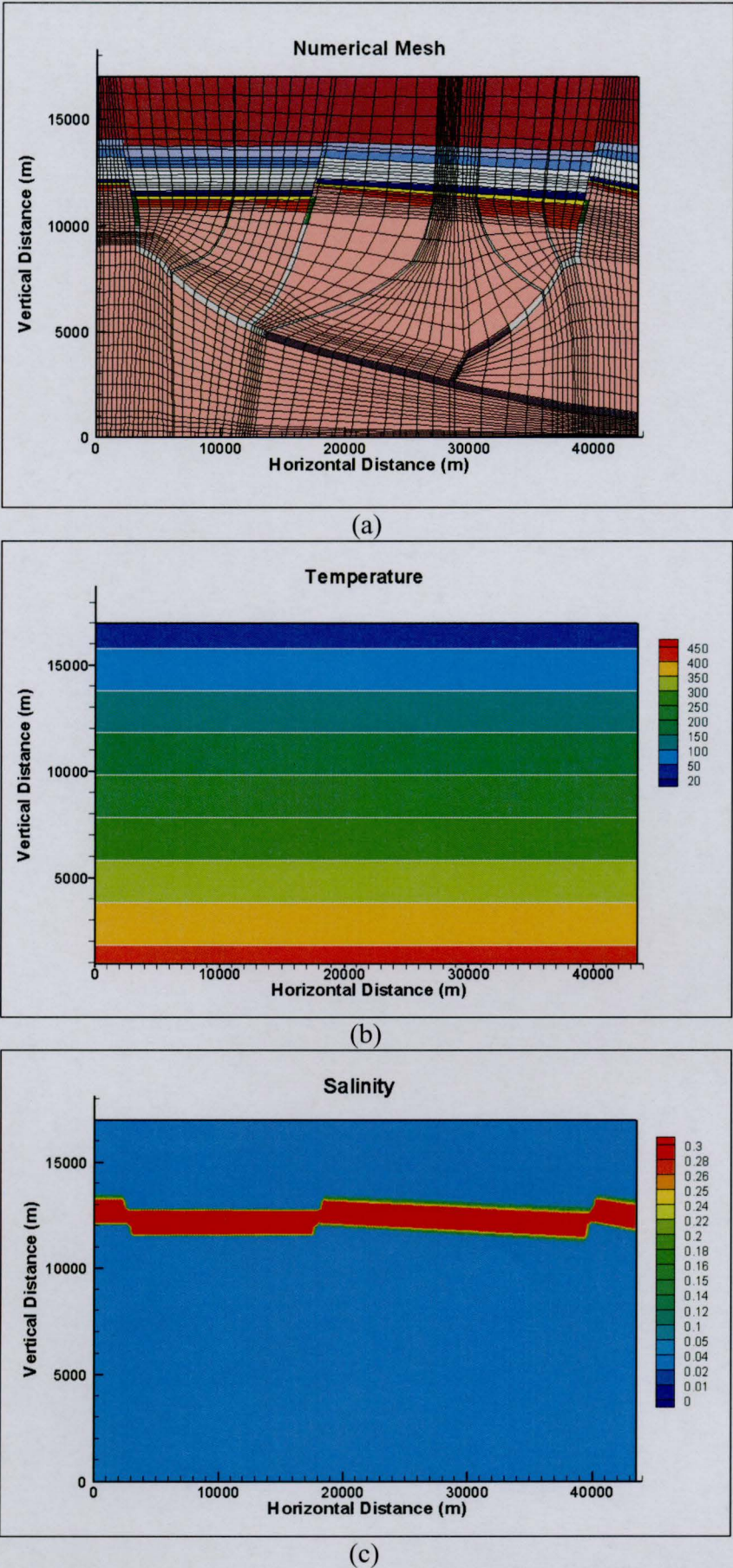
(a)



(b)



(c)

**Figure 6.1 ZCB. (a) Two-dimensional finite-element mesh built for the basic hydrostratigraphy of the section. (b) Initial temperature distribution. (c) Initial salinity distribution.**
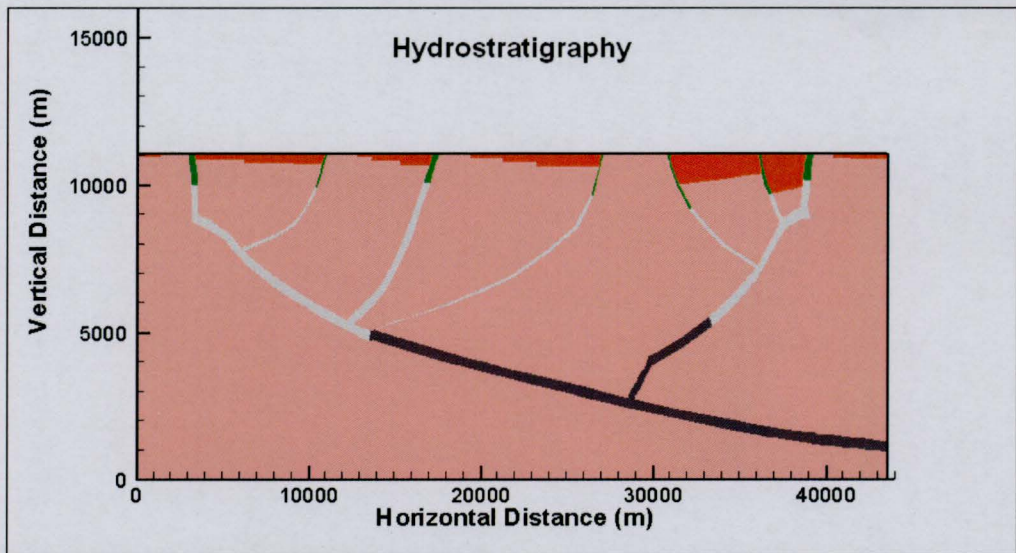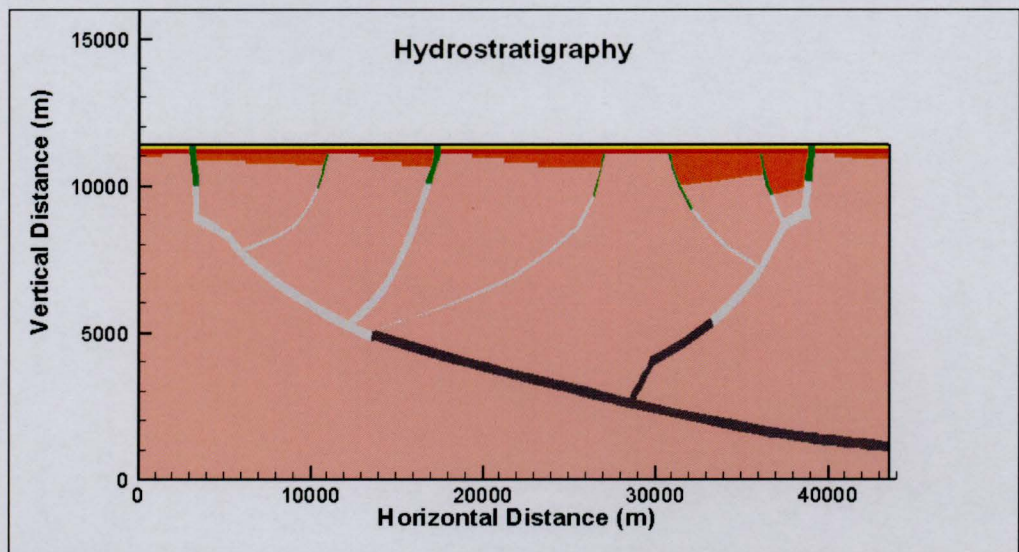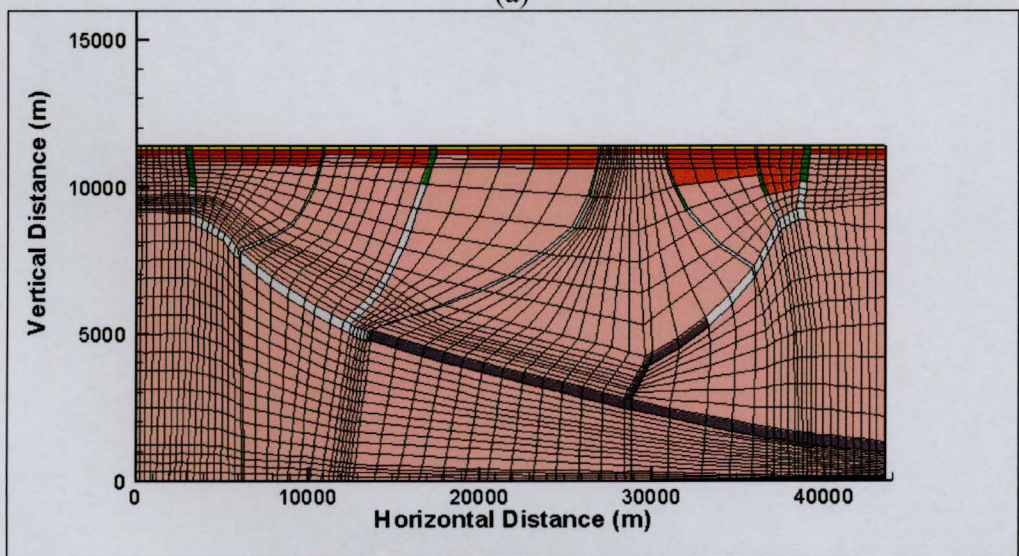
**Figure 6.2 ZCB. Case 1. "Rift initiation" stage. Numerical hydrostratigraphy of the model section.**

(a)

(b)

**Figure 6.3 ZCB. Case 2. "Rift climax" stage. (a) Numerical hydrostratigraphy of the model section. (b) Modified finite element mesh.**
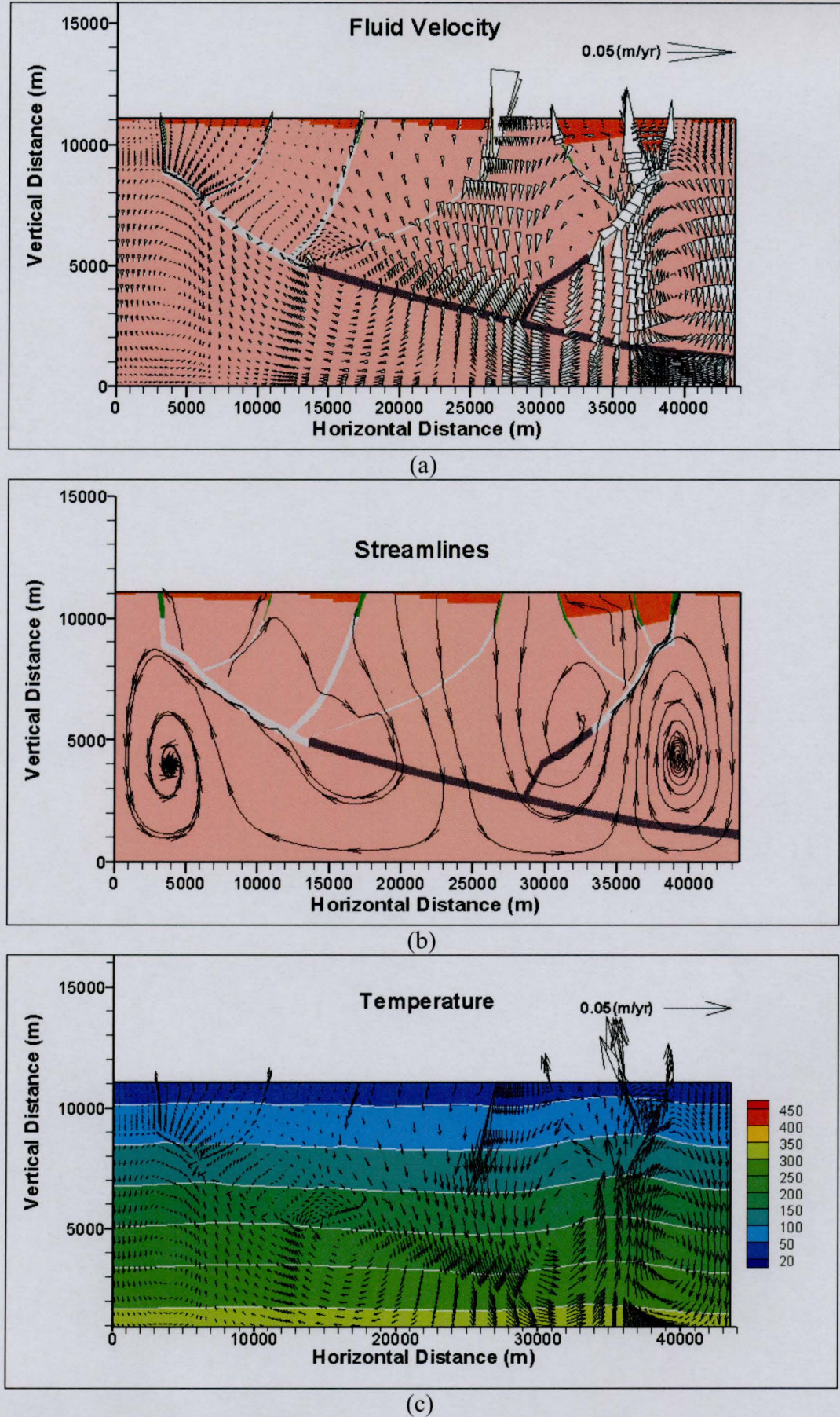
152

(a)



(b)



(c)

**Figure 6.4 ZCB. Case 1. "Rift initiation" stage at T2. (a) Fluid velocities, (b) streamlines and (c) temperature distribution. (The spiral shape of the streamlines is a feature of the graphic software, Tecplot, used for visualization)**
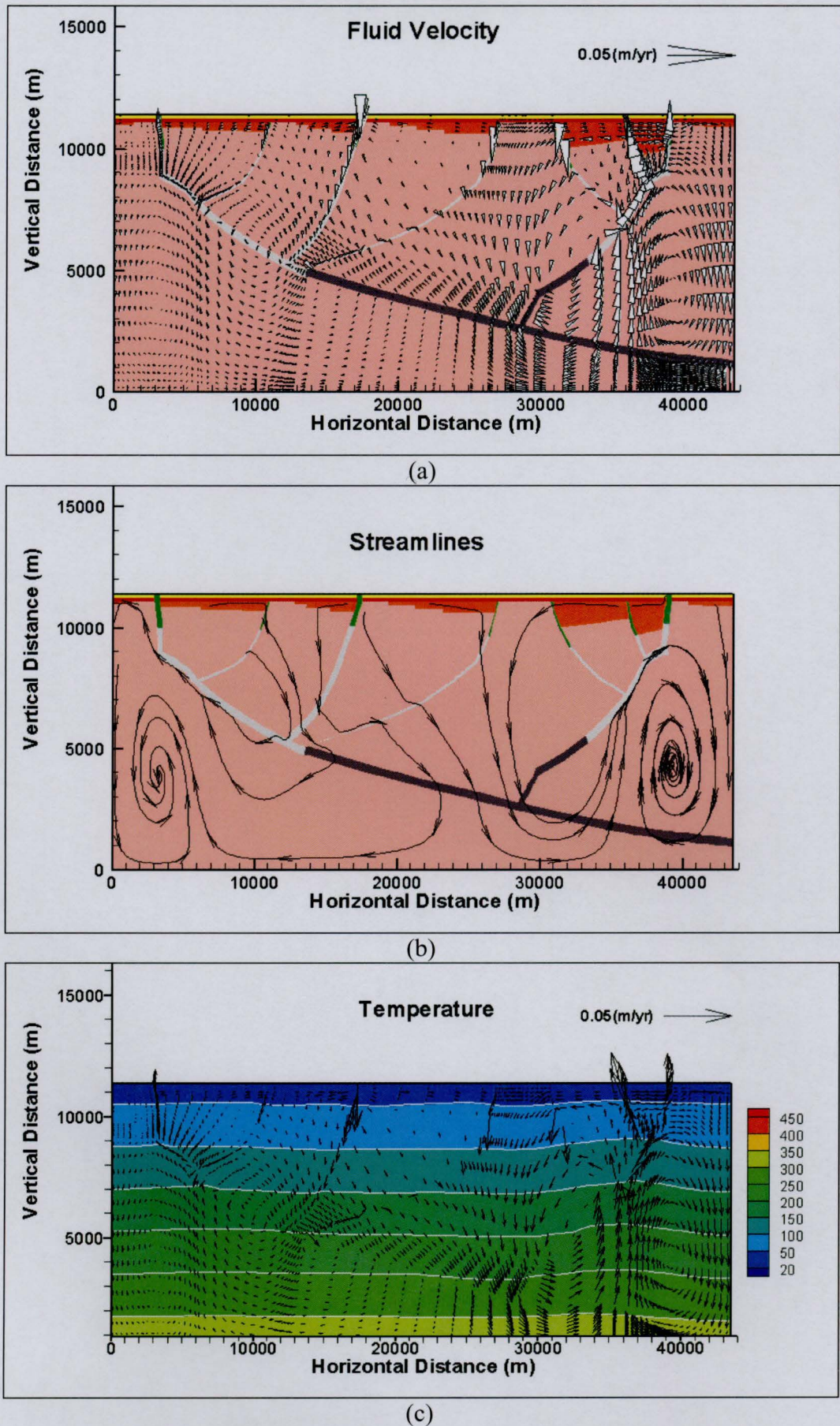
(a)

(b)

(c)

**Figure 6.5 ZCB. Case 2. "Rift climax" stage at T2. (a) Fluid velocities, (b) streamlines, and (c) temperature distribution.**
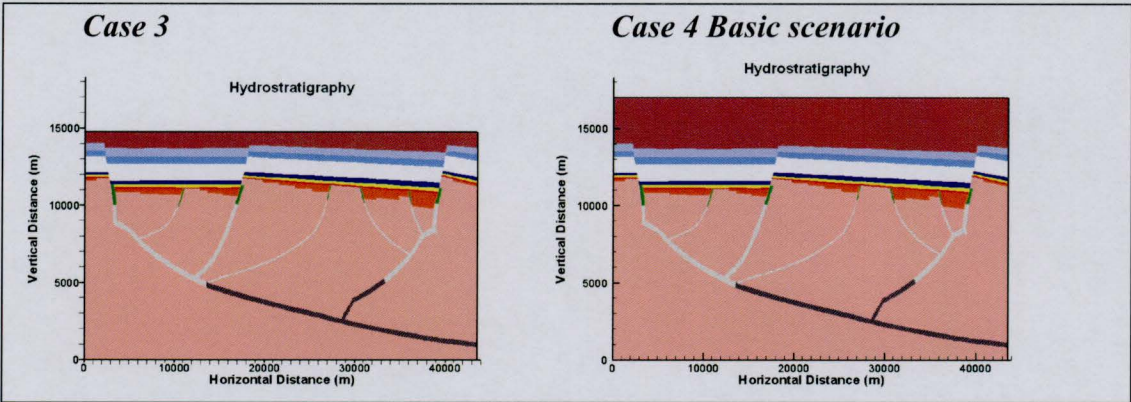
**Figure 6.6 ZCB. Case 3. The initial stage of the Kundelungu deposition. Numerical hydrostratigraphy of the model section compared with the basic hydrostratigraphy.**
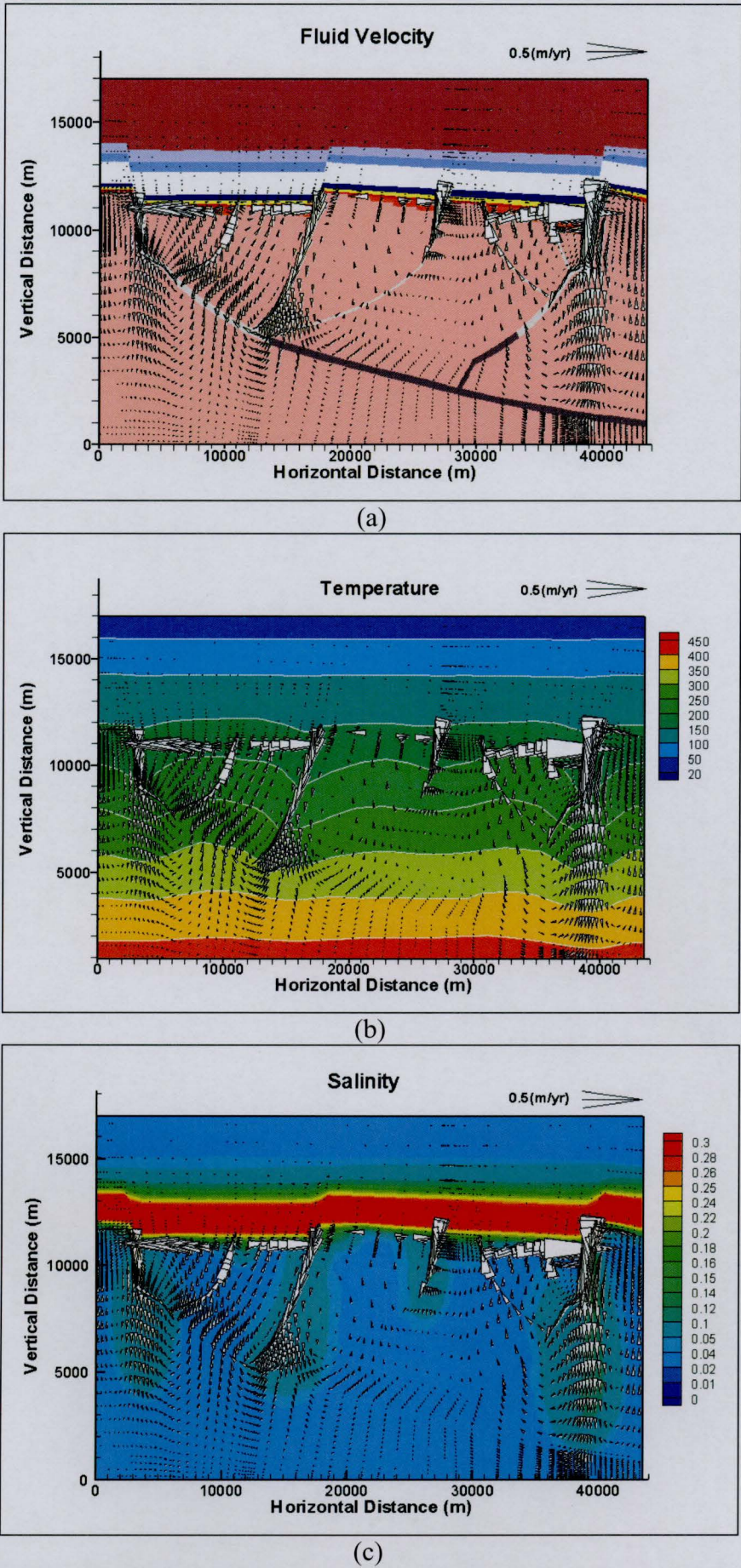
(a)



(b)



(c)

**Figure 6.7 ZCB. Case 4. Basic scenario at T1. (a) Fluid velocities, (b) temperature and (c) salinity distributions.**
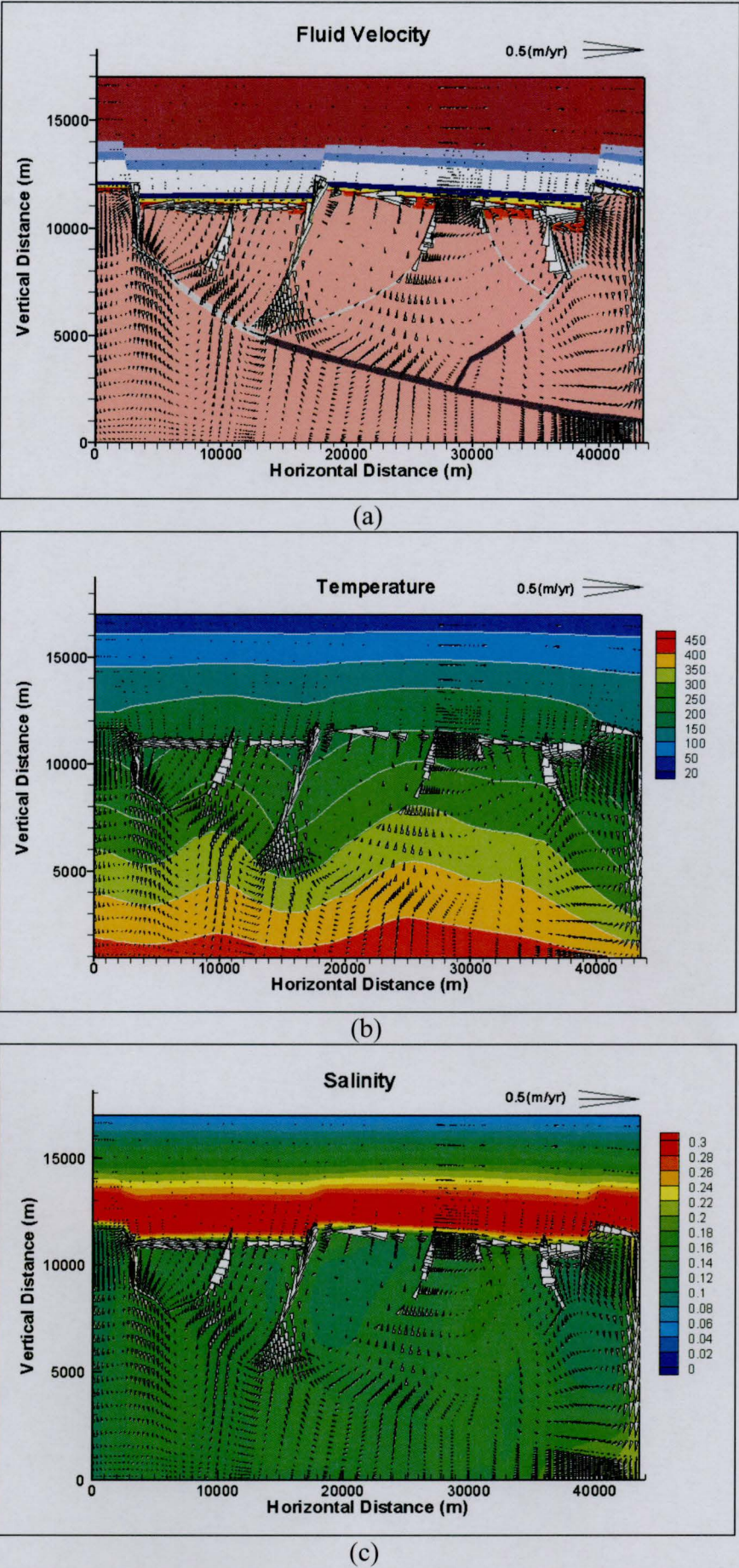
(a)

(b)

(c)

**Figure 6.8 ZCB. Case 4. Basic scenario at T2. (a) Fluid velocities, (b) temperature and (c) salinity distributions.**
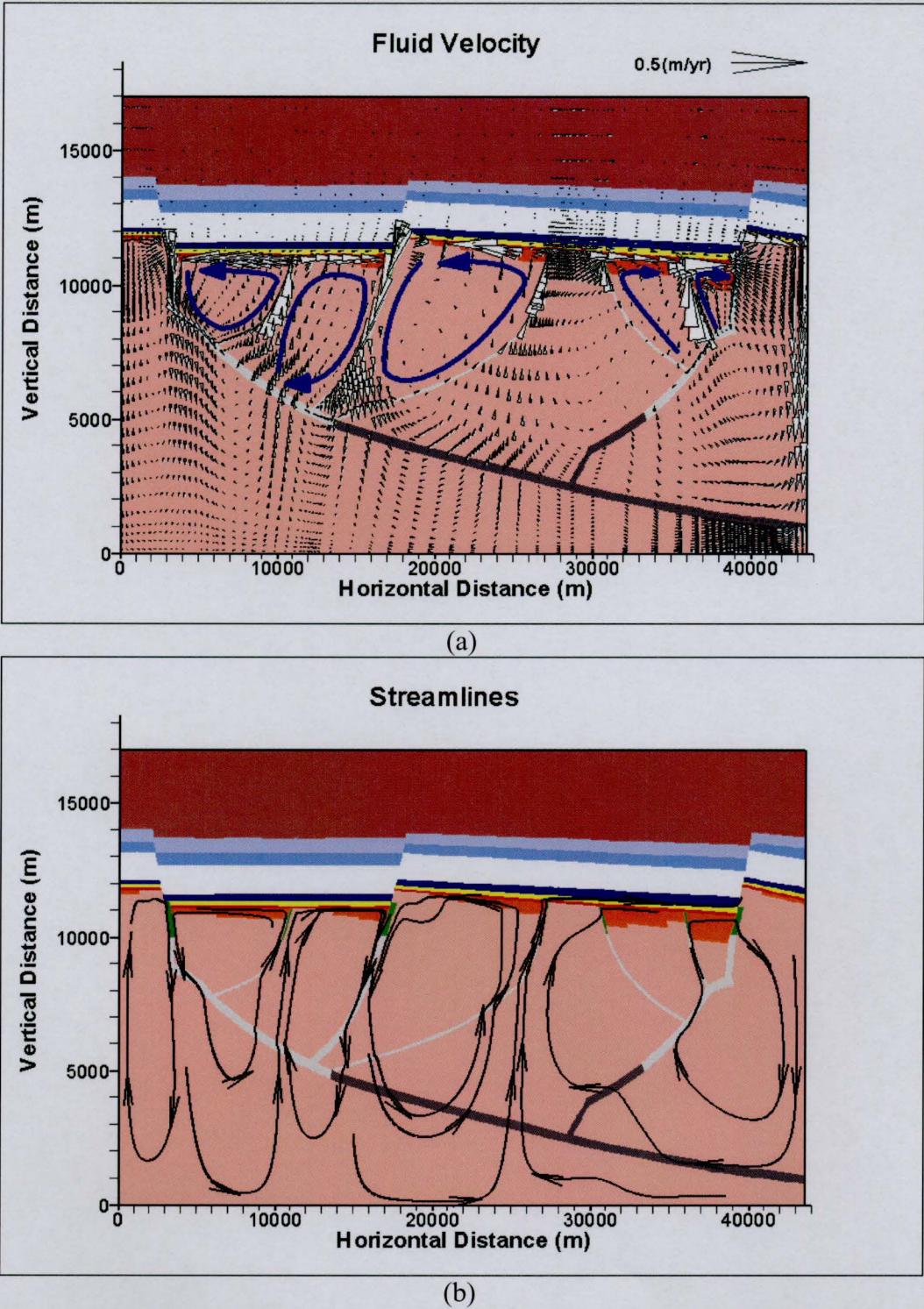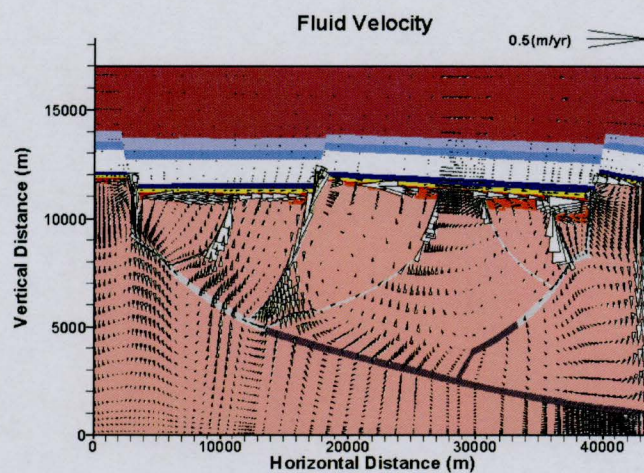
**Figure 6.9 ZCB. Case 4. Basic scenario at T2. (a) Fluid circulation direction in the permeable units and (b) streamlines.**

(a)



(b)



(c)
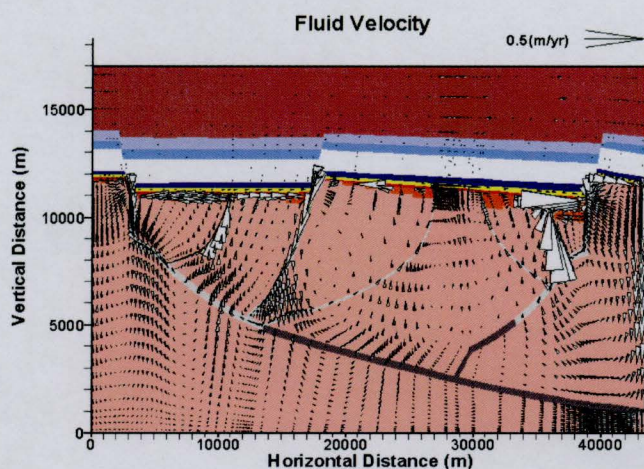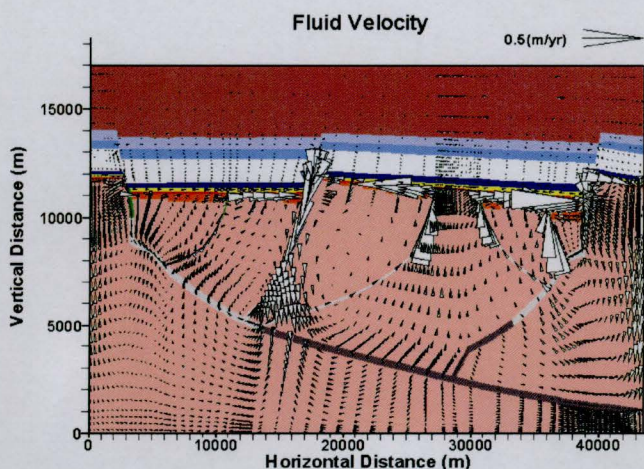
**Figure 6.10 ZCB. Effect of the salt layer isotropy/anisotropy. Comparison of the fluid flow fields at T2. (a) Case 4 (the salt layer is anisotropic, $k_{horizontal}=10^{-16}\ m^2$, $k_{vertical}=10^{-18}\ m^2$); (b) Case 4A (the salt layer is isotropic, $k_{horizontal}=k_{vertical}=10^{-18}\ (m^2)$); (c) Case 4B (the salt layer is isotropic, $k_{horizontal}=k_{vertical}=10^{-16}\ (m^2)$).**

**Case 4**



(a)

**Case 4A**



(b)

**Case 4B**



(c)

**Figure 6.11 ZCB. Effect of the salt layer isotropy/anisotropy. Comparison of temperature distributions at T2. (a) Case 4 (the salt layer is anisotropic, $k_{horizontal} = 10^{-16} \ m^2, k_{vertical} = 10^{-18} \ m^2$); (b) Case 4A (the salt layer is isotropic, $k_{horizontal} = k_{vertical} = 10^{-18} \ (m^2)$); (c) Case 4B (the salt layer is isotropic, $k_{horizontal} = k_{vertical} = 10^{-16} \ (m^2)$).**

**Case 4**



(a)

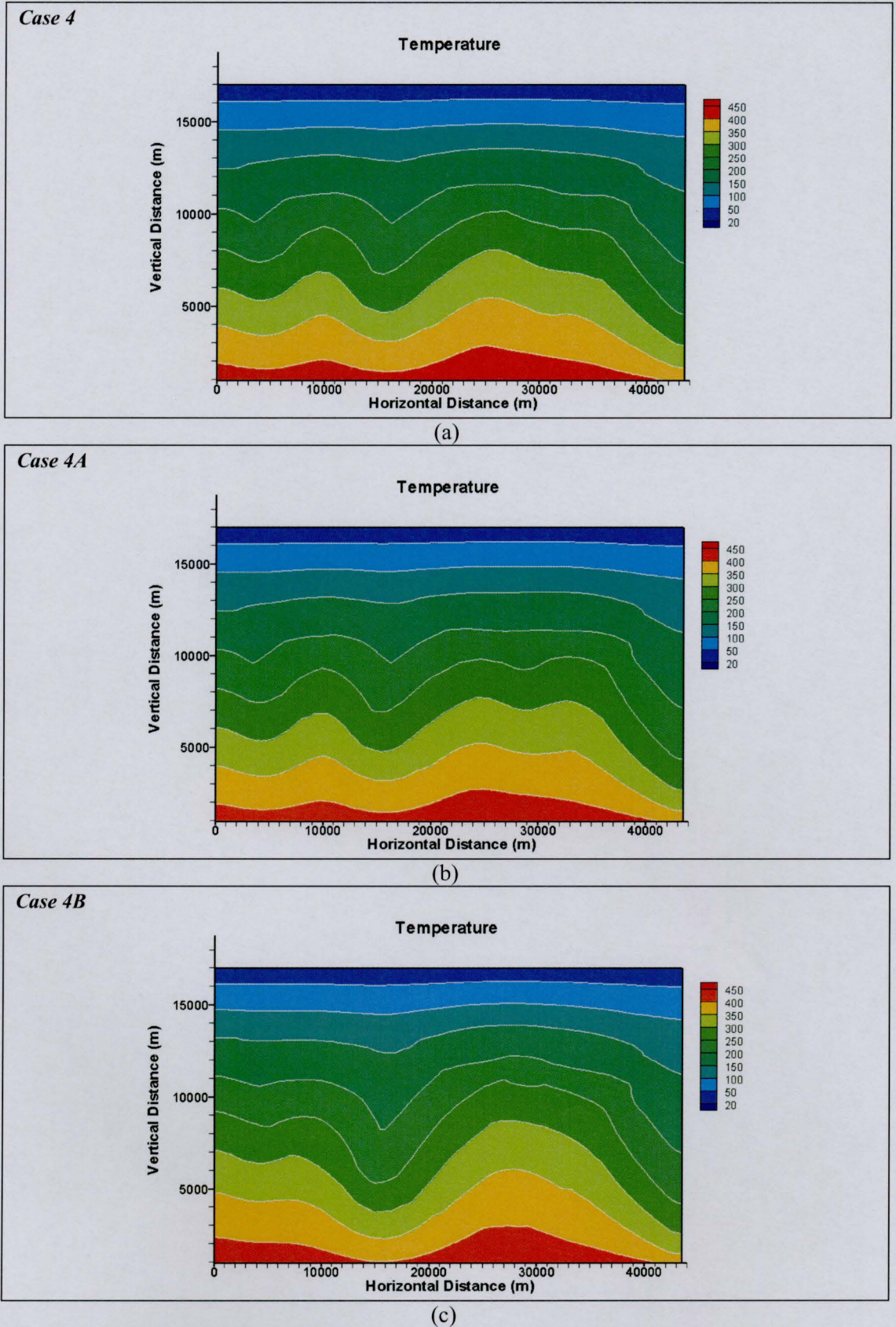**Case 4A**



(b)

**Case 4B**



(c)
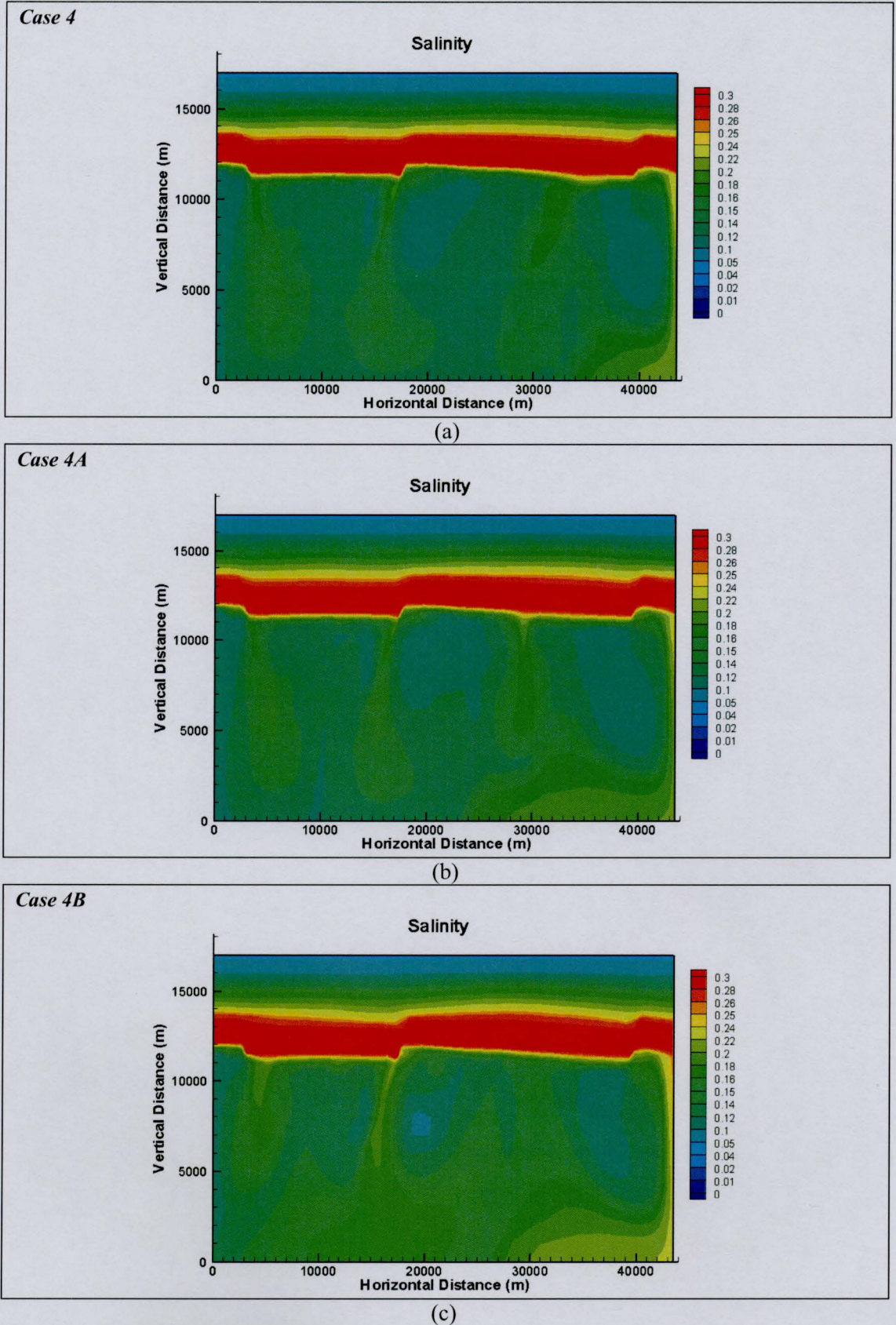
**Figure 6.12 ZCB. Effect of the salt layer isotropy/anisotropy. Comparison of salinity distributions at T2. T2. (a) Case 4 (the salt layer is anisotropic, $k_{horizontal} = 10^{-16}\ m^2, k_{vertical} = 10^{-18}\ m^2$); (b) Case 4A (the salt layer is isotropic, $k_{horizontal} = k_{vertical} = 10^{-18}\ (m^2)$); (c) Case 4B (the salt layer is isotropic, $k_{horizontal} = k_{vertical} = 10^{-16}\ (m^2)$).**

(a)
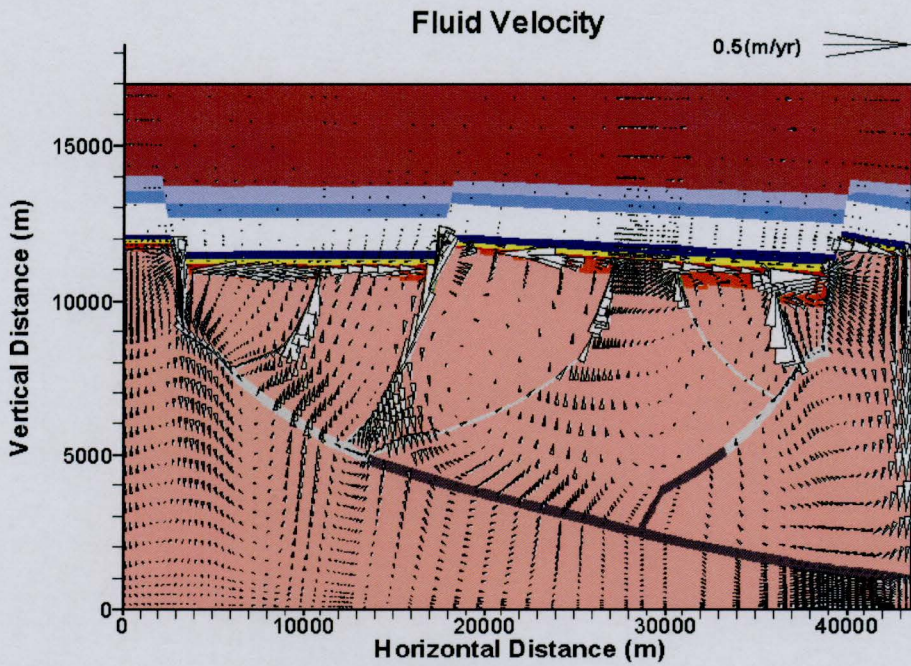


(b)

**Figure 6.13 ZCB. Effect of the high permeability of the salt layer. Comparison of the fluid flow fields at T2. (a) Case 4** $k_{horizontal} = 10^{-16}\ m^2$, $k_{vertical} = 10^{-18}\ m^2$**); (b) Case 4C** ($k_{horizontal} = 10^{-14}\ m^2$, $k_{vertical} = 10^{-16}\ m^2$**).**

*Case 4*



(a)

*Case 4C*



(b)

**Figure 6.14 ZCB. Effect of the high permeability of the salt layer. Streamlines comparison at T2.**
**(a)      Case      4      ( $k_{horizontal} = 10^{-16} \ m^2, k_{vertical} = 10^{-18} \ m^2$ );      (b)      Case      4C**
**( $k_{horizontal} = 10^{-14} \ m^2, k_{vertical} = 10^{-16} \ m^2$ ).**

**Case 4**



(a)
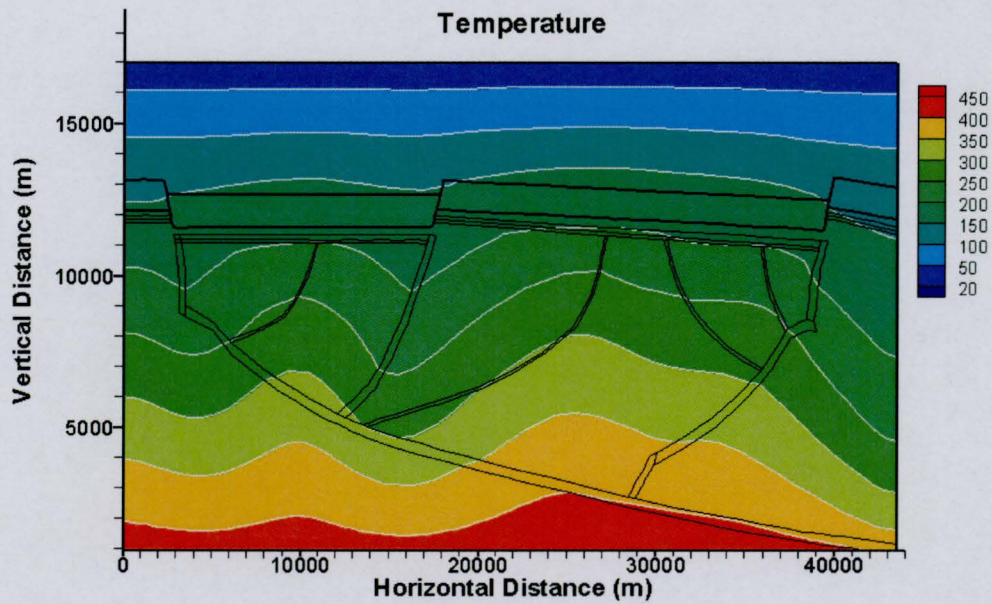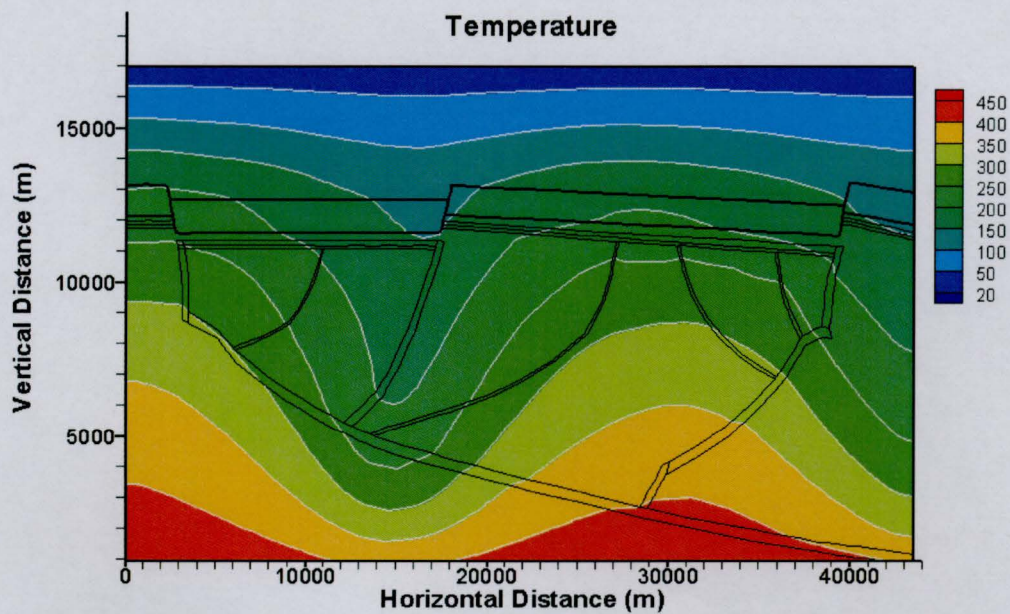
**Case 4C**



(b)

**Figure 6.15 ZCB. Effect of the high permeability of the salt layer. Comparison of temperature fields at T2. (a) Case 4** $k_{horizontal} = 10^{-16} \ m^2, k_{vertical} = 10^{-18} \ m^2$ **); (b) Case 4C** ( $k_{horizontal} = 10^{-14} \ m^2, k_{vertical} = 10^{-16} \ m^2$ **).**
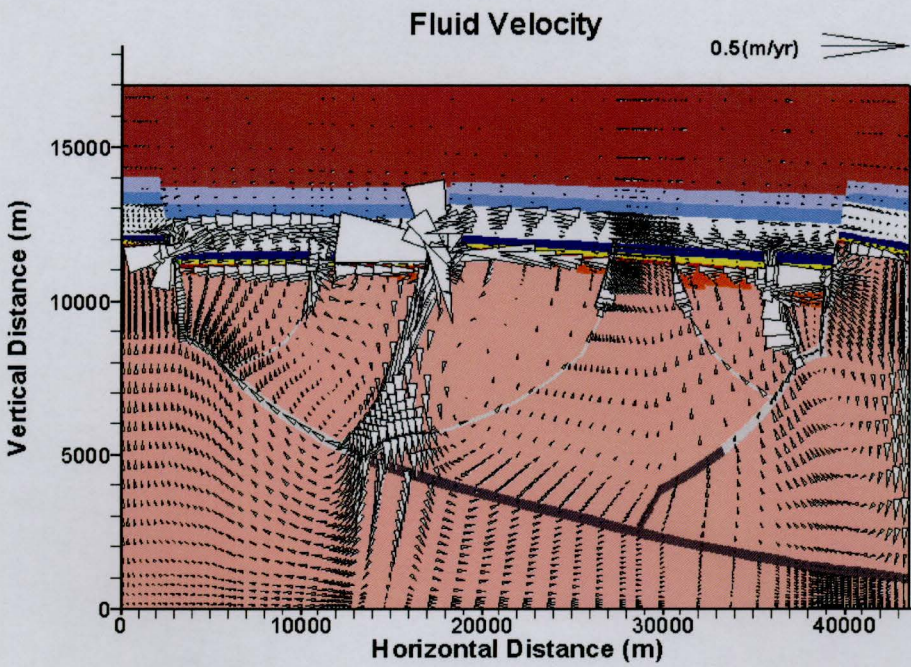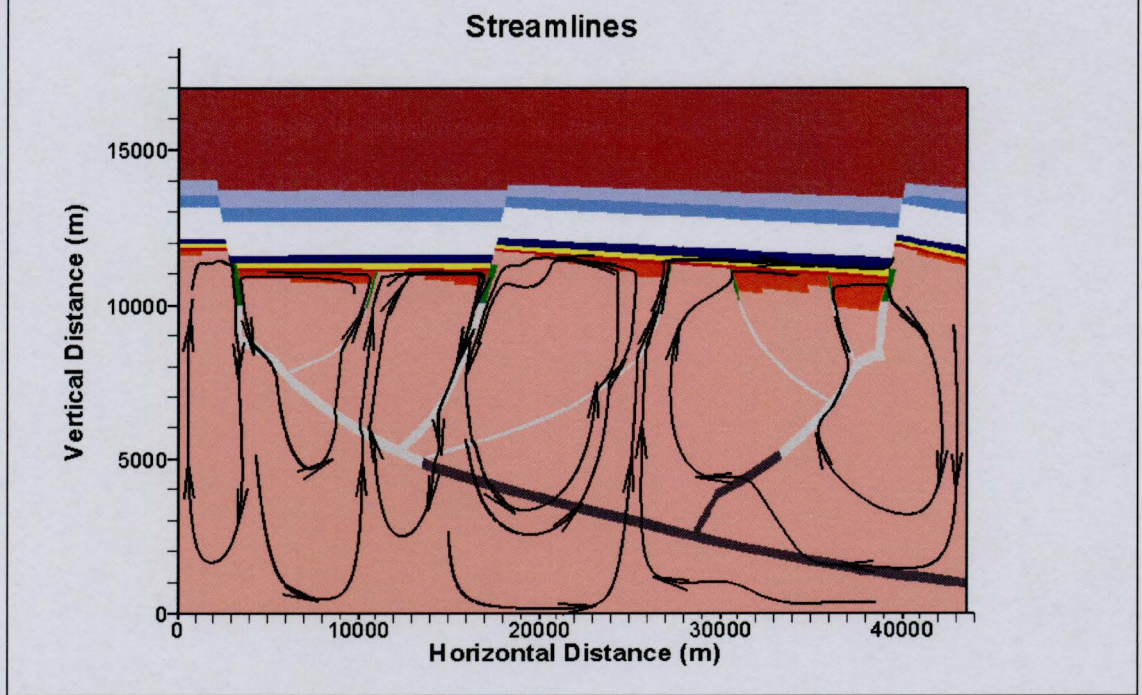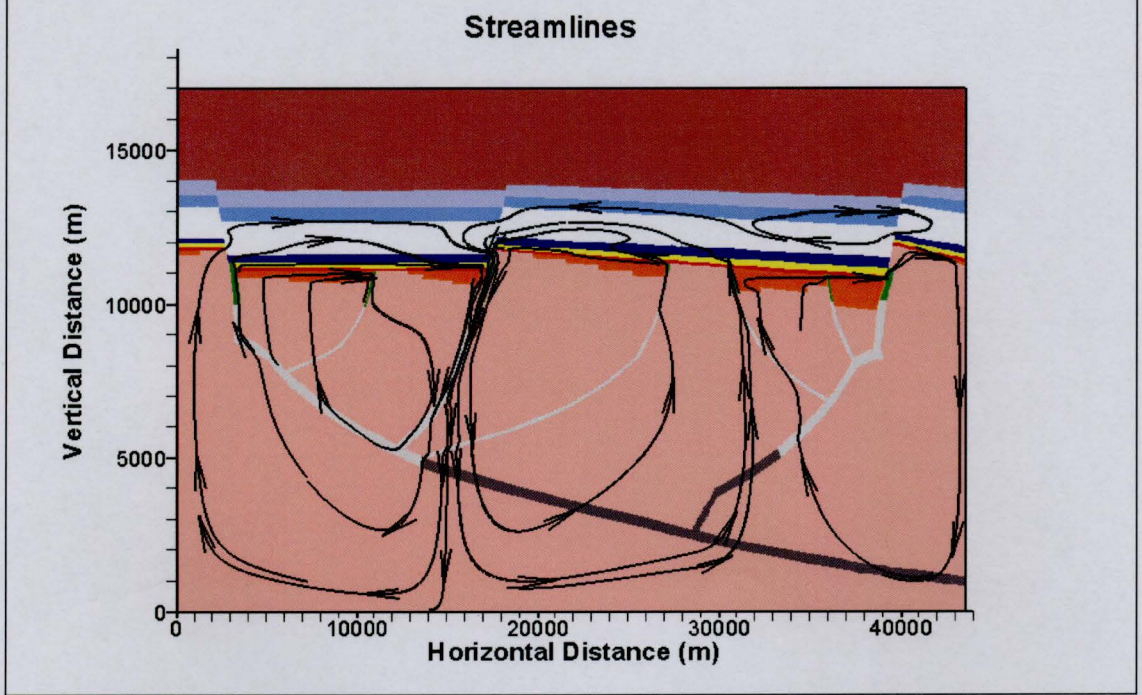
*Case 4*



(a)
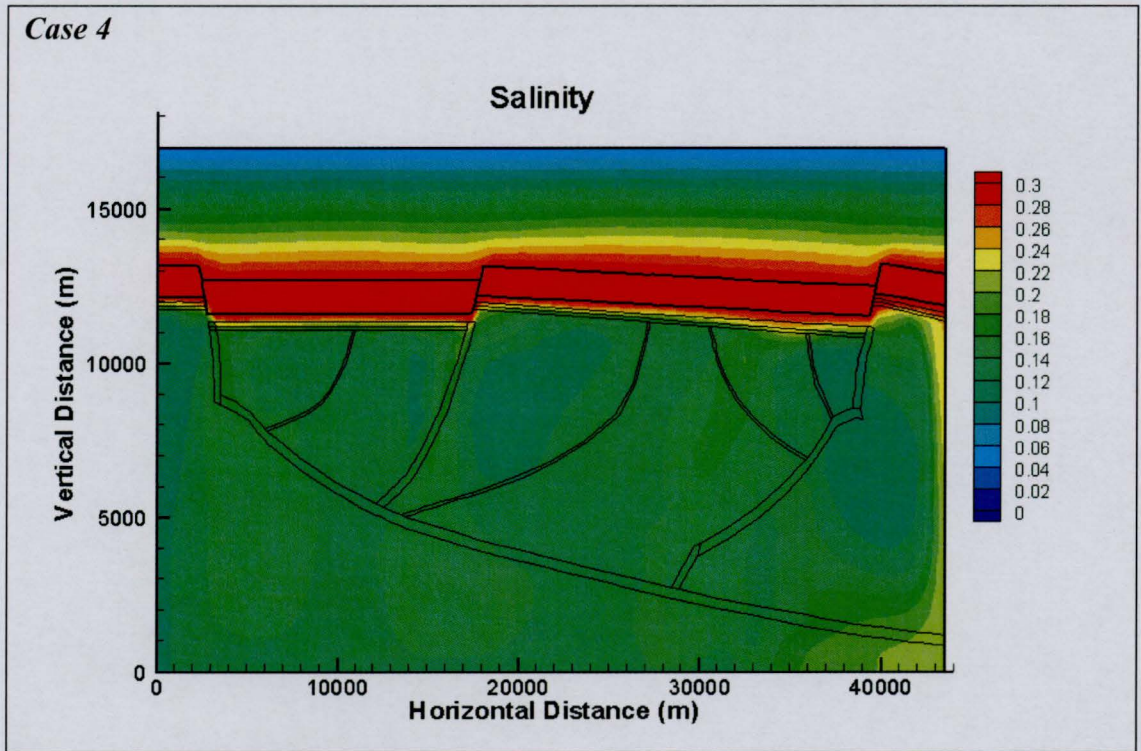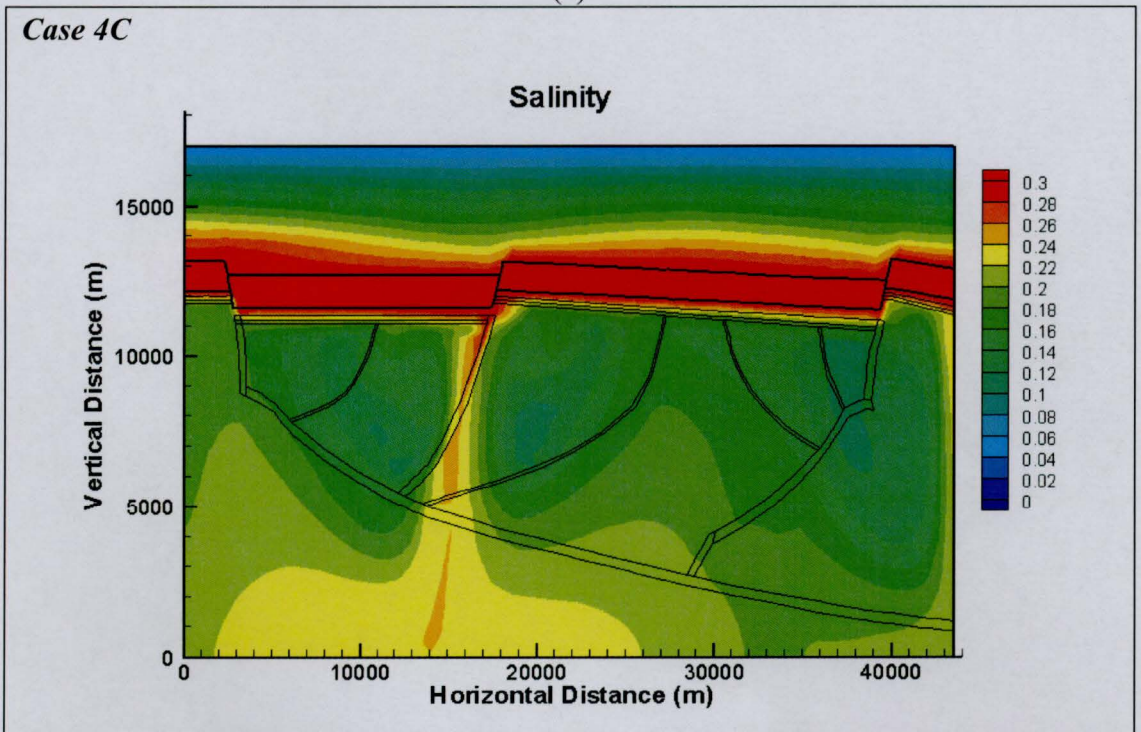
*Case 4C*



(b)

**Figure 6.16 ZCB. Effect of the high permeability of the salt layer. Comparison of salinity fields at T2. (a) Case 4** $k_{horizontal}=10^{-16}\ m^2$, $k_{vertical}=10^{-18}\ m^2$); **(b) Case 4C** ($k_{horizontal}=10^{-14}\ m^2$, $k_{vertical}=10^{-16}\ m^2$).

(a)



(b)
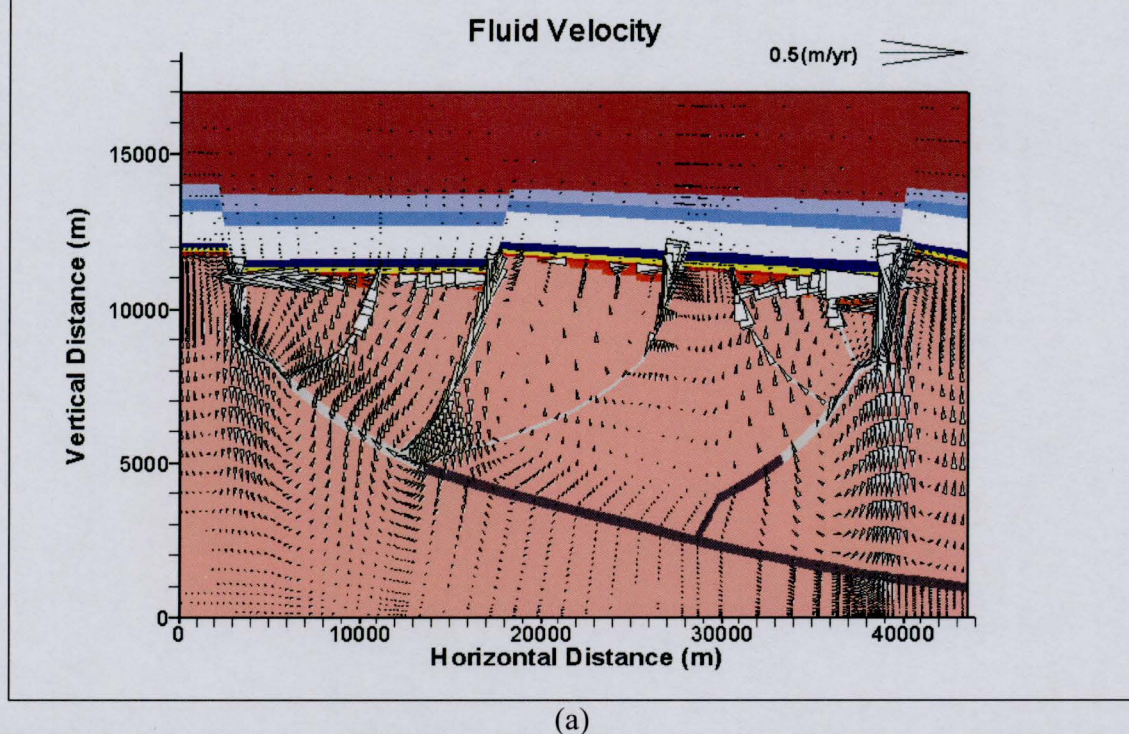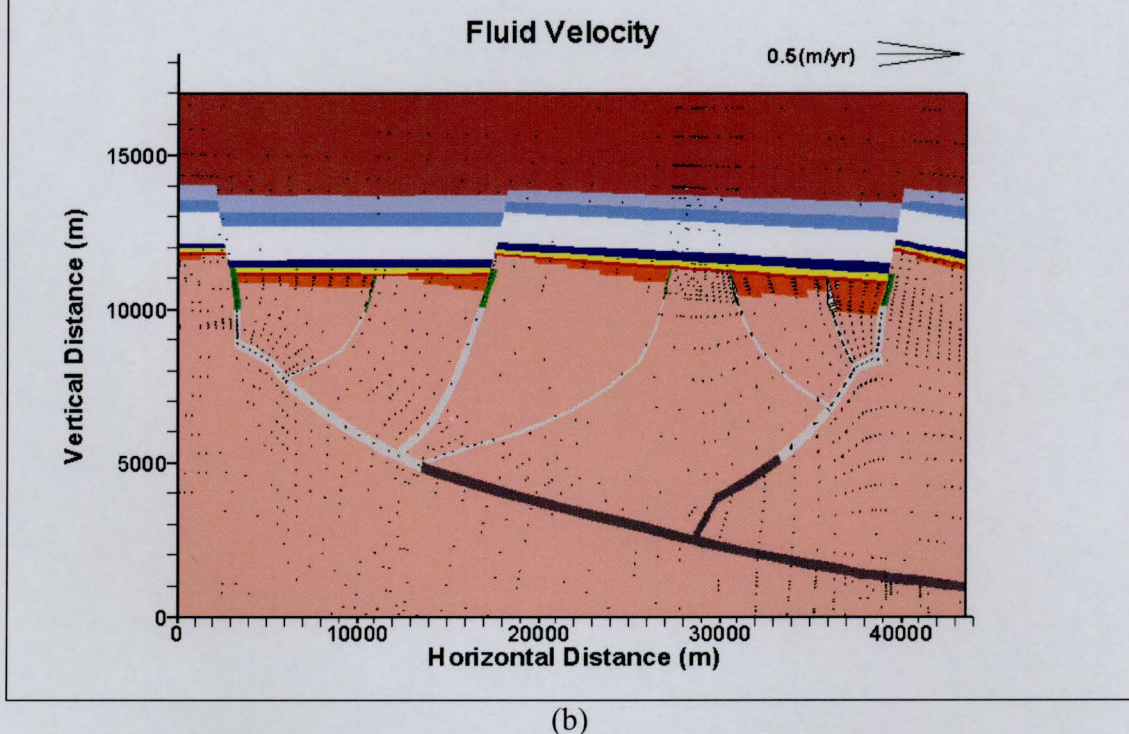
**Figure 6.17 ZCB. Effect of salt transport. Comparison of fluid velocity fields at T1. (a) Case 4 (basic scenario); (b) Case 5 (fresh water scenario).**
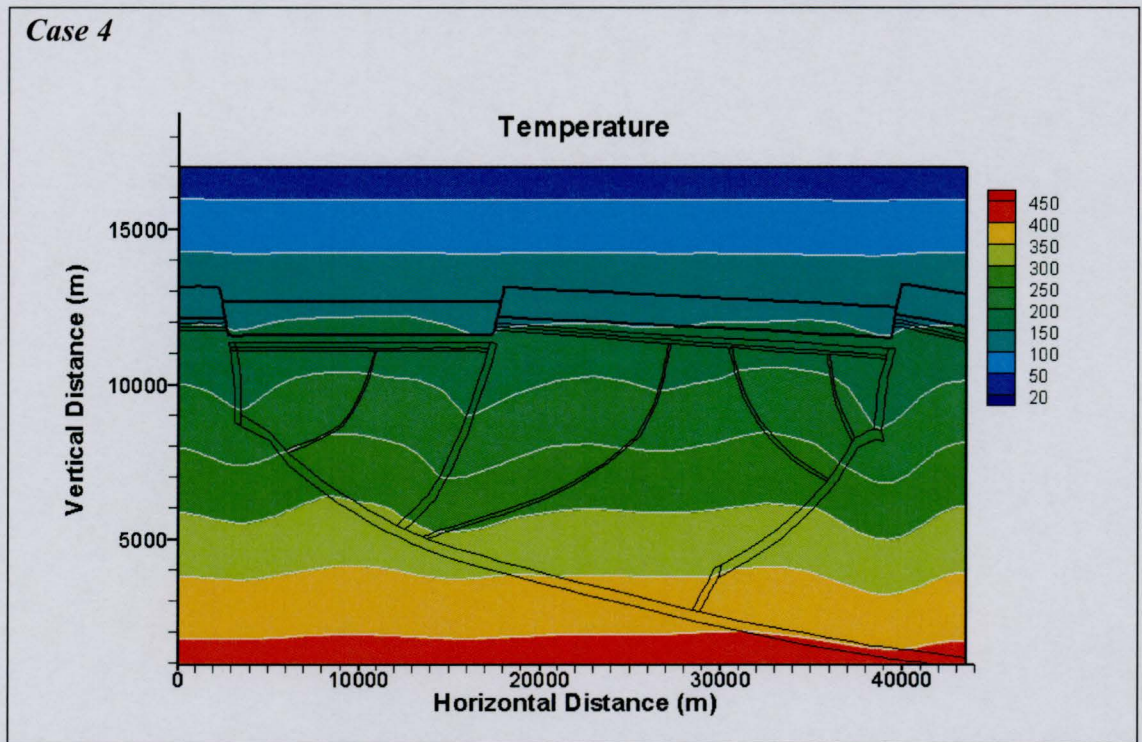
*Case 4*



(a)
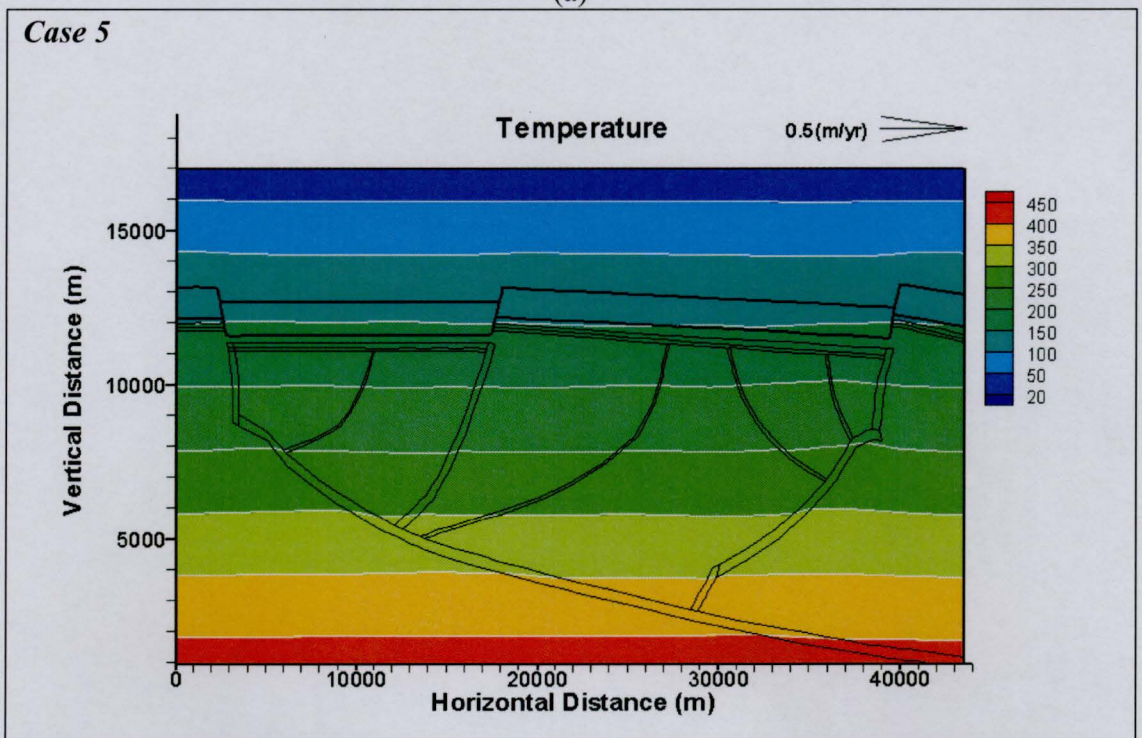
*Case 5*



(b)

**Figure 6.18 ZCB. Effect of salt transport. Comparison of temperature fields at T1. (a) Case 4 (basic scenario); (b) Case 5 (fresh water scenario).**

*Case 4*



(a)

*Case 5*



(b)
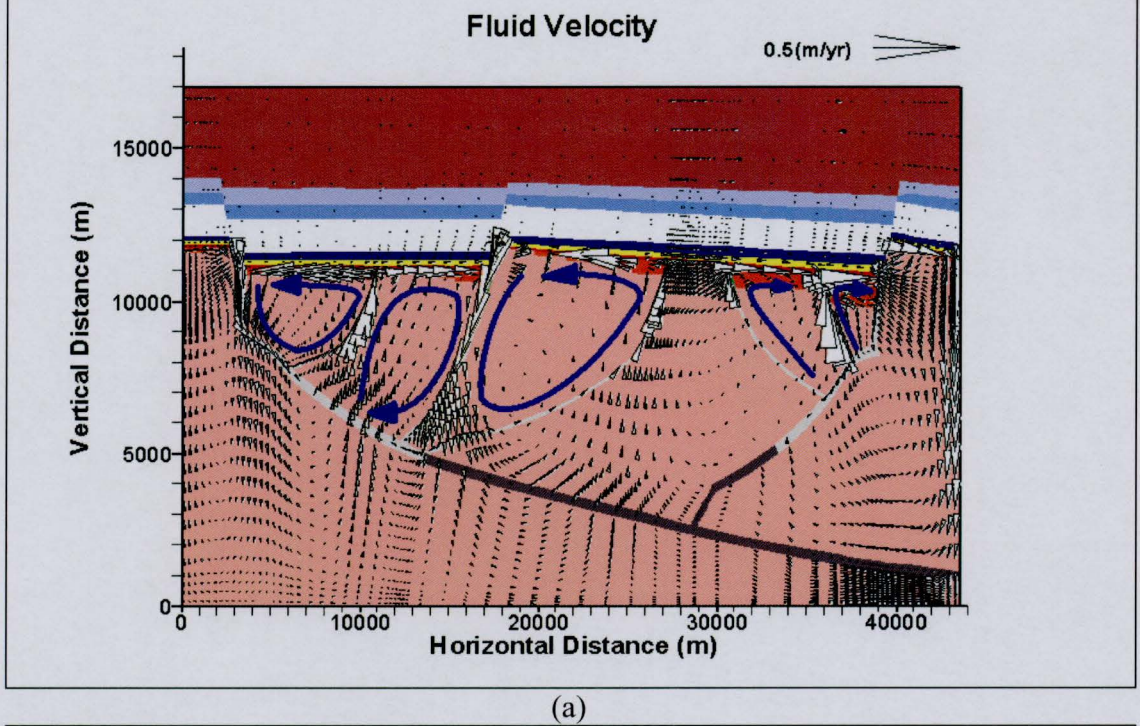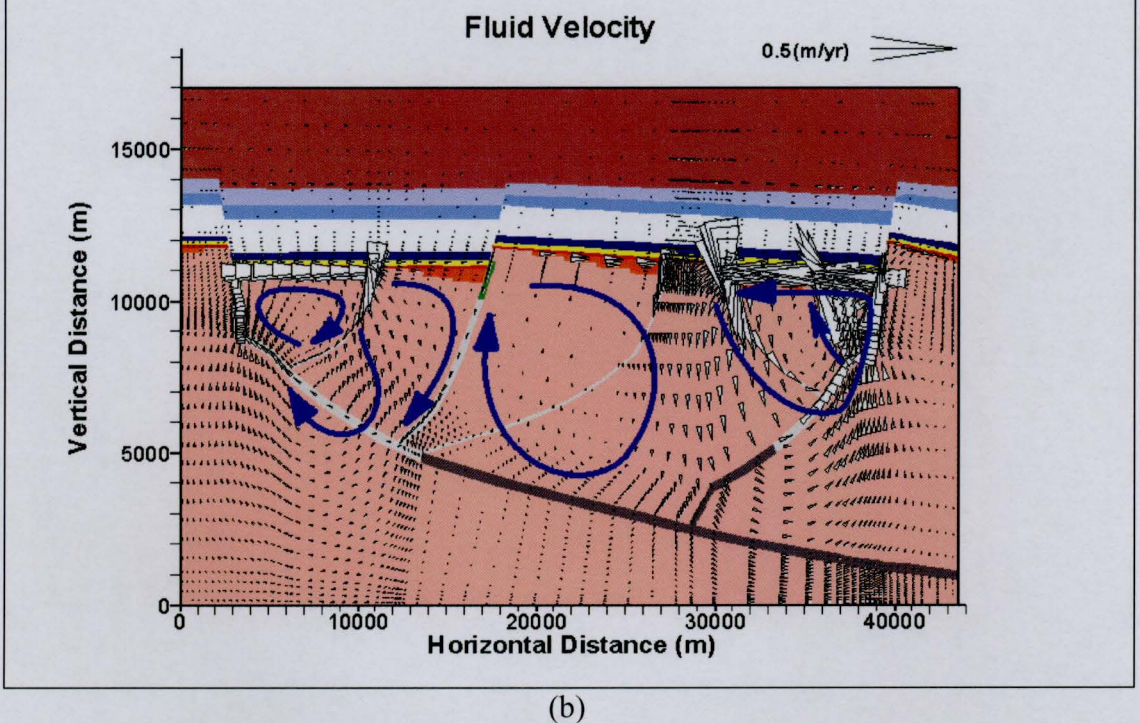
**Figure 6.19 ZCB. Effect of salt transport. Comparison of fluid velocity fields and circulation patterns in permeable units at T2. (a) Case 4 (basic scenario); (b) Case 5 (fresh water scenario).**

*Case 4*



(a)

*Case 5*



(b)
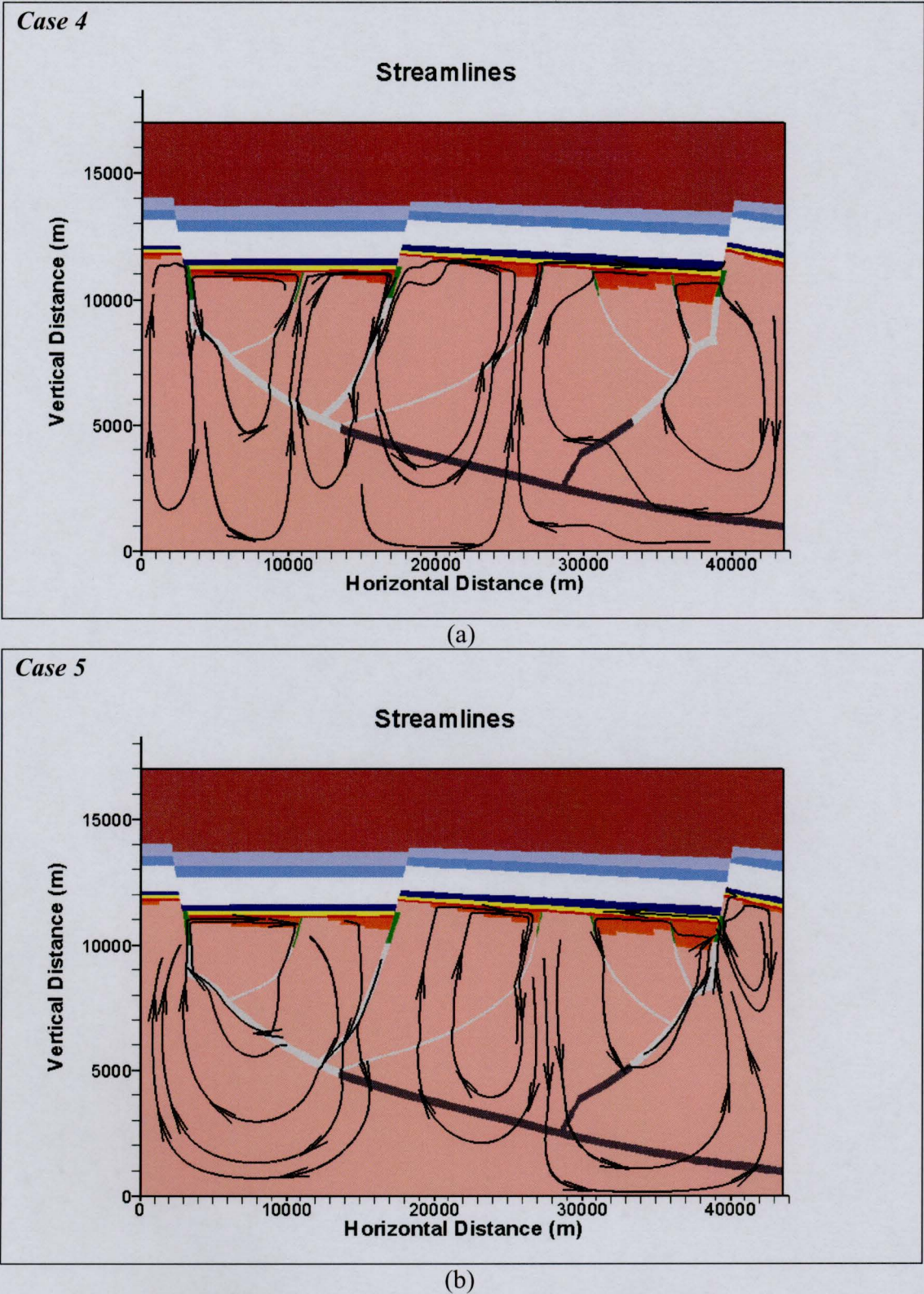
**Figure 6.20 ZCB. Effect of salt transport. Streamlines at T2. (a) Case 4 (basic scenario); (b) Case 5 (fresh water scenario).**
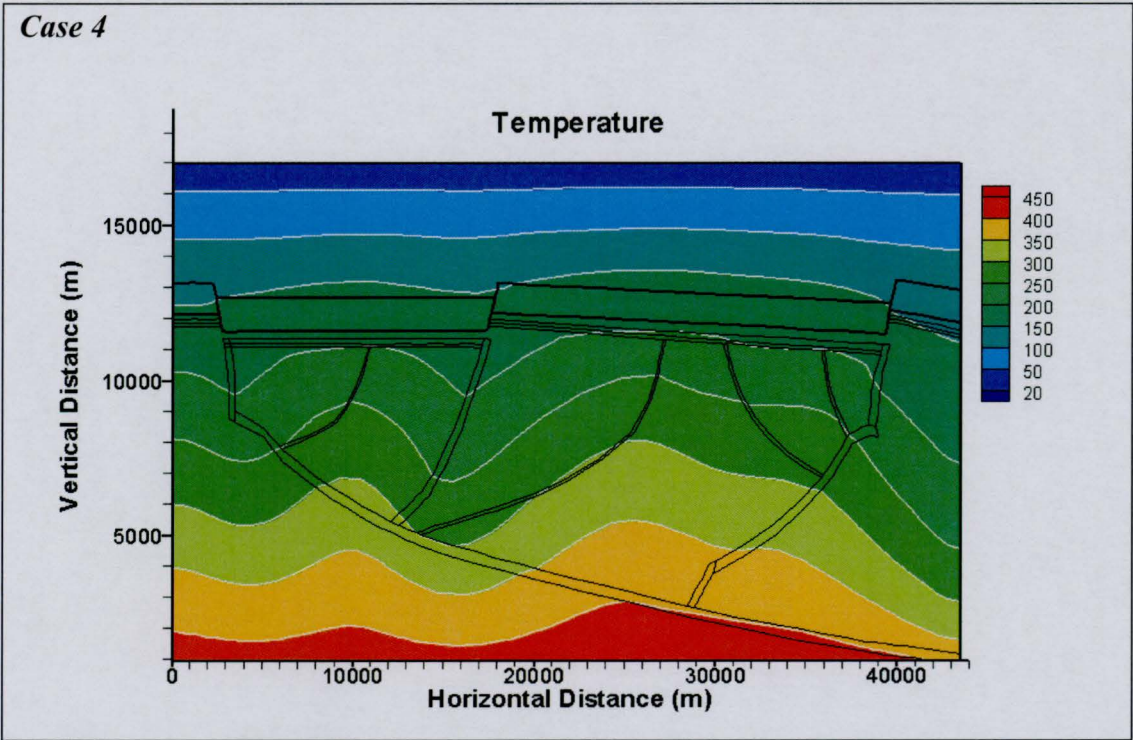
**Case 4**



(a)
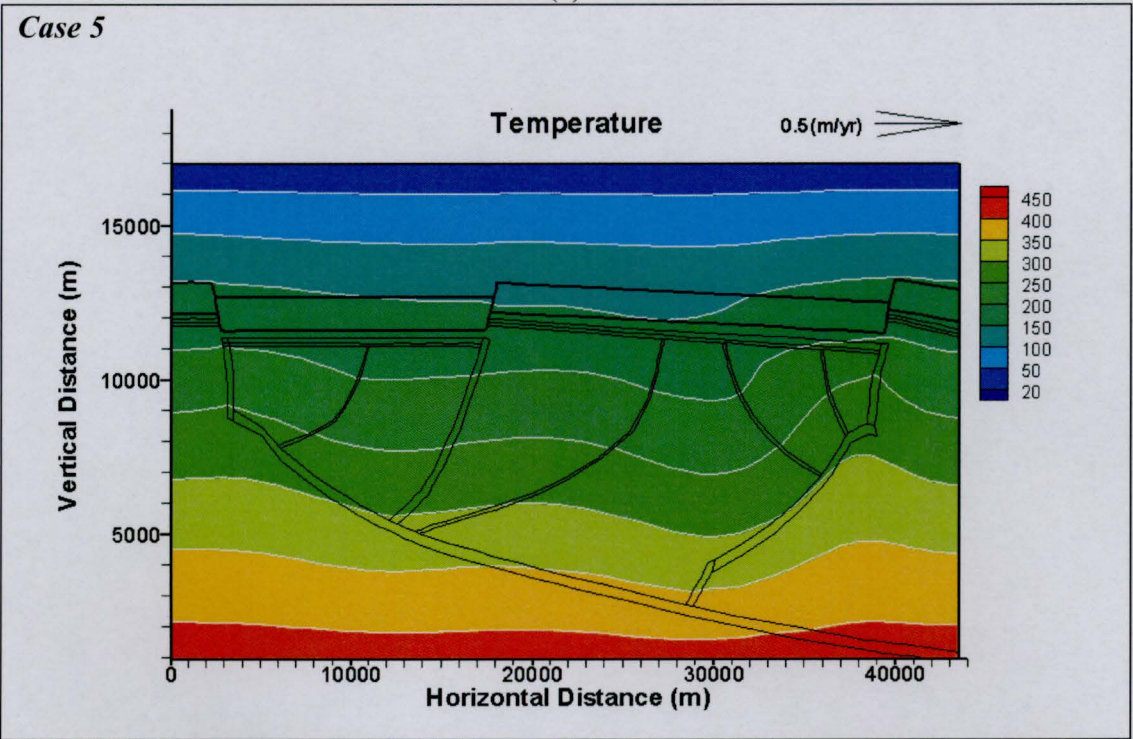
**Case 5**



(b)

Figure 6.21 ZCB. Effect of salt transport. Comparison of temperature fields at T2. (a) Case 4 (basic scenario); (b) Case 5 (fresh water scenario).

170

(a)



(b)
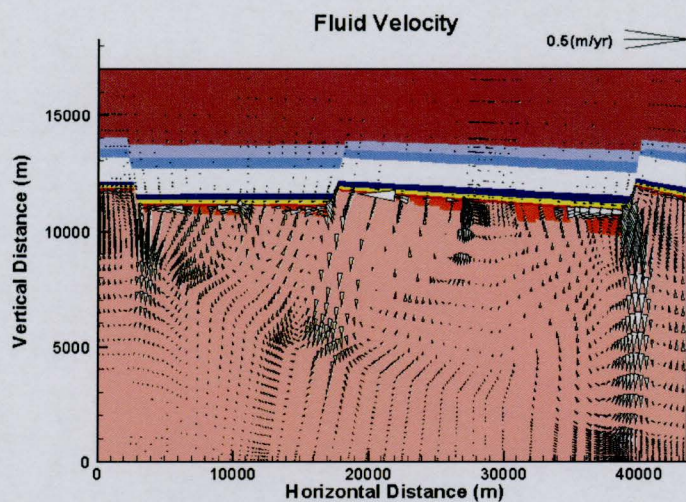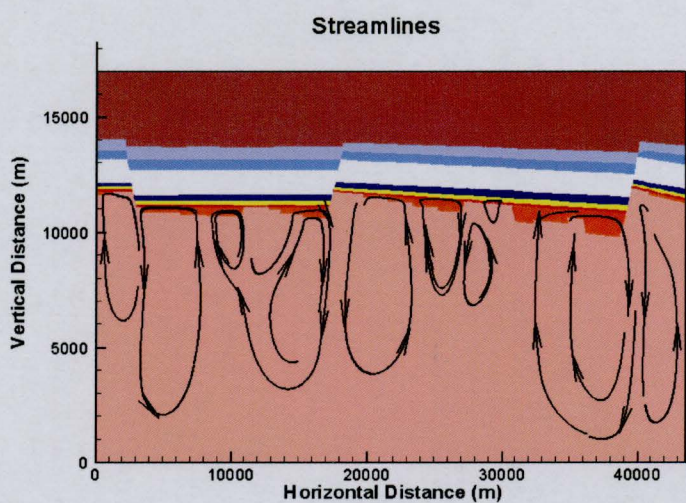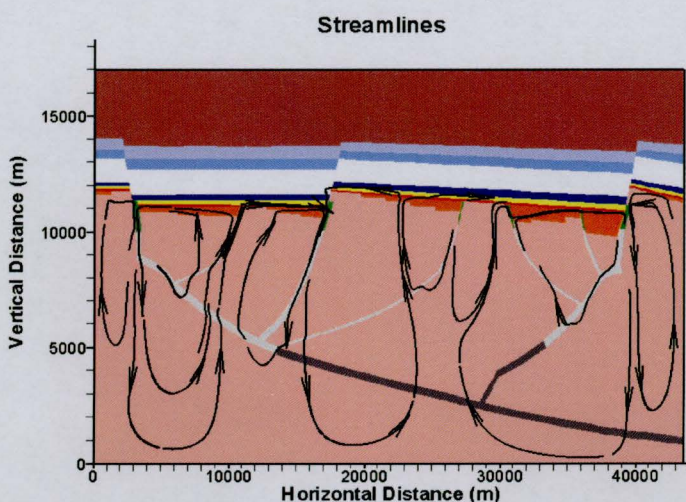


(c)

**Figure 6.22 ZCB. Fault network effect at T1. (a) Case 6 (no permeable faults) fluid velocities and (b) streamlines compared with (c) the streamline pattern for the basic scenario, Case 4.**
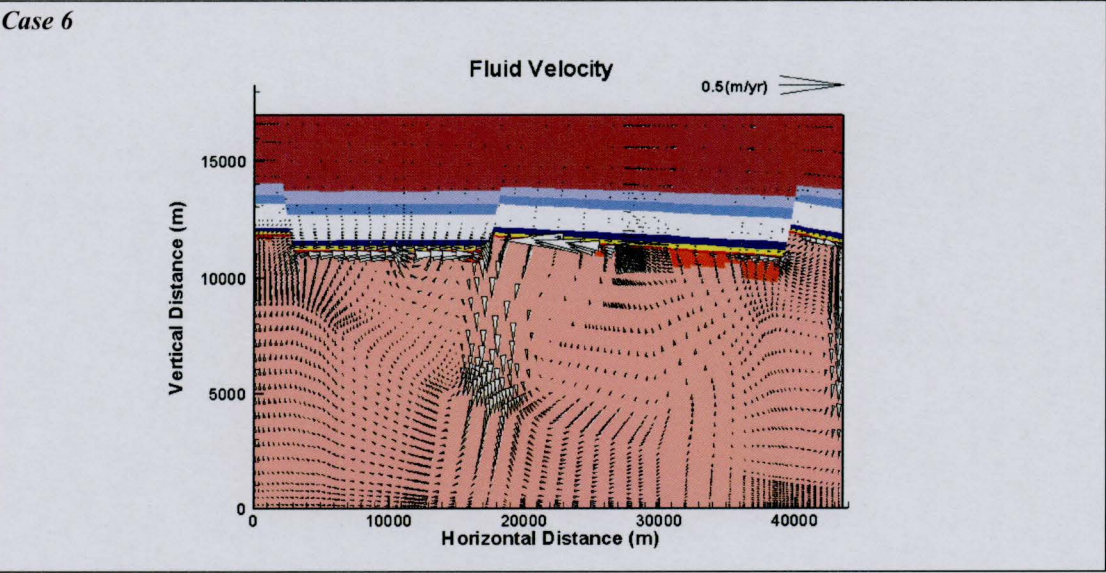
(a)
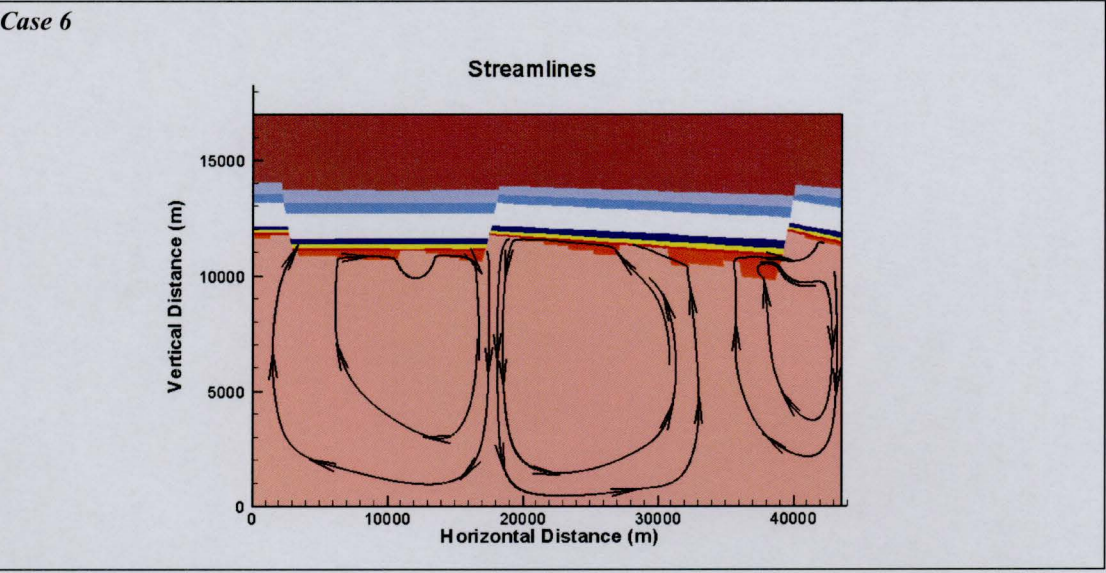


(b)
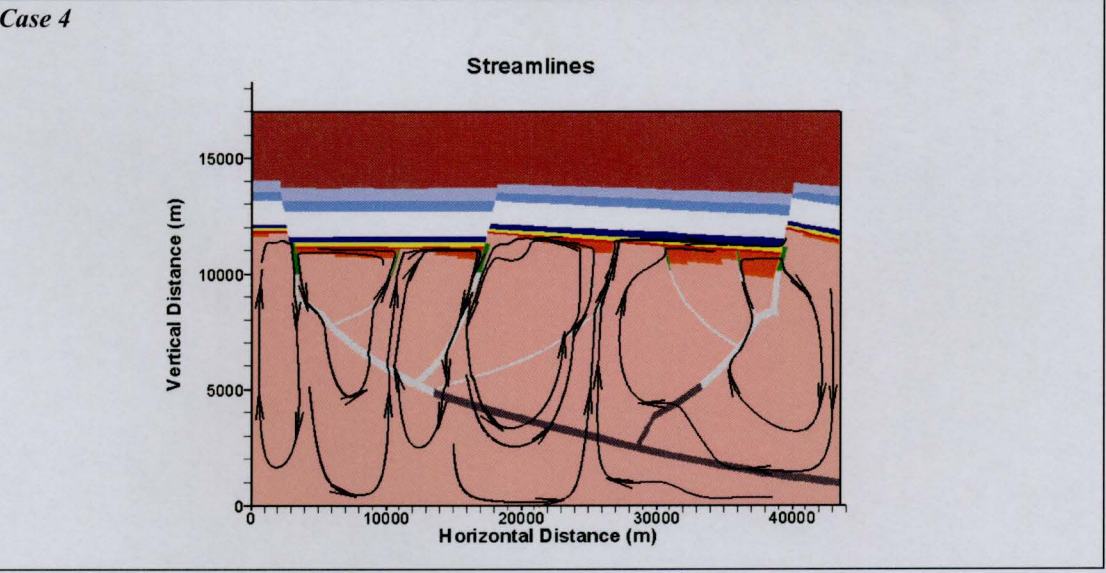


(c)

**Figure 6.23 ZCB. Fault network effect at T2. (a) Case 6 (no permeable faults) fluid velocities and (b) streamlines compared with (c) the streamline pattern for the basic scenario, Case 4 (c).**

172

(a)
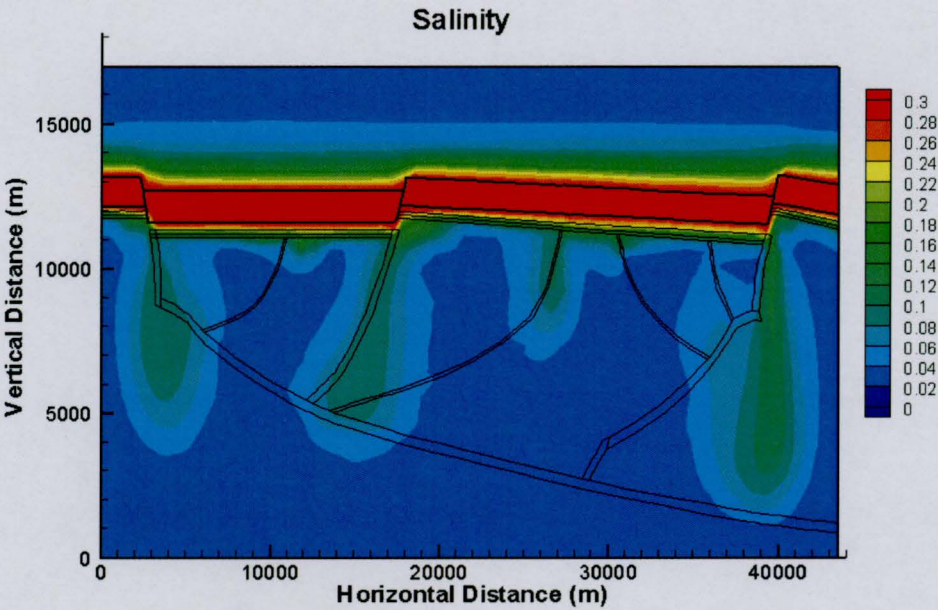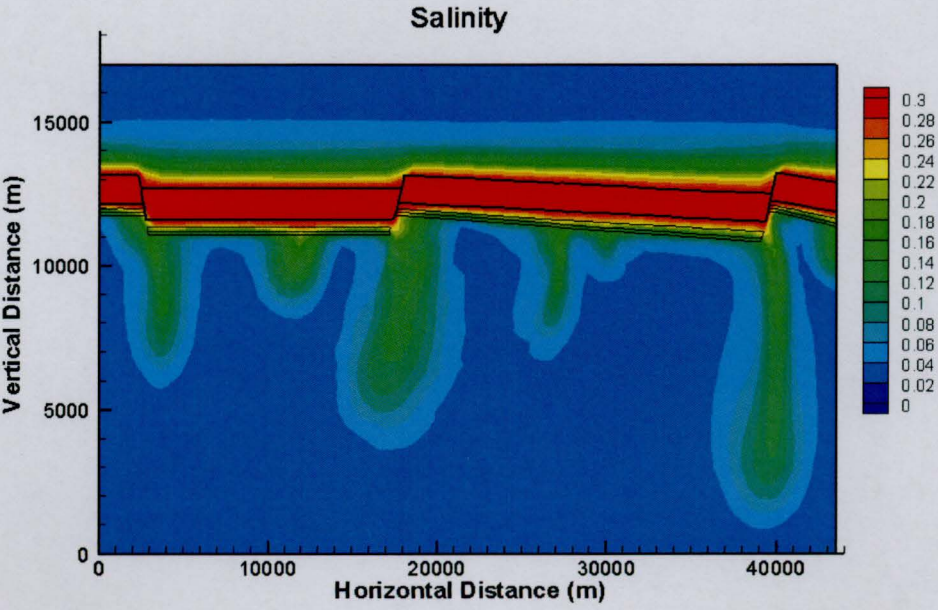


(b)

**Figure 6.24 ZCB. Fault network effect. Comparison of salinity distributions at T1. (a) Case 4 (basic scenario) and (b) Case 6 (no permeable faults).**

(a)



(b)
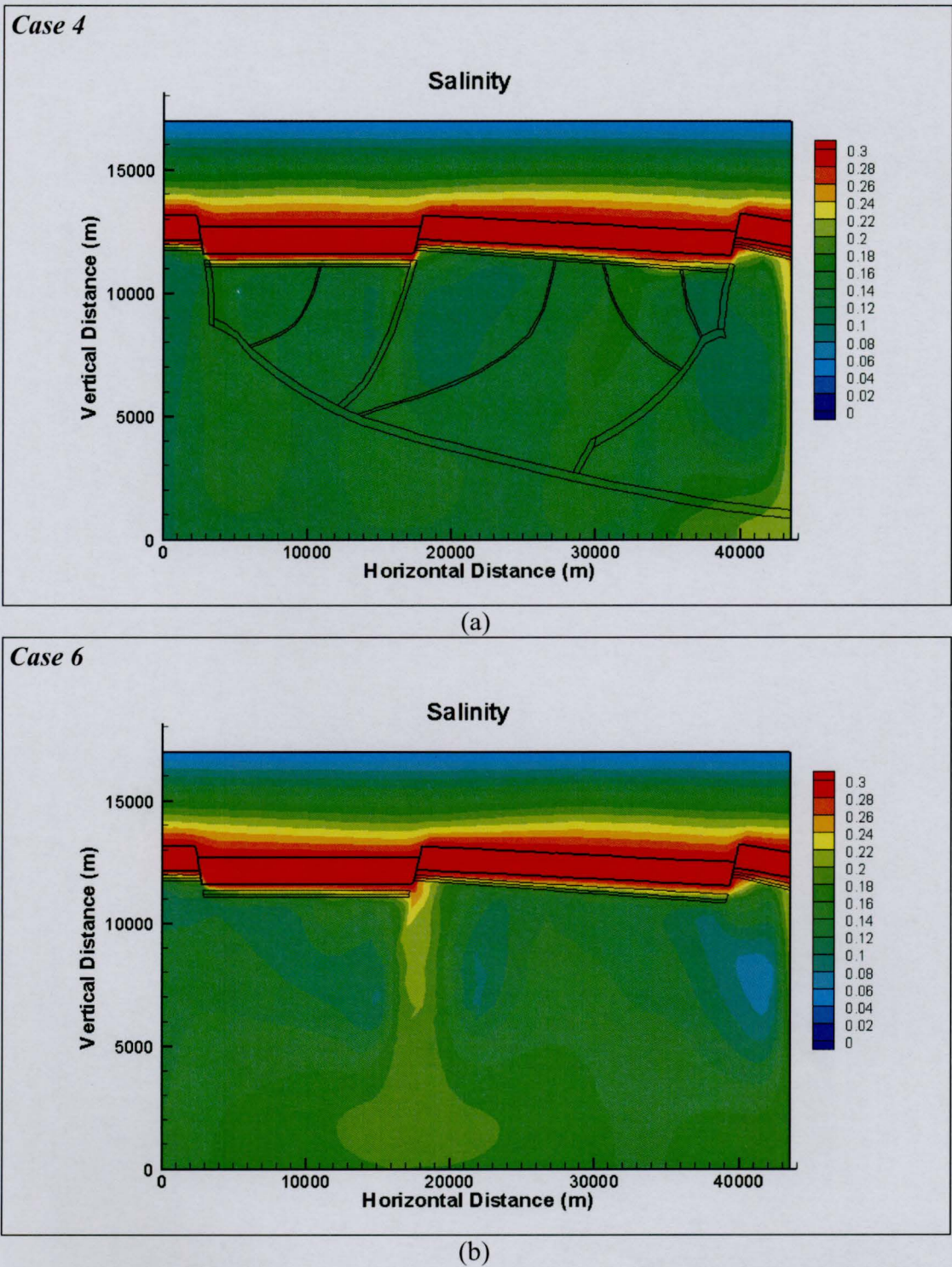
**Figure 6.25 ZCB. Fault network effect. Comparison of salinity distributions at T2. (a) Case 4 (basic scenario) and (b) Case 6 (no permeable faults).**

*Case 4*



(a)
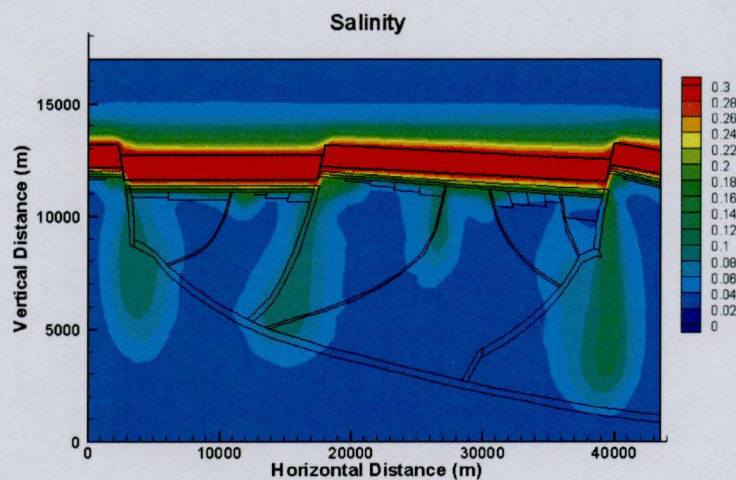
*Case 6*
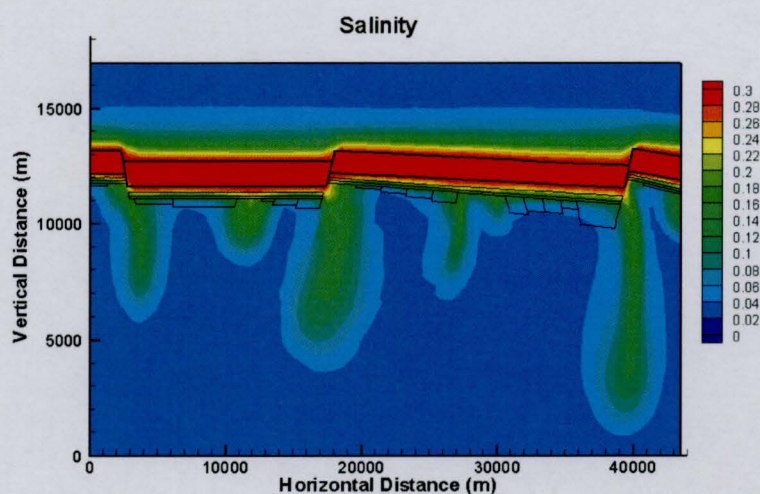


(b)

*Case 7*
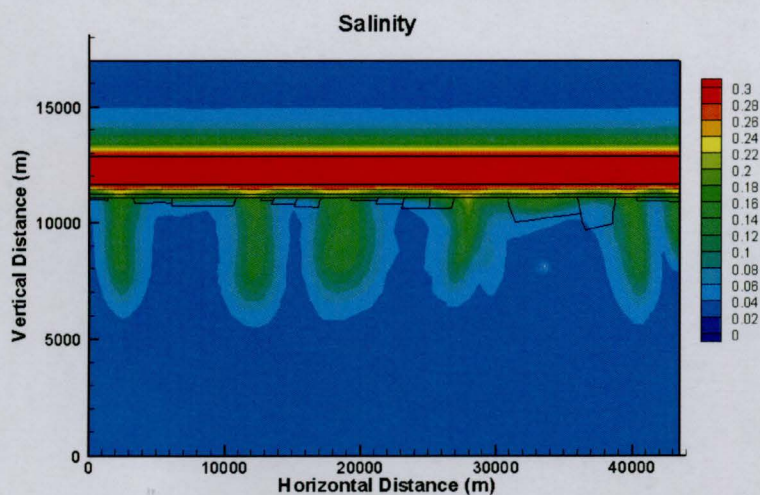


(c)

**Figure 6.26 ZCB. Effect of the salt layer geometry. Comparison of salinity fields at T1. (a) Case 4 (basic scenario), (b) Case 6 (no permeable faults), and (c) Case 7 (flat Upper Roan Salt and the overlying layers).**

(a)



(b)
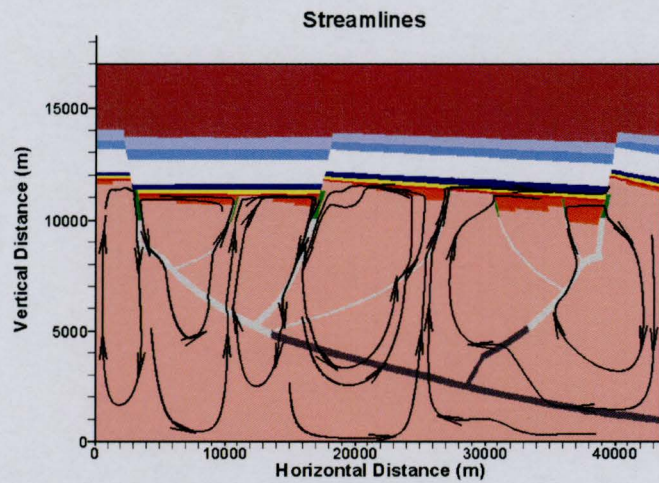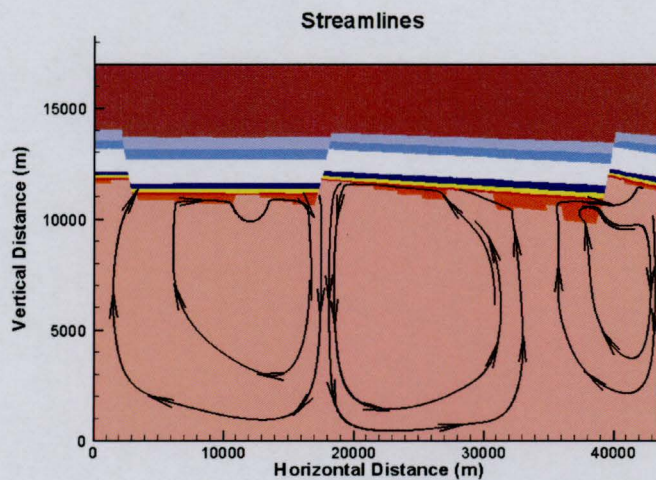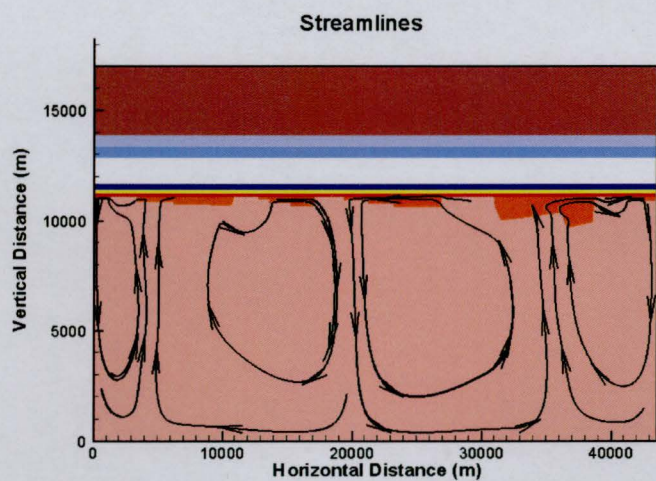


(c)

**Figure 6.27 ZCB. Effect of the salt layer geometry. Comparison of streamline patterns at T2. (a) Case 4 (basic scenario), (b) Case 6 (no permeable faults), and (c) Case 7 (flat Upper Roan Salt and the overlying layers).**

**Case 4**



(a)
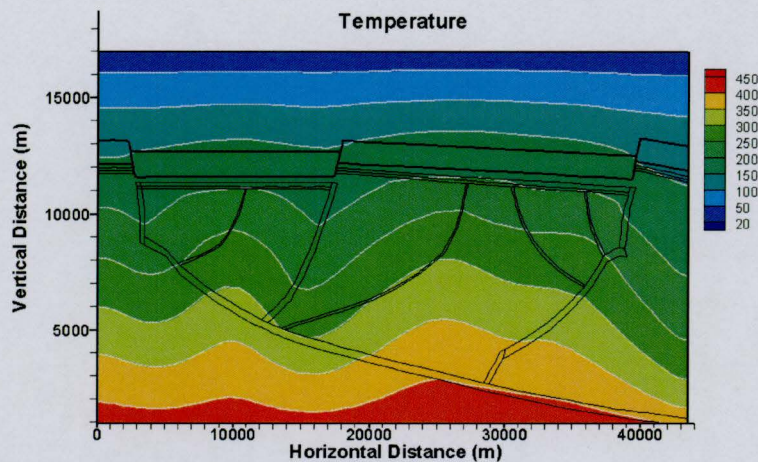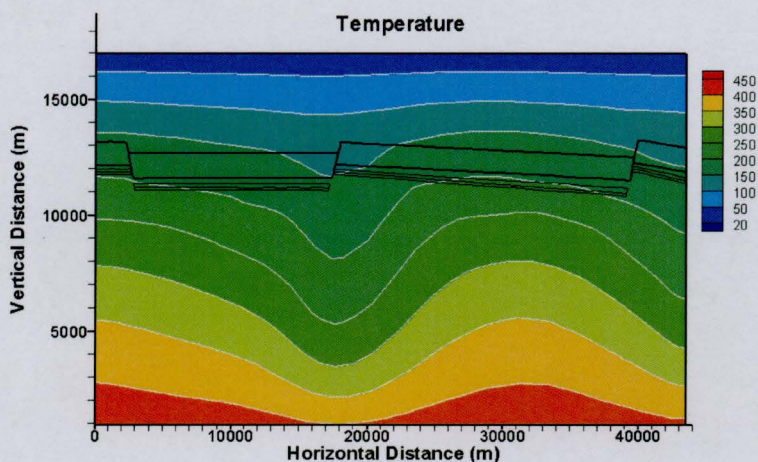
**Case 6**



(b)
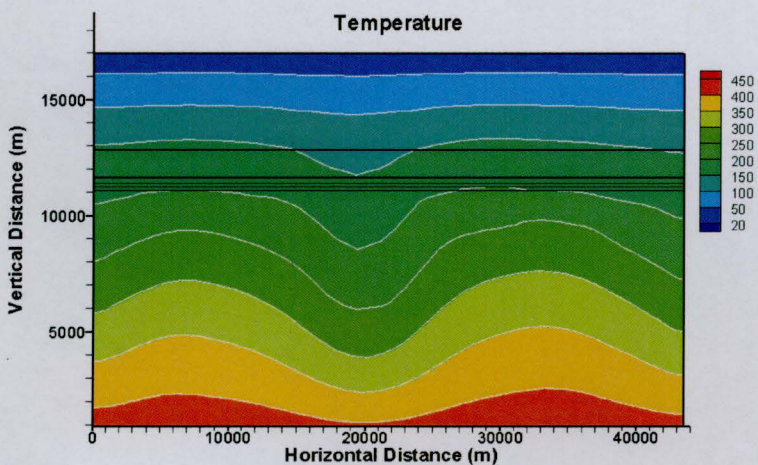
**Case 7**



(c)

Figure 6.28 ZCB. Effect of the salt layer geometry. Comparison of temperature fields at T2. (a) Case 4 (basic scenario), (b) Case 6 (no permeable faults), and (c) Case 7 (flat Upper Roan Salt and the overlying layers).

**Case 4**



(a)
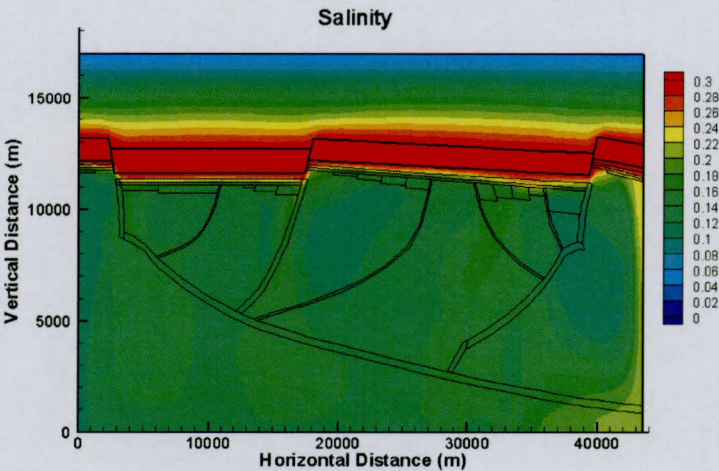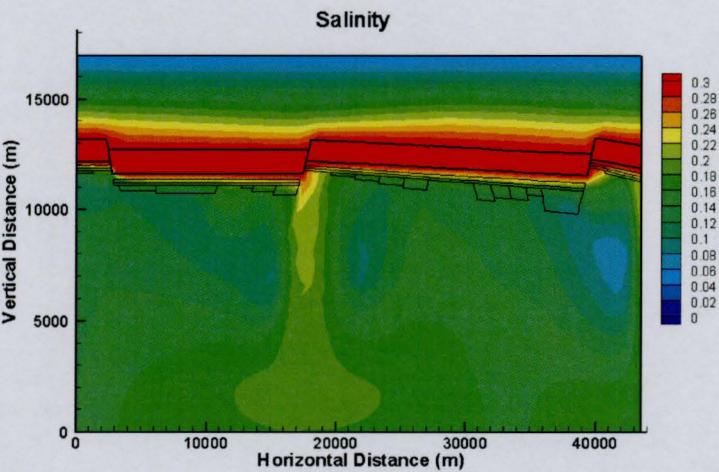
**Case 6**



(b)
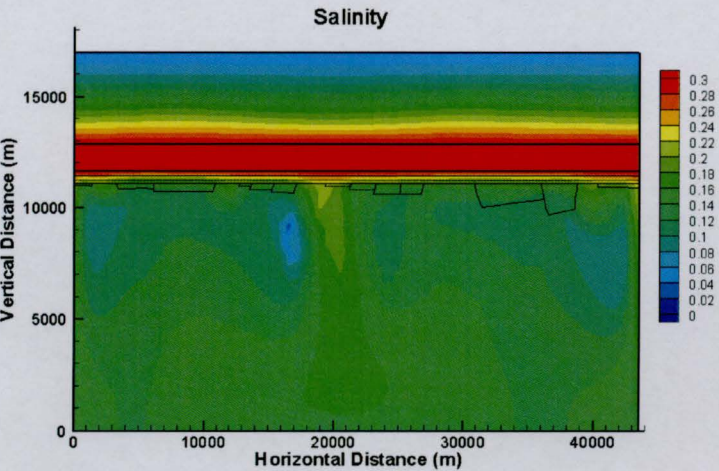
**Case 7**



(c)

**Figure 6.29 ZCB. Effect of the salt layer geometry. Comparison of salinity fields at T2. (a) Case 4 (basic scenario), (b) Case 6 (no permeable faults), and (c) Case 7 (flat Upper Roan Salt and the overlying layers).**

*Case 8*

### Hydrostratigraphy



(a)
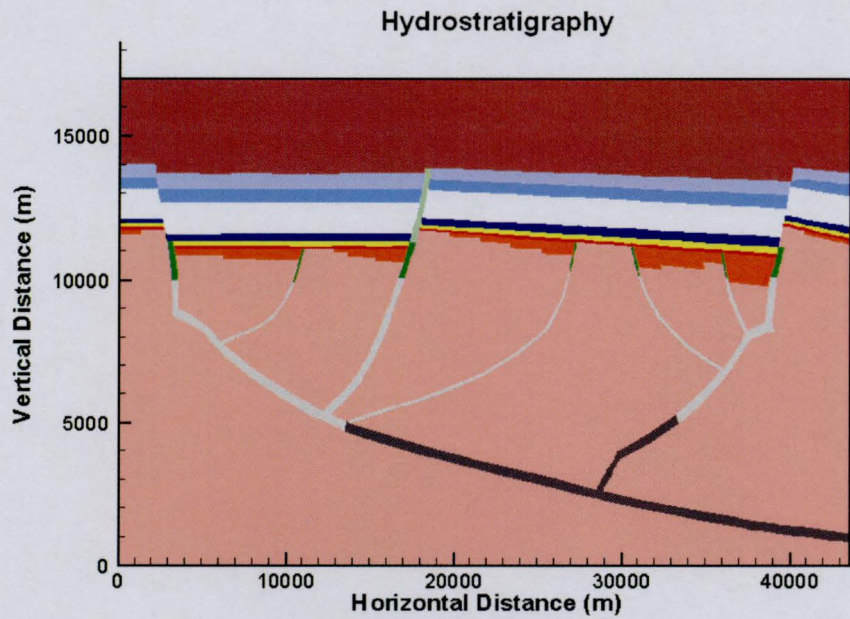
*Case 8A*

### Hydrostratigraphy
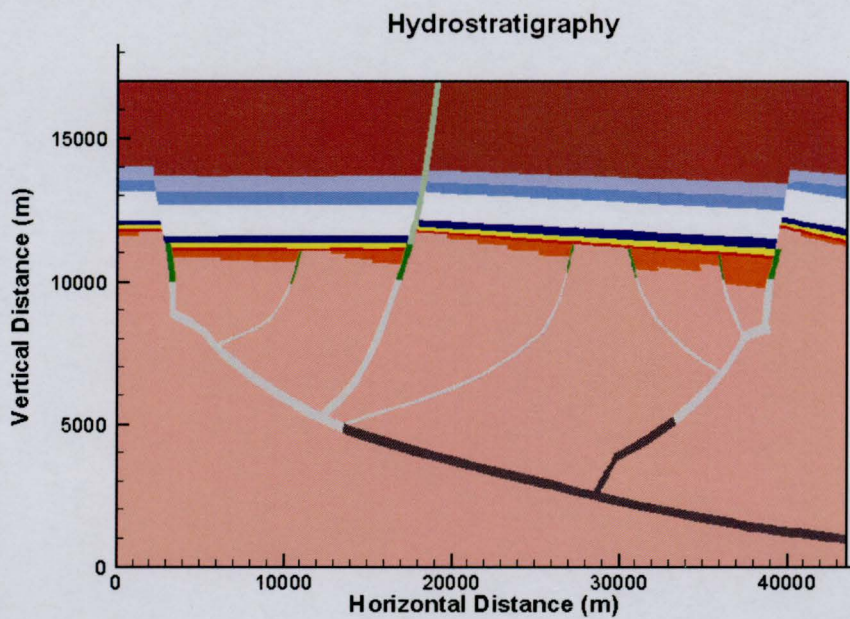


(b)

**Figure 6.30 ZCB. Effect of the piercement structures cutting low-permeable Upper Roan and Lower Mwashia strata. Numerical hydrostratigraphy of the section: (a) Case8: The middle primary fault is extended to the contact 'Upper Mwashia Siliciclastic Member – Kundelungu'; (b) Case 8A: The middle primary fault is extended to the surface.**

(a)



(b)



(c)
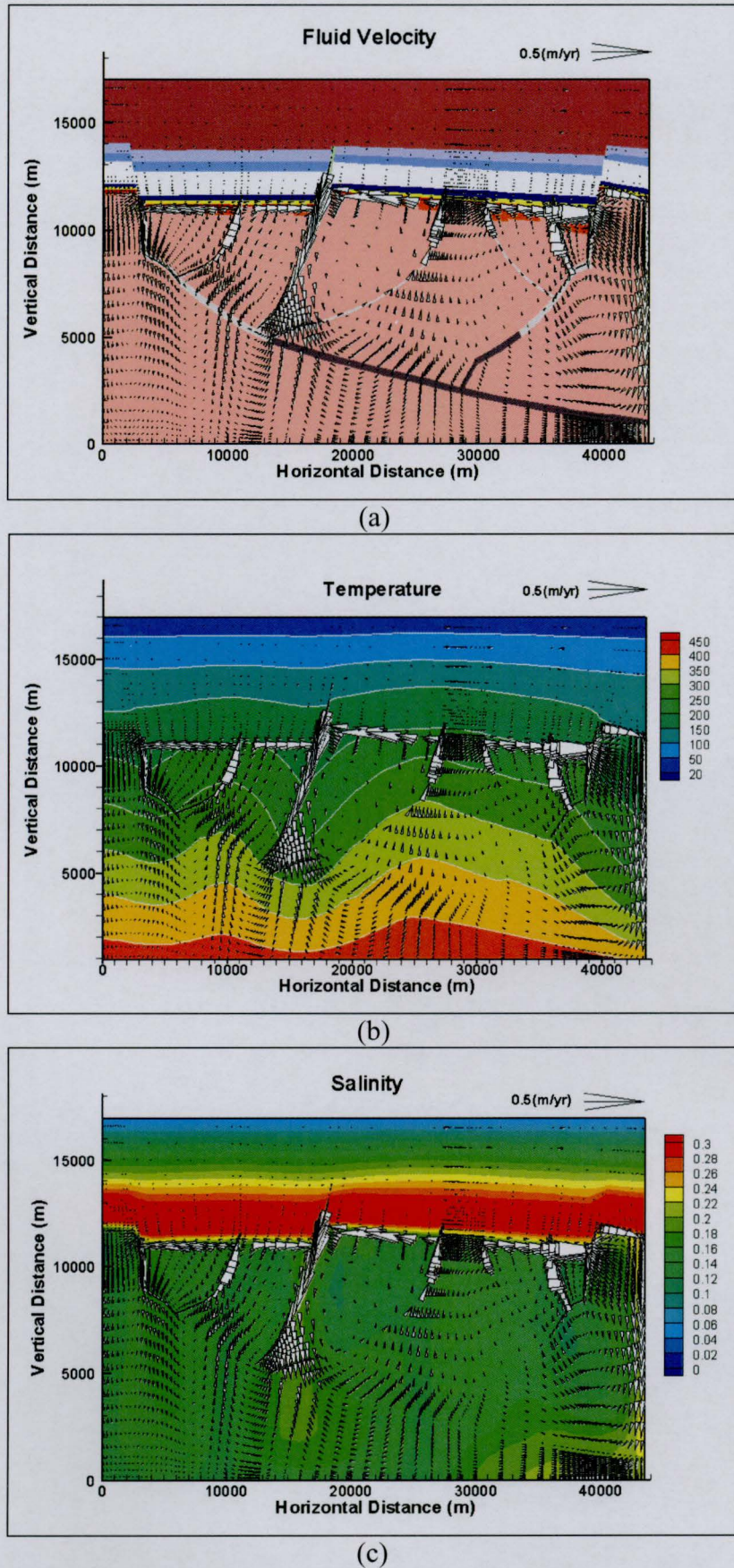
**Figure 6.31 ZCB. Effect of the piercement structures cutting low-permeable Upper Roan and Lower Mwashia strata. Case8 (The middle primary fault is extended to the contact 'Upper Mwashia Siliciclastic Member – Kundelungu'). Presented at T1 (a) fluid velocity, (b) temperature, and (c) salinity fields.**

(a)



(b)



(c)
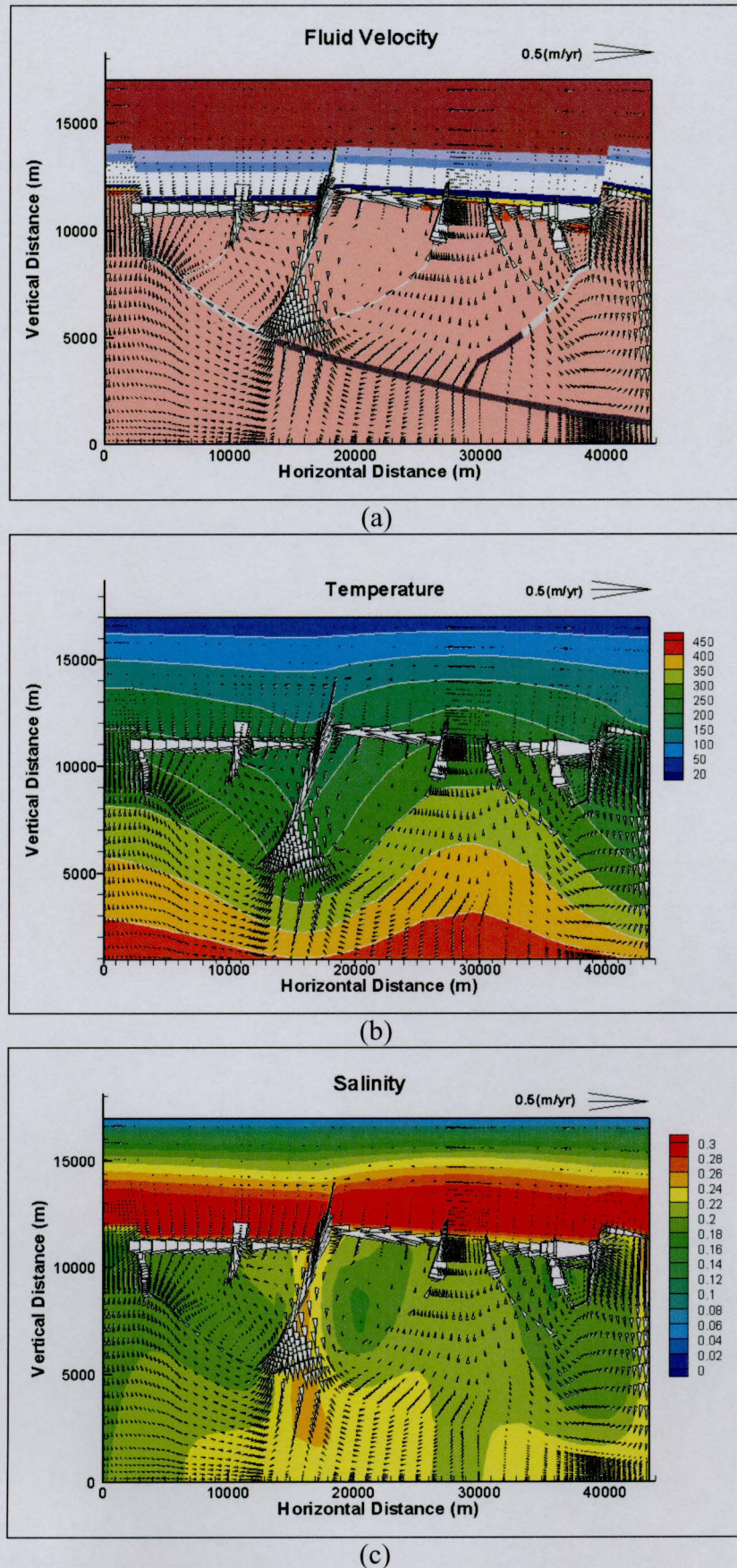
**Figure 6.32 ZCB. Effect of the piercement structures cutting low-permeable Upper Roan and Lower Mwashia strata. Case8 (The middle primary fault is extended to the contact 'Upper Mwashia Siliciclastic Member – Kundelungu'). Presented at T2 (a) fluid velocity, (b) temperature, and (c) salinity fields.**

(a)
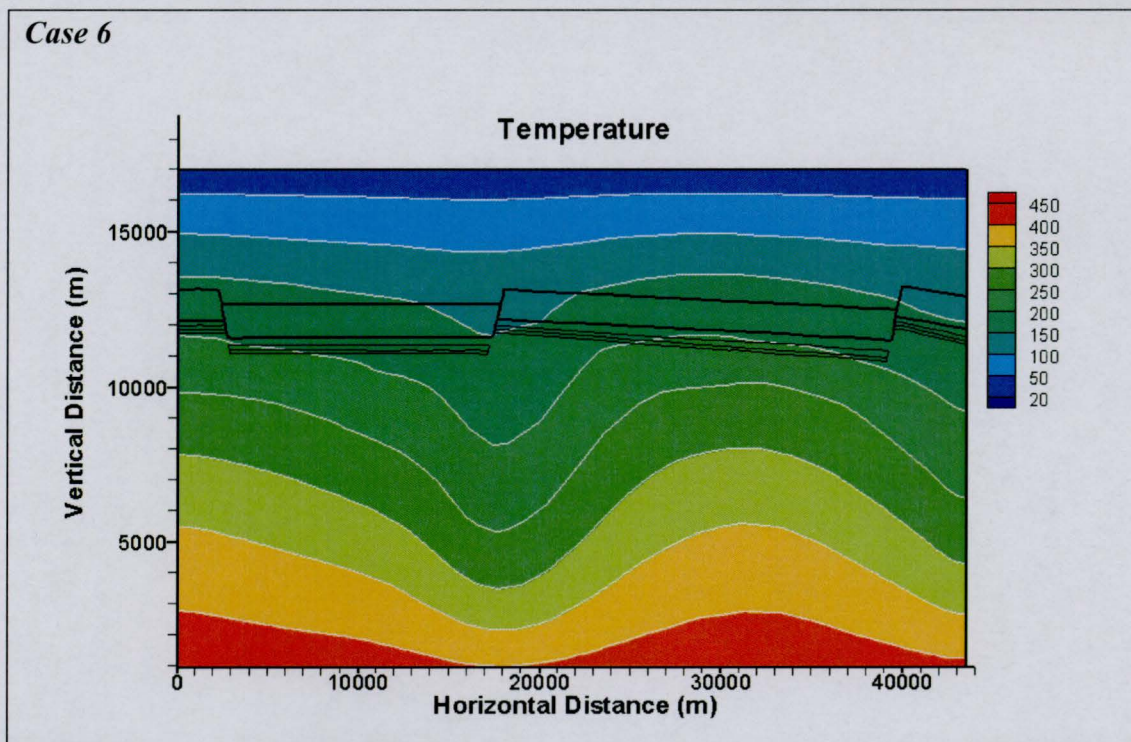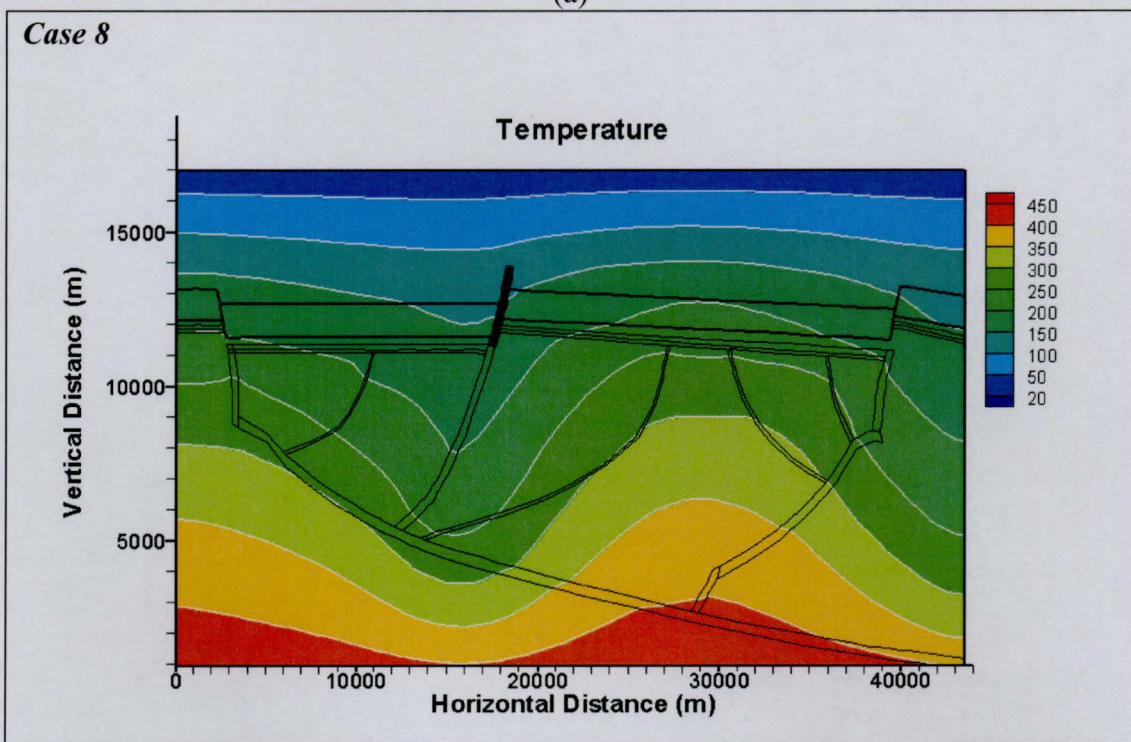


(b)

**Figure 6.33 ZCB. Effect of piercement structures cutting low-permeable Upper Roan and Lower Mwashia strata. Comparison of temperature fields at T2 (a) Case 6 (no permeable faults) (b) Case 8 (the middle master fault is extended to the contact 'Upper Mwashia Siliciclastic Member – Kundelungu').**

*Case 6*

### Fluid Velocity



(a)
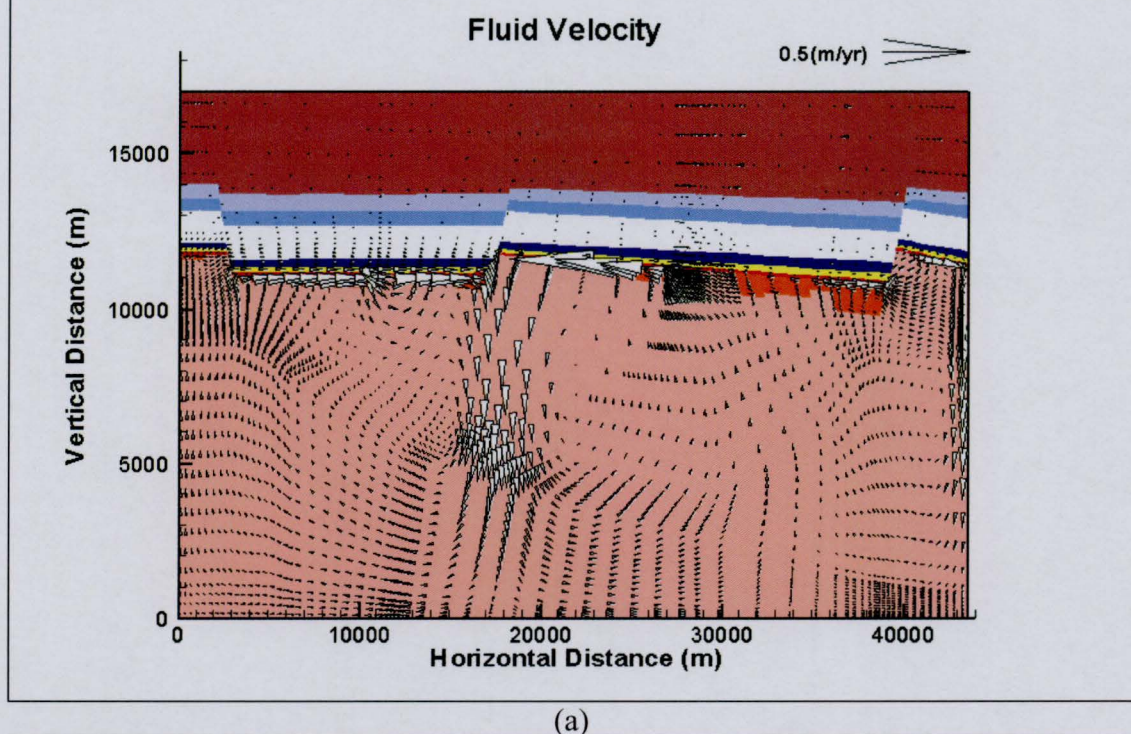
*Case 8*
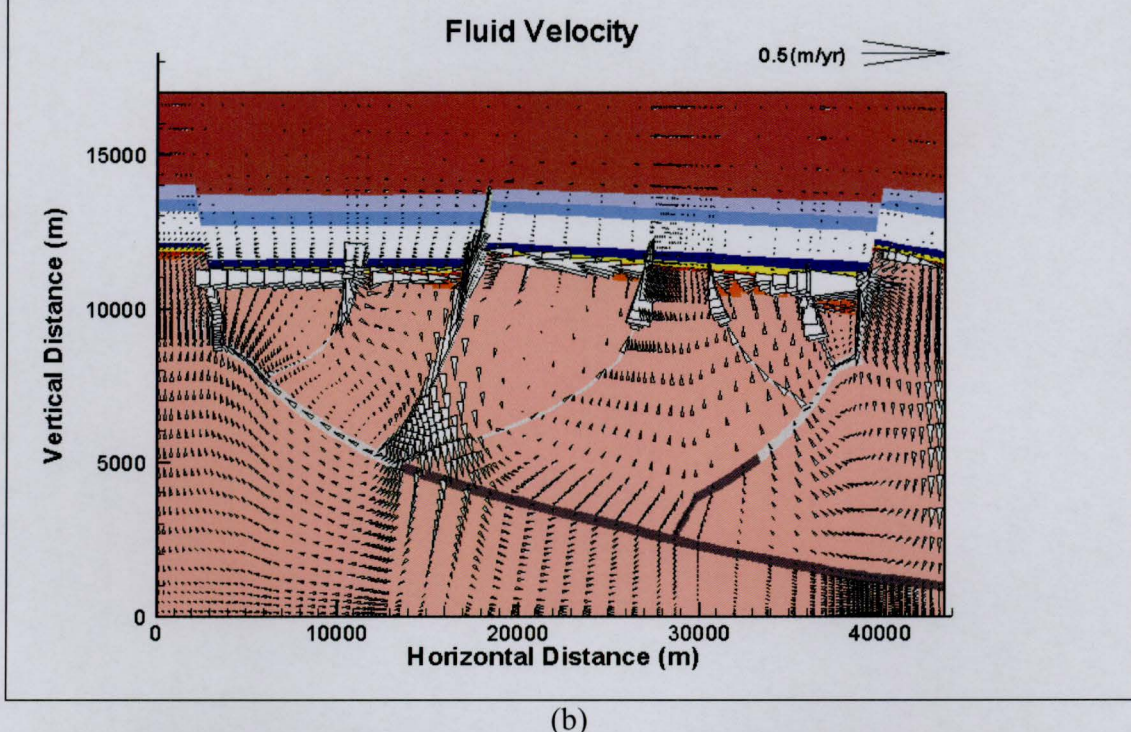
### Fluid Velocity



(b)

**Figure 6.34 ZCB. Effect of piercement structures cutting low-permeable Upper Roan and Lower Mwashia strata. Comparison of fluid velocity fields at T2. (a) Case 6 (no permeable faults); (b) Case 8 (the middle master fault is extended to the contact 'Upper Mwashia Siliciclastic Member – Kundelungu').**

**Case 6**

### Streamlines



(a)

**Case 8**

### Streamlines



(b)
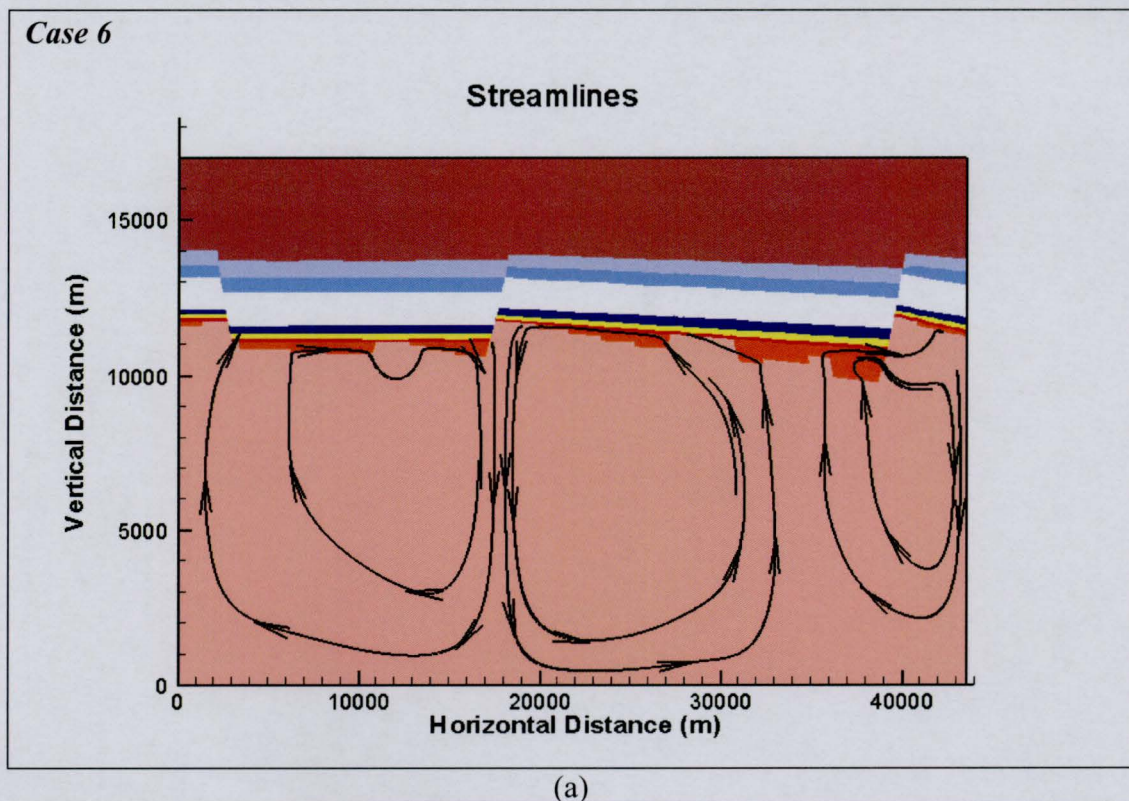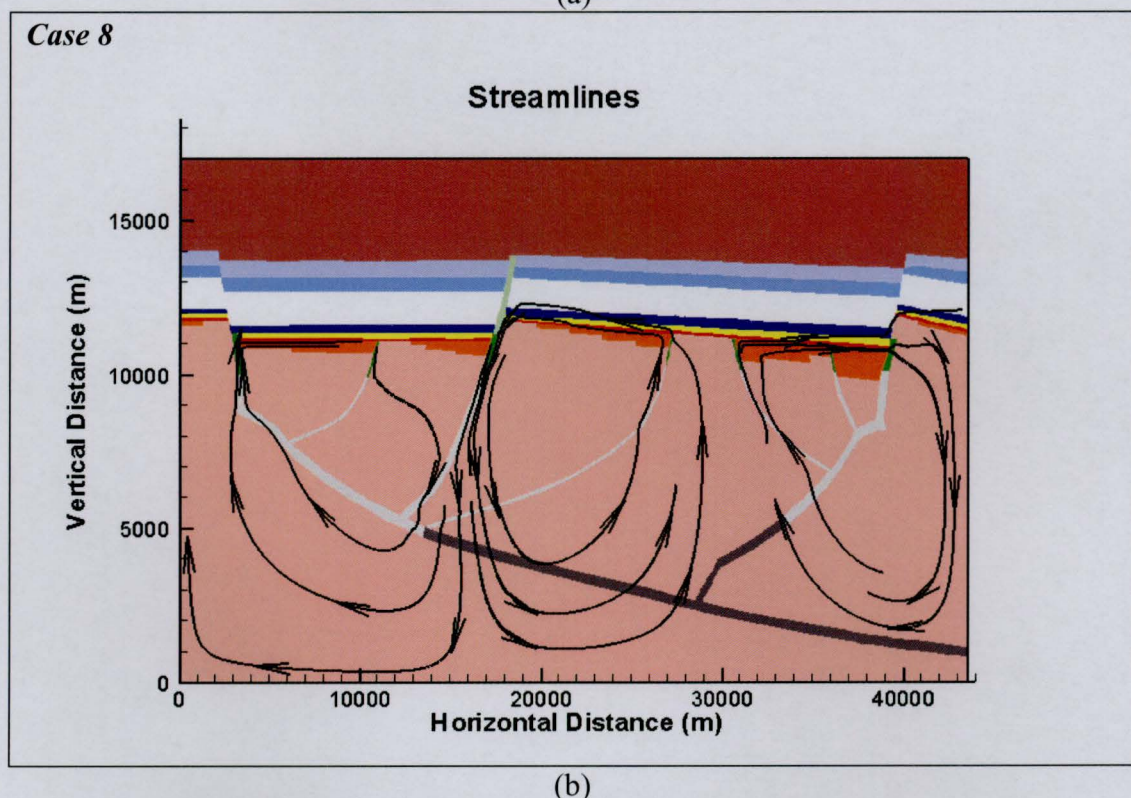
**Figure 6.35 ZCB. Effect of piercement structures cutting low-permeable Upper Roan and Lower Mwashia strata. Comparison of streamlines at T2. (a) - Case 6 (no permeable faults); (b) Case 8 (the middle master fault is extended to the contact 'Upper Mwashia Siliciclastic Member – Kundelungu').**

**Initial state**



(a)

*T1*



(b)

*T2*



(c)
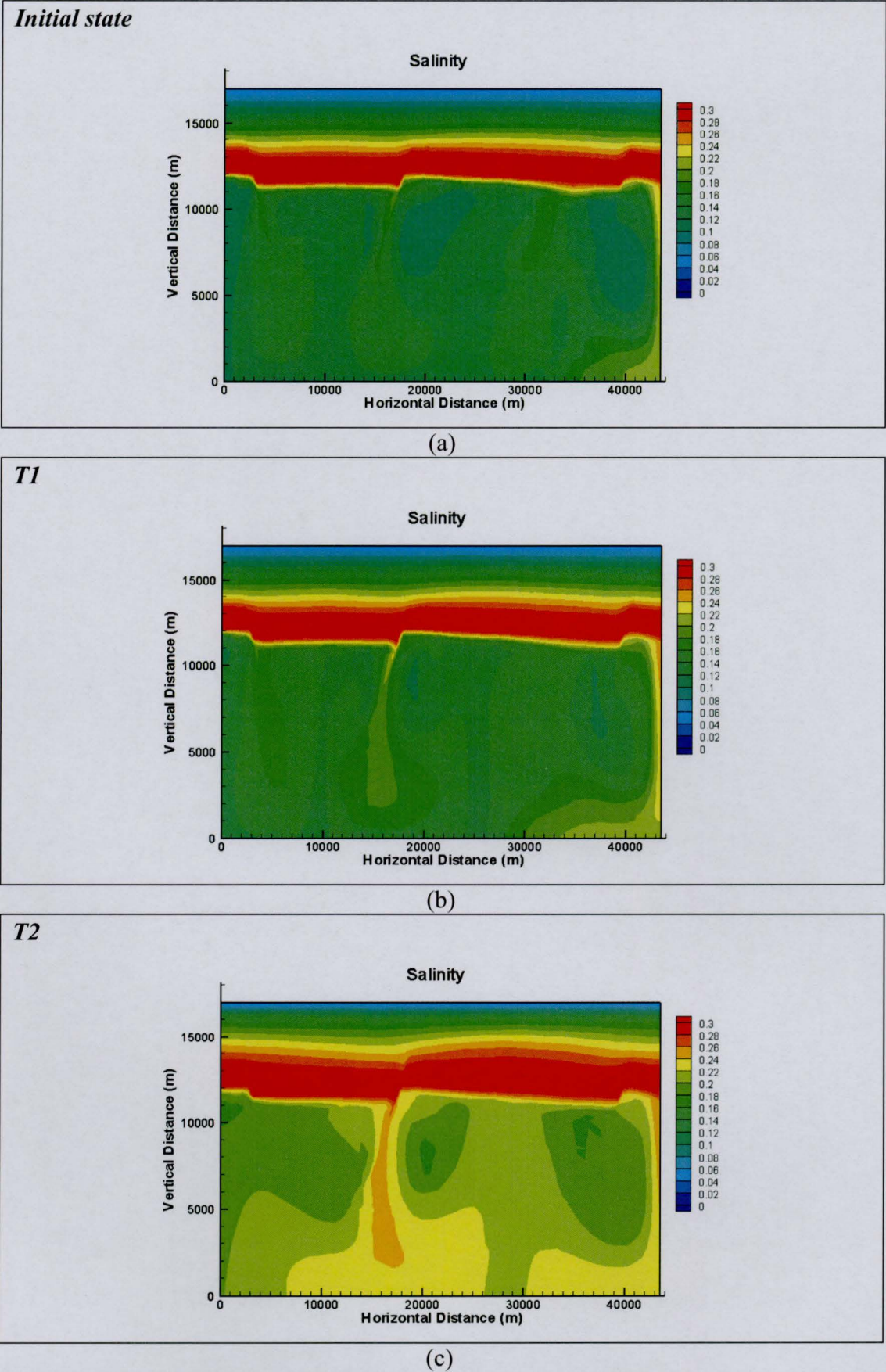
**Figure 6.36 ZCB. Effect of piercement structures cutting low-permeable Upper Roan and Lower Mwashia strata. Case 8 (the middle master fault is extended to the contact 'Upper Mwashia Siliciclastic Member – Kundelungu'). Salinity field dynamics: (a) initial state, (b) T1, (c) T2.**

(a)



(b)
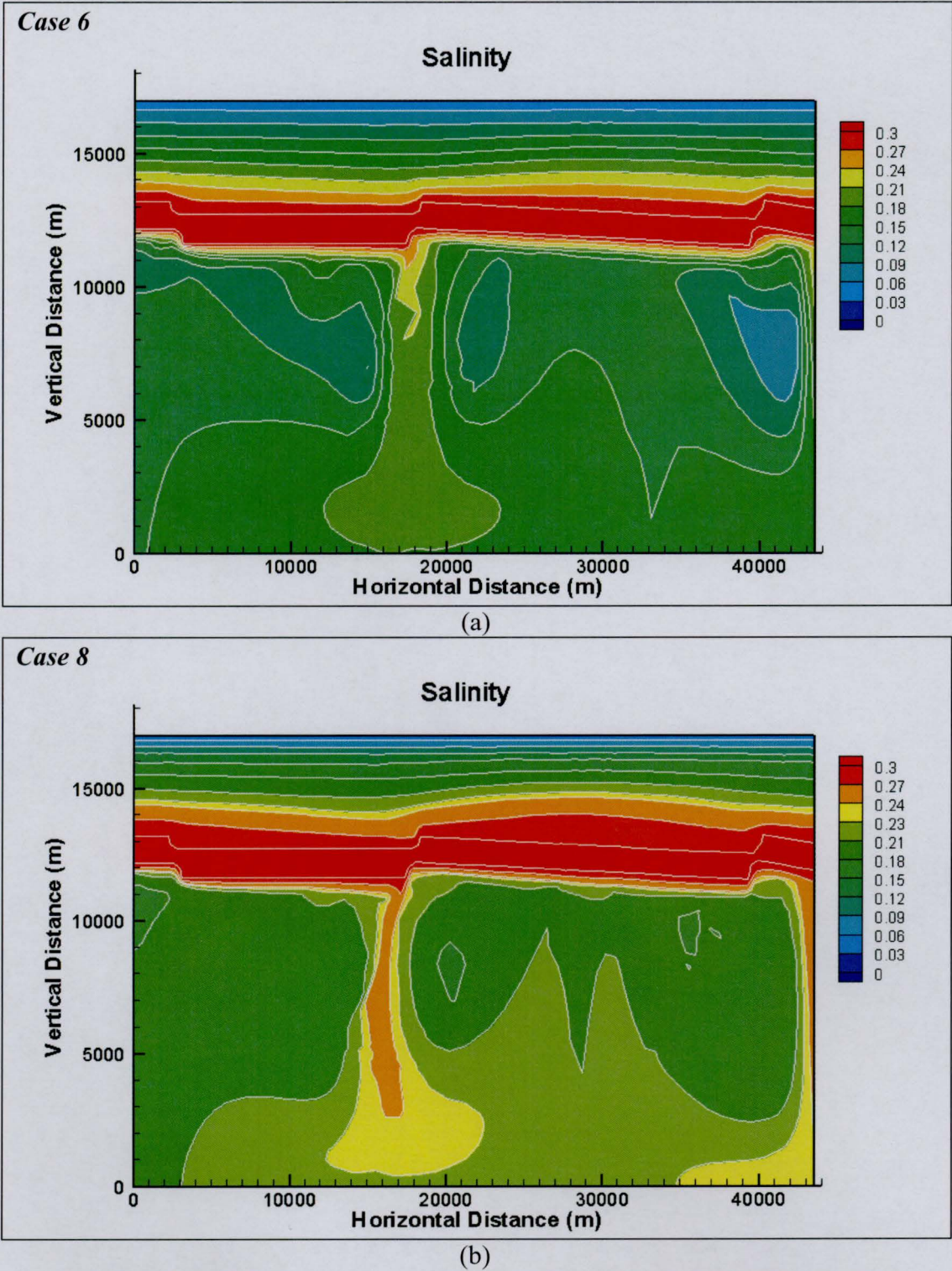
**Figure 6.37 Effect of piercement structures cutting low-permeable Upper Roan and Lower Mwashia strata. Comparison of salinity distrinutions at T2. (a) Case 6 (no permeable faults; (b) Case 8 (the middle master fault is extended to the contact 'Upper Mwashia Siliciclastic Member – Kundelungu').**

Case 9
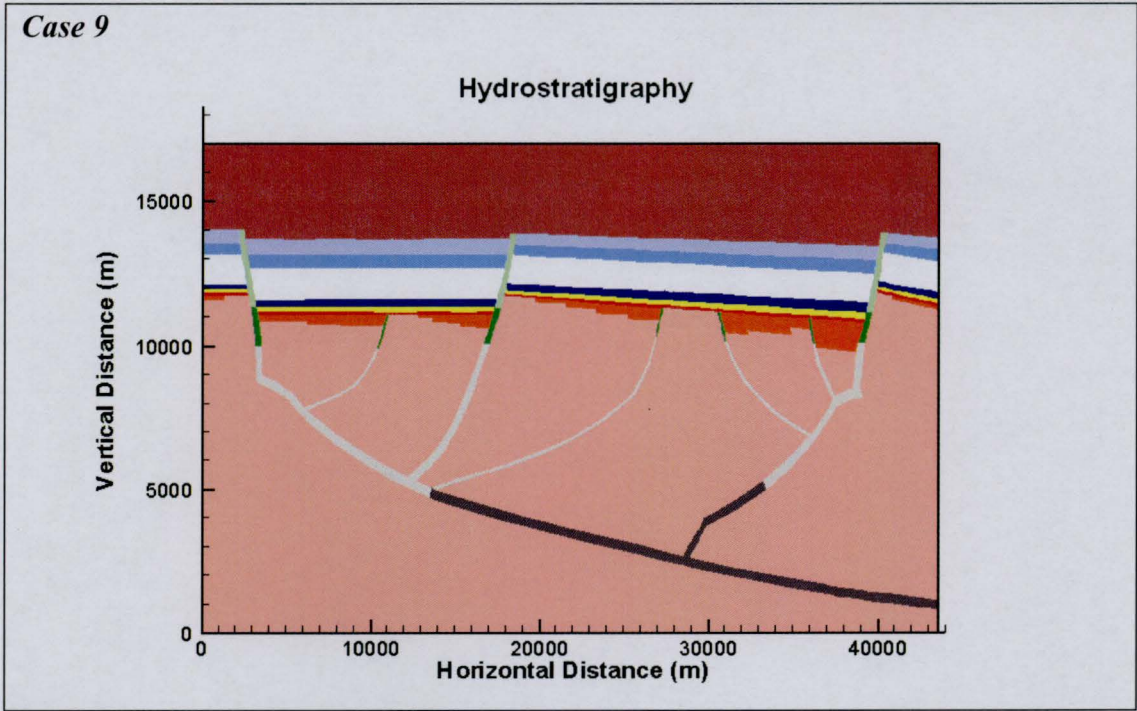


**Figure 6.38 ZCB. Effect of piercement structures cutting low-permeable Upper Roan and Lower Mwashia strata. Case 9 (all master faults are extended to the contact 'Upper Mwashia Siliciclastic Member' – 'Kundelungu'). Numerical hydrostratigraphy of the model section.**

*Case 8*
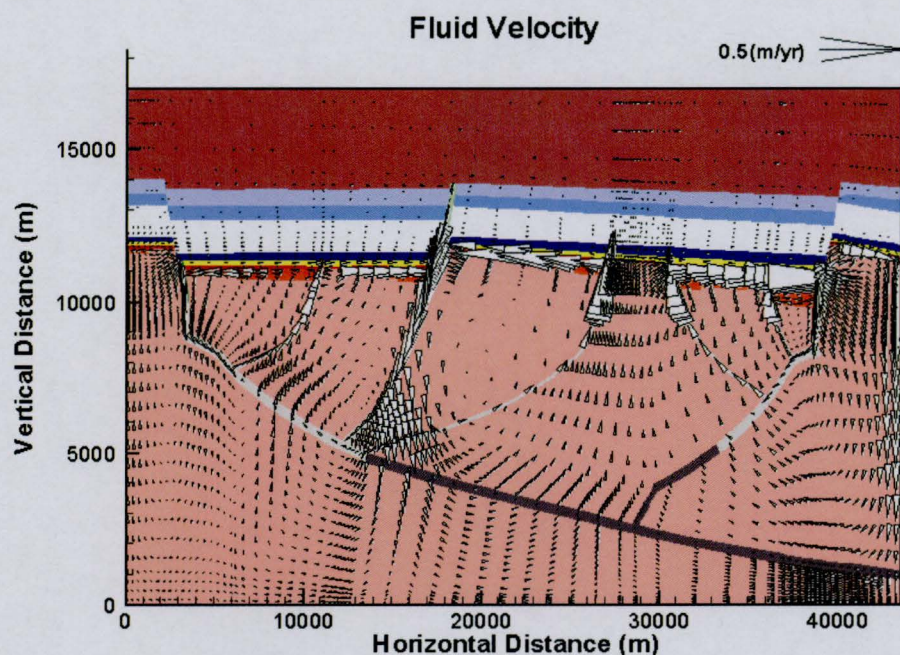


(a)

*Case 9*
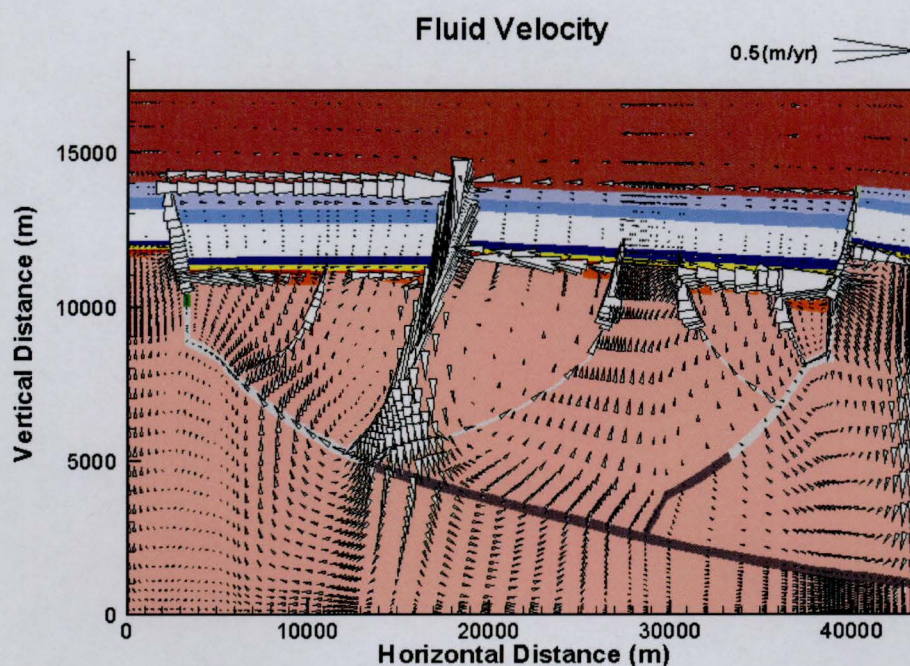


(b)

**Figure 6.39 Effect of piercement structures cutting low-permeable Upper Roan and Lower Mwashia strata. Comparison of fluid velocity fields at T3. (a) Case 8 (the middle master fault is extended to the contact 'Upper Mwashia Siliciclastic Member – Kundelungu') (b) Case 9 all master faults are extended to the contact 'Upper Mwashia Siliciclastic Member' – 'Kundelungu').**
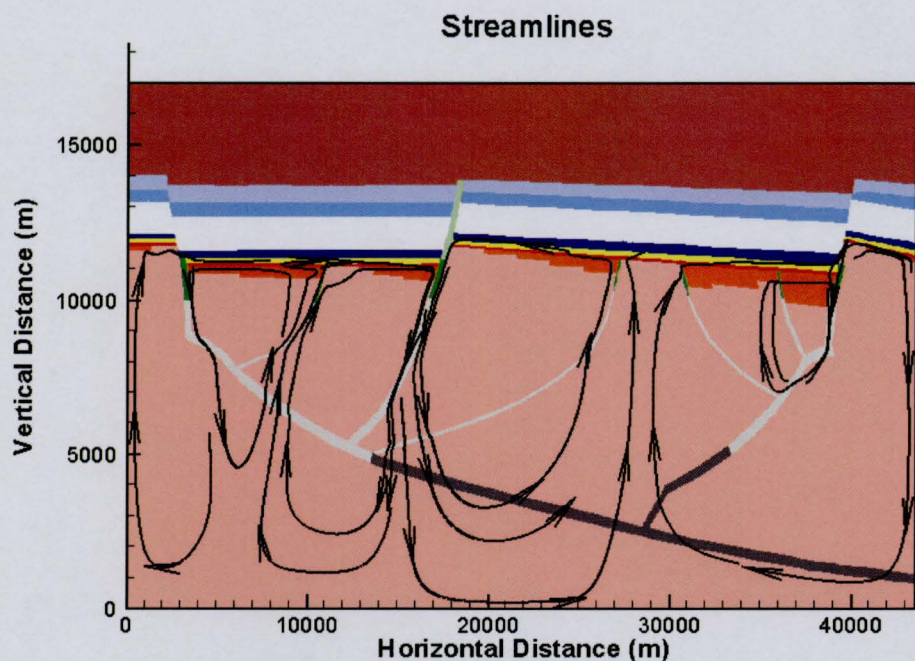
**Case 8**



(a)

**Case 9**
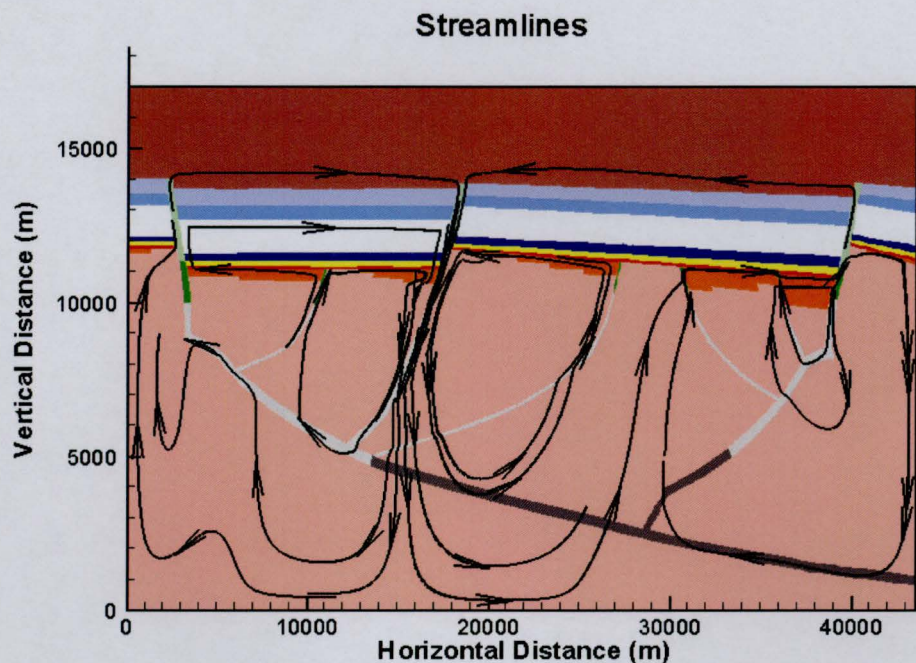


(b)

**Figure 6.40 Effect of piercement structures cutting low-permeable Upper Roan and Lower Mwashia strata. Comparison of streamlines at T3. (a) Case 8 (the middle master fault is extended to the contact 'Upper Mwashia Siliciclastic Member – Kundelungu') (b) Case 9 all master faults are extended to the contact 'Upper Mwashia Siliciclastic Member' – 'Kundelungu').**

*Case 8*

**Temperature**



(a)
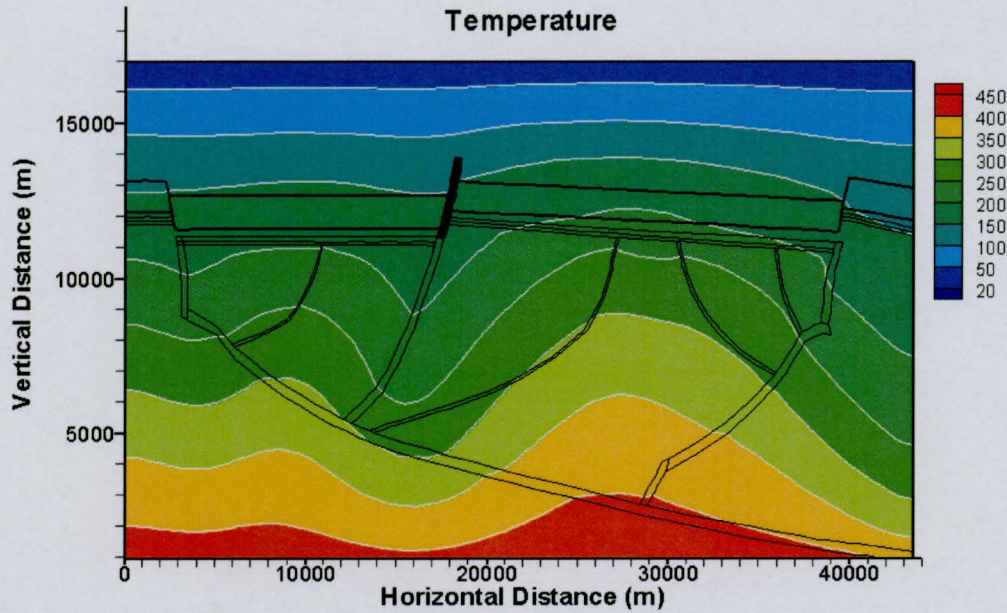
*Case 9*
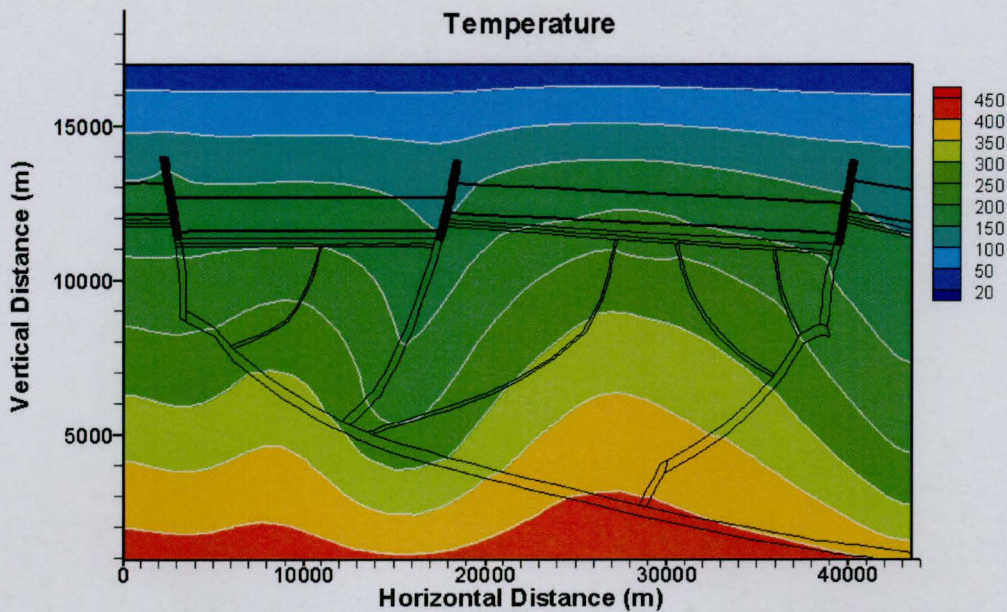
**Temperature**



(b)

**Figure 6.41 Effect of piercement structures cutting low-permeable Upper Roan and Lower Mwashia strata. Comparison of temperature fields at T3. (a) Case 8 (the middle master fault is extended to the contact 'Upper Mwashia Siliciclastic Member – Kundelungu') (b) Case 9 all master faults are extended to the contact 'Upper Mwashia Siliciclastic Member' – 'Kundelungu').**

*Case 8*



(a)

*Case 9*



(b)
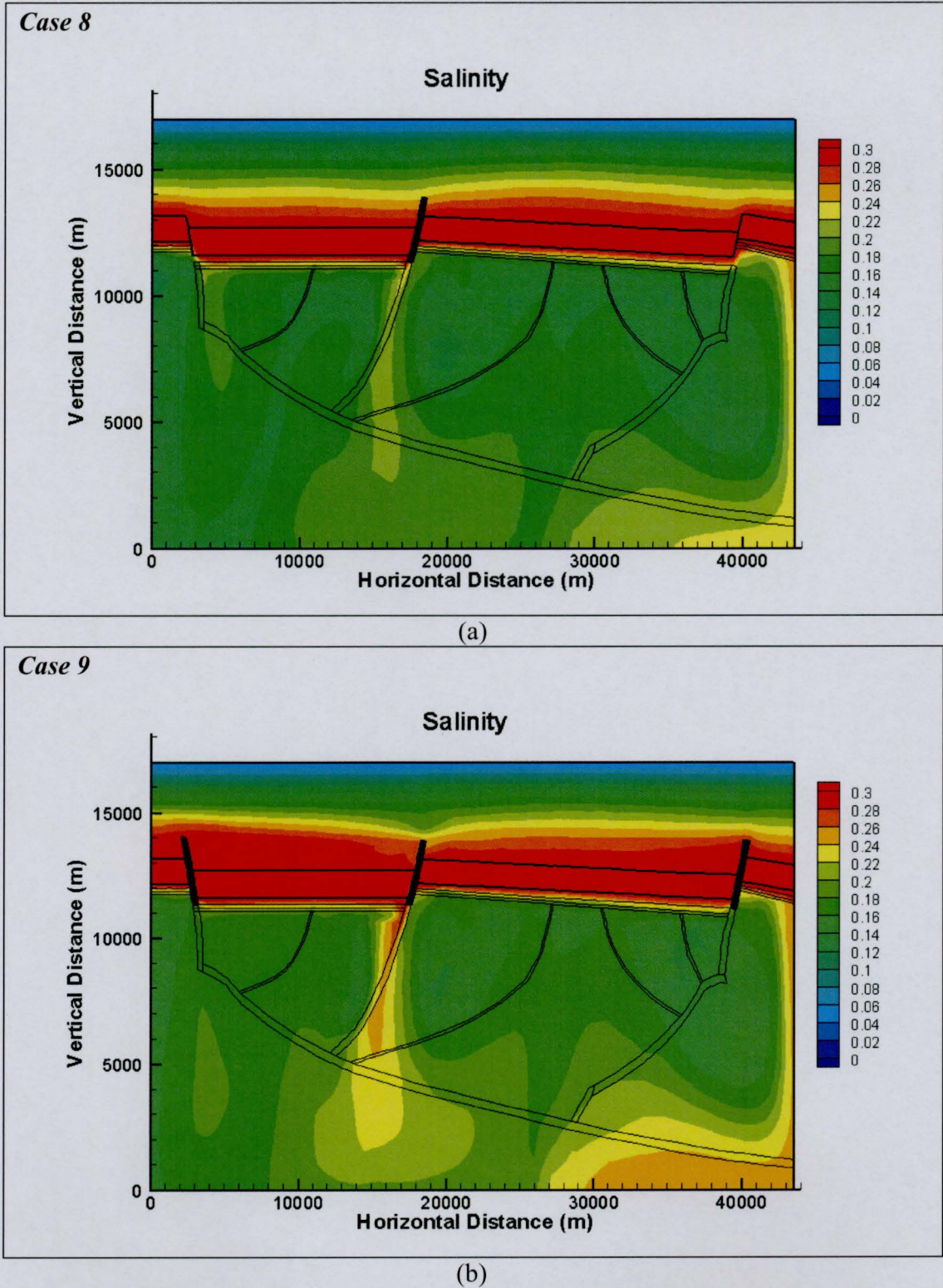
**Figure 6.42 Effect of piercement structures cutting low-permeable Upper Roan and Lower Mwashia strata. Comparison of salinity fields at T3. (a) Case 8 (the middle master fault is extended to the contact 'Upper Mwashia Siliciclastic Member – Kundelungu') (b) Case 9 all master faults are extended to the contact 'Upper Mwashia Siliciclastic Member' – 'Kundelungu').**
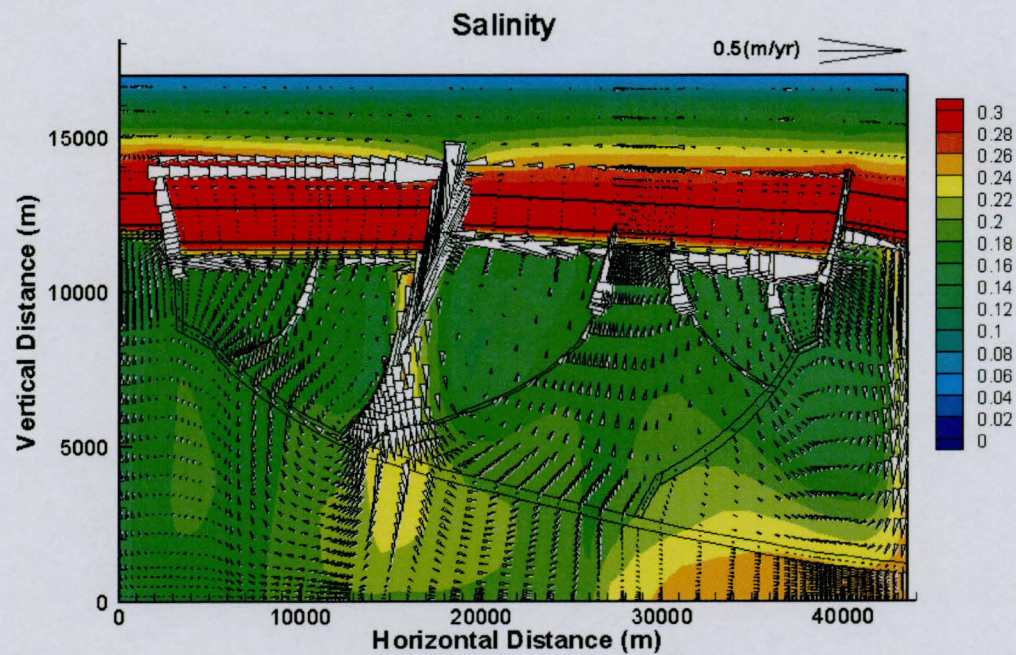
**Figure 6.43 Effect of piercement structures cutting low-permeable Upper Roan and Lower Mwashia strata. Case 9 (all master faults are extended to the contact 'Upper Mwashia Siliciclastic Member' – 'Kundelungu'). Fluid velocities superimposed onto the salinity field at T3.**

## 6.7 Discussion of the simulation results. Factors controlling the flow regime in the ZCB

Simulations for the two scenarios related to the early stages of the basin evolution (*Cases 1, 2*) showed that until the Upper Roan strata are deposited, there is no significant flow within the profile due to the small thickness of the sedimentary section at this stage and also because of the absence of the salt layer. Deposition of the fine-grained and low-permeable shale comprising Copperbelt Orebody Member inhibits the system dynamics even further, as it prevents any significant discharge-recharge through the open top boundary and ultimately decreases fluid velocities by one half.

The Upper Roan Salt was shown to be a key element influencing the intensity of the flow and its configuration. The constant source of NaCl, supplied by Roan Salt dissolution, enhances the existing thermal perturbations due to the geothermal gradient. This factor together with the increased thickness of the stratigraphic section at later stages (*Cases 3, 4*) intensifies fluid convection resulting in almost one order of magnitude rise in fluid velocities. The comparison with the fresh water scenario (*Case 5*) emphasizes the impact of the salt transport and dissolution on the system. Exclusion of the salinity effect results in a different structure and lower intensity of the flow and changes in the temperature field.

The salt layer properties, in particular its permeability and degree of anisotropy, affect the system as they can facilitate the increased salt influx into the system. The simulations also showed that the fact that the salt sheet is isotropic or anisotropic makes no difference as long as the vertical permeability remains low (*Cases 4A, 4B*). However, a notable rise in the salt layer permeability (*Case 4C*) leads to higher fluid flow rates through the stratum, intensified rock salt dissolution, increased influx of the dense brine, and ultimately restructuring of the fluid flow beneath the salt sheet.

The case studies with the sealed fault network (*Case 6*) showed that the absence of permeable conduits beneath the Upper Roan strata alters the flow pattern in the basement, increasing the aspect ratio of convective cells. At the same time, the numerical experiment with the faults set inactive, and the level salt sheet (*Case 7*) confirmed that the domain geometry and, in particular, breaks and displacements in the salt layer, define the position of downwelling solute plumes rather than permeable conduits beneath the Upper Roan Salt.

Dissolution of the Roan Salt, enhancing density instability below this stratum, boosts free convection in the lower part of the section. At the same time, above the Roan Salt, the salinity gradient, on the contrary, stabilizes the system overpowering the temperature contrast. One can observe rapid salt diffusion upwards, however, there is no advective motion. Simulations showed that the existing geothermal gradient is insufficient to activate a convective flow of the stably stratified fluid in the upper part of the basin above the salt layer. Even the introduction of highly permeable structures above the Roan strata (*Cases 10, 10A*) does not facilitate convection. The interstitial fluid in the upper part of the basin remains in equilibrium at rest until the low-permeable Roan and Mwashia strata are breached. If the breach occurs in a single location, it is immediately occupied by sinking heavy brine formed within the salt layer (*Cases 8, 8A*) and there is no effect in the Upper Mwashia and Kundelungu. However, if the low-permeable layers are broken in more than one location and, what is essential, both Roan Salt and Mwashia Dolomites are pierced through, this provides access for the hot brines into the upper permeable strata followed by intensive fluid circulation through the Kundelungu stratigraphy (*Case 9*).

A common feature of all the considered scenarios is that they show a significant convective flow through the basement. Even though this unit was attributed to have low permeability and porosity, the effect of the geothermal gradient coupled with the dissolution of the Upper Roan Salt is sufficient to initiate intensive convection in the basement. The presence of highly permeable faults is not shown to be a requisite condition for basement convection; they rather redistribute the flow pattern guiding fluid fluxes. This means that the substantial fluid flow through the volcanic and granite basement has the capacity to leach out and transport into the overlying hosting sediments a significant amount of the base metal, if at least minimal permeability can be maintained.

## 6.8 Local analysis and Cu precipitation

Simulations presented in the previous sections give a general picture of the migration of the interstitial water. In this section, a local analysis of metal-bearing fluid properties is presented. The time dynamics of fluid temperature, salinity and velocity is studied to draw implications for the base metal precipitation.

### 6.8.1 Local analysis of the time dynamics of the metal-bearing fluid properties

This analysis is carried out for two rock elements in the finite element mesh which mark plausible locations of the two types of ore bodies: 1) shale or argillite hosted copper deposits, within the Copperbelt Orebody Member and 2) arenite hosted copper deposits within the lowermost Roan, Mindola Clastic Formation (Selley et al., 2005).

As a sediment-hosted stratiform copper deposit, which typically occur in reduced beds at the top of continental volcanic and redbed sequences (Jowett, 1989), the major ZCB ore systems are confined to siliciclastic units of the Lower Roan and occur in two basic lithofacies, argillites and arenites (Selley et al., 2005).

Common for many deposits is their systematic association with 'basement highs'. Thus, ore bodies of both 'footwall' and 'hangingwall' arenite-hosted deposits are laterally terminated at the fringes of uplifted basement blocks. Most of argillite-hosted deposits overlie the position where the underlying Mindola Clastic Formation is confined by relief culminations.

Stratigraphically, the limits of ore in many arenite-hosted deposits coincide with the transition to more argillaceous or dolomitic strata. The majority of argillite-hosted deposits occur within the lower third of the Copperbelt Orebody Member, a roughly 10m thick interval (Selley et al., 2005).

In Figure 6.44, two elements used for the analysis are shown. The upper mesh element, marked '1', is situated within the 'Ore Shale' unit, the lower one, element '2', sits immediately beneath, in the uppermost, approximately 130m thick, part of the Mindola Clastic Formation. '1' and '2' stand for argillite- and arenite-hosted ore bodies respectively. Both points are located above the fringe of the uplifted basement block at the lateral termination of the thinning Mindola Clastic segment. The point

within the 'Ore Shale' unit marks the ore body location typical for the Chambishi deposit, the element '2' (within the Mindola Clastic Formation) is distinctive for Nchanga-Chingola deposit (Selley et al., 2005). A half-graben used in the analysis is adjacent to the middle primary fault and located in the centre of the numerical domain. This was done to avoid a strong boundary effect from the right boundary of the domain (Section 6.2.1).
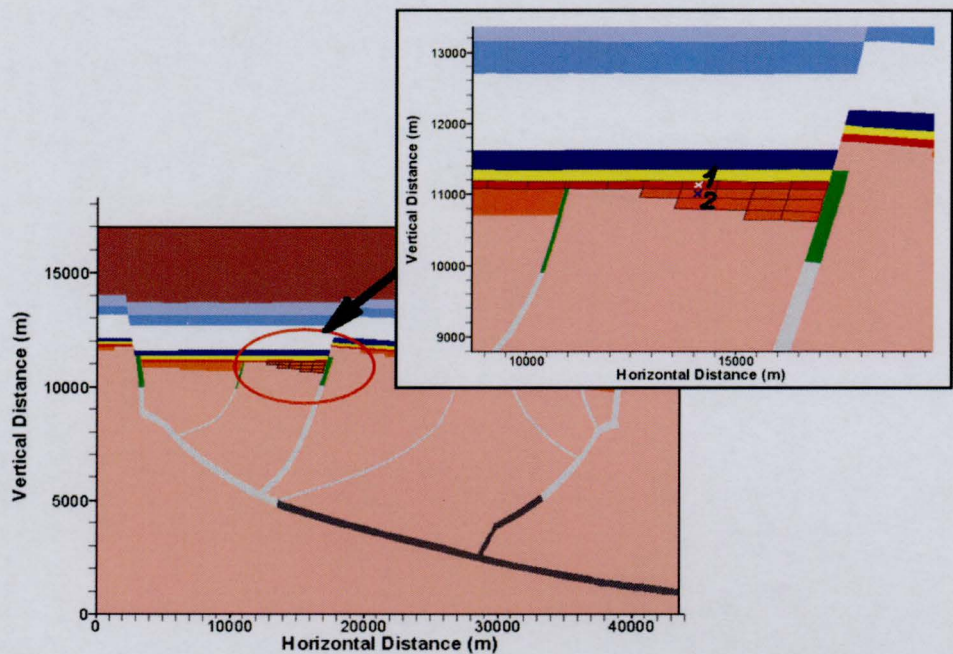


**Figure 6.44 Position of two elements selected as plausible locations of argillite-hosted ore body, '1', and arenite-hosted ore body, '2'.**

Three scenarios were chosen for consideration. They represent chronologically consequent stages of the basin evolution;

Case 2 – rift climax stage;

Case 3 – initial stage of the Kundelungu deposition;

Case 4 – basic scenario.

Figure 6.45 shows the temporal dynamics of the absolute value of the fluid velocity vector, temperature, and salinity at points '1' and '2'.

**Case 2**

*'rift climax' stage*

**Case 3**

*initial stage of
Kundelungu deposition*

**Case 4**

*basic scenario*
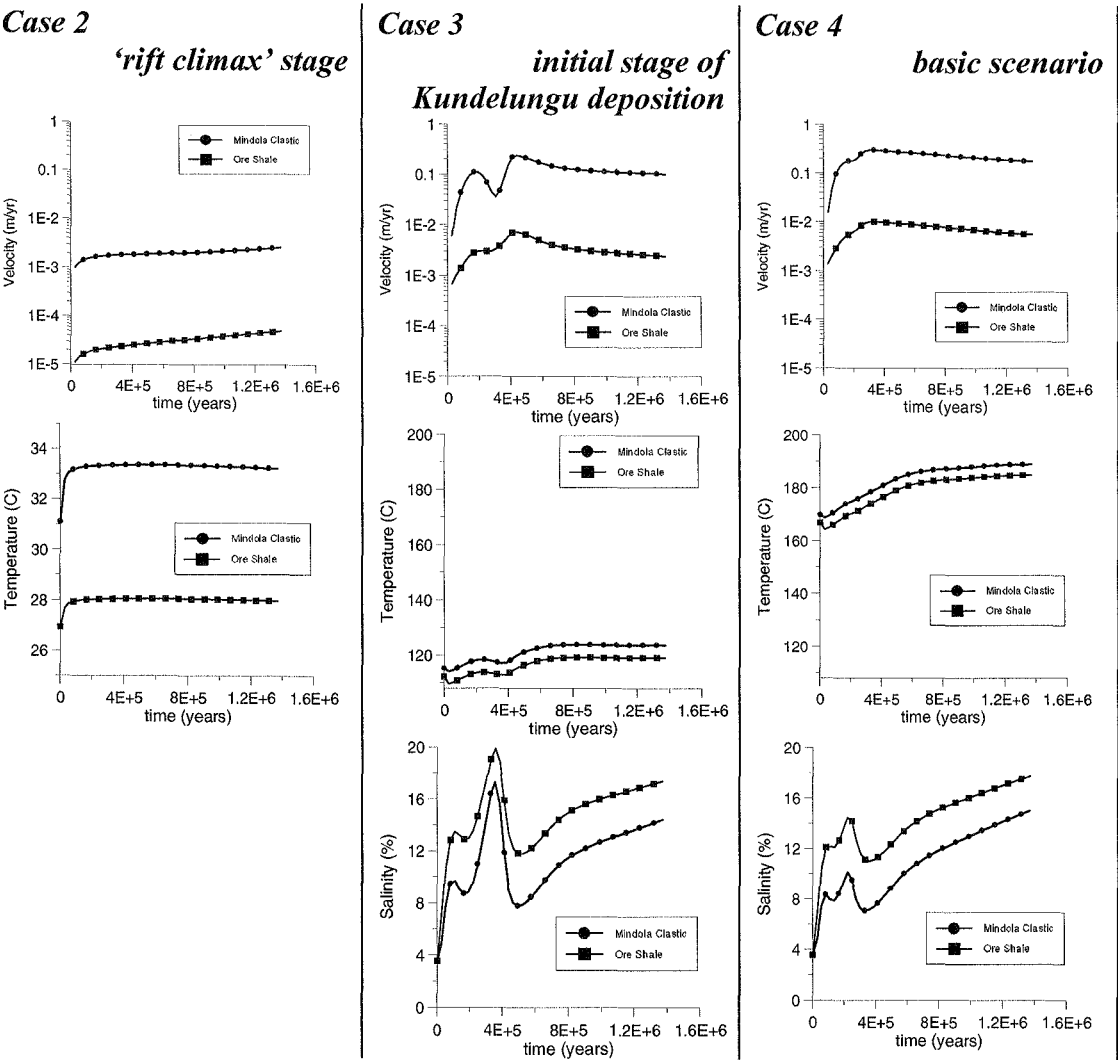


**Figure 6.45 Temporal dynamics of the absolute value of the fluid velocity vector, temperature and salinity in element '1' (Ore Shale) and '2' (Mindola Clastic) for Cases 2, 3, and 4.**

197

Common for all case studies are the higher velocity and temperature values in the mesh element '2' (Mindola Clastic Formation) than in the element '1' belonging to the Ore Shale. Salinity, on the contrary is higher in the Ore Shale. The reasons are obvious: higher permeability of the Mindola Clastic Formation determines more than one order of magnitude higher velocities. The Mindola Clastic layer is more deeply buried and therefore saturating fluid has a higher temperature (unless the flow introduces some thermal anomaly, which is not observed in this case). The difference in temperature is about $4\,^{0}C$. The Mindola Clastic Formation is separated from the source of solute, Upper Roan Salt, by the Ore Shale, hence in the latter, naturally, salinities are higher (around 3wt%).

The comparison also shows, on a local scale, the differences between the previously discussed scenarios. Thus, Case 2 is distinguishable from others by almost two orders of magnitude less fluid velocities and considerably lower temperature (salinity was not involved, as the interstitial fluid was assumed fresh at this stage of the basin evolution). As was discussed earlier, at the 'rift climax' stage, the only mechanism driving fluid flow, the geothermal gradient, is not very effective within the section of small thickness (which therefore has a less significant temperature contrast) sealed by the low-permeable shales. In Case 3 (the initial stage of Kundelungu sediment deposition), one can see a substantial rise in fluid velocities. They are now comparable with those for Case 4 (the basic scenario), since the additional driving mechanism, Roan Salt dissolution, has come into play. However, the velocity values are lower than those for the case study with the full thickness of the Kundelungu layer, Case 4 (see Figure 6.46).
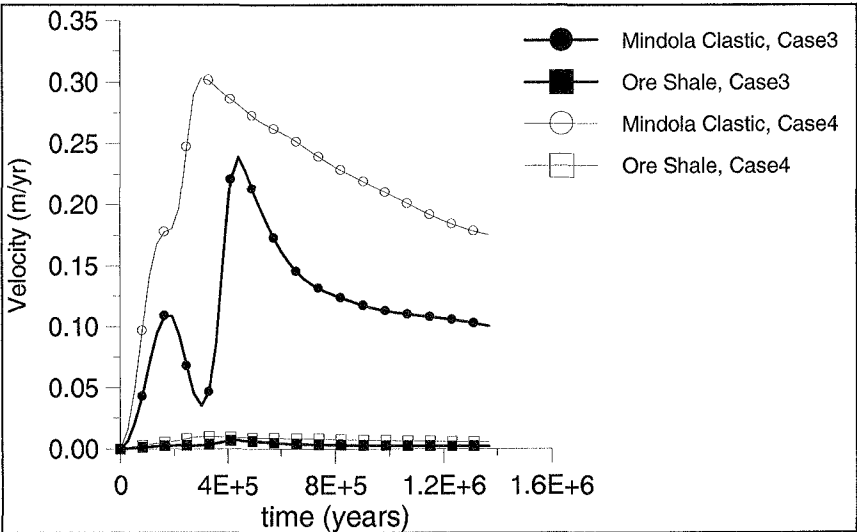


**Figure 6.46 Comparison of the fluid velocity absolute value in the two selected points within the Mindola Clastic Formation and Ore Shale layer for Case 3 (initial stage of the Kundelungu deposition) and Case 4 (basic scenario).**

Less intensive fluid circulation in Case 3, due to smaller thickness of the section, results in approximately $60\,^{0}C$ lower temperatures than in Case 4 (Table 6.1). At the same time, local salinity values seem to be influences by this to a lesser extent. Identical positioning relative to the salt layer of the analyzed elements, and strong downwelling solute fluxes, appear to be the chief determining factors. Table 6.1 shows that time-averaged salinity values for Case 3 and Case 4 are close.

| | Temperature ($^{0}C$) | | Salinity (%) | |
|---|---|---|---|---|
| | Mindola Clastic | Ore Shale | Mindola Clastic | Ore Shale |
| *Case 3* | 121.4 | 116.7 | 11.4 | 14.7 |
| *Case 4* | 183.3 | 179.0 | 10.8 | 14.1 |

**Table 6.1 Time-averaged temperature and salinity values in the two selected points within the Mindola Clastic Formation and Ore Shale layer for Case 3 (initial stage of the Kundelungu deposition) and Case 4 (basic scenario).**

Thus, from the local analysis of the average temperatures and salinities (Table 6.1) one can draw a conclusion that the thermal regime within the ore-hosting horizons is mainly dependent on the thickness of the section. In other words, temperatures tend to be higher at the later stages of the basin development when a thicker portion of the overlying layers is accumulated. At the same time, salinity values are not dependent on this factor to any significant degree.

Except for the early stage scenario, Case 2, the two other considered case studies show the span for temperature values at elements '1' and '2' of $108$ - $190\,^{0}C$ throughout the simulation. In Cases 3 and 4, ignoring the short period of salinity field adjustment from the initial sea-water value, the salinities fit within the range 7.1 – 20.4%. Haynes (1986a), analyzing stratiform copper deposits hosted by low-energy sediments, shows that chloride concentrations were likely to have been about six times seawater, which is approximately 21%. The simulation results are in agreement with this statement.

The results are also consistent with the fluid inclusion data from (Annels, 1989) which show that "the early mineralization event at Chambishi Southeast would have occurred over a temperature range $160$ - $170\,^{0}C$ and at salinity of 13 equiv. wt. % NaCl. Values as high as $193\,^{0}C$ were recorded... Deposition of copper rich sulphides during the later phase probably took place over a temperature range of $150$ - $160\,^{0}C$ and at salinity of 19%" (Annels, 1989: p.444). The simulation by the basic scenario,

Case 4, gives the temperature range 164 - 185 $^{0}C$ and salinity of 11.0 – 17.8% within the Ore Shale element '1'. At Chambishi deposit, Annels reports that "initial fluid temperature temperatures may have been as high as 213 $^{0}C$, with most of the paragenetically early minerals being deposited at a temperature close to 197 $^{0}C$ and at a salinity of 13%. Deposition of the later phases occurred mainly over a temperature range of 166 - 181 $^{0}C$ and at a salinity of 19%" (Annels, 1989: p.444). Thus, simulations show a similar pattern with the fluid inclusion data from Annels (1989).

## 6.8.2 Cu grade evaluation

Using the local fluid velocity values determined above, it is possible to evaluate the amount of interstitial water that passed through the rock. Further, assuming a certain amount of base metal in the fluid and efficiency of its precipitation within a rock unit, an estimate of the amount of the metal deposited can be obtained.

Haynes and Bloom (1987) came to the conclusion that a likely minimum Cu concentration in the metal-transporting waters must be 100ppm to form an ore which grades 1% or more copper. A study by Yardley (2005) of metal concentrations in crustal fluids presents the analysis of a database of saline fluid composition. Though no data on Cu content for sedimentary formation waters are presented, the value of 100ppm Cu is a reasonable and often-encountered magnitude for a wide range of fluids at different temperatures and Cl concentrations. So this conservative estimate is used in the further analysis.

Considering the deposition within elements '1' and '2', it was taken into account that the Copperbelt Orebody Member is a major source of organic material in the section (Selley et al., 2005) and represents a highly effective chemical trap, providing reducing conditions for Cu precipitation. Therefore, the deposition efficiency (the percentage of transported metal which is precipitated in 1 $m^3$ of rock within the element) was assumed 100% in the Ore Shale element '1'. The underlying clastic strata, was able to supply much less reductant hydrocarbon compared to the Ore Shale, and was assumed to have 200 times less metal deposition efficiency (0.5%).

Based on the estimate of 100ppm Cu in the interstitial fluid and 100% deposition efficiency in element '1' and 0.5%, respectively, in element '2', Figure

6.47 shows the amount of Cu precipitated in $1\,m^3$ within the Ore Shale and Mindola Clastic elements. The results are presented as *g* of Cu per *tonne* of the host rock.

*Case 2*
"rift climax"
stage
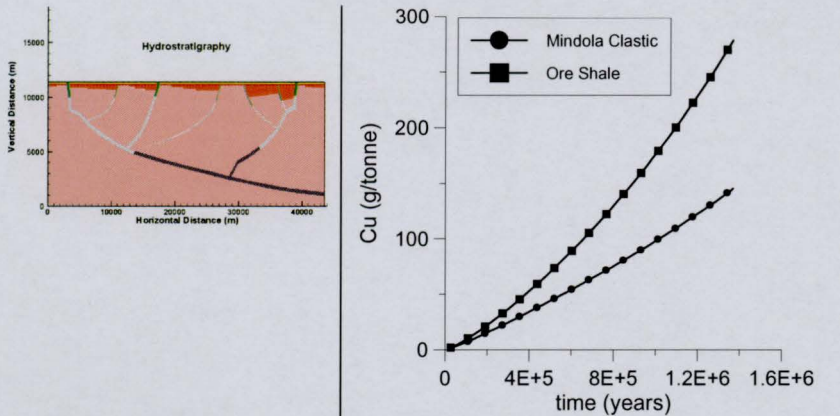
*Case 3*
initial stage of
the Kundelungu
deposition
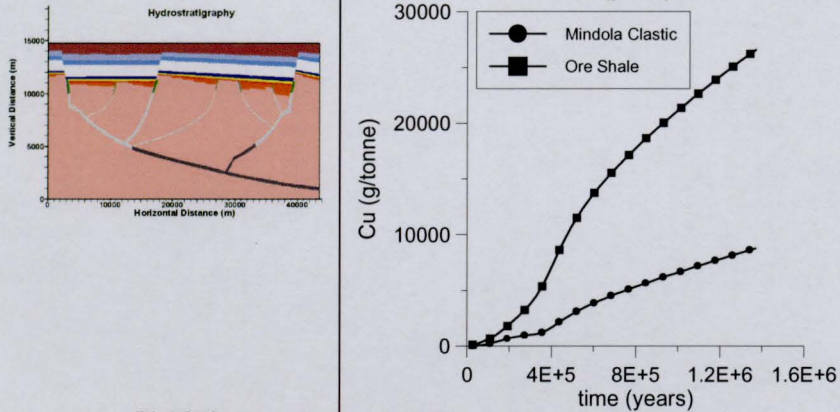
*Case 4*
basic scenario
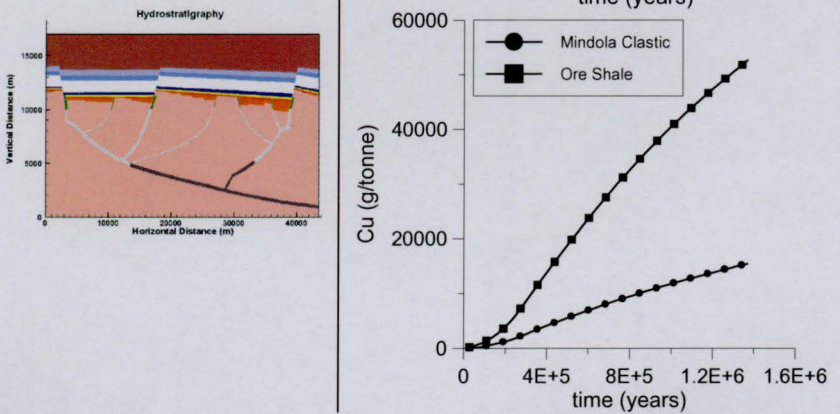
**Figure 6.47 Amount of Cu that would precipitate within $1\,m^3$ of the Ore Shale element '1' and Mindola Clastic element '2' under assumption 100ppm Cu content in the interstitial water, 100% deposition efficiency of the Ore Shale and 0.5% of the Mindola Clastic Formation.**

One can see that the amount of Cu precipitated for the same time interval is very much dependent on the hydrological scenario. Thus, after 1.4 million years for Case 2 ('rift climax' stage) the amount of accumulated Cu is 145ppm in 1 $m^3$ of the Mindola Clastic element and 278ppm within the Ore Shale one, while for Case 3 (the initial stage of the Kundelungu precipitation) the values are almost two orders of magnitude higher, 8777ppm and 26606ppm respectively. When the full thickness of the Kundelungu layer is considered (basic scenario, Case 4), the numbers increase two times: 15434ppm for the Mindola Clastic Formation and 52701ppm for the Ore Shale (Table 6.2).

| Scenario | Cu (ppm)=(g/ton) | |
|---|---|---|
| | _Mindola_ | _Ore Shale_ |
| _Case 2_ | 145 | 278 |
| _Case 3_ | 8777 | 26606 |
| _Case 4_ | 15434 | 52701 |

**Table 6.2 The amount of Cu precipitated within 1 $m^3$ of the Ore Shale element '1' and Mindola Clastic cell '2' at T2.**

One can also see that, despite the fact that the deposition efficiency of the Mindola Clastic Formation was assumed 200 times lower than of the Ore Shale, the amount of Cu accumulated over the simulation period in the Mindola Clastic is only about 2 to 3 times less than in the Ore Shale. It means that much higher flow rates in the clastic unit compensate for its being a less effective deposition environment. This result also agrees with the chemical and petrographical analysis by Sutton and Maynard (2005) which showed for some core samples significant concentrations of Cu in the footwall (Sutton and Maynard, 2005: pp. 104, 106).

What is also important, that not only the absolute amount of Cu, but the character of the time dynamics, differs from one case study to another. Thus, the trend curve, based on the last 200 thousand years of the simulation in the early-stage fresh-water Case 2 grows fast as a power function. For Cases 3 and 4, when the salt sheet dissolution is involved, it behaves as a logarithmic function and therefore, the Cu content would increase more slowly. The conclusion is that different configurations of the section and hydrological scenarios influence not only the amount of the precipitated base metal but also affect the rate of its accumulation.

Evaluation of the amount of the precipitated base metal can also show a drastic difference between the fresh-water scenario and a simulation involving the salt sheet

dissolution as an additional driving mechanism. In Figure 6.48, the comparison of the Cu amount that would precipitate under the same assumptions is presented for the basic Case 4 and the fresh-water scenario Case 5. It is necessary to note here that, strictly speaking, the supposition about 100ppm Cu content in fresh water is unjustifiable, because Cu is generally accepted to migrate as cuprous chloride complexes (Haynes and Bloom, 1987; Walker, 1989). This number is kept only for the purpose of a 'clean' comparison, as both scenarios use the same setting, only the salt transport is excluded from consideration in Case 5.

One can see that the resulting metal amount for the fresh-water Case 5 is almost 3.5 times less in the Ore Shale element '1' and 9.8 times less in the Mindola Clastic element '2' (Table 6.3)



(a)                                        (b)
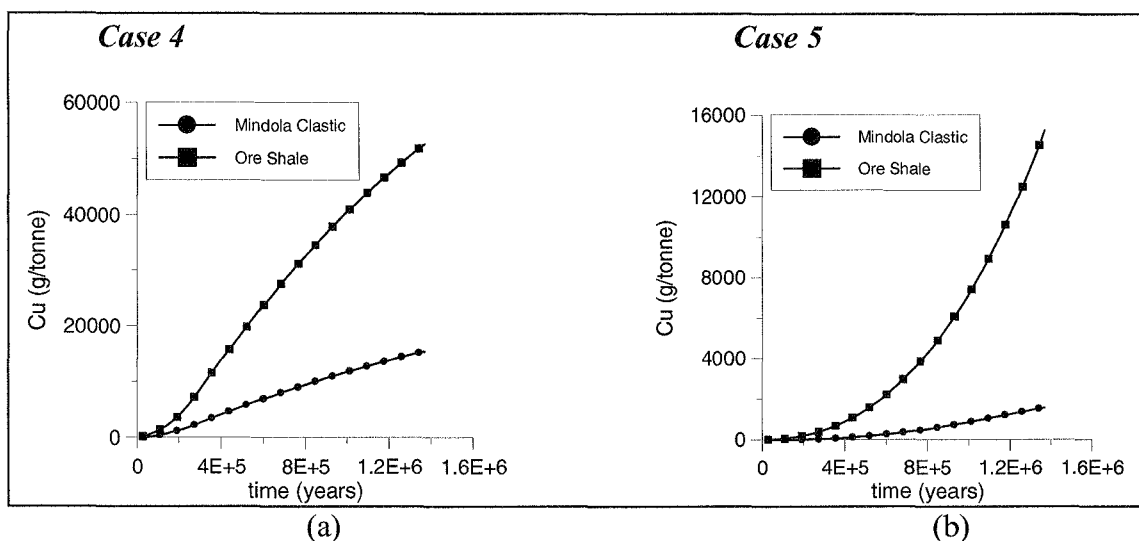
**Figure 6.48 Cu amount that would precipitate within** $1\,m^3$ **of the Ore Shale element '1' and Mindola Clastic element '2' under assumption 100ppm Cu content in the interstitial water, 100% deposition efficiency of the Ore Shale and 0.5% of the Mindola Clastic Formation: (a) – salt-water basic scenario Case 4; (b) – fresh-water scenario Case 5.**

| Scenario | Cu (ppm)=(g/ton) | |
|---|---|---|
| | *Mindola* | *Ore Shale* |
| *Case 4*, basic scenario | 15434 | 52701 |
| *Case 5*, fresh-water scenario | 1577 | 15266 |
| | 9.8 times less | 3.5 times less |

**Table 6.3 Cu contents at the end of the simulation (1.4 m.y.) in** $1\,m^3$ **of the Ore Shale element '1' and Mindola Clastic element '2' under assumption 100ppm Cu content in the interstitial water, 100% deposition efficiency of the Ore Shale and 0.5% of the Mindola Clastic Formation.**

This observation, once again, confirms that in basins, where the presence of massive halite volumes is recorded, a fresh-water simulation can generate a radically differing result and would not produce significant Cu mineralization.

The result on Cu amount precipitated within the Ore Shale, 5.3%, seems to be a slightly overstated value. Selley et al. (2005) report Cu grade for the argillite-hosted Konkola deposit 3.59% and 2.71% for Chambishi. The maximum fluctuation for Ore Shale Cu content in Sutton and Maynard's (2005) data is about 4%. One possible reason that could have lead to the overestimate is the assumption that the permeability of the rock units comprising the section maintained throughout the full period. A second point is that in reality most mineralization occurs within the lower part of the Copperbelt Orebody Member: a roughly 10m thick interval according to (Selley et al., 2005); 'within 50 cm of the surface of the host sediment' - (Haynes, 1986: p.258). Sutton and Maynard's core examination showed that the highest Cu values are at the base of Ore Shale and decrease upward (Sutton and Maynard, 2005: p.104). However, in this model, the 'Ore Shale' unit is presented by a single layer of finite elements (approximately 100 thick) and the spatial scale of the simulation does not allow further detalization of the layer in the vertical direction. Without this, it is problematic to make any reasonable suggestions about how the flow rate may vary in this lowermost part of the Ore Shale layer.

The averaged (by stratigraphic unit) Cu content in the footwall, according to Sutton and Maynard's (2005) data, lies within the range approximately 6.3 – 251.2 ppm, although the actual values at the interface with the Ore Shale reach up to 2.7%. The simulation result, 1.5% Cu grade in the element '2' is within the acceptable limit for the 'footwall – Ore Shale' contact. Selley et al. (2005) provides data on the similarly located Nchanga-Chingola lower orebody and gives Cu grades of 2.5%, which is approximately 1.7 times higher than the numerical result. However, considering all the rough simplifying suppositions explained before and very approximate way of obtaining the Cu grade estimates, it, nevertheless, lies within the feasible limits and shows the possibility of formation of high-grade stratiform copper deposits.

# 7 Conclusions

The presented work complements parallel studies on the Zambian Copperbelt (Selley, 2005; Hitzman, 2005) providing a new insight to many of the basin-scale processes. The two-dimensional numerical model, developed as a key tool of the project, based on the extensive validation carried out, proved to produce non-contradictory results for various settings. Thus, its application to the section representing the ZCB is believed to illustrate paleo-flow of the mineralizing fluid in this sediment-hosted stratiform copper system.

A set of basin configurations built on the basis of the current understanding of the ZCB architecture, allowed consideration of the evolution of basin hydrology with time. The numerical study presented in the previous chapter not only gives a general picture of migration of interstitial water but also enables an understanding of factors controlling circulation of metal-bearing fluid in regards to the flow pattern, direction of fluxes, fluid velocity values, salinity and temperature variation. They were also used for the analysis of properties of the ore-forming fluid and assessment of the possibility of ore body formation at favorable locations.

Based on the results of the numerical simulations, several conclusions can be drawn. First, all the case studies show a significant basement involvement into the circulation of the hydrothermal fluid. Despite the low permeability and porosity attributed to this stratigraphic unit in the simulations, fluid density perturbations show to be an efficient mechanism able to initiate and maintain the convective flow. It means that if there is a mechanism capable to sustain or reactivate at least minimum permeability of the basement, a significant amount of fluid can pass through this volcanic and granite unit. In this case, the crystalline basement can be considered as a potential source of the base metals, especially taking into account a significant metal content in the ore-bearing horizons, which cannot be supplied by the low-volume/low-capacity red-beds.

The network of high-permeable faults does not seem to be a required condition to secure a cross-stratal flow in the lower part of the section. Even in the absence of permeable conduits, the driving capacity of the fluid density gradient is powerful enough to support the convection through the basement. Faults rather redistribute the flow structure directing fluid fluxes along easy-accessible pathways.

Simulation showed an exceptional impact of the Upper Roans Salt onto the system dynamics. Distributed salt sources arising from salt sheet dissolution drastically enhance density instability caused by the geothermal gradient. The geometry of the salt layer and any changes in its properties, that can increase the brine influx, affect the flow pattern and temperature field. If the salinity effect is excluded from the simulation, as shown by the fresh water simulation, it leads to a totally different flow regime in terms of its configuration, intensity, and fluid temperature distribution. The influence of Roan Salt dissolution is also illustrated by simulations of early stages of basin evolution. When no salt sheet is formed yet, and the layer of deposited sediments is not thick enough to result in a significant temperature contrast, flow rates are almost one order of magnitude lower than in all later case studies.

Low-permeable Upper Roan and Lower Mwashia strata play the role of a barrier separating two hydrological compartments. If in the lower one, the Roan Salt dissolution leads to an unstable fluid density distribution triggering free convection, in the upper compartment, rapid salinity diffusion upwards creates a strong stable stratification of the interstitial fluid. The existing temperature gradient appears to be insufficient to overpower the stabilizing effect of salinity. As a result, no fluid motion can be activated in the upper compartment unless the barrier is breached. Moreover it should be pierced through in more than one location. Otherwise, a single breach becomes occupied by the heavy downwelling solute plume, excluding any possibility for the hot less dense fluid of the lower compartment to rise above the seal.

The local analysis of metal-bearing fluid properties was carried out for two elements, which mark plausible locations for an argillite-hosted orebody (similar to Chambishi deposit) and a footwall deposit (analogous to Nchanga-Chingola deposit).

For the three scenarios selected to represent consequent phases of the basin evolution, temperature and salinity values appeared to correspond with the results of geothermometric studies (Annels, 1989) and fit well within the range required for the mineralization. The salinity values (11-16% in the Mindola Clastic element and 14-19% within the Ore Shale element) ensure the availability of chloride-rich formation waters which favour Cu transport.

Comparison of the different scenarios led to the conclusion that, on the local scale, the thermal regime within the ore-hosting horizons is mainly influenced by the overall thickness of the section and, therefore, stage of deposition. Minor changes of

the basin architecture also make an effect, though of lesser importance. At the same time, local salinity values are less sensitive to the thickness of the section, as long as the element location with respect to the salt layer is the same. Any changes that affect the salt influx into the system also have a natural response on a local scale.

Local fluid velocities seem to be a characteristic most sensitive to the variations of the section configuration, especially to the changes in the thickness of overlying strata. As a result, the volume of fluid passing through the rock and, therefore, the amount of the precipitated base metal can increase up to two orders of magnitude at the later phases of basin development.

High flow rates in the Mindola Clastic Formation can lead to the formation of high-grade orebodies within the footwall. Even assuming the deposition efficiency of this rock unit to be two orders of magnitude lower than of the Ore Shale, the amount of the precipitated base metal is only about two to three times lower than within the argillaceous strata.

The comparison with the fresh water scenario showed the importance of the involvement into the simulation of salt transport and salt sheet dissolution. Even assuming the same Cu content in fresh water (which is very unlikely in reality, as it has much lower capacity to transport Cu), the amount of the precipitated base metal appeared to be almost 3.5 times less in the Ore Shale and 9.8 times less within the Mindola Clastic element than for a saline water scenario.

A very approximate evaluation based on the conservative 100ppm Cu content in the interstitial fluid shows that the copper grade may reach up to 5.3% within the Ore Shale and 1.5% in the Mindola Clastic. Although this very rough evaluation was done under a set of simplifying assumptions (Section 6.8), it demonstrates the scale and ore potential of the salt enhanced density driven flow in this model of fluid flow in the Zambian Copper Belt.

# References

Adams J.J. and Bachu S. (2002) Equations of state for basin geofluids: algorithm review and intercomparison for brines. Geofluids, 2, 257-271.

Ahlstrom S.W., Foote H.P., Arnett R.C., Cole C.P., and Serne R.J. (1977) Multicomponent mass transport model: theory and numerical implementation (discrete-particle-random-walk-version). Rep. BNWL-2127, Battelle Pac. Northwest Lab., Richland, Wash.

Annels, A.E. (1974) Some aspects of the stratiform ore deposits of the Zambian Copperbelt. In: Bartholomé, P. (Ed.) Gisement Stratiformes et Provinces Cuprifères, Société Géologique de Belgique, 235-254.

Annels A.E. (1984) The geotectonic environment of Zambian copper-cobalt mineralization, Journal of the Geological Society of London, 141, 279-289.

Annels A.E. (1989) Ore genesis in the Zambian Copperbelt, with particular reference to the northern sector of the Chambishi Basin. In: Boyle R. W., Brown A. C., Jefferson C.W., Jowett E.C. and Kirkham R.V., (Eds.), Sediment-hosted Stratiform Copper Deposits, Geological Association of Canada, Special Paper 36, 427–452.

Annels, A.E., Vaughan, D.J. and Craig, J.R. (1983) Conditions of ore mineral formation in certain Zambian Copperbelt deposits with special reference to the role of cobalt. Mineralium Deposita, 18, 71-88.

Appold M.S. and Garven G. (2000) Reactive models of ore formation in the Southeast Missouri District. Economic Geology, 95, 1605-1626.

Armstrong R.A., Robb L.J., Master S., Kruger F.J., and Mumba P.A.C.C. (1999) New U-Pb age constraints on the Katangan Sequence, Central African Copperbelt: Journal of African Earth Sciences. Special Abstracts Issue, GSA 11: Earth Resources for Africa, 28, 6-7.

Barron J. W. (2003) The stratigraphy, metamorphism, and tectonic history of the Solwezi area, Northwest Province, Zambia: Integrating geological field observations and airborne geophysics in the interpretation of regional geology. Unpub. Ph.D., Colorado School of Mines, Golden, CO., USA, 233pp.

Bateman A.M. (1930) Ores of the Northern Rhodesian Copperbelt. Economic Geology, 25, 365-418.

Batzle M. and Wang Z. (1992) Seismic properties of pore fluids. Geophysics, 57, 1396-1408.

Bear J. (1972) Dynamics of Fluids in Porous Media. American Elsevier, 764pp.

Bear J. and Corapcioglu M.Y. (Eds.) (1982) Fundamentals of Transport Phenomena in Porous Media, 1003pp.

Bense V.F. and Person M.A. (2006) Faults as conduit-barrier systems to fluid flow in siliciclastic sedimentary aquifers. *Water Resources Research*, **42**, W05421, doi:10.1029/2005WR004480.

Bethke C.M. (1986) Roles of sediment compaction, tectonic compression, and topographic relief in driving deep groundwater migration. Geological Society of America, Abstracts with programs, 18, 540.

Bethke C.M. and Corbet T.F. (1988) Linear and non-linear solutions for one-dimensional compaction flow in sedimentary basins. *Water Resources Research*, **24**, 461-467.

Binda, P.L and Mulgrew, J.R. (1974) Stratigraphy of copper occurrences in the Zambian Copperbelt. In: Bartholomé, P. (Ed.) Gisement Stratiformes et Provinces Cuprifères. Société Géologique de Belgique, 215-233.

Binda P.L. and Porada H. (1995) Observations on the Katangan breccias of Zambia: Royal Museum of Central Africa (Belgium), Annales de la Société Géologique, 101, 49-62.

Bodnar R.J. (2003) Introduction to aqueous-electrolyte fluid inclusions. In: Samson I., Anderson A., and Marshall D. (Eds.) Fluid Inclusions. Analysis and Interpretation. Mineralogical Association of Canada, 374pp.

Boyle R.W. (1989) Preface. In: Boyle R. W., Brown A. C., Jefferson C.W., Jowett E.C. and Kirkham R.V., (Eds.), Sediment-hosted Stratiform Copper Deposits, Geological Association of Canada, Special Paper 36, vii-viii.

Bradford S.F. and Katopodes N.D. (2000) The anti-dissipative, non-monotone behavior of Petrov-Galerkin upwinding. International Journal for Numerical Methods in Fluids, 33, 583-608.

Bredehoeft J.D. (1988) Will salt repositories be dry? Eos (Transactions, American Geophysical Union), 69, 121-131.

Breit G.N., Meunier J.D., Rowan E.L., and Goldhaber M.B. (1987) Alteration related to red bed copper mineralizing brines and other fault-controlled solutions in Lisbon Valley, Utah, and the Slick Rock district, Colorado (abstract). In: Sommerville Sach J. (Ed.) USGS Research on Mineral Resources – 1987, Programs and Abstracts: United States Geological Survey, Circular 995, 7-8.

Cailteux, J. (1994) Lithostratigraphy of the Neoproterozoic Shaba-type (Zaire) Roan Supergroup and metallogenesis of associated stratiform mineralization. Journal of African Earth Sciences, 19, 279–301.

Cailteux, J.L.H., and Kampunzu, A.B.H. (2002) Lithostratigraphic Position and Petrological Characteristics of R.A.T. (Roches Argilo-Talqueuses) Subgroup Sedimentary Rocks, Neoproterozoic Katangan Belt (Congo): 11th IAGOD Symposium and Geocongress, Windhoek, Namibia, Geological Survey Namibia.

Caine J.S., Evans J.P., and Forster C.B. (1996) Fault zone architecture and permeability structure. *Geology*, **24**, 1025-1028.

Campbell H.E., Dierker P.F. (1976) Calculus. Prindle, Weber & Schmidt, Inc., 752pp.

Casas E. and Lowenstein T.K. (1989) Diagenesis of saline pan halite: comparison of petrographic features of modern, Quaternary and Permian halites. Journal of Sedimentary Petrology, 59, 724-739.

Christie I., Griffiths D.F., Mitchell A.R., Zienkiewicz O.C. (1976) Finite element methods for second order equations with significant first derivatives. International Journal for Numerical Methods in Engineering, 10, 1389-1396.

Clemmey, H. (1974) Sedimentary geology of a Late Precambrian copper deposit at Kitwe, Zambia. In: Bartholomé, P. (Ed.) Gisements Stratiformes et Provinces Cuprifères. Société Géologique de Belgique, 255-265.

Clemmey, H. (1976) Aspects of stratigraphy, sedimentology and ore genesis on the Zambian Copperbelt: PhD thesis, Leeds University, 357pp.

Clemmey, H. (1978) A Proterozoic lacustrine interlude from the Zambian Copperbelt.In: Matter, A. and Tucker, M.E. (Eds) Modern and ancient lake sediments: proceedings of a symposium: Special Publication of the International Association of Sedimentologists, 2, 259-278.

Combarnous M.A. and Bories S.A. (1975) Hydrothermal convection in saturated porous media. Advances in Hydroscience, 10, 232-307.

Conybeare C.E.B. (1979) Lithostratigraphic Analysis of Sedimentary Basins. Academic Press, 555pp.

Daly M.C., Chakraborty S.K., Kasolo P., Musiwa M., Mumba P., Naidu B., Nameteba C., Ngambi O., and Coward M.P. (1984) The Lufilian Arc and Irumide belt of Zambia: results of a geotraverse across their intersection. Journal of African Earth Sciences, 2, 311-318.

Duff I.S., Erisman A.M., Reid J.K. (1986) Direct Methods for Sparse Matrices. Clarendon Press, 341pp.

Elder J. W. (1967) Steady free convection in a porous medium heated from below. Journal of Fluid Mechanics, 27, part 1, 29-48.

Evans D.G., Nunn J.A. and Hanor J.S. (1991) Mechanism driving groundwater flow near salt domes. Geophysical Research Letters, 18, №5, 927-930.

Fleischer, V.D. (1984) Discovery, geology and genesis of copper-cobalt mineralization at Chambishi Southeast prospect, Zambia. Precambrian Research, 25, 119-133.

Fleischer V.D., Garlick W.G., and Haldane R. (1976) Geology of the Zambian Copperbelt. In: Wolf, K.H. (Ed.), Handbook of Strata-bound and Stratiform Ore deposits, v. 6, 223-352.

Fletcher C.A.J. (1984) Computational Galerkin Methods. Springer-Verlag, 309pp.

Gablina I.F. (1997) Formation conditions of large cupriferous sandstone and shale deposits, Geology of Ore Deposits, 39, 320-333.

Garlick, W.G. (1961) Structural evolution of the Copperbelt. IN: Mendelsohn, F. (Ed.) The Geology of the Northern Rhodesian Copperbelt, London, MacDonald, 89–105.

Garlick W.G. and Brummer J.J. (1951) The age of the granites of the Northern Rhodesian Copperbelt. Economic Geology, 46, 478-498.

Garlick, W.C. and Fleischer, V.D. (1972) Sedimentary environment of Zambian copper deposition. Geologie en Minbouw, 51, 277-298.

Garven G. (1985) The role of regional fluid flow in the genesis of Pine Point deposit, Western Canada Sedimentary Basin. Economic Geology, 80, 307-324.

Garven G. (1989) A hydrogeologic model for the formation of the giant oil sands deposits of the Western Canada Sedimentary Basin. American Journal of Science, 289, 105-166.

Garven G. and Freeze R.A. (1984) Theoretical analysis of the role of groundwater flow in the genesis of stratabound ore deposits. I. Mathematical and numerical model. American Journal of Science, 284, 1085-1124.

Garven G., Ge S., Person M.A., Sverjensky D.A. (1993) Genesis of stratabound ore deposits in the Midcontinent Basins of North America. 1. The role of regional groundwater flow. American Journal of Science, 293, 497-568.

Garven G., Bull S.W., Large R.R. (2001) Hydrothermal fluid flow models of stratiform ore genesis in the McArthur Basin, Northern Territory, Australia. Geofluids, 1, 289-311.

Golub G.H., Van Loan C.F. (1989) Matrix Computations. The Johns Hopkins University Press, 642pp.

Graf T. (2004) On the use of the Elder (1967) convection experiment as a benchmark problem for variable-density transport model. The Geological Society of America, 2004 Denver Annual Meeting, paper № 68-2.

Griffiths R.W. (1981) Layered double-diffusive convection in porous media. Journal of Fluid Mechanics, 102, 221-248.

Grove D.B. (1977) The use of Galerkin finite-element methods to solve mass transport equations. Rep. USGS/WRD/WRI-78/011, U.S. Geol. Surv., Denver, Colo. (Available as NTIS PB 277-532 from Natl. Tech. Inf. Serv., Springfield, Va.)

Haynes D.W. (1986) Stratiform copper deposits hosted by low-energy sediments: I. Timing of Sulfide Precipitation – An Hypothesis. Economic Geology, 81, 250-265.

Haynes D.W. (1986a) Stratiform copper deposits hosted by low-energy sediments: II. Nature of source rocks and composition of metal-transporting water. Economic Geology, 81, 266-280.

Haynes D.W. and Bloom M.S. (1987) Stratiform copper deposits hosted by low-energy sediments: III. Aspects of metal transport. Economic Geology, 82, 635-648.

Heinrich J.C., Huyakorn P.S., Zienkiewicz O.C., Mitchell A.R. (1977) An 'upwind' finite element scheme for two-dimensional convective transport equation. International Journal for Numerical Methods in Engineering, 11, 131-143.

Herbert A.W., Jackson C.P., and Lever D.A. (1988) Coupled groundwater flow and solute transport with fluid density strongly dependent upon concentration. Water Resources Research, 24, 1781-1795.

Hitzman M.W. (2000) source basins for sediment-hosted stratiform Cu deposits: implications for the structure of the Zambian Copperbelt. Journal of African Earth Sciences, 30, 855-863.

Hitzman M., Kirkham R., Broughton D., Thorson J., and Selley D. (2005) The Sediment-Hosted Stratiform Copper Ore System, Economic Geology 100th Anniversary Volume, Society of Economic geologists, Inc., 609-642.

Hoeve J., and Quirt D. (1989) A common diagenetic-hydrothermal origin for unconformity-type uranium and stratiform copper deposits. In: Boyle R. W., Brown A. C., Jefferson C.W., Jowett E.C. and Kirkham R.V., (Eds.), Sediment-hosted Stratiform Copper Deposits, Geological Association of Canada, Special Paper 36, 151–172.

Holzbecher E. (1998) Modeling Density-Driven Flow in Porous Media. Springer, 286pp.

Horne R.A. (1969) Marine Chemistry. Wiley-Interscince, 568pp.

Ingebritsen S.E. and Manning C.E. (2002) Diffuse fluid flux through orogenic belts: Implications for the world ocean. PNAS, 99, 9113-9116.

Jackson G.C.A. (1932) The ores of the N'changa Mines and extensions of Northern Rhodesia. Economic Geology, 27, 247-280.

Jackson, M.P.A., Warin, O.N., Woad, G.M., and Hudec, M.R. (2003) Neoproterozoic allochthonous salt tectonics during the Lufilian orogeny in the Katangan Copperbelt, central Africa. Geological Society of America Bulletin, 115, 314-330.

Jiang Z., Oliver N.H.S., Barr T.D., Power W.L., and Ord A. (1997) Numerical modeling of fault-controlled fluid flow in the genesis of tin deposits of the Malage ore field, Gejiu mining district, China. Economic Geology, 92, 228-247.

Jowett E.C. (1986) Genesis of Kupferschiefer Cu-Ag deposits by convective flow of rotliegende brines during Triassic Rifting. Economic Geology, 81, 1823–1837.

Jowett E.C. (1989) Effects of continental rifting on the location and genesis of stratiform copper-silver deposits. In: Boyle R. W., Brown A. C., Jefferson C.W., Jowett E.C. and Kirkham R.V., (Eds.), Sediment-hosted Stratiform Copper Deposits, Geological Association of Canada, Special Paper 36, 53-66.

Kampunzu A.B. and Cailteux J. (1999) Tectonic evolution of the Lufilian Arc (Central Africa Copper Belt) during Neoproterozoic Pan African orogenesis, Gondwana Research, 2, 401-421.

Kemp N.P., Thomas D.C., Atkinson G., Atkinson B.L. (1989) Density modeling for brines as a function of composition, temperature and pressure. SPE Production Engineering, 4, 394-400.

Kestin J., Khalifa H.E., Correia R.J. (1981) Tables of the dynamic and kinematic viscosity of aqueous NaCl solutions in the temperature range of 20-150$^0 C$ and the pressure range of 0.1-35 MPa. Journal of Physical and Chemical Reference Data, 10, 71-87.

Key R.M., Liyungu A.K., Njamu F.M., Somwe V., Banda J., Mosley P.N., and Armstrong R.A. (2001) The western arm of the Lufilian Arc in NW Zambia and its potential for copper mineralization. Journal of African Earth Sciences, 33, 503-528.

Kirkham R.V. (1989) Distribution, setting, and genesis of sediment-hosted stratiform copper deposits. In: Boyle R. W., Brown A. C., Jefferson C.W., Jowett E.C. and Kirkham R.V., (Eds.), Sediment-hosted Stratiform Copper Deposits, Geological Association of Canada, Special Paper 36, 3-38.

Knauth L.P., Kumar M.B., and Martinez J.D. (1980) Isotope geochemistry of water in Gulf Coast salt domes. Journal of Geophysical Research, 85, 4863-4871.

Korn G.A., Korn T.M. (1961) Mathematical Handbook for Scientists and Engineers. McGraw-Hill Book Company, Inc., 943pp.

Land L.S., Kupecz J.A., and Mack L.E. (1988) Louann Salt geochemistry (Gulf of Mexico sedimentary basin, USA): A preliminary synthesis. Chemical Geology, 74, 25-35.

Lee C.-H. and Farmer I. (1993) Fluid Flow in Discontinuous Rocks. Chapman & Hall, 169pp.

Lefebvre, J.J. (1989) Depositional Environment of Copper-Cobalt Mineralization in the Katangan Sediments of Southeast Shaba, Zaire. In: Boyle, R.W., Brown, A.C., Jefferson, C.W., Jowett, E.C. and Kirkham, R.V. (Eds.) Sediment-hosted Stratiform Copper Deposits, Geological Association of Canada, Special Paper, 36, 401–426.

Lein H. and Tankin R. S. (1992) Natural convection in porous media – I. Nonfreezing. International Journal of Heat and Mass Transfer, 35, №1, 175-186.

Lewis S. and Holness M. (1996) Equilibrium halite-H2O dihedral angles: High rock-salt permeability in the shallow crust. Geology, 24, 431-434.

Light M.P., Posey H.H., Kyle J.R., and Price P.E. (1987) Model for the origins of geopressured bribes, hydrocarbons, cap rocks and metallic mineral deposits: Gulf Coast, USA. In: Lerche I. and O'Brien J.J. (Eds) Dynamical Geology of Salt and Related Structures. Academic Press, Inc., Orlando, 789-830.

Loytsyanski L. (1970). Mechanics of Fluid and Gas. Nauka, 904pp. (in Russian).

Lur'ye A.M. and Gablina I.F. (1972) The copper source in the production of Manfeld-type deposits in the West Ural foreland. Geochemistry International, 9, 56-57.

Lustwerk R.L. and Wasserman M.D. (1989) Water-escape structures in the Coates Lake Group, Northwest Territories, Canada, and their relationship to mineralization at the Redstone Stratiform Copper Deposit. In: Boyle R. W., Brown A. C., Jefferson C.W., Jowett E.C. and Kirkham R.V., (Eds.), Sediment-hosted Stratiform Copper Deposits, Geological Association of Canada, Special Paper 36, 207-224.

Malki-Epshtein L., Phillips O.M. and Huppert H.E. (2004) The growth and structure of double-diffusive cells adjacent to a cooled sidewall in a salt-stratified environment. Journal of Fluid Mechanics, 518, 347-362.

Marjonen, R.K. (2000) Geology of the Mufulira – Kitwe area: explanation of degree sheet 1228, part of NW quarter and SW quarter. Report of the Geological Survey of Zambia, No. 60, 31pp.

Mauk J.L., Kelly W.C., van der Plujim B.A., and Seasor R.W. (1992) Relations between deformation and sediment-hosted copper mineralization: Evidence form the White Pine part of the Midcontinent rift system, Geology, 20, 427-430.

Mendelsohn, F. (1961) (Ed.) The Geology of the Northern Rhodesian Copperbelt. London, MacDonald, 523 pp.

McCain W.D. Jr. (1991) Reservoir fluid property correlations – state of the art. SPE Reservoir Engineering, 6, 266-272.

Miller, R.McG. (1983) The Pan-African Damara Orogen of South West Africa/Namibia. In: Miller, R.McG. (Ed.) Evolution of the Damara Orogen of South West Africa/Namibia. Geological Society of South Africa Special Publication, 11, 431-515.

Munyanyiwa, H., Hanson, R.E., Blenkinsop, T.G. and Treloar, P.J. (1997) Geochemistry of amphibolites and quartzofeldspathic gneisses in the Pan-African Zambezi belt, northwest Zimbabwe: evidence for bimodal magmatism in a continental rift setting. Precambrian Research, 81, 179-196.

Nield D.A. (1968) Onset of thermohaline convection in porous medium. Water Resources Research, 4, №3, 553-560.

Oldenburg C.M. and Pruess K. (1995) Dispersive transport dynamics in a strongly coupled groundwater-brine flow system. Water Resources Research, 31, 289-302.

214

Oliver J. (1986) Fluids expelled tectonically from orogenic belts: their role in hydrocarbon migration and other geologic phenomena. Geology, 14, 99-102.

Oliver N.H.S., McLellan J.G., Hobbs B.E., Cleverley J.S., Ord A., and Feltrin L. (in press) Numerical models of deformation, heat transfer and fluid flow across basement-cover interfaces during basin-related mineralization.

Palliser C. and McKibbin R. (1998a) A model for deep geothermal brines, I: T-P-X state-space description. Transport in Porous Media, 33, 65-80.

Palliser C. and McKibbin R. (1998b) A model for deep geothermal brines, II: Thermodynamic properties - density. Transport in Porous Media, 33, 129-154.

Palliser C. and McKibbin R. (1998c) A model for deep geothermal brines, III: Thermodynamic properties – enthalpy and viscosity. Transport in Porous Media, 33, 155-171.

Palm E., Weber J. E. and Kvernvold O. (1972) On steady convection in a porous medium. Journal of Fluid Mechanics, 54, part1, 153-161

Person M., Garven G. (1994) A sensitivity study of the driving forces on fluid flow during continental-rift basin evolution. Geological Society of America Bulletin, 106, 461-475.

Pettijohn F.J. (1975) Sedimentary Rocks. Harper & Row, 628pp.

Phillips O.M. (1991) Flow and Reactions in Permeable Rocks. Cambridge University Press, 285pp.

Phillips S.L., Igbene A., Fair J.A., Ozbek H., Tavana M. (1981) A Technical Databook for Geothermal Energy Utilization. Lawrence Berkeley Laboratory Report 12810.

Popov Y., Tertychnyi V., Romushkevich R., Korobkov D., Pohl J. (2003) Interrelations between thermal conductivity and other physical properties of rocks: experimental data. Pure and Applied Geophysics, 160, 1137-1161.

Porada H. and Berhorst V. (2000) Towards a new understanding of the Neoproterozoic-Early Paleozoic Lufilian and Northern Zambezi belts in Zambia and Congo/Zaire. Journal of African Earth Sciences, 30, 727-771.

Prosser, S. (1993) Rift-related linked depositional systems and their seismic expression. In: Williams, G.D. and Dobb, A. (Eds) Tectonics and seismic sequence stratigraphy, Geological Society Special Publication, 71, 35-66.

Rabinowitz D.D. and Gross G.W. (1972) Environmental tritium as a hydrometeorologic tool in the Roswell Basin, New Mexico, Tech. Completion Rep. OWRR :A-037-NMEX, N.M. Water Resour. Res. Inst., Las Cruces.

Raffensperger J.P. and Vlassopoulos D. (1999) The potential for free and mixed convection in sedimentary basins. Hydrogeology Journal, 7, 505-520.

Rawling G.C., Goodwin L.B., and Wilson J.L. (2001) Internal architecture, permeability structure, and hydrologic significance of contrasting fault zone types. *Geology*, **27**, 43-46.

Renfro A.R. (1974) Genesis of evaporite-associated stratiform metalliferous deposits – a sabkha process. Economic Geology, 69, 33-45.

Ribando R. J. and Torrance K. E. (1976) Natural convection in a porous medium: effects of confinement, variable permeability, and thermal boundary conditions. Journal of Heat transfer, 98, 42-48.

Robertson J.B. (1974) Digital modeling of radioactive and chemical waste transport in the Snake River Plain aquifer of the National Reactor Testing Station, Idaho. U.S. Geol. Surv. Open File Rep., IDO-22054.

Robertson J.B. and Barraclough J.T. (1973) Radioactive and chemical transport in groundwater of National Reactor Testing Station: 20-year case history and digital model. Underground Waste Manage. Artif. Recharge. Prepr. Pap. Int. Symp. 2nd, 1, 291-322.

Rosenberg N.D. and Spera F.J. (1992) Thermohaline convection in a porous medium heated from below. International Journal of Heat and Mass Transfer, 35, №5, 1261-1273.

Rowe A.M. and Chou J.C.S. (1970) Pressure-volume-temperature-concentration relation of aqueous NaCl solutions. Journal of Chemical Engineering Data, 15, 61-66.

Ruelle J.C. (1982) Depositional environments and genesis of stratiform copper deposits of the Redstone copper belt, MacKenzie Mountains, N.W.T. In: Hutchinson R.W., Spence C.D., and Franklin J.M. (Eds.) Precambrian Sulphide Deposits (H.S. Robinson Memorial Volume). Geological Association of Canada, Special Paper 25, 701-737.

Sarkar A., Nunn J.A. and Hanor J.S. (1995) Free thermohaline convection beneath allochthonous salt sheets: an agent for salt dissolution and fluid flow in Gulf Coast sediments. Journal of Geophysical Research, 100, №B9, 18085-18092.

Schardt C., Yang J., and Large R. (2005) Numerical heat and fluid-flow modeling of the Panorama volcanic-hosted massive sulfide district, Western Australia. Economic Geology, 100, 547-566.

Schoofs S., Spera F.J. and Hansen U. (1999) Chaotic thermohaline convection in low-porosity hydrothermal systems. Earth and Planetary Science Letters, 174, 213-229.

Schubert G. and Straus J. M. (1979) Three-dimensional and multicellular steady and unsteady convection in fluid-saturated porous media at high Rayleigh numbers. Journal of Fluid Mechanics, 94, 25-38.

Selley D., Broughton D., Scott R., Hitzman M., Bull S., Large R., McGoldrick P., Croaker M., Pollington N., and Barra F. (2005) A New Look at the Geology of the

Zambian Copperbelt. In: J.W. Hedenquist, J.F.H. Thompson, R.J. Goldfarb, and J.P. Richards (Eds) Economic Geology 100th Anniversary Volume, p.965-1000.

Sharp, I.R., Gawthorpe, R.L., Armstrong, B. and Underhill, J.R. (2000) Propagation history and passive rotation of mesoscale normal faults: implications for synrift stratigraphic development. Basin Research, 12, 285-305.

Simmons C.T., Fenstemaker T.R. and Sharp J.M.Jr. (2001) Variable-density groundwater flow and solute transport in heterogeneous porous media: approaches, resolutions and future challenges. Journal of Contaminant Hydrology, 52, 245-275.

Simms M.A. and Garven G. (2004) Thermal convection in faulted extensional sedimentary basins: theoretical results from finite-element modeling. Geofluids, 4, 109-130.

Smith G.E. (1976) Sabkha and tidal-flat facies control of stratiform copper deposits in north Texas. In: Johnson K.S. and Croy R.L. (Eds.) Stratiform Copper Deposits of the Midcontinent region, a Symposium: Oklahoma Geological Survey, Circular 77, 25-39.

Smith L., Forster C.B., and Evans J.P. (1990) Interaction of fault zones, fluid flow, and heat transfer at the basin scale. In: Hydrogeology of permeability environments: International Association of Hydrogeologists, 2, 41-67.

Sperrevik S., Gillespie P.A., Fisher Q.J., Halvorsen T., and Knipe R.J. (2002) empirical estimation of fault rock properties. In: Koestler A.G. and Hunsdale R. (Eds) *Hydrocarbon Seal Quantification, NPF Spec. Publ.*, v.11, Elsevier, New York, 109-125.

Sterner S.M., Hall D.L., and Bodnar R.J. (1988) Synthetic fluid inclusions. V. Solubility relations in the system NaCl-KCl-H2O under vapor-saturated conditions. Geochemical et Cosmochimica Acta, 52, 989-1006.

Sutton S.J. and Maynard J.B. (2005) A fluid mixing model for copper mineralization at Konkola North, Zambian Copperbelt. Journal of African Earth Sciences, 42, 95-118.

Sverjensky D.A. (1989) Chemical evolution of basinal brines that formed sediment-hosted Cu-Pb-Zn deposits. In: Boyle R. W., Brown A. C., Jefferson C.W., Jowett E.C. and Kirkham R.V., (Eds.), Sediment-hosted Stratiform Copper Deposits, Geological Association of Canada, Special Paper 36, 127-134.

Sweeney, M.A. and Binda, P.L. (1989) The role of diagenesis in the formation of the Konkola Cu-Co orebody of the Zambian Copperbelt. In: Boyle, R. W., Brown, A. C., Jefferson, C.W., Jowett, E. C. and Kirkham, R.V. (Eds.) Sediment-hosted Stratiform Copper Deposits. Geological Association of Canada, Special Paper, 36, 499-518.

Swenson J.B., Person M., Raffensperger J.P., Cannon W.F., Woodruff L.G., and Berndt M.E. (2004) A hydrogeologic model of stratiform copper mineralization in the Midcontinent Rift System, Northern Michigan, USA. *Geofluids*, 4, 1-22.

Tamma K.K., Zhou X., Sha D. (1999) Transient algorithms for heat transfer: general developments and approaches for theoretically generating Nth-order time-accurate operators including practically useful second-order forms. International Journal for Numerical Methods in Engineering, 44, 1545-1572.

Telford W.M., Geldart L.P., and Sheriff R.E. (1990) Applied Geophysics. Second Edition. Cambridge University Press, 770 pp.

Tyn Myint-U (1973) Partial Differential Equations of Mathematical Physics. American Elsevier Publishing Company, Inc., 365pp.

Tihonov A., Samarskiy A. (1999) Equations of Mathematical Physics. Moscow University Publishing House, 798pp. (in Russian)

Trevisan O.V. and Bejan A. (1987) Mass and heat transfer by high Rayleigh number convection in a porous medium heated from below. International Journal of Heat and Mass Transfer, 30, 2341-2356.

Trevisan O.V. and Bejan A. (1990) Combined heat and mass transfer by natural convection in a porous medium. Advances in Heat Transfer, 20, 314-352.

Unrug R. (1988) Mineralization controls and source of metals in the Lufilian Fold Belt, Shaba (Zaire), Zambia and Angola. Economic Geology, 83, 1247-1258.

Vaccaro J.J. and Bolke E.L. (1983) Evaluation of water quality characteristics of part of the Spokane aquifer, Washington and Idaho, using a solute transport digital model, U.S. Geol. Surv. Open File Rep., 82-769.

van Eden, J.G. and Binda, P.L. (1972) Scope of stratigraphic and sedimentologic analysis of the Katanga sequence, Zambia. Geologie en Minbouw, 51, 321-328.

Vaughan D.J., Sweeney M., Friedrich G., Diedel R., and Haranczyk C. (1989) The Kupferschiefer: An overview with an appraisal of the different types of mineralization, Economic Geology, 84, 1003-1027.

Volodin R.N., Chechetkin V.S., Bogdanov Y.V., Narkelyun L.F., and Trubachev A.I. (1994) The Udokan cupriferous sandstones deposit (eastern Siberia), Geology of Ore Deposits, 36, 1-25.

von Hoyningen-Huene E. (1963) Zur Palaohydrogeologie des Oberrotliegeden und des Zechsteins im Harzvorland: Deutsche Gesellschaft fur geologische Wissenschaften: Berichte, 8, 201-220.

Walker T.R. (1989) Application of diagenetic alterations in redbeds to the origin of copper in stratiform copper deposits. In: Boyle R. W., Brown A. C., Jefferson C.W., Jowett E.C. and Kirkham R.V., (Eds.), Sediment-hosted Stratiform Copper Deposits, Geological Association of Canada, Special Paper 36, 85-96.

Wang H.F., Anderson M.P. (1982) Introduction to Groundwater Modeling. W.H.Freeman and Company, 237pp.

Warren J. (1999) Evaporites. Their Evolution and Economics. Blackwell Science, 438pp.

Watson J.T.R, Basu R.S., Sengers J.V. (1980) An improved representative equation for the dynamic viscosity of water substance. Journal of Physical Chemical Reference Data, 9, №4, 1255-1290.

Wendorff M. (2000a) Genetic aspects of the Katangan megabreccias. Journal of African Earth Sciences, 30, 703-715.

Wendorff M. (2000b) Revision of the stratigraphical position of the "Roches Argilo-Talqueuse" (R.A.T.) in the Neoproterozoic Katangan Belt, south Congo. Journal of African Earth Sciences, 30, 717-726.

Wendorff M. (2003) Stratigraphy of the Fungurume Group – evolving foreland basin succession in the Lufilian fold-thrust belt, Neoproterozoic – Lower Paleozoic, Democratic Republic of Congo. South African Journal of Geology, 106, 17-34.

White W.S. (1971) A paleohydrologic model for mineralization of the White Pine copper deposit, northern Michigan. Economic Geology, 66, 1-13.

Wood W. (1981) A geochemical method of determining dispersivity of regional ground water systems, J. Hydrol., 54(1/3), 209-224.

Yang J., Bull S., and Large R. (2004a) Factors controlling free thermal convection in faults in sedimentary basins: implications for the formation of zinc-lead mineral deposits. Geofluids, 4, 237-247.

Yang J., Bull S., and Large R. (2004b) Numerical investigation of salinity in controlling ore-forming fluid transport in sedimentary basins: example of the HYC deposit, Northern Australia, Mineralium Deposita, 39, 622-631.

Yaramanci U. (1994) Relation of in situ resistivity to water content in salt rocks. Geophysical Prospecting, 41, 229-239.

Yardley B.W.D. (2005) Metal concentration in crustal fluids and their relationship to ore formation. Economic Geology, 100, 613-632.

Yechieli Y., Ronen D. and Berkowitz B. (1995) Are sedimentary salt layers always impermeable? Geophysical Research Letters, 22, 2761-2764.

Yielding G. (2002) Shale Gouge Ratio – calibration by geohistory. In: Koestler A.G. and Hunsdale R. (Eds) *Hydrocarbon Seal Quantification, NPF Spec. Publ.*, v.11, Elsevier, New York, 1-15.

Zienkiewicz O.C. (1977) The Finite Element Method. McGRAW-HILL Book Company (UK) Limited, 787pp.

Zienkiewicz O.C., Heinrich J.C. (1978) The finite element method and convection problems in fluid mechanics. In: Gallagher R.H., Zienkiewicz O.C., Oden J.T., Morandi Cecchi M., and Taylor C. (Eds.) Finite Elements in Fluids, volume3. John Willey & Sons, 396pp.

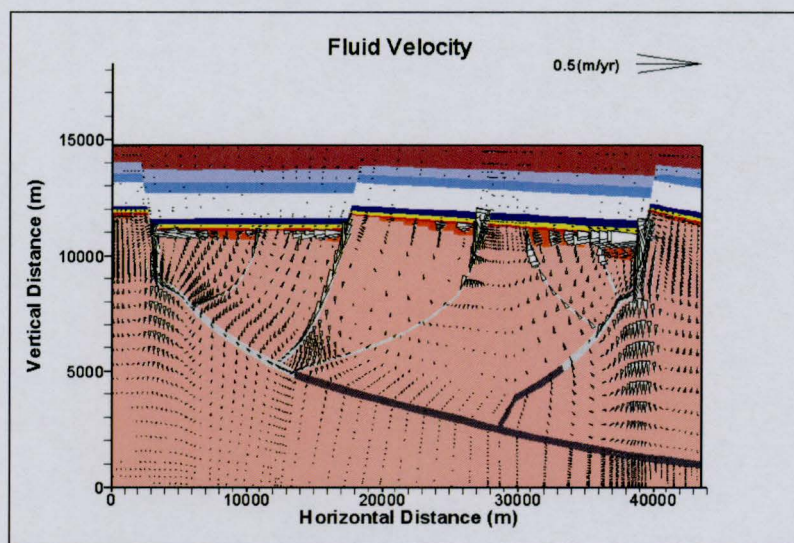Zienkiewicz O.C., Taylor R.L. (2000) The Finite Element Method. Vol.3: Fluid Dynamics. Batterworth-Heinemann, 334pp.
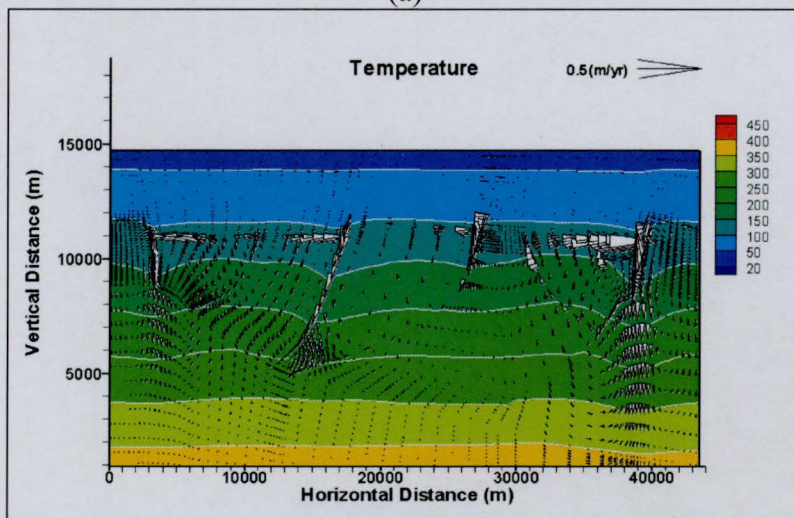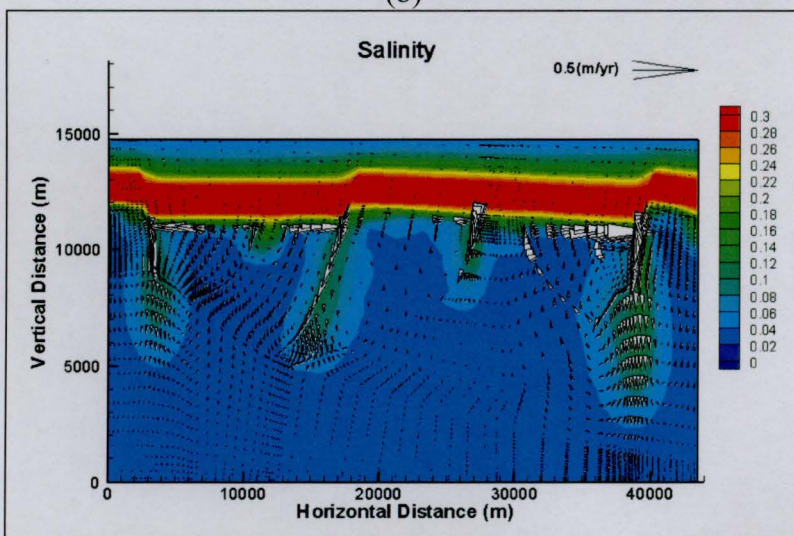
# Appendices

***Appendix 1*** Case3 (the initial stage of the Kundelungu deposition). Supplementary figures
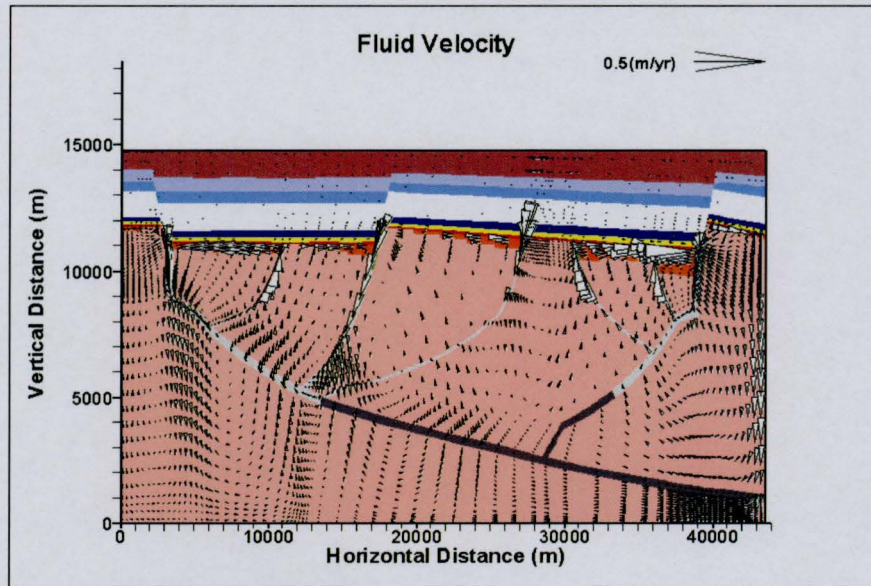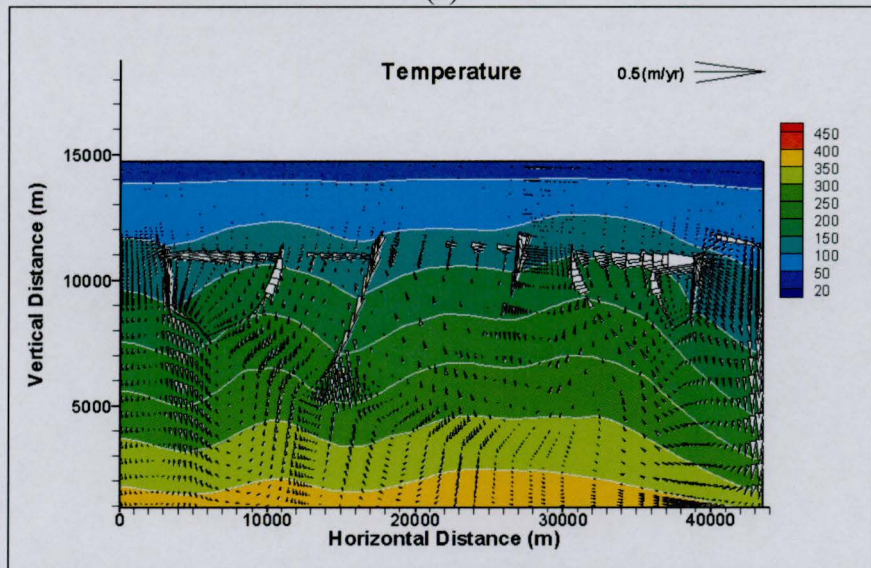


(a)



(b)



(c)

**Figure A 1.1 ZCB. Case3. The initial stage of the Kundelungu deposition. T1: (a) fluid velocities, (b) temperature and (c) salinity distributions.**
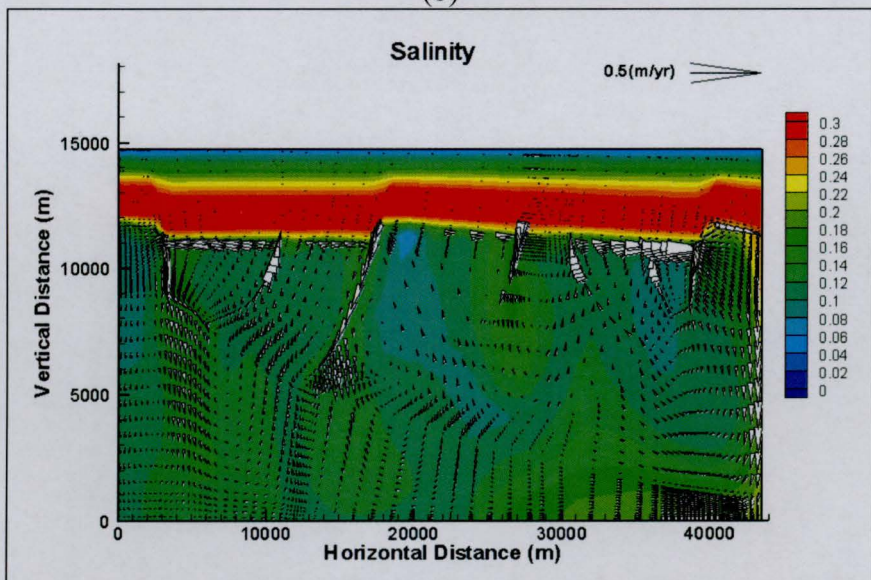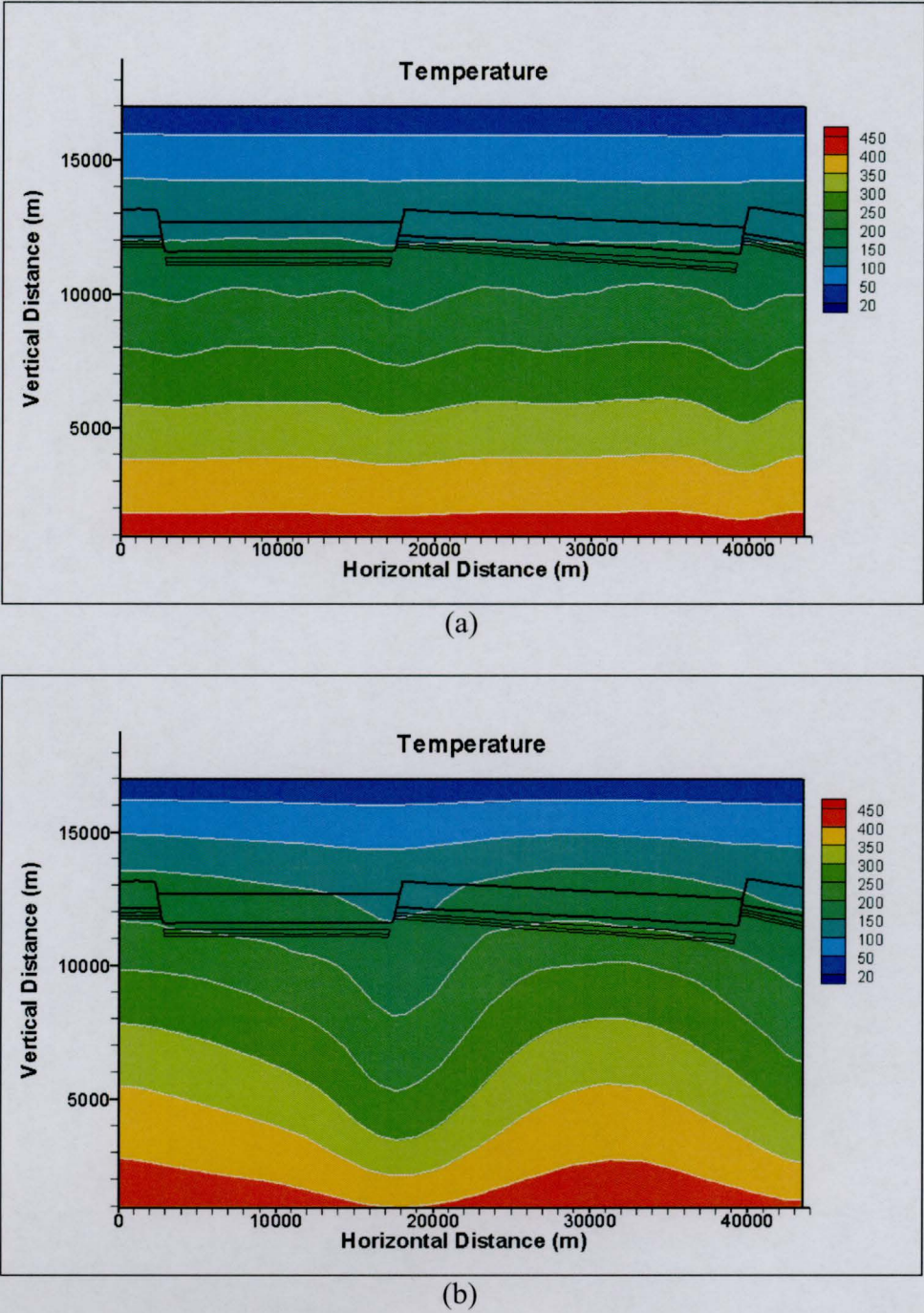
(a)

(b)

(c)

**Figure A 1.2 ZCB. Case3. The initial stage of the Kundelungu deposition. T2: (a) fluid velocities, (b) temperature and (c) salinity distributions.**

### *Appendix 2* Case 6 (no permeable faults). Supplementary figures



(a)



(b)

**Figure A 2.1 ZCB. Case 6. No permeable faults. Temperature distributions (a) at T1 and (b) at T2.**

## *Appendix 3* Active diapirism above the Upper Roan Salt

The object of the following two case studies was to investigate the possible effect of the formation of diapiric salt structures. Salt dissolution/diapiric mobilization can lead to formation of highly permeable zones in strata overlying the salt sheet. On the one hand, it can be a result of brecciation around the building diapir, on the other it can be a consequence of caving of the overlying rock above the location where the salt layer is thinned out.

To avoid a significant modification of the section hydrostratigraphy and numerical mesh, in *Case 10*, the Upper Roan Salt was connected with the surface by three permeable segments (fault continuations) located above the positions of the master faults in the basic hydrostratigraphy of the section.

These fault segments (marked light green in Figure A 3.1(a)) are prescribed a high permeability $10^{-14} \, m^2$, similar to the Mindola Clastic Formation and Kundelungu strata. However, unlike these sedimentary units, the segments are isotropic and therefore have two orders of magnitude higher vertical permeability. They were also made more porous. The full list of physical properties is shown in Table 5.1 as 'faults: uppermost section'.

Strictly speaking, this scenario is not an accurate simulation of a diapir, not only because of the schematic geometry, but also as it does not take into account linked thermal effects (high thermal conductivity of salt structures) and additional salinity sources (in the elements representing the diapir). The aim of this case study was to see solely the effect of diapir associated zones of high permeability.

The fault network below the Upper Roan Salt is considered inactive, that allows the simulation results to be compared with Case 6 (no permeable faults) and to see solely the effect of the diapiric structures.

Diagrams showing fluid velocity field, temperature and salinity distributions at T1 and T2 are presented in Figure A 3.2–Figure A 3.3 respectively.

Comparing the results of the simulation in Case 10 and Case 6 (no permeable faults) scenarios, one can see that they are practically identical. The only difference is a very weak upflow in the permeable conduits at the very end of the simulation. The salinity distribution in the Kundelungu is slightly modified, but there is little impact on the temperature field (Figure A 3.2). The reason for this is the strong stable stratification of the pore fluid above the Upper Roan Salt (as a result of diffusion). This leads to a subdued thermal instability until the moment when the

temperature at the bottom of the Kundulungu rises enough (chiefly due to conduction rather than advection) to initiate the upflow in the uppermost part of the piercement structure.

At this fault configuration, there is no connection between the layers above and below the impermeable Upper Roan Salt. Hence, there is no access to the pore fluid of a higher temperature or a lower salinity that could destabilize the system and activate convective flow.

In ***Case 10A***, the uppermost layer of the Roan Salt (horizontal light green zone in Figure A 3.1(b)), approximately 160m thick, was set as permeable as the conduits simulating diapirs. A layer like this may develop as a result of brecciation at the onset of salt dissolution/mobilization.

However, this addition, that was intended to provide a convenient pathway connecting the vertical permeable zones, cannot facilitate any convection above the salt layer. The results of the simulation (Figure A 3.4Figure A 3.5) are hardly distinguishable from Figure A 3.2Figure A 3.3. Only very weak fluid flow can be seen in this additional permeable horizontal layer and immediately above the Upper Mwashia – Kundelungu contact. However, it does not affect either temperature or salinity distributions.

Thus, Cases 10 and 10A demonstrate that it is impossible to activate any significant fluid flow above the salt layer unless the fluid from below the Upper Roan Salt has an access into the top clastic strata.
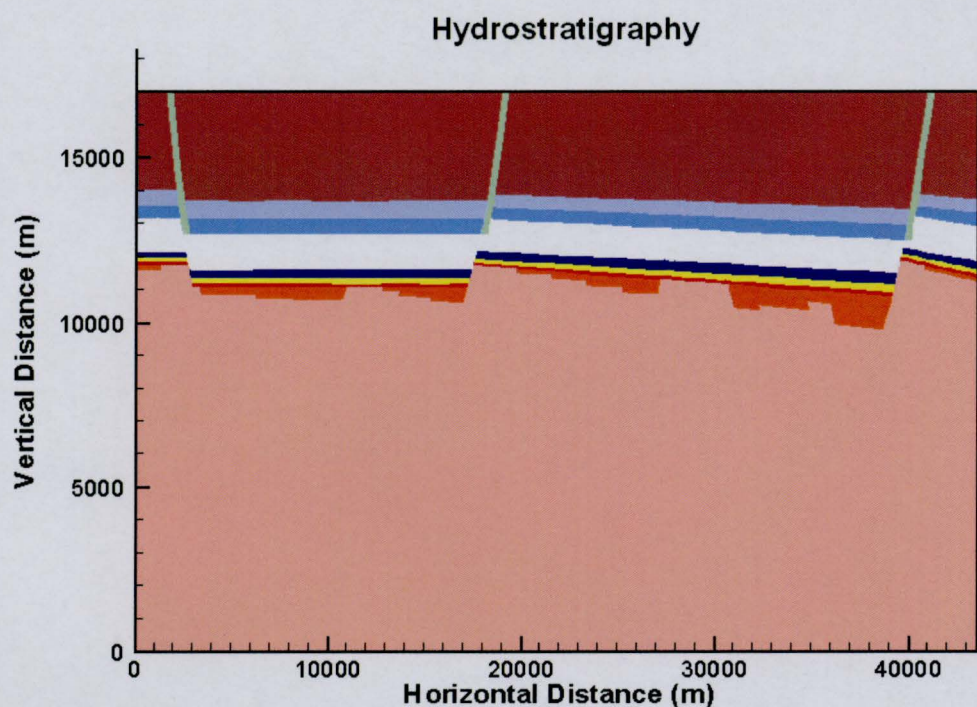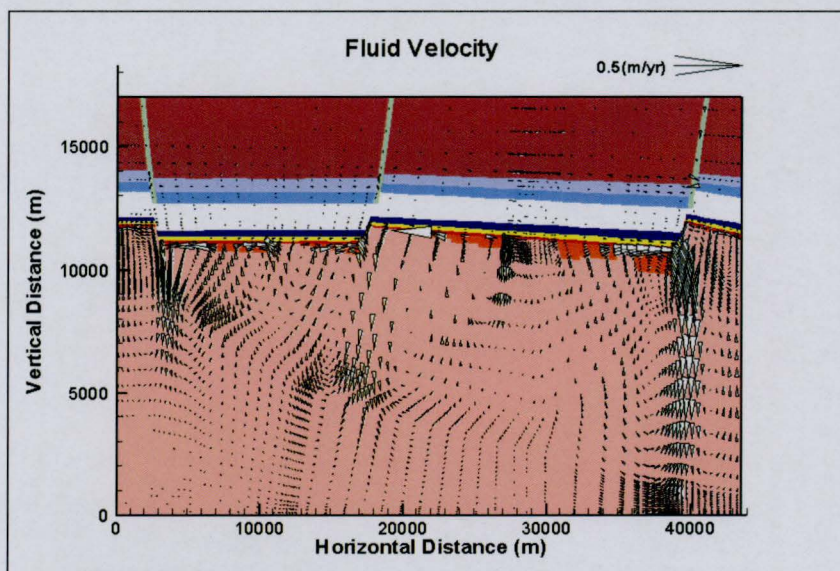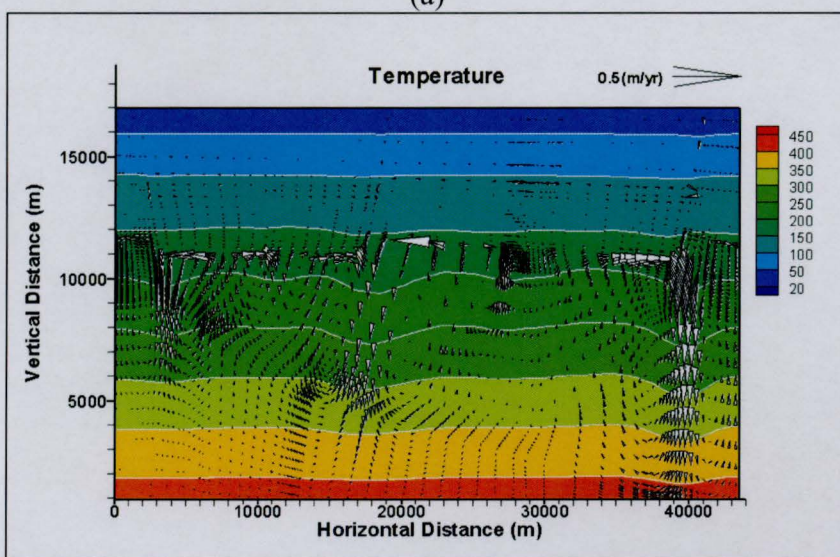
(a)
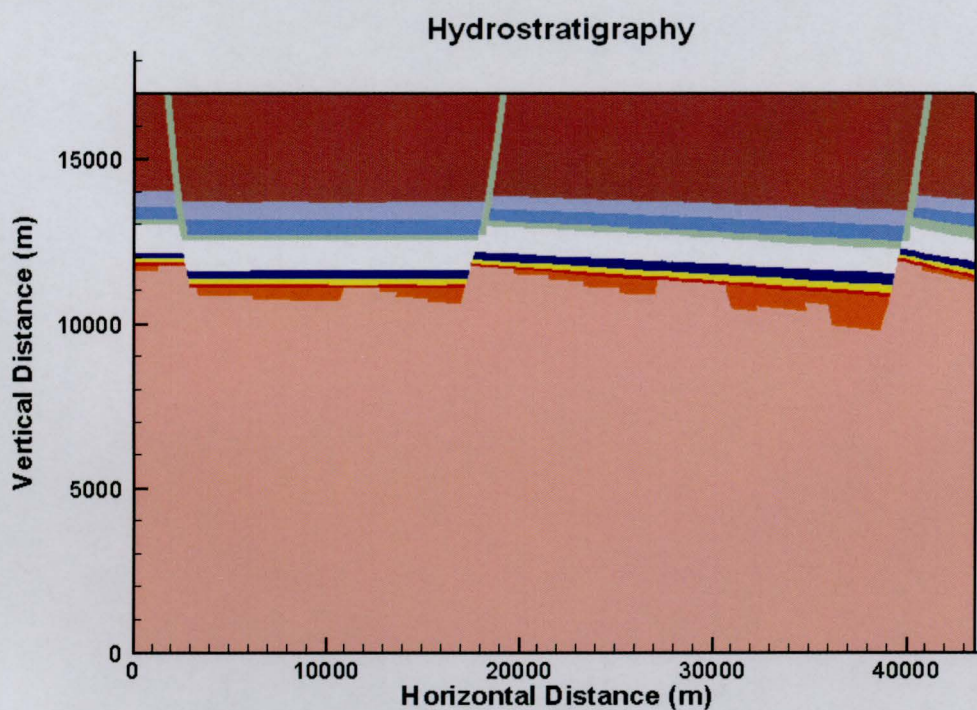


(b)

**Figure A 3.1 ZCB. Active diapirism above the Upper Roan Salt. Numerical hydrostratigraphy of the model section. (a) Case 10: no permeable fault zones below the Upper Roan Salt. Permeable segments above the locations of master faults. (b) Case10A: a permeable horizontal layer within the Upper Roan Salt is added to connect the vertical conduits.**
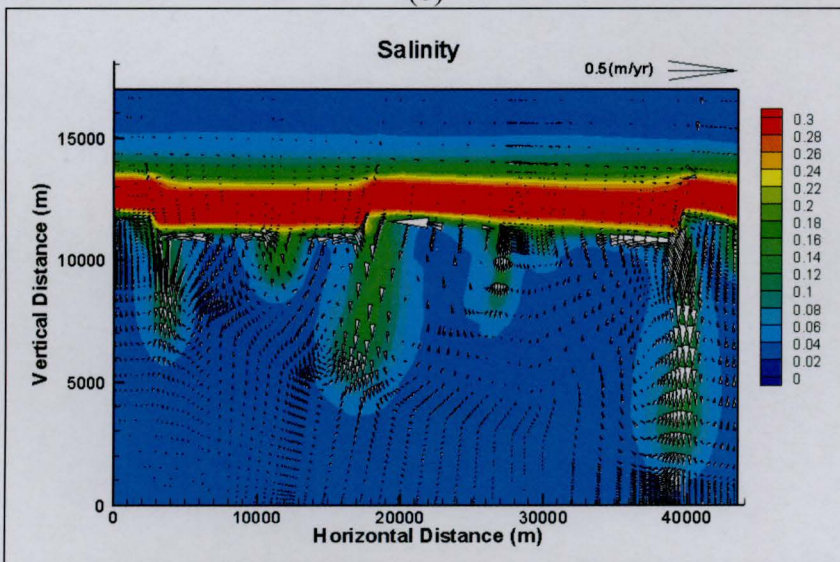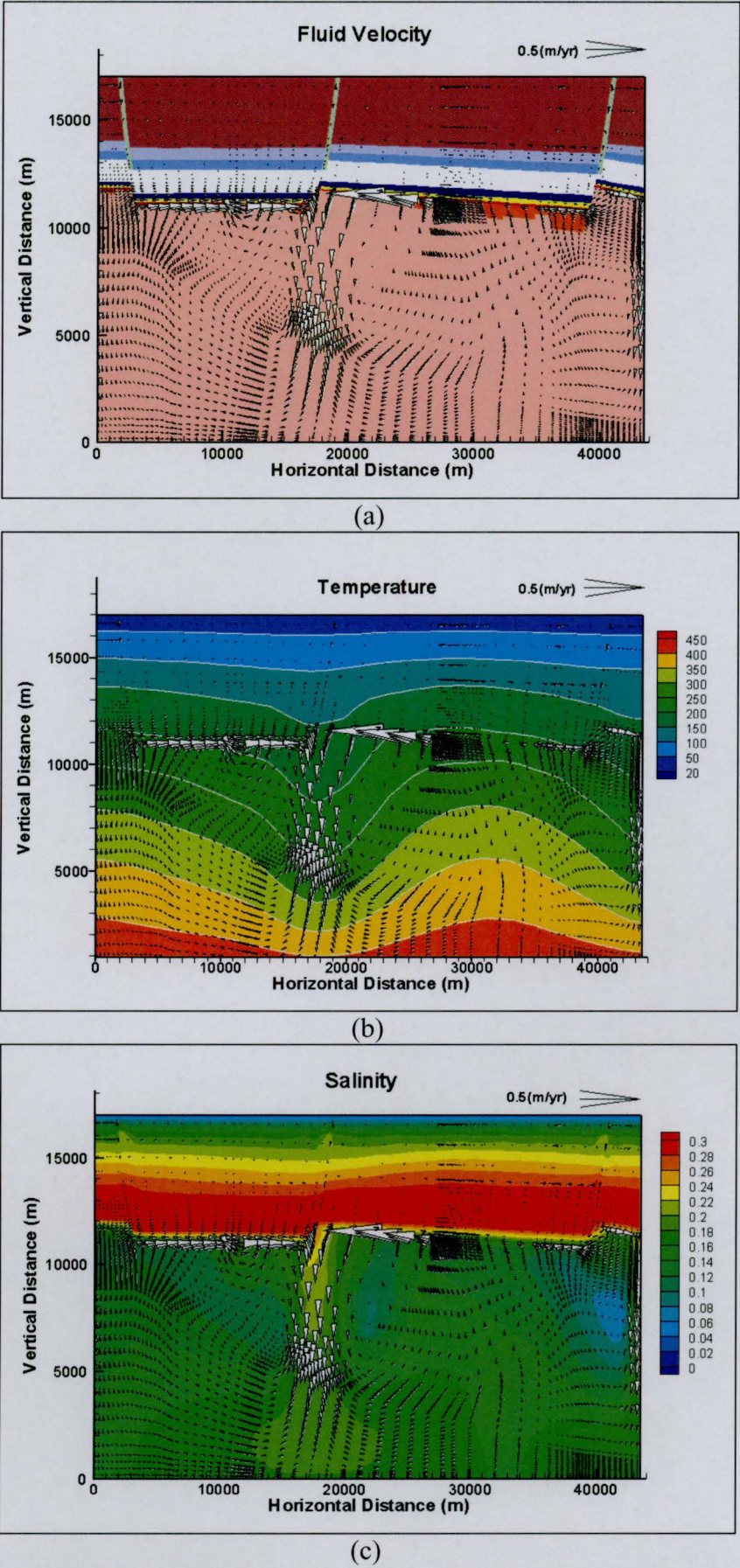
**Figure A 3.2 ZCB. Active diapirism above the Upper Roan Salt. Case 10: No permeable fault zones below the Upper Roan Salt. Permeable segments above the locations of master faults. T1: (a) fluid velocity, (b) temperature, and (c) salinity fields.**
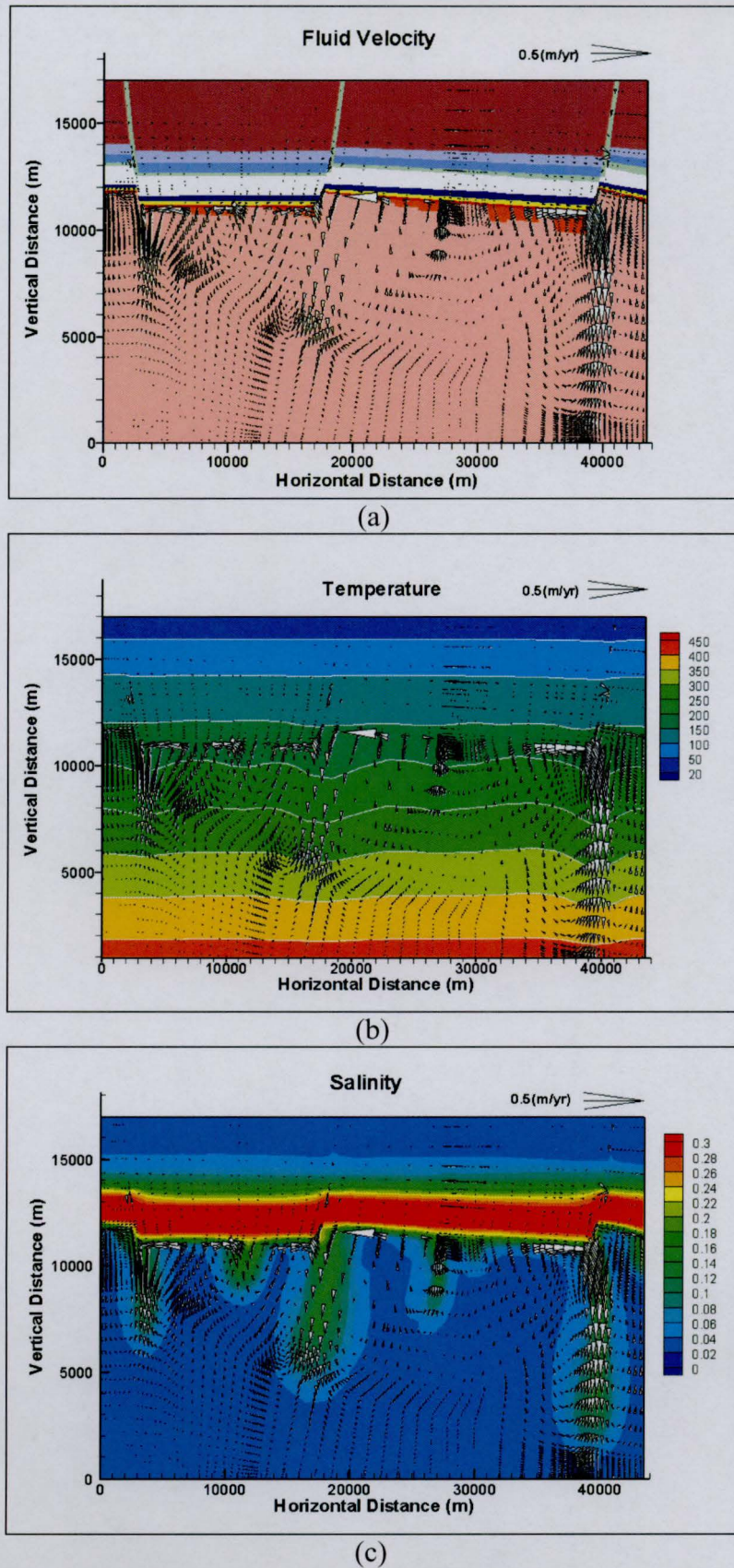
228

(a)

(b)

(c)

**Figure A 3.3 ZCB. Active diapirism above the Upper Roan Salt. Case 10: No permeable fault zones below the Upper Roan Salt. Permeable segments above the locations of master faults. T2: (a) fluid velocity, (b) temperature, and (c) salinity fields.**

(a)



(b)



(c)

**Figure A 3.4 ZCB. Active diapirism above the Upper Roan Salt. Case 10A: No permeable fault zones below the Upper Roan Salt. Permeable segments above the locations of master faults. A permeable horizontal layer within the uppermost part of the Upper Roan salt is added. T1: (a) fluid velocity, (b) temperature, and (c) salinity fields.**
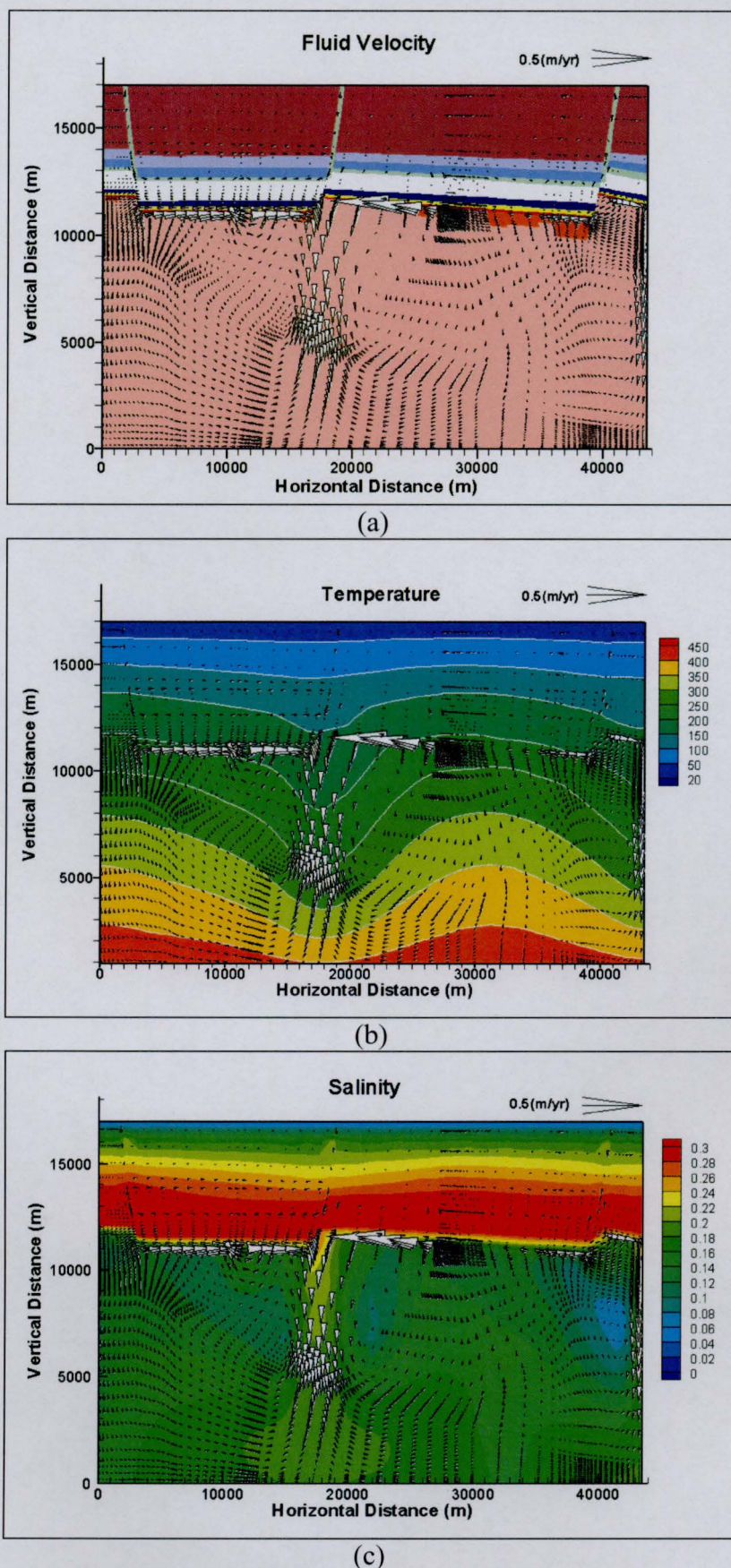
230

(a)



(b)



(c)

**Figure A 3.5 ZCB. Active diapirism above the Upper Roan Salt. Case 10A: No permeable fault zones below the Upper Roan Salt. Permeable segments above the locations of master faults. A permeable horizontal layer within the uppermost part of the Upper Roan salt is added. T2: (a) fluid velocity, (b) temperature, and (c) salinity fields.**

231

## *Appendix 4*  Middle primary fault extension. Supplementary figures
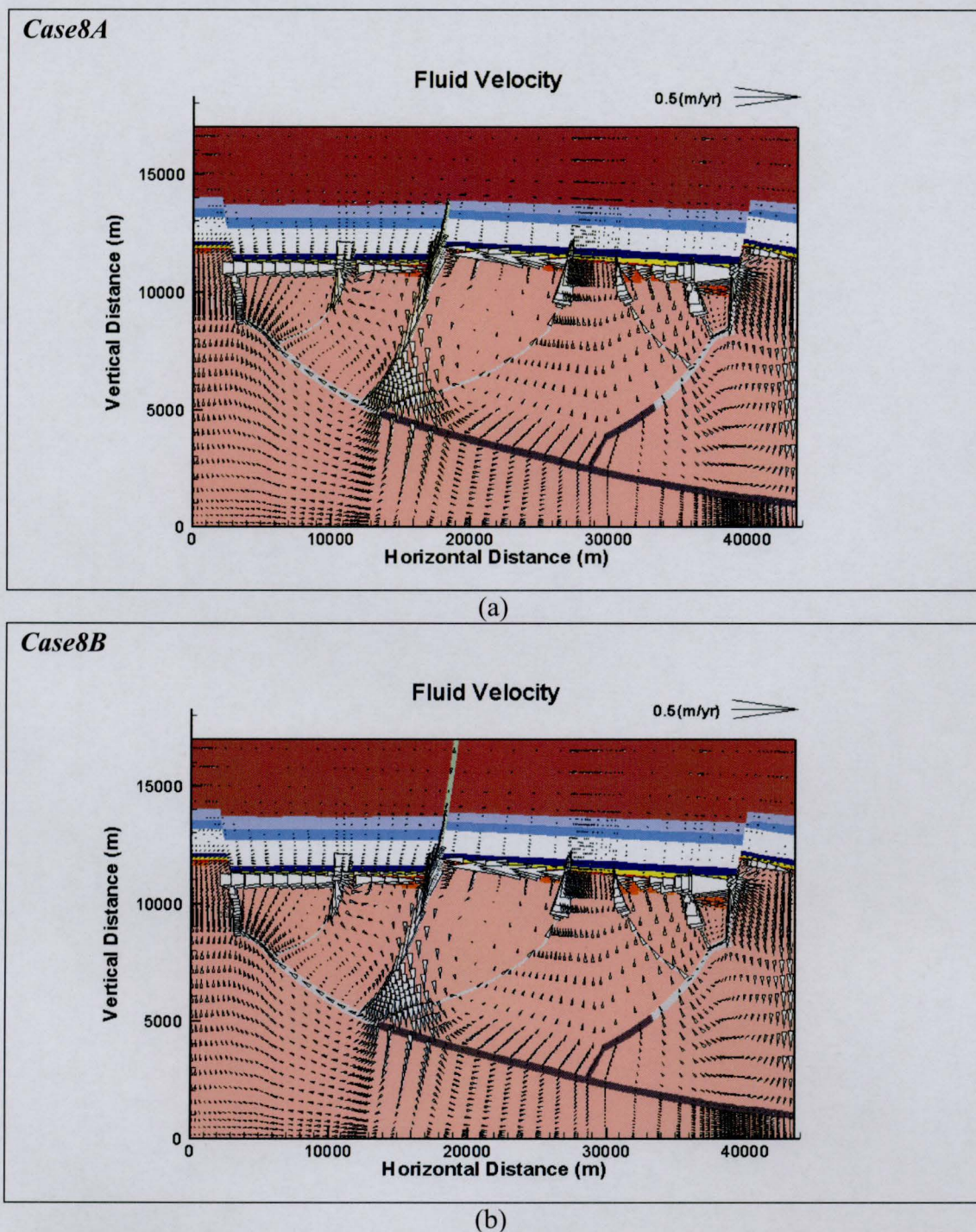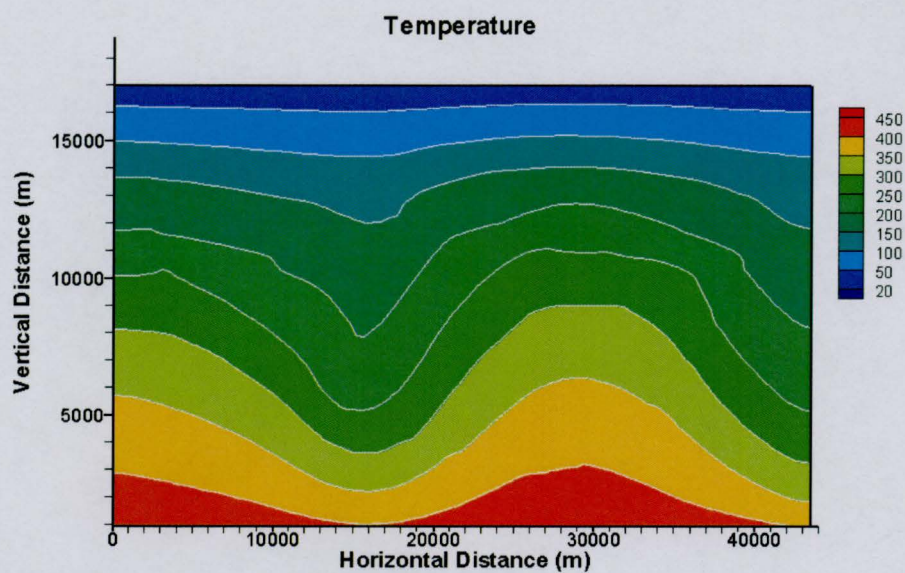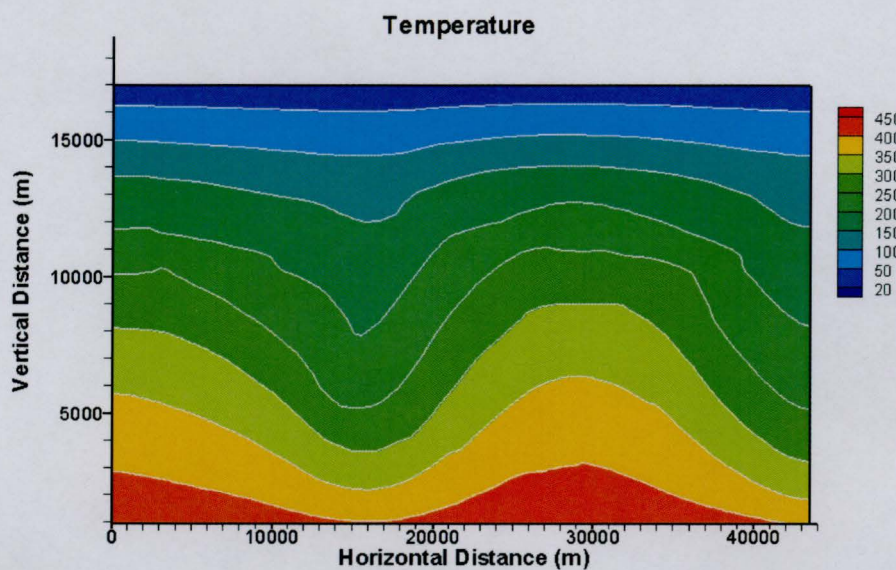


(a)



(b)

**Figure A 4.1 ZCB. Effect of piercement structures cutting the Upper Roan Salt. Comparison of fluid velocity fields at T2.**
**(a) Case8A (the middle master fault is extended to the contact 'Upper Mwashia Siliciclastic Member' – 'Kundelungu'); (b) Case8B (the middle master fault is extended to the surface).**

(a)



(b)

**Figure A 4.2 ZCB. Effect of piercement structures cutting the Upper Roan Salt. Comparison of temperature fields at T2.**
(a) Case8A (the middle master fault is extended to the contact 'Upper Mwashia Siliciclastic Member' – 'Kundelungu'); (b) Case8B (the middle master fault is extended to the surface).